Feedback from groundwater and irrigation on past and future climate simulated by the IPSL climate model

Pedro Felipe Arboleda-Obando

Doctorat de Sorbonne Université

École doctorale n° 398 : Géosciences, Ressources Naturelles et Environnement

THÈSE

pour obtenir le grade de docteur délivré par

Sorbonne Université

Spécialité : Hydrologie

présentée et soutenue publiquement par

Pedro Felipe Arboleda-Obando

le 22 mars 2023

Feedback from groundwater and irrigation on past and future climate simulated by the IPSL climate model

Devant le jury conposé par:

M. Olivier Boucher,	Directeur de recherche LMD - Sorbonne U.	Président
M. Gonzalo Miguez-Macho,	Professeur, U. de Santiago de Compostela	Rapporteur
Mme Isabelle Braud,	Directrice de recherche, RiverLy INRAE	Rapporteur
Mme Sandrine Anquetin,	Directrice de recherche, IGE U. Grenoble Alpes	Examinateur
M. Aaron Boone,	Directeur de recherche, CNRM-Météo-France	Examinateur
Mme Agnès Ducharne,	Directrice de recherche, METIS - Sorbonne U.	Directrice de thèse
Mme Frédérique Cheruy,	Chargé de recherche, LMD - Sorbonne U.	Invitée

Sorbonne Université
UMR Milieux environnementaux, transferts et interactions dans les hydrosystèmes et les sols (METIS)

Case 105 - Tour 46/56 - 3^{eme} etage - 4 place Jussieu - 75252 Paris Cedex 05 - France

El coronel necesitó setenta y cinco años —los setenta y cinco años de su vida, minuto a minuto— para llegar a ese instante. Se sintió puro, explícito, invencible, en el momento de responder:
—Mierda.

El Coronel No Tiene Quien le Escriba
Gabriel García Márquez

Summary

Continental fluxes play an important role in the water cycle, and in the evolution of climate at different time scales. It is particularly interesting to note the control that soil moisture can exert on evapotranspiration, since an anomaly of the former can induce a change of the latter. This produces changes in the seasonal and long-term evolution of climatic variables such as precipitation and temperature. The coupling between soil moisture and evapotranspiration, and their effects on climate, have led to focus on those landscape factors that have some effect on soil moisture. This study focuses on two: downward hillslope flows (surface and subsurface) caused by topography, of natural origin, and water transfers for irrigation activities, of human origin. One of the tools for studying climate is the use of general circulation models, consisting of an atmospheric model and a land surface model. Land surface models, although increasingly complex, have limited or no representation of the effect of topography on land surface fluxes and of the anthropogenic effects on water resources. The objective of this thesis is to understand the effect of each landscape driver on terrestrial fluxes and on present and future climate, using the ORCHIDEE land surface model, which is part of the IPSL climate model.

The first part of this thesis uses a simple representation of hillslope flows within ORCHIDEE. The typical model grid-cell is divided into an upland and lowland zone to represent the topography, with the lowland fraction being potentially wetter. LMDZOR, which couples ORCHIDEE to the IPSL atmospheric model, known as LMDZ, was used to run two long-term simulations (between 1980 and 2100) under climate change, with and without hillslope flow. The results show increases in soil moisture and evapotranspiration, a slight increase in rainfall and lower air temperature. Under climate change, hillslope flows attenuate part of the climate change-induced decreases in soil moisture, evapotranspiration and precipitation, and slightly decrease warming.

In the second part, an irrigation scheme was implemented in ORCHIDEE, for use at global scale. The water demand is calculated according to the soil moisture deficit and the irrigated area, and the supply depends on natural reservoirs under two constraints: a volume left available for ecosystems (ecological flow) and water allocation according to existing local infrastructure. The new scheme was tested in offline mode, (forced with meteorological data). Comparison with observed data shows that including irrigation decreases negative modeling biases for evapotranspiration, but increases positive biases for leaf area index (except in intensively irrigated areas, where the negative bias of leaf area index decreases). Likewise, irrigation decreases the discharge of large rivers, but this does not lead to a better representation of discharge dynamics compared to observations.

The results show that landscape drivers increase certain fluxes of the water and energy balances, and in the case of hillslope flows, attenuates part of the decreases due to climate

change. In the case of irrigation, online simulations are needed to know its effect on the evolution of hydroclimatic variables under climate change. In addition, considering the joint effects of the two landscape drivers is necessary, which calls for including hillslope flows and irrigation in a new version of ORCHIDEE.

Résumé

Les flux terrestres jouent un rôle important dans le cycle de l'eau et dans l'évolution du climat à différentes échelles de temps. Il est intéressant de noter le contrôle que l'humidité du sol peut exercer sur l'évapotranspiration, puisqu'une anomalie de la première peut induire une perturbation sur la seconde. Cela produit des changements dans l'évolution saisonnière et à long terme des variables climatiques telles que les précipitations et la température. Le couplage entre l'humidité du sol et l'évapotranspiration et ses effets sur le climat ont conduit à se pencher sur les éléments du paysage qui ont un certain effet sur l'humidité du sol. Cette thèse se concentre sur deux d'entre elles : les écoulements descendants des pentes (de surface et souterrains) causés par la topographie d'origine naturelle et les transferts d'eau pour les activités d'irrigation d'origine humaine.

L'un des outils d'étude du climat est l'utilisation de modèles de circulation générale, qui couple un modèle atmosphérique et un modèle de surface terrestre. Les modèles de surface, bien que de plus en plus complexes, ont une représentation limitée ou nulle de l'effet de la topographie sur les flux de surface terrestre et des effets anthropiques sur les ressources en eau. L'objectif de cette thèse est de comprendre l'effet de chaque élément du paysage sur les flux terrestres et sur le climat actuel et futur, en utilisant le modèle de surface terrestre ORCHIDEE, qui fait partie du modèle climatique IPSL.

La première partie de cette thèse utilise une représentation simple des écoulements des pentes dans ORCHIDEE. La maille est divisée en une zone haute et une zone basse pour représenter la topographie, cette derniere étant potentiellement plus humide. LMDZOR, qui couple ORCHIDEE à LMDZ (le modèle atmosphérique de l'IPSL) a été utilisé pour effectuer deux simulations à long terme (entre 1980 et 2100) sous changement climatique, avec et sans écoulement de pente. Les résultats montrent une augmentation de l'humidité du sol et de l'évapotranspiration, une légère augmentation des précipitations et une baisse de la température de l'air. Dans le cadre du changement climatique, les écoulements de pente atténuent une partie des diminutions de l'humidité du sol, de l'évapotranspiration et des précipitations liés au changement climatique, et diminuent légèrement le réchauffement.

La deuxième partie présente un schéma d'irrigation inclu dans ORCHIDEE, pour une utilisation à l'échelle mondiale. La demande en eau est calculée à partir du déficit hydrique du sol et de la surface irriguée. L'approvisionnement dépend des réservoirs naturels sous deux contraintes : un volume laissé disponible pour les écosystèmes (flux écologique) et une répartition de l'eau en fonction des infrastructures locales existantes. Le nouveau schéma a été testé en mode offline (forcé avec les données météorologiques). La comparaison avec les données observées montre que l'inclusion de l'irrigation diminue les biais négatifs de modélisation pour l'évapotranspiration, mais augmente les biais positifs pour l'indice de surface foliaire (sauf dans les zones d'irrigation intensive où le biais négatif de l'indice diminue).

De même, l'irrigation diminue le débit des grands fleuves, mais cela ne conduit pas à une meilleure représentation de la dynamique du débit par rapport aux observations.

Les résultats montrent que les éléments du paysage augmentent certains flux des bilans hydriques et énergétiques et, pour les écoulements de pente, atténuent une partie des diminutions dues au changement climatique. Dans le cas de l'irrigation, des simulations online sont nécessaires pour connaître son effet sur l'évolution des variables hydroclimatiques dans le cadre du changement climatique. De plus, il est nécessaire de considérer les effets conjoints des deux éléments du paysage, ce qui demande d'inclure les flux de pente et l'irrigation dans une nouvelle version d'ORCHIDEE.

Resumen

Los flujos continentales juegan un rol importante en el ciclo del agua, y en la evolución del clima a diferentes escalas de tiempo. De especial interés es el control que puede ejercer la humedad del suelo sobre la evapotranspiración, ya que una anomalía de la primera puede inducir un cambio de la segunda. Esto produce cambios en la evolución estacional y en la evolución a largo plazo, de variables climáticas como la precipitación y la temperatura. El acoplamiento humedad del suelo-evapotranspiración, y sus efectos sobre el clima, han llevado a interesarse por aquellos controladores del paisaje con algún efecto sobre la humedad del suelo. Esta tesis se concentra en dos: los flujos descendentes de pendiente (superficiales y subsuperficiales) provocados por la topografía, de origen natural, y las transferencias de agua para actividades de riego, de origen humano. Una de las herramientas para estudiar el clima es el uso de modelos de circulación general, conformado por un modelo atmosférico y un modelo de superficie terrestre. Los modelos terrestres, pese a ser cada vez más complejos, representan de manera limitada o nula el efecto de la topografía sobre los flujos de la superficie terrestre, y los efectos antrópicos sobre los recursos hidrológicos. El objetivo de esta tesis es entender el efecto de cada controlador de paisaje en los flujos terrestres y en el clima presente y futuro, utilizando como herramienta el modelo de superficie terrestre ORCHIDEE, que hace parte del modelo climático del IPSL. La primera parte de este trabajo utilizó una representación simple de los flujos de pendiente dentro de ORCHIDEE. La celda de cuadrícula típica del modelo se dividió en una zona alta y otra baja para representar la topografía, siendo la zona baja potencialmente más húmeda. Se utilizó el sistema LMDZOR, que acopla ORCHIDEE al modelo atmosférico del IPSL, conocido como LMDZ, para realizar dos simulaciones de largo plazo (entre 1980 y 2100) bajo efectos de cambio climático, con y sin flujos de pendiente. Los resultados muestran incrementos de humedad del suelo y de la evapotranspiración, un ligero aumento de la lluvia y menor temperatura del aire. Bajo cambio climático, los flujos de pendiente atenúan parte de las disminuciones provocadas por cambio climático sobre humedad del suelo, evapotranspiración y precipitación, y reducen ligeramente el calentamiento. En la segunda parte se implementó un esquema de riego en ORCHIDEE, para uso a escala global. La demanda de agua se calcula según el déficit de humedad del suelo y la fracción irrigada, y la oferta depende de los almacenamientos naturales bajo dos restricciones: un volumen disponible para los ecosistemas (caudal ecológico) y la asignación del agua según la infraestructura local existente. El nuevo esquema se probó en modo offline, (forzado con datos meteorológicos). La comparación con datos observados muestra que incluir el riego disminuye los sesgos negativos de la modelación en la evapotranspiración, pero aumenta los sesgos positivos para el índice de área foliar (excepto en áreas intensamente regadas, donde el sesgo negativo del índice disminuye). Así mismo, el riego disminuye los caudales de los grandes ríos, pero esto no se traduce en una mejor representación

de la dinámica de los caudales frente a los datos observados. Los resultados muestran que los controladores del paisaje aumentan ciertos flujos de los balances hídricos y energéticos, y para el caso de los flujos de pendiente, atenúan parte de las disminuciones producto del cambio climático. Para el caso de riego, se necesitan simulaciones online para conocer su efecto en la evolución de las variables hidroclimáticas bajo cambio climático. Además, es necesario considerar los efectos conjuntos de los dos controladores del paisaje, lo que llama a incluir los flujos de pendiente y el riego en una nueva versión de ORCHIDEE.

Résumé étendu

La partie continentale du cycle de l'eau joue un rôle important dans les flux du cycle de l'eau et dans l'évolution du climat à différentes échelles de temps. Le contrôle que l'humidité du sol peut exercer sur les flux à la surface du sol, en particulier l'évapotranspiration, ou la chaleur latente en termes d'énergie, est particulièrement intéressant. En effet, dans les zones où l'énergie est disponible en abondance mais où l'humidité du sol est limitée, une anomalie dans la valeur de l'humidité du sol peut augmenter ou diminuer l'évapotranspiration, ce qui a un impact sur la répartition de l'énergie et la température de surface. Ce processus peut avoir des effets sur l'évolution saisonnière des températures et des précipitations, ainsi que sur l'évolution à long terme sous l'effet du changement climatique en cours. L'importance du couplage entre l'humidité du sol et l'évapotranspiration, et les effets que ce couplage peut avoir sur le climat actuel et futur, a conduit à un intérêt pour les facteurs paysagers qui peuvent exercer un contrôle sur l'humidité du sol. Deux d'entre elles présentent un intérêt particulier : les écoulements de pente induits par la topographie, avec des écoulements de surface et de subsurface vers le bas de la pente, un processus naturels, et les transferts d'eau pour les activités d'irrigation, due à l'activité humaine. Ces deux facteurs paysagers auront tendance à augmenter l'humidité du sol dans certaines zones, et peuvent donc exercer un contrôle sur le couplage avec l'évapotranspiration et avoir un effet sur le climat.

Pour représenter le système climatique, on utilise des modèles de circulation générale, qui emploient, entre autres, un modèle atmosphérique et un modèle de surface terrestre. Bien que les modèles de surface terrestre deviennent de plus en plus complexes et représentent explicitement un plus grand nombre de processus, dans de nombreux cas, ils ne représentent en general l'effet de la topographie sur les flux hydrologiques et les effets anthropiques sur les ressources hydrologiques, que de manière limitée ou totalement absente. Cela empêche l'utilisation de modèles couplés atmosphère-surface terrestre pour comprendre les effets des écoulements de pente et de l'irrigation sur le climat actuel et sur l'évolution du climat futur. Dans le cadre de ce travail, nous présentons d'abord une paramétrisation simple des écoulements de pente dans la composante terrestre du modèle climatique de l'IPSL, appelée ORCHIDEE. Cette nouvelle paramétrisation divise la cellule de surface typique en une zone supérieure et une zone inférieure, la zone inférieure agissant comme un tampon entre les écoulements de surface et de subsurface de la zone supérieure et du système fluvial. Ainsi, la zone basse est potentiellement plus humide, et peut interagir avec l'atmosphère. La nouvelle paramétrisation est utilisée dans le système LMDZOR, qui couple ORCHIDEE au modèle atmosphérique IPSL, connu sous le nom de LMDZ. Deux simulations à long terme (entre 1980 et 2100) ont été réalisées sous les effets du changement climatique, avec et sans écoulements de pente.

Les résultats montrent que les écoulements de pente ont un effet sur les valeurs moyennes

de certaines variables hydro-climatiques sous le climat actuel, et sur l'évolution de ces variables sous le changement climatique futur. Dans le climat actuel, les écoulements de pente conduisent à une augmentation de l'humidité du sol. Par conséquent, l'évapotranspiration augmente et le ruissellement diminue dans les zones où il y a de l'énergie disponible. Dans certaines régions, on observe une augmentation des précipitations comme réponse de l'atmosphère, ce qui peut contrebalancer la diminution du ruissellement. De même, le flux de chaleur sensible diminue en raison de l'augmentation du flux de chaleur latente (c'est-à-dire l'eau évaporée), et la température de l'air près de la surface diminue également.

Quant à l'évolution des variables dans le cadre du changement climatique futur, l'effet des écoulements de pente dépendra des effets du changement climatique. Dans les zones où le changement climatique diminuera les taux de précipitations, les écoulements de pente atténueront la diminution de l'humidité du sol et de l'évapotranspiration. En réponse à l'atmosphère, la diminution des précipitations sera également atténuée, ce qui à son tour atténuera la diminution du ruissellement. Dans les zones où les précipitations augmenteront en raison du changement climatique, les écoulements de pente accéléreront l'augmentation de l'évapotranspiration, mais atténueront les augmentations de l'humidité du sol, des précipitations et du ruissellement. Dans tous les cas, les flux de pente entraînent un réchauffement de l'air légèrement plus lent.

Au cours de la deuxième partie du travail, une nouvelle paramétrisation de l'irrigation a été mise en œuvre au sein d'ORCHIDEE, basée sur les expériences précédentes, mais pour être utilisée à l'échelle globale. Ce nouveau paramétrage calcule la demande en eau de la plante en fonction d'un déficit hydrique et de la surface équipée pour l'irrigation, puis la compare à la disponibilité de l'eau dans les réservoirs naturels. Deux éléments supplémentaires sont pris en compte dans ce paramétrage : la nécessité de laisser un volume disponible pour les écosystèmes, qui représente le débit écologique, et la présence d'infrastructures de prise des eaux. Enfin, l'eau est transférée vers la partie culture de la cellule pour être infiltrée et éventuellement utilisée par la plante. Le nouveau schéma a été testé en mode hors ligne, c'est-à-dire forcé avec des données météorologiques, mais sans tenir compte de la réponse de l'atmosphère.

Les résultats montrent que le module d'irrigation augmente l'évapotranspiration et l'indice de surface foliaire dans les zones où les activités d'irrigation sont importantes, tout en diminuant les volumes d'eau stockés dans les aquifères et les réseaux fluviaux. Une comparaison avec les valeurs observées montre que l'inclusion de l'irrigation diminue les biais négatifs de modélisation pour l'évapotranspiration, mais augmente les biais positifs dans le cas de l'indice de surface foliaire. De même, bien que l'inclusion de l'irrigation diminue les débits des grands fleuves, cela ne se traduit pas nécessairement par une meilleure représentation de la dynamique des débits. Enfin, l'effet de l'irrigation sur le stockage total de l'eau est mineur. Dans le cas des débits et du stockage total de l'eau, cela peut être dû au manque de représentation d'autres processus liés à l'irrigation, tels que la gestion des réservoirs et le prélèvement d'eau souterraine fossile.

En conclusion, l'effet des écoulements de pente et de l'irrigation sur l'échange d'eau et d'énergie entre la surface et l'atmosphère, ainsi que sur le climat actuel et futur, peut être résumé en quatre hypothèses principales :

- Les facteurs paysagers augmentent l'humidité du sol et, si l'énergie est disponible, augmentent l'évapotranspiration. Cela entraîne des changements dans l'équilibre hydrique et énergétique.
- La réponse atmosphérique est une augmentation des précipitations et une diminution de la température de l'air dans le cas des écoulements de pente.
- Ces écoulements de pente modulent l'évolution des variables hydro climatiques dans le cadre du changement climatique futur.
- Ces modulations incluent une réponse atmosphérique qui contribue à maintenir les flux d'eau et d'énergie.

Cependant, nos résultats présentent des limites pour soutenir les hypothèses énumérées ci-dessus. Dans le cas des écoulements de pente, il existe des incertitudes liées à la paramétrisation. Par exemple, la représentation des écoulements dans ORCHIDEE ne tient pas compte de la nature dynamique des zones basses, ni de la déconnexion possible entre les eaux souterraines et les eaux de surface, qui rendrait impossible l'apport d'humidité dans la zone basse. En ce qui concerne l'irrigation, la principale limite est l'utilisation de simulations hors ligne, c'est-à-dire ORCHIDEE forcé par une base de données météorologiques, ce qui empêche l'analyse de la réponse de l'atmosphère aux changements de la surface terrestre. Enfin, bien qu'en réalité les deux phénomènes se produisent en même temps, ce travail a considéré chaque processus de manière isolée. Une nouvelle version d'ORCHIDEE incluant les deux processus est nécessaire pour étudier l'effet des deux facteurs paysagers en même temps, pour une utilisation couplée sous changement climatique futur.

Remerciements/Agradecimientos

Je tiens tout d'abord à remercier ma directrice de thèse, Agnès Ducharne, pour l'opportunité de réaliser ce doctorat. Ce furent trois années (et demi) de dur travail et d'apprentissage. Je remercie également les rapporteurs Isabelle Braud et Gonzalo Miguez-Macho, ainsi que les examinateurs Olivier Boucher, Sandrine Anquetin et Aaron Boone. Enfin, je remercie Frédérique Cheruy et Jean-Philippe Vidal, pour les échanges et les observations apportées à mon travail.

Ensuite, je me permets de remercier ceux qui ne sont plus à METIS, mais qui m'ont reçu au début de cette thèse : Mohamed Saadi (et ses discussions sur les différences métaphysiques entre GR4 et ORCHIDEE), Marc Dumont (le rire de Jussieu, et âme des sciences en face du campus), Paul Passy et Sylvain Théry (merci pour la garde partagée du petit), véritables piliers de la vie sociale du laboratoire, que j'ai tenté d'imiter sans grand succès. Également je remercie aux permanents du couloir hydro : Ludovic (et merci aussi pour ta participation aux comités de suivi et aux discussions sur des questions hydrologiques), Valérie, Danielle (la course dans le jardin des plantes), Simon, Anne et Vincent, et les doctorants et posdoc : Etienne (père de Hanz), Gurpreet, Patricia, Deniz, Morgane (la vraie, même si elle parle espagnol chilien), Pierre (le vieux) et Pierre (le nouveau), Nouradine, Rojin, Gauthier, Elijah, Leslie (reine des tortues), Peng, Luiza, Thibault (avec qui on a partagé les mêmes tribulations de la thèse aux mêmes moments), Julie (âme libre et reine de l'hydroéconomie), Salomé (reine des champignons de Compiègne, la meilleure ville de France semble-t-il), Antoine, Axel, Radegonde, et les ingénieurs Alexandre (vive la Savoie), Maxime (vive la Normandie), Nesrine (arrête de donner des pièces jaunes aux étrangers) et Marie. Finalement, mais pas moins important, aux gens des autres couloirs du labo : l'équipe administratif Valérie, Benedicte, Aurélien et Montse, le directeur Jean-Marie Mouchel, Aurélien Baro, et tout l'équipe geophy : Ludovic, Damien, Roger, Julio, Aïda, et Fabrice, Thomas, Sylvain S et Romane. Finalement, spécial mention pour ma famille française, Remi et Isabelle, et à Marie Laure et Brent, Muriel et Sam, Lionel, et aux enfants. Et aux autres personnes que j'ai croisé pendant ces trois ans et demi mais qui ne sont pas nomme ici (l'espace est court, la mémoire l'est parfois aussi), qui de près ou de loin ont aidé à construire un parcours de souvenirs mémorable et unique. Encore merci à tous.

Ahora en español, aprovecho para agradecer a mi familia, a mis padres Carlos y Cristina, y a mi hermano Juan Francisco, por su apoyo incondicional en este duro proceso. Un especial agradecimiento a Laura y a Ciro, con quienes he compartido las soledades de la vida en París, las tribulaciones, pero también las pequeñas victorias y los buenos momentos, compartiendo una cerveza, un café, una charla, o un restaurante escondido en una calle solitaria, que resulta ser una pequeña gema. También besos y abrazos para Sami y Will, quienes se han convertido en grandes amigos en los vericuetos de esta ciudad. Indudablemente, es necesario agradecer

a mis amigos de Popayán que me apoyaron desde la distancia, Alejandro, Guillermo, Daniel y Sandra, quienes siempre estuvieron pendientes y enviaron mensajes de apoyo en momentos muy duros de estos tres años, a Polo, Santiago, Miguel, Luis Carlos, Charlie y Natalia y tantos otros amigos de Bogotá que desde lejos me sostuvieron en negros momentos. Y por supuesto, quiero agradecer a todas las personas que conocí durante mi maestría en la UNAL, en especial a Edwin y a Leonardo, con quienes compartí a la distancia la experiencia del migrante latino que se acomoda a una nueva cultura, y que descubre nuevos modos de vida. Por último, pero no menos importante, debo agradecer al antiguo grupo del E2O, Erasmo, Carolina y Camila, Nicolas D. y Nicolás C., David, Juan Pablo, quienes desde tan lejos, cada uno llevando sus vidas, siempre tuvieron cinco minutos para preguntar cómo iba. Y a todas las personas que he conocido de cerca y de lejos a lo largo de estos años, a las que no incluyo por falta de espacio o de memoria, y que me han ayudado a recorrer este camino y a superar los obstáculos de cada etapa del viaje.

Ha sido un proceso largo, solitario, exigente y agotador. Fue realizado en medio de un periodo completamente extraño para todos, lleno de incertidumbres y miedos. Lo hice poniendo todo lo que podía poner en la mesa, quizá incluso más de lo que debería haber puesto de mi parte. Pero en esta loca carrera, lo que he hecho, lo he hecho con el corazón, y con la tranquilidad de intentarlo todo honesta y correctamente. Que sea el preludio del futuro.

Contents

List of Figures

List of Tables

Chapter 1

Introduction

1.1 The water cycle and the soil moisture - atmosphere interaction

1.1.1 General overview

Water is essential for life, and fresh water is essential for human existence. The link between water and life is observed, for example, in the distribution of vegetation, which is partially dependent on the existence (or absence) of water (Feddema, 2005). Similarly, the local water supply is a strong conditioning factor for human activities, from agriculture to industry (Wada and Bierkens, 2014). In addition, the analysis of the continuous water flow (i.e. the water cycle) substantially affects other processes inside the climate system. For instance the water cycle affects the earth's energy balance, mainly through the phase change during evaporation from the ocean and lands and from plant transpiration[1], and the carbon cycle mainly due to the correlation of water availability and plant CO_2 uptake.

The interest in the water cycle has led to study the fluxes across the ocean, the atmosphere and the land (see Fig. 1.1). Radiation from the sun enables the phase change of water from liquid to vapor, and allows the transfer of mass from ocean to land. Water vapor in the atmosphere will eventually condense and fall as rain or snow. For terrestrial hydrology, freshwater that does not evaporate back may return to the ocean as runoff and river discharge, may be stored in lakes and wetlands or simply as soil moisture, or may drain to groundwater as recharge. Finally, solid water in form of ice, snow and permafrost may cover large extensions of continental land, interacting with the atmosphere through sublimation and in some cases maintaining streamflow during warm seasons.

The ocean accounts for a large portion of the water (97% worldwide) while saline/fossil groundwater accounts for 1% (Gleeson et al., 2016). Freshwater represents the remaining portion, but a large fraction of freshwater is stored as ice (96% of freshwater), and solely 4%

[1]Transpiration is the loss of water through the stomata in the plant leaves during the carbon exchange.

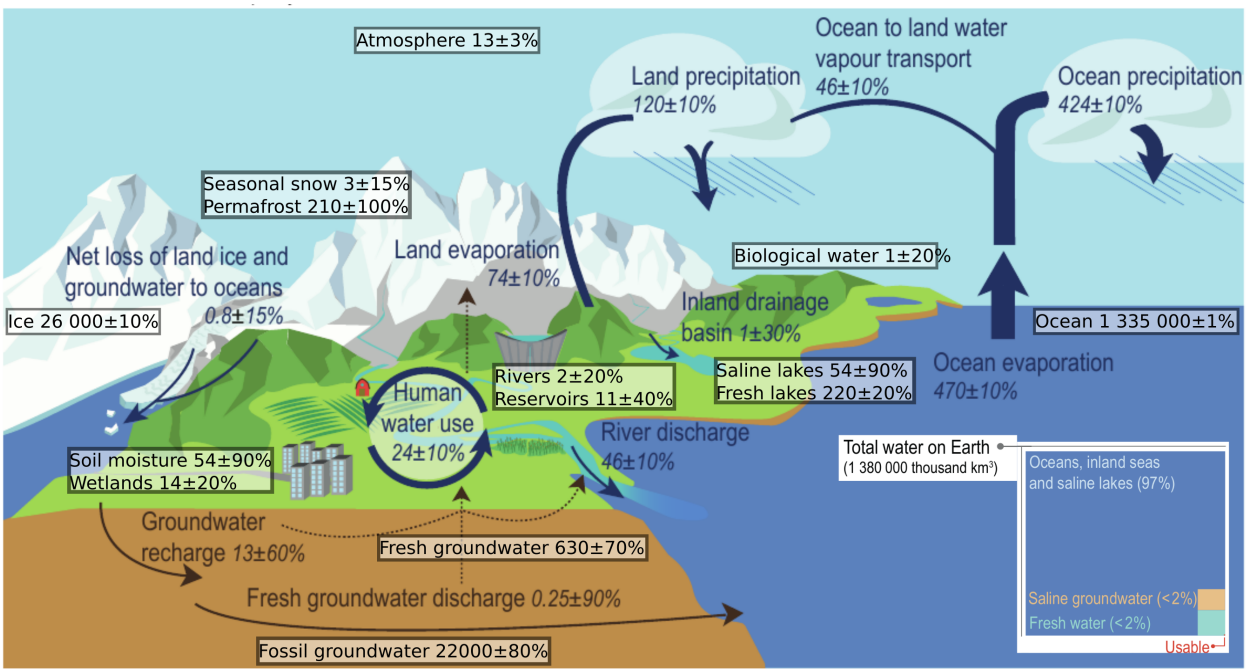

Figure 1.1: Depiction of present-day water cycle, inside the boxes the water storage volumes, lines represent water fluxes. Inset represent the fraction of every water storage in the earth respect to the total water volume. Units in km^3 and $km^3/year$. Figure from IPCC, 2021, adapted to include both stores and fluxes.

is stored mainly as fresh groundwater (Gleeson et al., 2016), but also in lakes and artificial reservoirs, rivers, wetlands and as soil moisture. The water in the atmosphere accounts for only 0.001% of water on earth. It is worth noting that these estimates in fluxes and storage are not in equilibrium, due to the ongoing climate change. For instance, global warming is melting ice sheets, and human water use may induce depletion in local freshwater storage like groundwater (Famiglietti, 2014; Rodell et al., 2018).

In recent years, there has been increasing interest in the interactions between the freshwater system (groundwater and surface water) and the atmosphere (Koster, 2004; Seneviratne et al., 2013) and their co-evolution. Before proceeding with the characteristics of that interaction, we must precisely define the terms interaction, coupling and feedback, which will be used throughout this manuscript. To do so, and following Seneviratne et al., 2010 (see Fig. 1.2), we refer to coupling as the degree of control of one variable on another by means of a relationship. In some cases, we may have a bidirectional coupling between two variables, i.e. each variable partially controls the other one by means of two different relationships. In the latter case, we may refer to the two-way coupling as feedback. Finally, the term "interaction" may refer to all the variables and the relationships that exist between them in a general way. In Fig. 1.2, the relationship a between variables A and B refers to a coupling, and relationships a and b between variables A and B refers to a bidirectional coupling, or feedback.

The interest in freshwater and atmosphere interactions seeks to understand not only

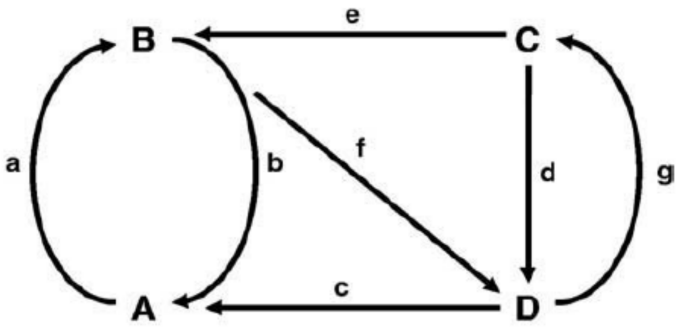

Figure 1.2: Diagram showing coupling, feedbacks and interactions. Upper-case letters A,B,C,D, refer to states or processes, lower-case letters a-g refer to corresponding relationships between the variables A-D. Figure taken from Seneviratne et al., 2010.

how climate affects the freshwater system, but also how the freshwater system, induced by natural or human processes, affects the atmosphere (see Fig. 1.3-a). The assessment of land-atmosphere interactions involves complex feedbacks that are difficult to disentangle, and there are strong limitations in the available tools, for example in the use of observations or the use of simplified models that may overlook some processes. As a proof of the interest in the water cycle and in particular, in the complex interaction between land surface and the atmosphere, the latest IPCC AR6 report (IPCC, 2021) devotes a full chapter, Chapter 8 (Douville et al., 2021), to the analysis of the evolution of hydrologic variables under the ongoing climate change.

1.1.2 The importance of soil moisture

Usually, the soil moisture (SM) is defined as the water contained in the unsaturated (vadose) soil zone, also referred to as the vadose zone (Seneviratne et al., 2010). The soil matrix (the solid phase of soils) will directly drive the saturated soil moisture value, i.e. the highest soil moisture content of the given soil, because it depends on the soil porosity. Two additional limits will be driven by soil properties: the field capacity soil moisture and the permanent wilting point. The first one is the limit between drainage driven by gravity and drainage driven by capillarity. The permanent wilting point is the limit between water extraction by the plants, and no extraction at all because water is held too strongly to the soil matrix. Field capacity constitutes a higher soil moisture than the wilting point. Between field capacity and wilting point, there is a critical soil moisture that constrains plant transpiration. Below the wilting point is the residual soil moisture, the lowest soil moisture value in a dry soil. These limits are important to understand the coupling of soil moisture and other variables (see Fig. 1.3-b).

1.1.2.1 Effects of soil moisture changes on climate

The SM plays a fundamental role in land-atmosphere interactions, as it can modulate the distribution of available water and energy at the surface. Indeed, SM can control the increase in evapotranspiration (ET), also called latent heat flux in energy terms. The phase change from water to vapor couples the energy and water balance at the surface (Seneviratne et al., 2010; D'Orgeval et al., 2008), and controls the energy and water available, for example, to heat the surface or produce runoff (Rodell et al., 2015; Short Gianotti et al., 2020, see Fig. 1.3-a). Note that an increase in ET causes a decrease in soil moisture, creating a negative feedback loop between SM and ET. We will go into this aspect in more detail below, but first we will discuss the direct coupling of soil moisture on ET.

In order to classify the SM influence on the land - atmosphere interaction, we can use the budyko framework (Budyko, 1974). The main hypothesis from Budyko is that the evapotranspiration rate for a long period (e.g. a year or more) is the result of the supply from the land, and the demand from the atmosphere. He represents this supply-demand tension by the ET ratio, i.e. the relation between the actual ET and the precipitation, and by the aridity, i.e. the relation between the potential ET and the precipitation (Condon and Maxwell, 2017). Potential ET refers to the rate of evapotranspiration when there is abundant moisture, and represents the demand from the atmosphere (Cai et al., 2016). The role that SM plays in the ET regime (see Fig. 1.3-b) is described by three areas with different features (Seneviratne et al., 2010; Liu et al., 2020):

- Energy limited regions: there is enough water (wet regions), but water demand drops below this availability (i.e. aridity index < 1), the ET constraint is the available energy. SM is above the critical soil humidity, over which ET is independent of SM . Tropical rainforest is a good example.

- Water limited regions: There is enough energy, but water availability drops below this demand (dry regions, i.e. aridity index > 1), the ET constraint is the available water. SM lays below the wilting soil humidity, under which ET does not occur. Tundra and other high-latitude areas, or hot deserts are good examples.

- Transition regions: changes in water availability highly impact ET rates. In these areas, soil moisture variability constrains ET, and SM is strongly coupled to ET. SM values lay between the wilting soil humidity and the critical soil humidity. A good example is the african Sahel.

The effect of the SM-ET coupling induces a feedback with some atmospheric variables, for instance with temperature and with precipitation. In the case of temperature (see Fig 1.4-a), if there is not enough soil moisture, ET will decrease. As a result, the near-surface atmosphere will be warmer because there is more available energy (Miralles et al., 2019). It leads to an increase of the atmosphere demand, and further drying of the shallower soil

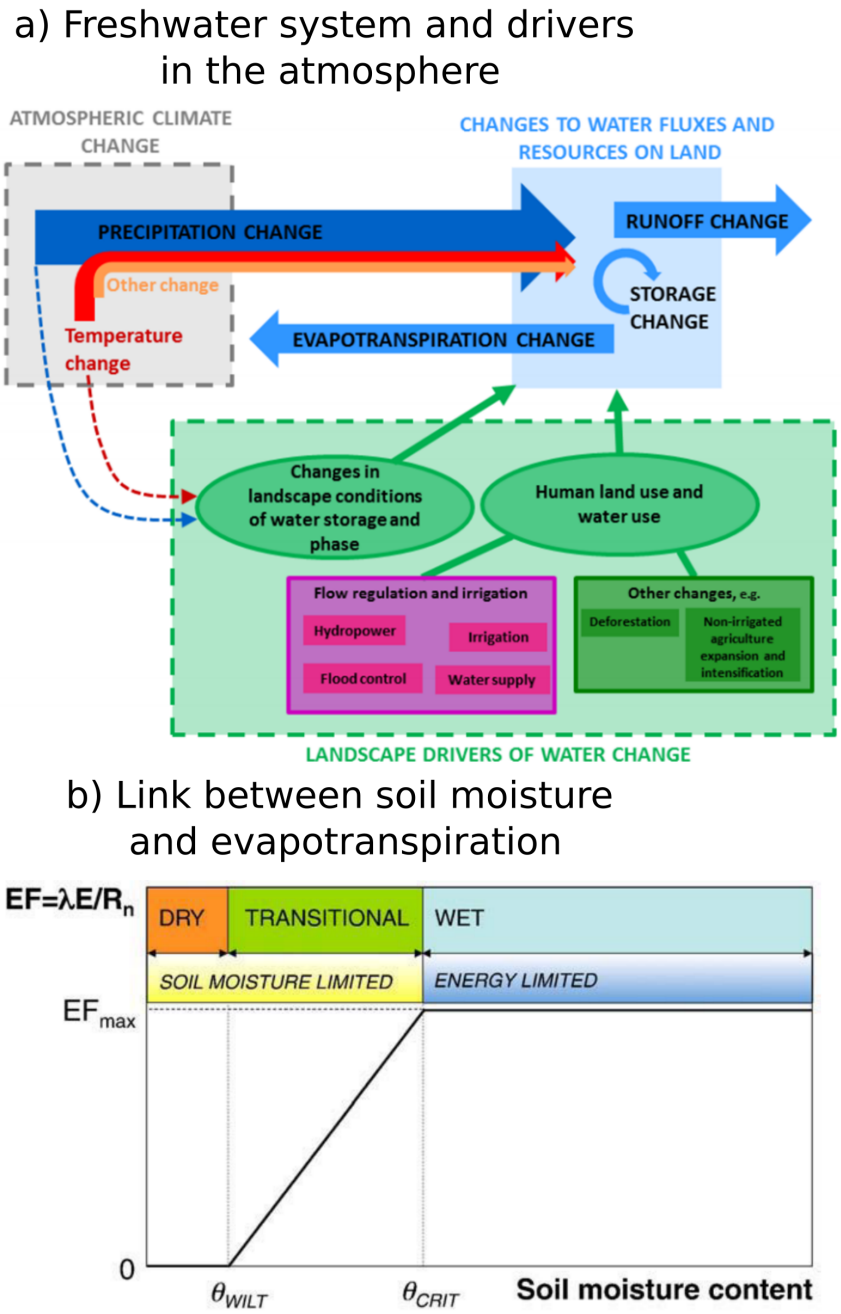

Figure 1.3: Changes on freshwater system and possible drivers in the atmosphere (a), taken from Jaramillo and Destouni, 2015. Link between soil humidity regimes and evapotranspiration regimes according to the conceptual framework from Budyko (b), taken from Seneviratne et al., 2010. θ_{wilt} and θ_{crit} are respectively the wilting point, and the critical soil moisture that constrains evapotranspiration, EF refers to the evaporative fraction from total rainfall, λ is the heat of vaporization, E is the evaporation mass, and R_n is the net radiation.

layers (Berg et al., 2014; Berg et al., 2017). For precipitation (see Fig 1.4-b), feedback is less certain because precipitation also depends on large-scale atmospheric dynamics, but if the soil is wet, and it enhances ET, the additional air moisture from ET may induce more

rainfall (Wei et al., 2013). It should be noted that other cases are possible: in arid areas, negative soil moisture anomalies can regulate atmospheric circulation, increasing moisture transport and rainfall. This is a consequence of a decrease in ET, which leads to an increase in air temperature (Zhou et al., 2021a).

One example of the effect of these complex interactions on climate, driven by SM-ET coupling, includes the evolution of seasonal values of precipitation and air temperature (Koster, 2004; Koster et al., 2006). For instance, a negative anomaly on soil moisture may lead to less rainfall and warmer temperature during the next weeks. In addition, some observations have suggested that soil moisture anomalies may reappear several months or even a year later, even when meteorological conditions are back to normal. This implies a possible effect on climate evolution that may last beyond several seasons (Kumar et al., 2019). In the case of Europe, observed evidence suggests that periods of droughts (abnormally dry periods over a region), and the corresponding negative SM anomalies during spring, intensifies heatwaves (days with extreme heat) during summer, while positive SM anomalies during spring lead to few hot days during summer (Quesada et al., 2012). The role of land conditions in the evolution of climatic events such as droughts and heat waves (see Fig 1.4-c), and how these land conditions can mitigate or enhance such events, has received considerable attention from the scientific community in recent years (Cook et al., 2018; Miralles et al., 2019; Vicente-Serrano et al., 2020).

1.1.2.2 Effects of soil moisture changes on hydrology

Soil moisture also plays an important role in defining hydrologic flows at the land surface. For example, over a hillslope, soil moisture is one of the aspects that determines if rainfall will generate runoff or will infiltrate into the soil. The oldest known mechanism is the *infiltration excess overland flow* (see Fig. 1.5-a). When rainfall intensity exceeds the infiltration capacity of the soil, the soil moisture near the surface will reach saturation, and the excess rainfall will become runoff (Horton, 1945). But it is not the only known mechanism. When a portion of the soil surface is saturated or near of saturation from below, rainfall will rapidly produce excess runoff over this area (Beven, 2012). This mechanism is referred to as *saturation excess overland flow* (see Fig. 1.5-b), and may be due to subsurface flow convergence in the valleys, which creates riparian wetlands (see Figure 1.4 from Beven, 2012 for a comparison of different runoff production mechanisms).

In reality, and depending on the characteristics of the hillslope and and the pre-existing conditions, only part of the surface may participate in the generation of runoff, while the rest of the hillslope may not (see Fig. 1.5-c). Furthermore, the area that participates in runoff generation may expand or shrink. This is often referred as a variable source response (Beven, 2012). These differences in runoff generation can be important not only at the hillslope scale, but also at the catchment scale. Following Brutsaert, 2005, we define a catchment here as the area contributing to the flow of the open channel at a given point along a river. The

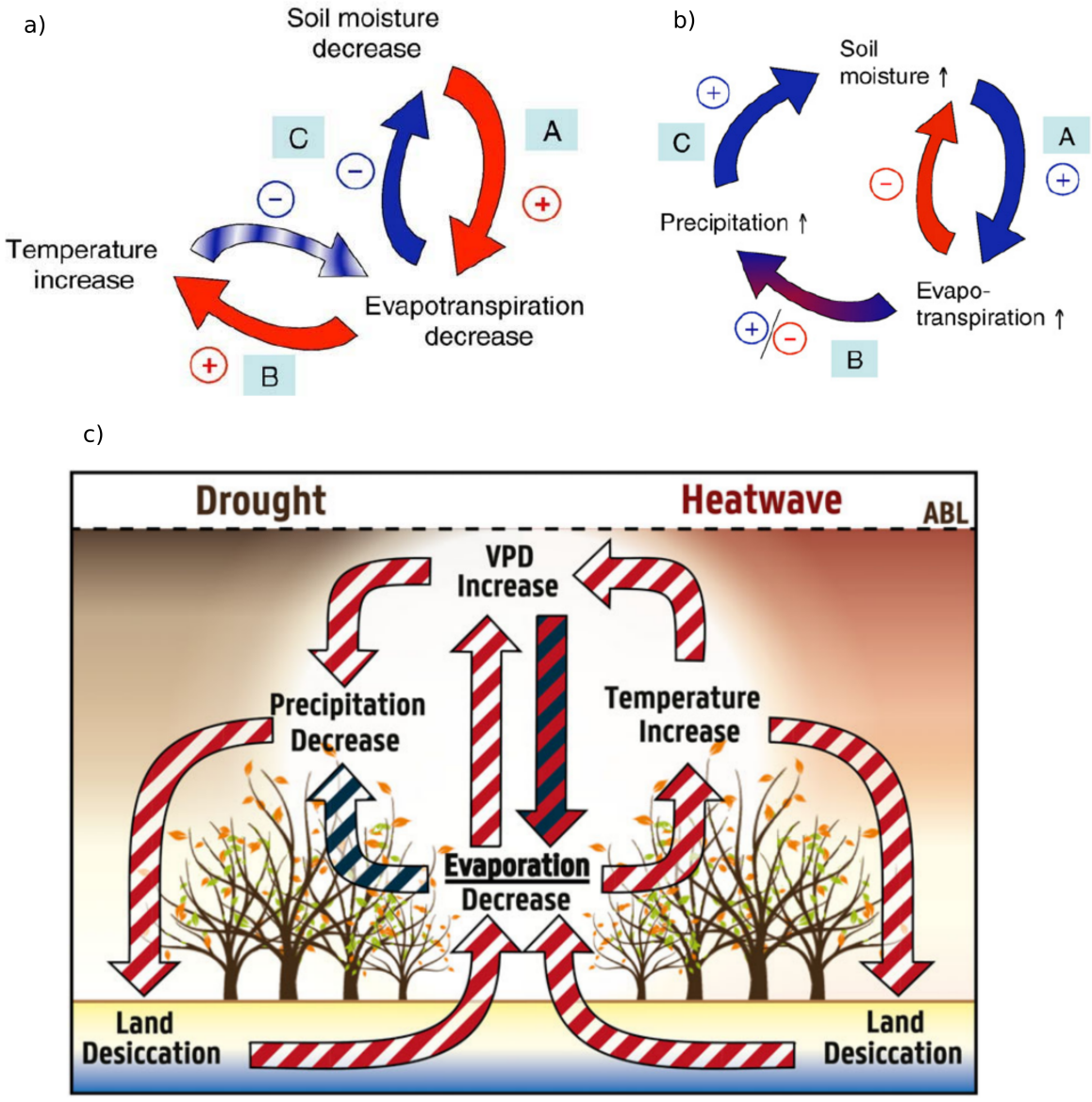

Figure 1.4: Soil moisture-temperature coupling (a), red arrows correspond to processes leading to drying/warming, blue arrows denote potential negative feedbacks (hatched blue arrow indicates the tendency of enhanced temperature to lead to more evaporative demand). Soil moisture-precipitation coupling (b), Blue arrows indicate processes leading to positive feedback resulting in wetting, the red arrow indicates a potential negative feedback damping the original soil moisture anomaly, and the red-blue arrow indicates the existence of both positive and negative feedbacks between evapotranspiration and precipitation anomalies. In both diagrams (a) and (b), A, B and C refer to different steps of the feedback loop. Both diagrams were taken from Seneviratne et al., 2010. Land feedbacks as local intensifiers of hydro-meteorological extremes (c). Here, red arrows mean positive relation (e.g. land drying leads to evaporation decrease), while blue arrows mean negative relation. VPD means vapor pressure deficit, and ABL means atmospheric boundary layer. Note that the conceptual diagram is boldly simplified. Figure was taken from Miralles et al., 2019.

delimitation of the catchment follows the topography, and usually the hillslope ridges are taken as boundaries. In hydrology, the catchment is considered as the unit that organizes water and energy flows across the landscape. (Fan et al., 2019).

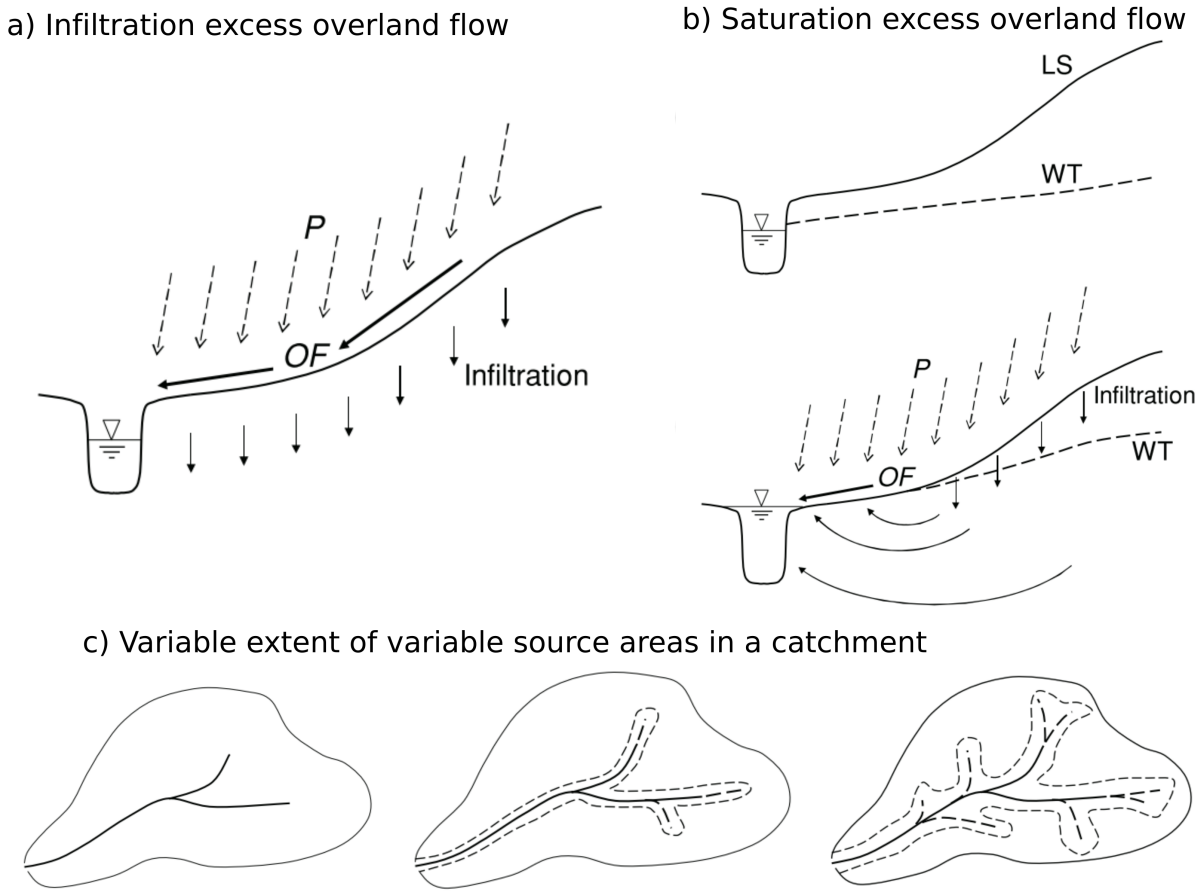

Figure 1.5: Illustration of the overland flow as infiltration excess (a). Precipitation rate P exceeds infiltration capacity, and the water table is at the ground surface. Illustration of the overland flow as saturation excess (b). Water table (WT) prior to the onset of precipitation and during the precipitation event. Precipitation rate P is smaller than the infiltration capacity over the unsaturated portion of the land surface; overland flow takes place where water table has risen to the ground. Schematic of a catchment, with the extent of variable source areas (dashed lines) on which overland flow takes place (c). First column is under drought flow conditions, second is under onset of precipitation and third is under wet conditions. Stream channels and saturated areas near the stream channels expand as precipitation continues. All diagrams are taken from Brutsaert, 2005.

We will now discuss the relationship between soil moisture and groundwater. For the sake of clarity, we define groundwater here as the water located in the saturated layers of soil or rock, as opposed to the soil moisture located in the vadose zone (but note that this classification is artificial). In addition, we will focus on fresh groundwater (see Fig. 1.1), i.e., groundwater that actively participates in the water cycle. We do not consider fossil groundwater, despite its large volume, because it does not actively interact with the

land surface. Finally, we do not explore here the diversity of groundwater formations, but concentrate on a single type, the unconfined aquifer, which is in direct contact with the land surface (Brutsaert, 2005).

An unconfined aquifer lies directly below the vadose zone, and the limit between the two zones is the water table (see Fig. 1.5-c), where the water pressure is atmospheric (note that the water table is taken as a free surface, even if in reality it is not). The water table is dynamic in time and space: it can become shallower during the wet season or deeper during the dry season, and it may roughly follow the topography due to a slow downward flow. When the water table and the surface intersect, we observe a water spring that contributes to the flow of the open channel (Schneider, 2017).

Water table dynamics has a strong influence on local and regional groundwater flows (Tóth, 1963). From a regional point of view, the water-table dynamics may be classified in two main types (Cuthbert et al., 2019; Gleeson et al., 2011):

- Topography-controlled: the water table follows closely the terrain topography. This feature is expected in wet regions, subdued topography, and low hydraulic conductivity.
- Recharge-controlled: the water table is largely disconnected from topography. This feature is expected in arid regions, mountainous topography, and high hydraulic conductivity.

The flow that comes from precipitation and reaches the aquifer is called recharge, and is the result of a complex interaction with landscape, topography, geology, the vadose zone, and eventually climate (Markovich et al., 2016; Smerdon, 2017). Soil moisture and surface soil characteristics partially control this flow, not only because they drive the partitioning of precipitation between runoff and infiltration, but also because SM may be coupled to ET, leaving less water for recharge. The value of recharge and the hydraulic properties of the soil or rock will control the depth of the water table, and ultimately the flow from the aquifer into the river stream through subsurface flows (Miller et al., 2016; Martínez-De La Torre and Miguez-Macho, 2019). This aquifer-river flow is referred to as baseflow, and plays a critical role in maintaining river discharge during dry seasons, which is essential for the sustainability of ecosystems and human communities (Schneider, 2017).

Finally, we will briefly discuss the interaction between soil moisture and vegetation. It is well known that plants transpire water as part of the the exchange of CO_2 with the atmosphere (specifically through the stomata, small openings on plant leaves, Jasechko et al., 2013; Moene and Dam, 2014), and that the plant will extract that water from the soil through its root system (Moene and Dam, 2014; Miguez-Macho and Fan, 2021). The soil moisture exerts a direct control on plant transpiration, because below the critical soil moisture value, plant transpiration starts to reduce due to water stress. When the soil moisture reaches the wilting point, all transpiration stops (Seneviratne et al., 2010). This coupling between SM and CO_2 exchange has two main effects: first, available soil moisture for the plant has an

impact on carbon cycle and other biogeochemical cycles driven by vegetation. And second, vegetation patterns will follow topography, to try to ensure access to the wettest soils in the valley areas following the subsurface flows (Fan et al., 2019).

On the other hand, vegetation modulates the partitioning of evapotranspiration between evaporation and transpiration (Jasechko et al., 2013; Wang et al., 2014; Wei et al., 2017; Lian et al., 2018; Forzieri et al., 2020). While bare soil evaporation comes from the first soil layers (McColl et al., 2017; Martens et al., 2017), plants can access deeper soil moisture through their root system to avoid water stress (Miguez-Macho and Fan, 2021). It should be noted here that, in the case that the groundwater is sufficiently shallow, the plant can interact directly with the aquifer by extracting water for transpiration. This appears to be the case in some areas, where groundwater sustains vegetation transpiration during droughts (Mu et al., 2021; Miguez-Macho and Fan, 2021). In addition, the vegetation canopy will add an additional source of water that is subject to evaporation. Canopy interception strongly depends on vegetation canopy, stage of development, and characteristics of the precipitation (Moene and Dam, 2014). Evaporation from canopy is referred to as canopy loss, while the water that finally reaches the land surface is known as throughfall. (Seneviratne et al., 2010; Moene and Dam, 2014; Wei et al., 2017).

1.1.3 Climate change and its effects on hydrology

Human activities over the last 150 years have changed the atmosphere composition, and have transformed large areas of the land surface (see Fig. 1.6). The result is a positive imbalance in the Earth's energy balance that is raising the air temperature worldwide. The fifth report of the IPCC (Intergovernmental Panel on Climate Change), AR5, reported a global temperature rise of 0.9 °K during the 20 th century (IPCC, 2013). The latest IPCC report (IPCC, 2021; Tebaldi et al., 2021), AR6, reported that greenhouse gas emissions keep increasing, resulting in an additional warming (+0.19 °K compared to AR5). And the projections depict a rise in temperature during the 21 th century, even if uncertainty remains large, because projections are based on scenarios of socio-economic development and future emissions. For example, CMIP6 (Coupled Model Intercomparison Project Phase 6), the projections dataset used for AR6, shows an effective climate sensitivity (i.e. mean global ultimate temperature for instantaneous doubling of CO_2) ranging 1.8 - 5.6 °K (Zelinka et al., 2020), confirming the need for urgent mitigation, as noted by Forster et al., 2020.

Global warming directly impacts the water that can be hold in the air, as warmer air holds a larger water volume (Chou et al., 2013), meaning that the atmospheric water demand increases under a warmer climate. A higher air moisture is directly related to increased precipitation rates at global scale (Tebaldi et al., 2021), but the positive magnitude of change for mean values is lower for precipitation than for air moisture, and the spatial distribution is heterogeneous (Fig. 1.7). We could summarize the change on precipitation with "wet gets wetter, dry gets drier", (Greve et al., 2014), even if there are uncertainties in the projections,

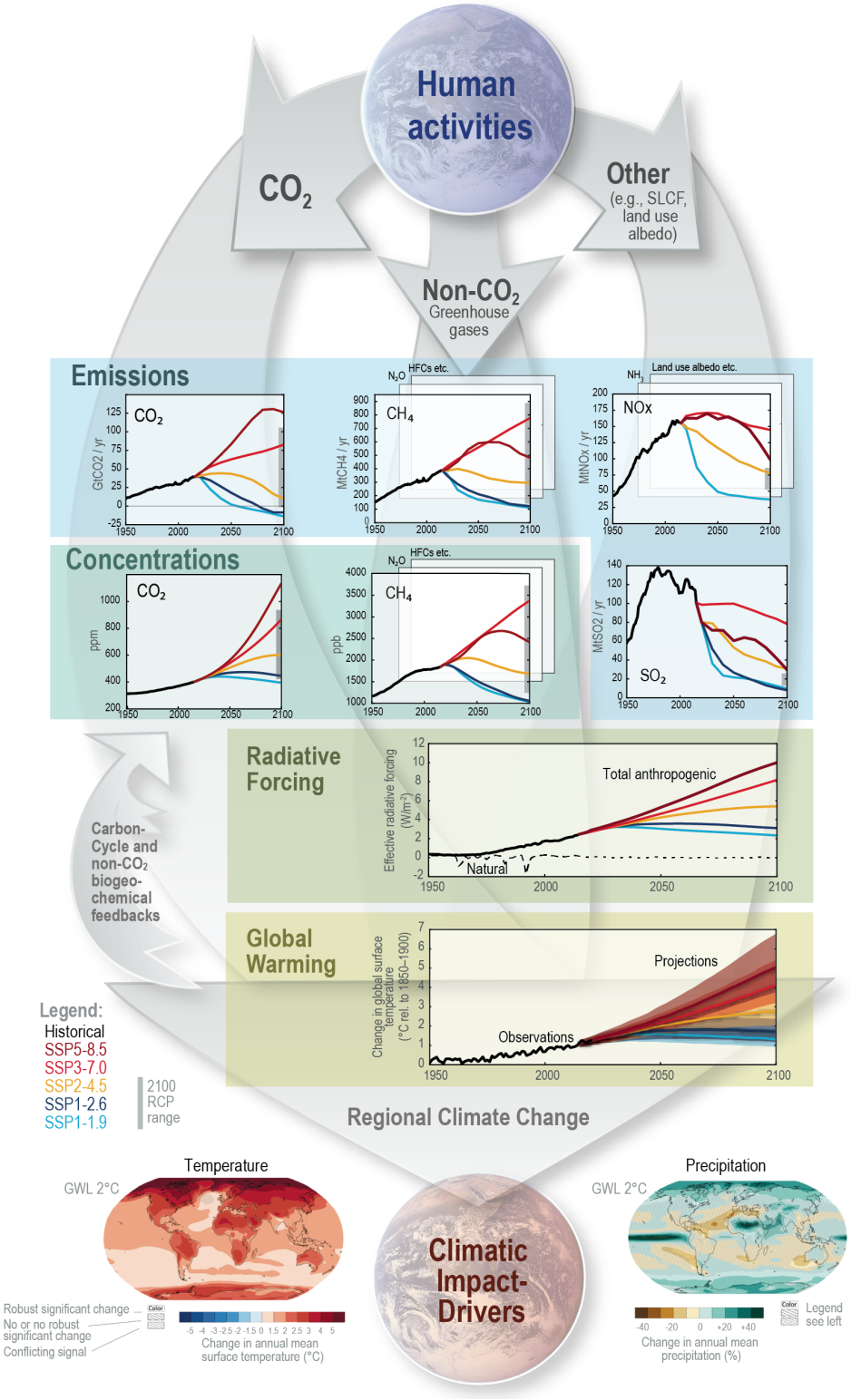

Figure 1.6: The climate change cause-effect chain. Illustration of the process chain from anthropogenic emissions, to change in atmospheric concentration, to changes in Earth's energy balance (forcing), to changes in global climate and regional climate, and climatic impact drivers. Figure TS.4 taken from the technical summary of AR6, IPCC, 2021.

and regionally some dry areas could even see a rise in rainfall (Chou et al., 2013).

Over land, evapotranspiration should increase under warming as well, following the increase of atmospheric water demand and precipitation (IPCC, 2013; IPCC, 2021), but modulated by soil moisture and vegetation changes (Vicente-Serrano et al., 2020). Projections from CMIP5 (Coupled Model Intercomparison Project Phase 5), the dataset that was used in AR5, also put in evidence possible changes in ET partitioning in the tropics, shifting to higher soil evaporation and lower transpiration. In high latitudes all three components of ET (transpiration, soil evaporation and canopy interception loss) should increase, while they should decrease in dry subtropics (Berg and Sheffield, 2019; Vicente-Serrano et al., 2020). Decrease of transpiration fraction in total ET in the tropic and dry subtropic areas is coherent with observed datasets that underline that plants use less water on transpiration, i.e. that water plant efficiency is higher (Forzieri et al., 2020) and are linked to physiological effects of CO_2 on stomata modulation (Vicente-Serrano et al., 2020).

There are large uncertainties regarding soil humidity (Fig. 1.7), but it seems plausible to observe a decline in the future (Berg et al., 2016; Cook et al., 2020). Regionally, soil humidity should likely decrease in the Mediterranean area and the U.S. Southwest area. On the other hand, changes in recharge patterns are largely uncertain, as there is no clear magnitude and direction in change (Wu et al., 2020). For instance, the areas most sensitive to recharge changes due to warming seem to be mountainous zones and arid areas (Smerdon, 2017). Runoff seems to increase under a warming climate and land use changes at the global scale (Piao et al., 2007), but CMIP6 projections show regional and seasonal differences on runoff trends (Cook et al., 2020). Extreme hydrologic values should increase alike (with seasonal and spatial differences) especially in the northern hemisphere (Giuntoli et al., 2015; Vidal et al., 2016), but the magnitude of change remains uncertain due to differences in the representation of processes in hydrologic models, especially in snow-driven and arid basins (Vidal et al., 2016).

In general, it is expected that warming increases the aridity on land. This means that the mean water availability will decrease (Vicente-Serrano et al., 2020). In any case, changes on aridity are the center of intense debates in recent years, not only due to aridity definition, but also due to the physiological plant response to increased CO_2 concentration and soil moisture-atmosphere feedbacks (Roderick et al., 2015; Milly and Dunne, 2016) which could mitigate part of the drying trend in some regions. For climate extremes, i.e. abnormal values for a certain variable at a certain location, projections put into evidence that climate change increases the magnitude, intensity and frequency of temperature extremes (Perkins, 2015). Projections on droughts show that areas exposed to extreme-to-exceptional events should also increase, even under the more aggressive mitigation pathways (Pokhrel et al., 2021; Cook et al., 2020).

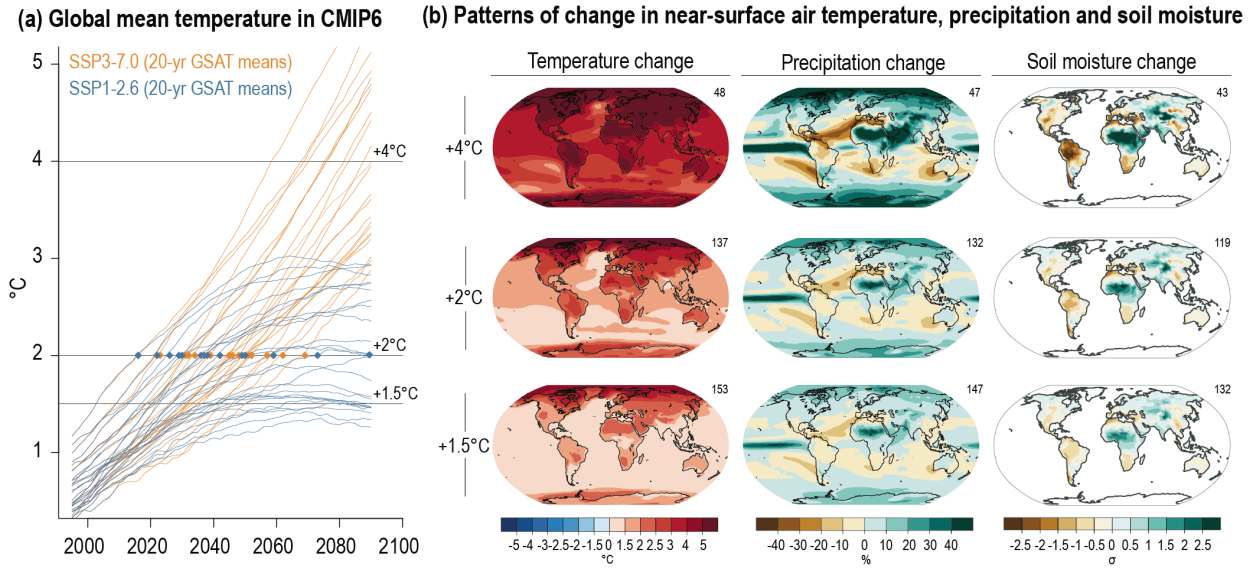

Figure 1.7: Scenarios, global warming levels, and patterns of change. Global Warming Levels (GWLs) are defined as global surface temperature responses to anthropogenic emissions for scenarios SSP1-2.6 and SSP3-7.0 (SSP for shared socioeconomic pathways) in CMIP6 simulations (a). Multi-model, multi-simulation average response patterns of change in near-surface air temperature, precipitation (in %) and soil moisture (in standard deviation of interannual variability) for three GWLs (b). Number in top of each map shows the number of model simulations averaged across all models that reach the corresponding GWL in nay of the five SSPs scenarios. Figure TS.5 taken from the technical summary of AR6, IPCC, 2021.

1.2 Effects of landscape drivers on soil moisture - atmosphere interaction

Changes in landscape conditions may induce a change in near surface SM, alter the ET rate and ultimately affect the atmosphere. Understanding the role of these landscape drivers (i.e. processes that drive those changes in landscape conditions) helps to constrain the land surface-atmosphere interaction (Jaramillo and Destouni, 2015). This section presents the effect of two landscape drivers, the first of natural origin, the hillslope flows, and the second of anthropic origin, the irrigation. We briefly underline the gaps and shortcomings in the understanding of the effects of landscape drivers.

1.2.1 Effects of groundwater and hillslope flow

We already described the effect of soil moisture on hydrology (section 1.1.2.2), and how soil moisture interacts with groundwater along the hillslope. We will now focus on the way this interaction between soil moisture and groundwater can alter the water storage near the surface, and what are the effects on the atmosphere.

We already defined the water table, and we described it as a free surface that may roughly

follow topography in some cases, due to slow flows from ridge to valley. At the hillslope foot, or in the valley at catchment scale, the water table may intersect the topography or at least approach the surface (see Fig. 1.8-a). This situation can induce higher surface soil moisture sustained by the aquifer (see Fig. 1.8-b), and lead to changes in surface conditions (Kollet and Maxwell, 2008). If energy is available at the surface, additional soil moisture can enhance evapotranspiration processes, but that will depend on the strength of the interaction between groundwater and surface soil moisture, driven by the depth of the water table (Miguez-Macho and Fan, 2021). Finally, the partitioning of the evapotranspiration rate between evaporation and transpiration will be modulated by vegetation (Maxwell and Condon, 2016). In the upland zone, near the ridges, the water table is likely to be deeper, preventing any groundwater extraction by the plant. In the lowland zone, the groundwater may be shallow enough to maintain higher soil moisture values in the root zone, allowing the plant to utilize that additional downflow water (see Fig. 1.9). If the water table crosses the surface, then groundwater is available to evaporate directly.

We have seen that soil moisture plays a key role on surface-atmosphere interaction, so it is not surprising that this joint interaction between groundwater, surface and the atmosphere may induce changes in the low-atmosphere variables, like a decrease of the air temperature (Gilbert et al., 2017; Keune et al., 2016). There is also evidence that locally induced ET from groundwater can mitigate remote land-atmosphere feedbacks caused by land-use change (Zipper et al., 2019). But large uncertainties remain on the effect at global scale.

1.2.2 Effects of irrigation

Today, about 70 % of world land surface is under human management. This human management includes land cover change, such as deforestation and a-posteriori development of crop fields (crop fields represent around 37% of total land area around 2015 according to Hurtt et al., 2020), but also land management, i.e. practices that do not change the land cover but intensify the land use (Luyssaert et al., 2014). One such management practice is field irrigation, an activity that involves artificially adding water to increase soil moisture and reduce crop water stress. The resulting benefit is increased crop yields, often by a factor of 2 in semi-arid regions, or simply allowing agriculture in arid areas where it would not otherwise be possible (Siebert et al., 2010). But all these benefits in food production directly alter the water cycle and other biogeochemical cycles, and have an impact on the surface water and energy balance (Piao et al., 2007; Vicente-Serrano et al., 2019; Jaramillo and Destouni, 2015).

Population and economic growth during the 20^{th} century has dramatically increased by 5 the irrigated area, from 63 millions ha (Mha) in 1900 to 306 Mha in 2005 (Siebert et al., 2015), with irrigation hotspots in Europe, south Asia and western USA (see Fig. 1.10). Today, irrigation plays a key role in food production; for example, 43% of cereal production was harvested on irrigated lands, and total production would decrease by 47% in the absence

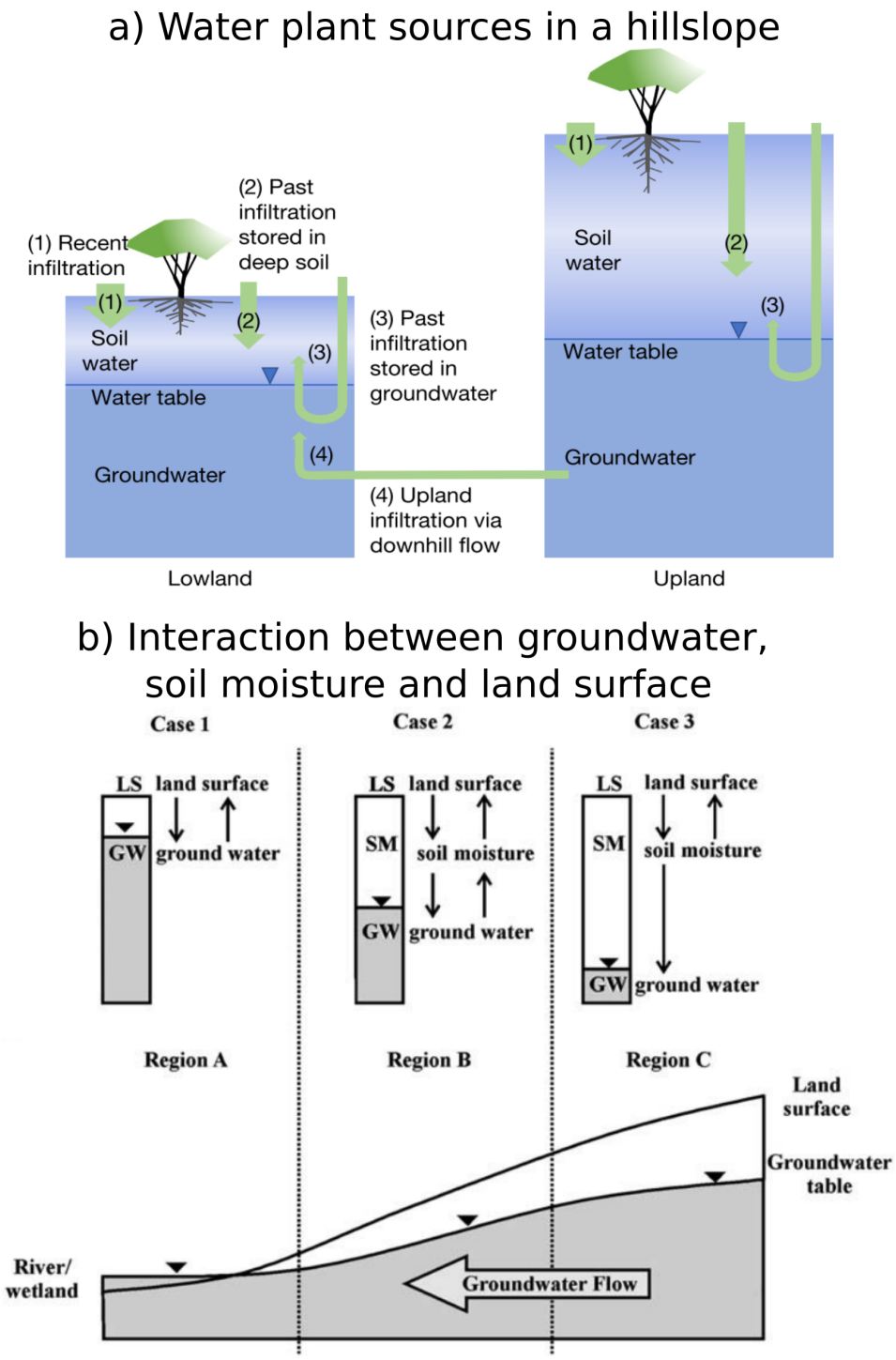

Figure 1.8: Schematic of plant water sources in a hillslope (a). Lowlands (left) and uplands (right) are connected by a down-valley flow. Note the shallow water table in the lowland and the thick vadose zone in the upland. Figure taken from Miguez-Macho and Fan, 2021. Schematic of the interconnection between groundwater (GW), shallow soil moisture (SM) and land surface (LS) processes, with schematic cross-section of land surface and water table, and theoretical delineation of three zones of influence of GW on land surface processes as function of groundwater depth (b). Figure taken from Kollet and Maxwell, 2008.

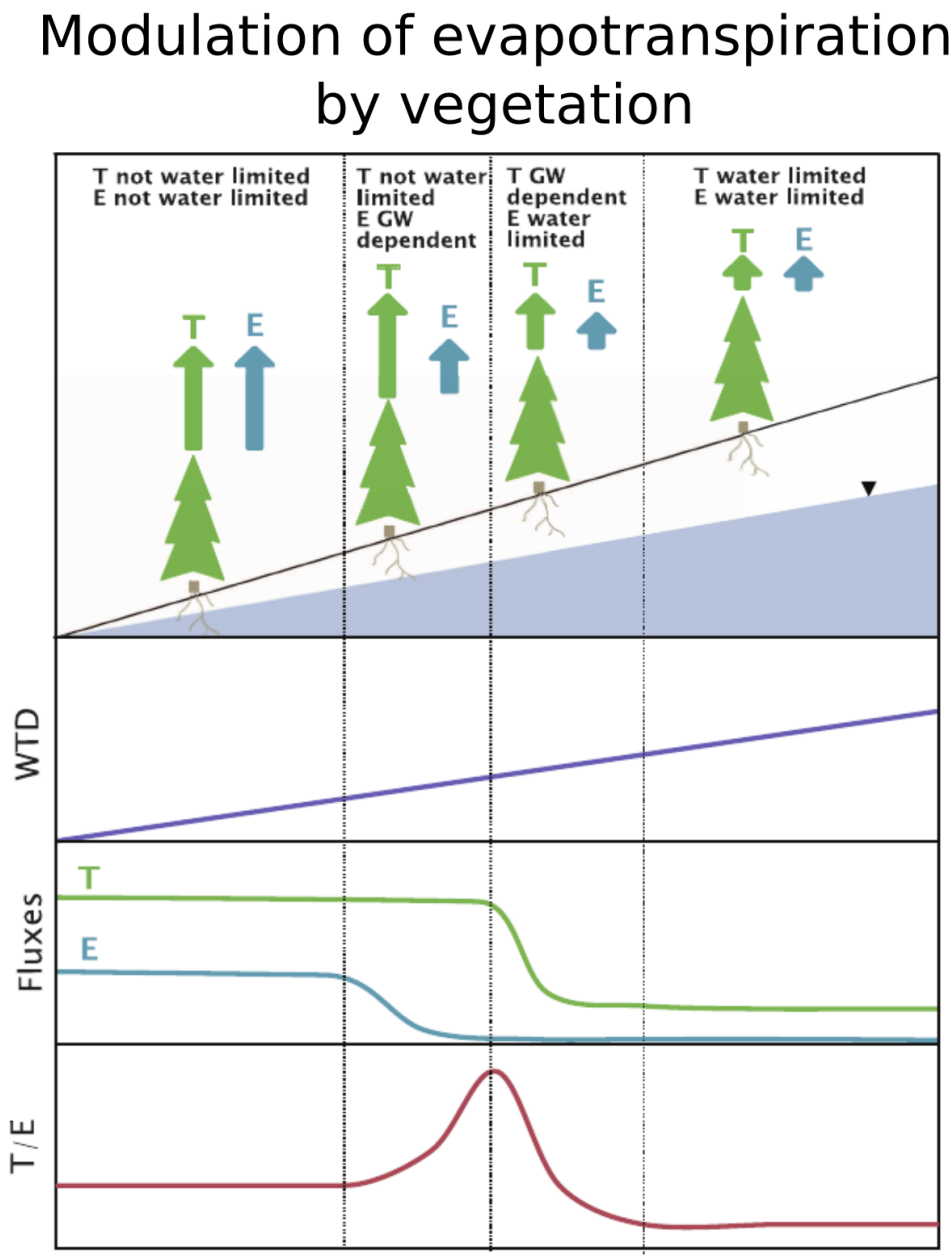

Figure 1.9: Relationship between groundwater depth and land-energy fluxes modulated by vegetation for an idealized hillslope. T for transpiration and E for evaporation, WTD for water table depth. The roots as drawn here are not to scale, and the presence of subsurface heterogeneity is not included. Taken from Maxwell and Condon, 2016.

of irrigation. For other crops such as citrus, cotton or sugar cane, production would decrease by 60% (Siebert and Döll, 2010). All of this production requires large volumes of water, which are typically drawn from surface sources such as rivers and lakes, or pumped from groundwater. Around the year 2000, water used for irrigation accounted for 70% of global water withdrawals (Siebert et al., 2010).

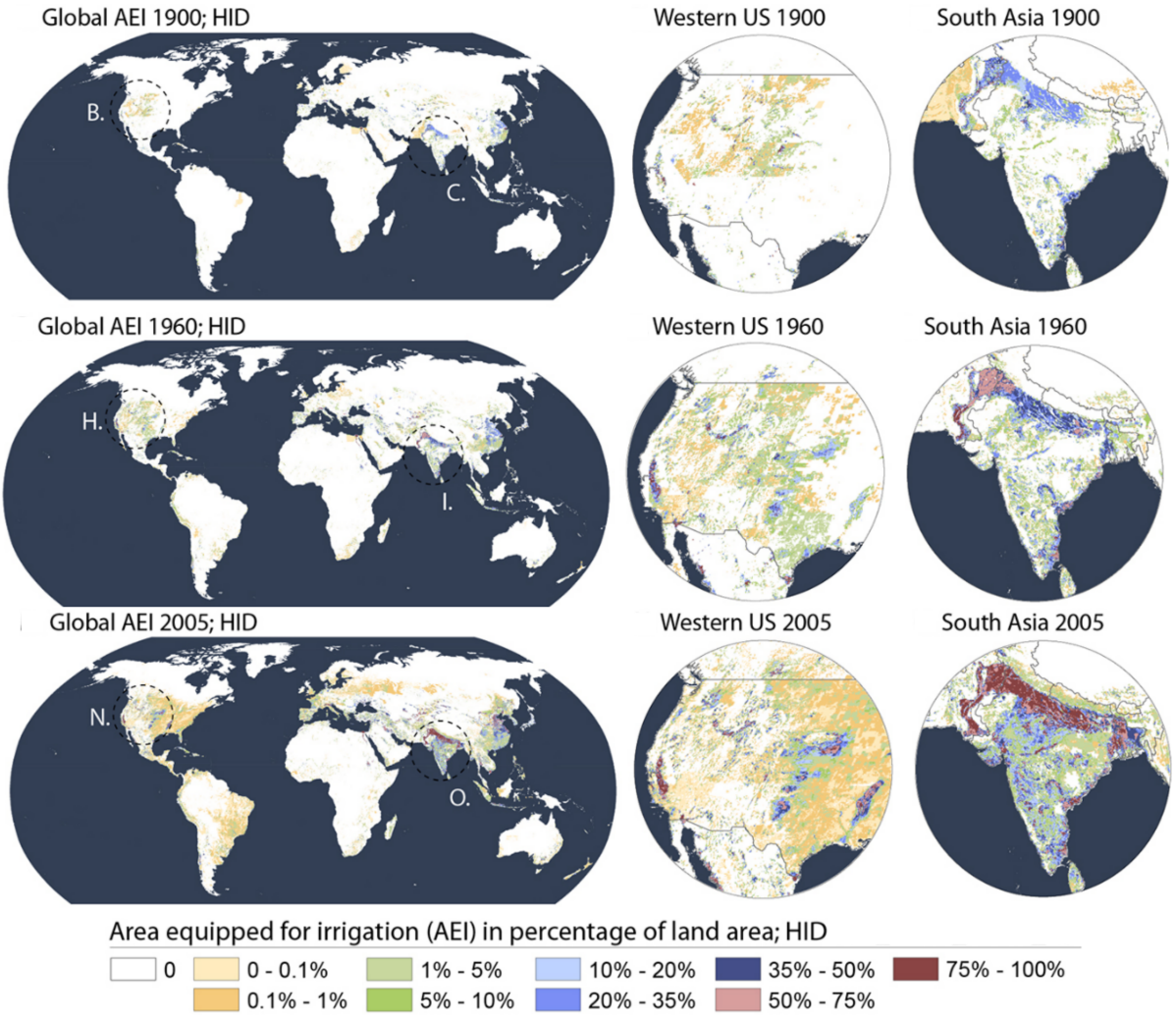

Figure 1.10: Spatial and temporal evolution of global area equipped for irrigation (AEI) for three time steps (1900,160,2005) based on the Historical Irrigation Dataset (HID). Maps include global and two selected close-up areas, namely western USA and South Asia. Figure taken from Siebert et al., 2015.

Irrigation activities transfer water from natural reservoirs (such as rivers or groundwater) to the soil surface during crop development (see Fig. 1.11). Thus, the plant can access this additional water and increase its transpiration. Not all of the transferred water will reach the field due to delivery losses (Hanasaki et al., 2018), and not all of the water that reaches the field will be used by the crops. In fact only a fraction is actually used as evapotranspiration, while the rest will be lost as surface runoff or as recharge. The fraction of water that is

actually used by the crop with respect to the total withdrawn volume is known as irrigation efficiency (Hoogeveen et al., 2015), but it should not include the fraction that is lost as evaporation, because this flux is not beneficial to the plant (Jägermeyr et al., 2015). It is worth noting here that the water that returns as runoff or recharge is considered a "loss" at the farm scale, because it leaves the field crop. But at the basin scale, there is no "loss," because the volume of water can be used by another farmer downstream of the river, or later in time by pumping from the aquifer. These flows, called return flows (Hanasaki et al., 2018), depend on landscape conditions (hydraulic properties of the soil, type of crop), but also on management activities and irrigation techniques.

Before exploring the effect of irrigation on the interaction between soil moisture and the atmosphere, we will discuss irrigation techniques (see detail in Fig. 1.11) and some management activities that can influence the effect of irrigation on hydrology (Jägermeyr et al., 2015). We can classify irrigation techniques into three main types (Koech and Langat, 2018; Grafton et al., 2018): sprinkler systems use a spray in overhead sprinklers to deliver water. Drip systems deliver water in small amounts through small nozzles in pipes or ribbons. Both sprinkler and drip systems use pressurized pipes and some form of water pumping (Jägermeyr et al., 2015). The third and most common irrigation technique is the surface system. It consists of supplying water by gravity force, which leads to flooding a basin or using furrows between row crops. A distinction can also be made between irrigation of rice fields and irrigation of other crops. Paddy irrigation involves using water to flood the field during crop development for weed control (Hoogeveen et al., 2015; Hanasaki et al., 2018). This technique based on water level control leads to lower irrigation efficiency than for other types of crops (Hanasaki et al., 2018).

In some cases, to ensure water supply for irrigation, water can be transferred between regions separated by tens of kilometers (Wada et al., 2012). In this case, water management requires the construction of infrastructure such as dams, reservoirs and canals. Excess water from rainfall can be stored during the wet season and used during the dry season, increasing the water supply. In other cases, water is simply adducted from the main river channel during the flood season (Leng et al., 2015; Yin et al., 2021). Water management is done at the basin level, or at least at subbasin level, as in the case of the Indus River Basin (Laghari et al., 2012) and the Yellow River Basin (Yin et al., 2021; Zhou et al., 2021b), which contain two of the most irrigated areas in the world. The result is that, in some cases, water is transferred to areas several kilometers away from the main river channel. In this case, irrigation demand is met in excess of local availability (Wada et al., 2014). The combination of these processes (dam management, water transfer and irrigation) further increases the pressure on the water resource and the effects on hydrology. In addition, it is difficult to assess processes like water transfer and withdrawal in most cases due to the lack of data (Wada et al., 2014).

The transfer and use of large water volumes for irrigation impacts the hydrology flows. For example, there is evidence that irrigation can change recharge patterns locally, and deplete or increase aquifer storage (Döll et al., 2012). Some observations also suggest that irrigation

helps to understand negative streamflow trends in southwestern Europe (Vicente-Serrano et al., 2019), and that irrigation could help to understand groundwater depletion in India, China, and North America (Famiglietti, 2014; Rodell et al., 2018).

Irrigation-driven increases in evapotranspiration, mainly due to higher plant transpiration induced by lower water stress, also change the partitioning of surface energy from sensible to latent heat[2] (Cook et al., 2015) and have a direct impact on local air temperatures, as increased ET rates lead to less warming of the lower atmosphere (Thiery et al., 2017; Thiery et al., 2020). The influence of irrigation on precipitation is more controversial. The literature describes local precipitation increases due to additional air moisture from irrigation activities (Wei et al., 2013). At the regional level, irrigation could induce increased precipitation downwind of irrigated areas (Al-Yaari et al., 2019), or may impact the atmospheric circulation and induce regional atmospheric convergence due to temperature gradients (Lo and Famiglietti, 2013). On the other hand, irrigation may induce a local decrease of precipitation, owing to an anomalous local divergence in the lower atmosphere (Lo et al., 2021) or a stabilization of the boundary layer and less convective processes (Al-Yaari et al., 2019). But precipitation decrease is also due to shifts of precipitation patterns at regional and seasonal scale (Guim-

[2]Sensible heat involves a temperature change and no phase change, latent heat refers to phase change without temperature change.

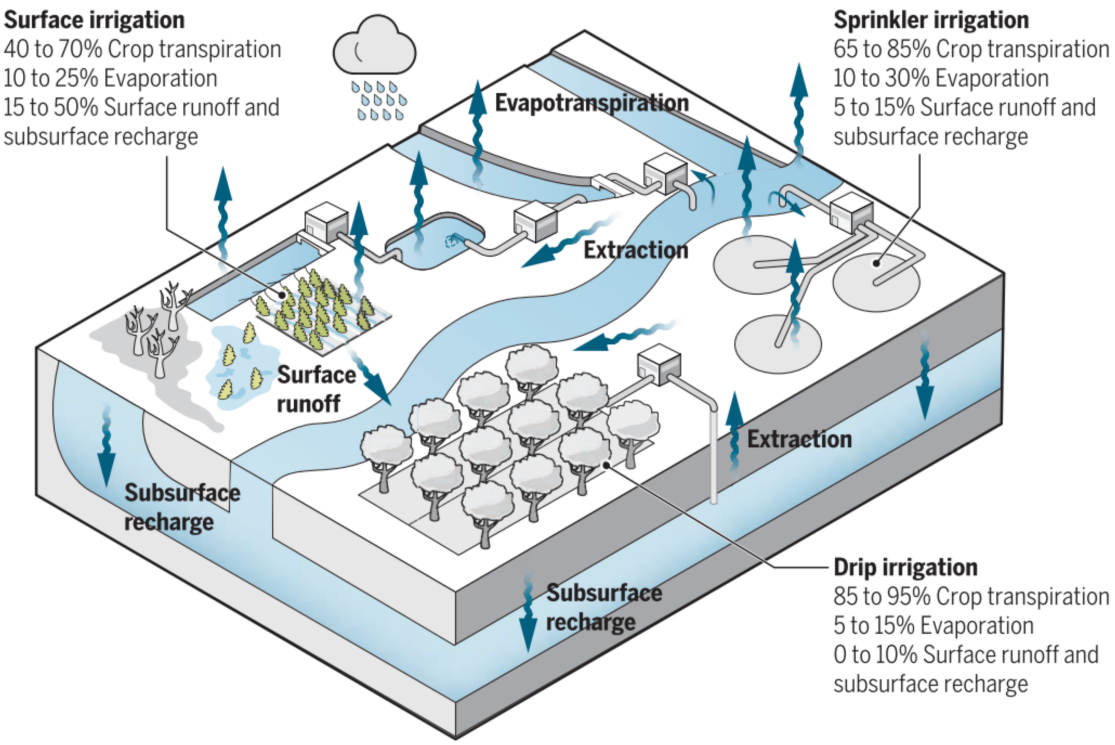

Figure 1.11: Water accounting for irrigation at the farm scale, and partitioning between evapotranspiration and return flows at a catchment scale. Percentages correspond to expert judgment ranges. Actual values depends on crop and soil types, weather and other factors. Figure taken from Grafton et al., 2018.

berteau et al., 2012a; Vrese et al., 2016a; Lo et al., 2021). In any case, uncertainties and gaps in knowledge remains at global and regional scale.

1.2.3 Uncertainty under climate change

Climate change has a direct impact on the effects of both landscape drivers (hillslope flow and irrigation), as a result of changes in precipitation patterns, atmospheric demand and warming. For instance, there is evidence that water table becomes deeper as a result of warming (Condon et al., 2020). Initially, hillslope flow will sustain ET rates and cool down the air, but as water table depletes, groundwater disconnects from the atmosphere at some point. But the experiment in Condon et al., 2020 does not account for the feedback from the atmosphere.

Irrigation adds complexity to these impacts and feedback. Projections suggest that irrigation demand will increase under climate change (Wada et al., 2013). Furthermore, there is evidence indicating that irrigation exacerbates climate change impacts on groundwater storage and stream discharge, especially in semi-arid basins (Ferguson and Maxwell, 2012), once again with no consideration for the atmosphere feedback. When considering the joint evolution of land and atmosphere, CMIP6 dataset under historical climate show that areas with irrigation activities exhibit a distinct behavior than if irrigation is not considered (Al-Yaari et al., 2022).

There are many gaps regarding the impacts and feedbacks of these two drivers under climate change, related to shortcomings or overlooked representation of them in the currently used models to simulate future climate (Clark et al., 2015; Fan et al., 2019). Improvement of the land surface representation in those models is needed to understand the joint evolution of atmosphere, land surface and landscape drivers. We will discuss about these models in the next section (section 1.3).

1.3 Interest of numerical modeling to understand the land-atmosphere interactions

Humans essentially live on land. Not surprisingly, many land surface processes and the interactions of the land with the atmosphere and the ocean are of vital importance for human societies. Therefore, understanding how climate and ongoing climate change affects living systems needs an accurate representation of land surface processes (Fisher and Koven, 2020).

1.3.1 General presentation of GCMs and ESMs

A general circulation model (GCM) is the tool that simulates the climate system at global scale (See Fig. 1.12). A GCM uses a grid-cell system to represent the state variables and

the fluxes between cells. The GCM is structured around four main models, each simulating a branch of the climate system:

- A general circulation atmospheric model
- A general circulation ocean model
- A sea ice model
- A land surface model
- A glacier model
- In some cases, a river routing model independent from the land surface model

Each of these models uses fundamental laws of physics, or empirical relationships established from observations, to represent water, momentum and energy dynamics. The most advanced models, called Earth system models (ESMs), also represent the carbon and other biogeochemical cycles across land surface, atmosphere and the ocean (See Fig. 1.12). The development of GCMs and ESMs has led to the participation of 39 different models in the last AR6 report (IPCC, 2021). One of these GCMs is the IPSL climate model, that couples ORCHIDEE land surface model to the LMDZ atmospheric model. As we will base our strategy on a modeling approach with ORCHIDEE, we will add more details on this model and the coupling to LMDZ in chapter 2.

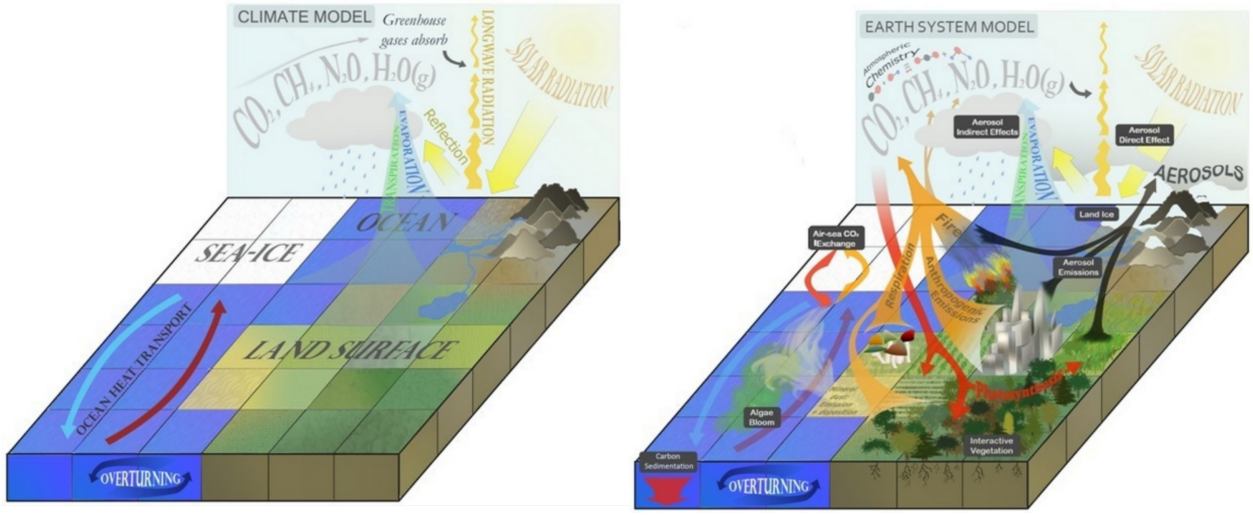

Figure 1.12: Key features of climate models and earth system models. The arrows represent the exchange of mass, energy and momentum fluxes between the components of the model. The process complexification is represented by the consideration of biological and chemical processes in the Earth system model. One example of these new processes is the aerosols. Taken from Heavens et al., 2013.

Land surface processes are represented in the land surface model (LSM). The LSM represents not only the lower boundary of the atmospheric model, but also the surface hydrology

and the continental branch of the water cycle. However LSMs, as idealized representations of land surface, have deficiencies that limit their use (Clark et al., 2015; Fan et al., 2019); for instance, on the understanding of the effects of the referred landscape drivers on hydrology and climate. In the next section (section 1.3.2), we will explore in more detail what LSM is, and how it can be used to understand the interaction between two components of the climate system, in this case the land and the atmosphere.

1.3.2 Land surface models, hydrologic processes and human water management

Originally, LSMs were developed to represent the physical boundary conditions of atmospheric models, simulating the exchange of water and energy fluxes through simple empirical equations for evaporation and soil storage (Manabe, 1969). The second generation of LSMs included a simple biophysical setup to represent the plant canopy and stomatal control of transpiration, and the third generation included the carbon cycle (Sellers et al., 1986; Krinner et al., 2005; Gascoin, 2009). As each process included in the LSM has its own characteristic duration and length due to differences in process scale, the model needs to aggregate and disaggregate the fluxes within the LSM components. This requirement also holds for information exchange with other components, such as the atmospheric model (Blyth et al., 2021). In addition, the process complexification, i.e. including more processes and more details, does not seem to stop as new challenges are addressed (Fisher and Koven, 2020; Blyth et al., 2021).

A LSM represents the land surface as grid-cells (following the GCM system, but note that other representations are possible, for instance using medium-sized catchments, like CATCHMENT Land Surface Model, Koster et al., 2000), and simulates the processes inside the grid-cells. For hydrologic processes there are similarities in representation inside the large scale LSMs, as reviewed by Clark et al., 2015. In general, many LSMs represent the storage and transmission of water in the soil with a 1-D Richards equation. Infiltration and runoff production uses a saturation excess approach, while the lower boundary condition uses a free drainage condition or simple groundwater dynamics at grid-cell scale (Clark et al., 2015) with representation of baseflow into the river channel.

On the other hand, hillslope flow is recognized as a key landscape feature that organizes water, energy and biogeochemical fluxes at subgrid scale, and has attracted considerable attention in recent years (Fan et al., 2019). But water flow across the landscape, i.e. lateral flow at hillslope scale and groundwater coupling with the surface, is not well represented or is simply missing within the models (Clark et al., 2015; Gleeson et al., 2021). Some models can include hillslope flow with the TOPMODEL framework, which was on of the first modeling efforts to include the effect of topography on hydrology (Beven and Kirby, 1979). In general, these models use a statistical approach to represent the topography. In other cases, models may represent the interaction between groundwater and soil moisture, i.e. capillary rise (Lo

and Famiglietti, 2011), but overlook the representation of topography. Still other models may represent topography by including subgrid soil columns and then simulating a flow between them. Finally, if the model is set up to be used at regional scale with a fine resolution, the effect of topography can be included by simulating the flow between grid-cells. A non-exhaustive summary of some LSMs, and the corresponding representation of groundwater-soil moisture interaction and hillslope flow, is presented in table 1.1.

Human water management is also lacking or is poorly represented in LSMs. Three main processes are considered to have a major impact in the regional and global water cycle: dams operation, groundwater pumping, and irrigation (Pokhrel et al., 2016). Irrigation has received special attention at least during the last two decades, but its representation may lack key aspects. To calculate the irrigation demand, some models use the evaporative demand, while others prescribe the demand from independent estimations, and finally some trigger irrigation when soil moisture drops below a certain threshold. In addition, irrigation in many cases is not limited by water availability, while water allocation, i.e. the rules of water use per source, has rarely been dynamically incorporated into the models. This representation allows to assess the effect on local and regional weather and climate, but prevents the representation of human impacts over water storage and other hydrologic flows (Pokhrel et al., 2016; Blyth et al., 2021). Recently, some LSMs have incorporated at regional scale new features into the corresponding irrigation scheme, to include differences in irrigation techniques and management strategies, and to explicitly specify the irrigation water source. A non-exhaustive summary of irrigation representation in LSMs is presented in table 1.2.

1.3.3 Modes of use of a LSM

A LSM uses meteorological information to calculate the water and energy budgets at the surface, and simulates the fluxes from the land surface to the atmosphere and the terrestrial hydrology. Meteorological forcing include precipitation (rainfall and snowfall), air temperature and humidity, downwelling shortwave and longwave radiation[3], surface wind and atmospheric pressure (Sellers et al., 1986). LSMs are built to operate in offline mode, i.e. with prescribed meteorological forcing from observed or reanalysis data (Vuichard and Papale, 2015), and in online mode, i.e. coupled to an atmospheric model (Pokhrel et al., 2016). In the latter case, sea surface temperature and sea ice content variables may be prescribed to force the atmospheric model, or the land surface-atmosphere simulation can be coupled to an ocean and sea ice models, according to the basic components of a GCM exposed in section 1.3.1 (Krakauer et al., 2016; Cheruy et al., 2020).

A LSM will calculate the radiative fluxes in both modes, which include upwelling short and longwave radiations, and to do so it will simulate the evolution of the albedo, i.e. the ratio of reflected to incoming shortwave radiation, and the emissivity and surface temperature

[3]Shortwave radiation refers to radiation from the sun, while longwave radiation refers to infrared radiation emitted by the atmosphere.

Table 1.1: Representation of groundwater-soil moisture interaction and hillslope flow in large LSMs. WT means water table, GW means groundwater, SM means soil moisture. Moving water table refers to a dynamic water table depth.

Model	**References**	**Domain**	**Topography heterogeneity**	**WT representation**	**GW/SM interaction**	**Coupling to GCM**
Catchment	Koster et al., 2000; Ducharne et al., 2000; Molod et al., 2015	Global	Statistical based on TOPMODEL	Mean water table depth	Moving water table and lateral flow within grid cell	Yes
CLM3.5	Niu et al., 2007; Lo and Famiglietti, 2011	Global	Not represented	Mean water table depth as moving boundary	Moving water table and capillary rise	Yes
CLM4.5	Zeng et al., 2018	Global	Explicit with a 2-D groundwater model	Mean and local water table depth	Moving water table	No
CLM5	Lawrence et al., 2016	Global	Not represented	Mean water table depth as moving boundary up to 8.5 meters depth	Moving water table	Yes
CLM5	Swenson et al., 2019	Global	Hillslope as interconnected columns	According to saturated layers in each column	Transfer between columns inside the grid cell	No
ISBA-TRIP	Vergnes et al., 2014; Decharme et al., 2019	Global	Represented by an elevation density function	Mean water table depth as moving boundary	Moving water table and lateral flow between grid cell	Yes

Table 1.1: Representation of groundwater-soil moisture interaction and hillslope flow in large LSMs (continuation).

Model	**References**	**Domain**	**Topography heterogeneity**	**WT representation**	**GW/SM interaction**	**Coupling to GCM**
LM3	Milly et al., 2014	Global	Statistical based on TOPMODEL	Mean water table depth	Moving water table and lateral flow within grid cell	No
LM3-TiHy	Subin et al., 2014	Global	Hillslope as interconnected columns	According to saturated layers in each column	Transfer between columns inside the grid cell	No
MATSIRO (MAT-GW)	Koirala et al., 2014; Yokohata et al., 2020	Global	No represented	Mean water table depth as moving boundary	Moving water table and capillary rise	Yes
ORCHIDEE	Tootchi, 2019; Arboleda Obando et al., 2022	Global	Hillslope as interconnected columns	Reservoir under upland soil column, WT in lowland fraction	Lateral flow within grid cell	Yes
LEAF2	Miguez-Macho et al., 2007; Fan and Miguez-Macho, 2011; Anyah et al., 2008	Regional	Explicit between grid cells	Mean water table depth as moving boundary	Moving water table and lateral flow between grid cells	Yes
VIC	Liang, 2003; Leung et al., 2011	Regional	No represented	Mean water table depth as moving boundary	Moving water table	No

Table 1.2: Representation of irrigation in large LSMs. SW and GW means surface water and groundwater, respectively. A virtual source of water means that an imaginary reservoir is used to meet the total demand, if SW stock runs out. Adduction refers to water transfer from non-local reservoirs. Water allocation (rules of water use per source for SW and GW) may use simple rules based on a predefined order, or be prescribed according to a map of fractions as in Siebert et al., 2010.

Model	**Reference**	**Domain**	**Irrigation demand**	**Water source**	**Irrigation supply**	**Water allocation**	**Coupling to GCM**
ORCHIDEE	Rosnay et al., 2003; Guimberteau et al., 2012b	Global	Evaporative demand	SW/GW, adduction	Restricted by natural stock	Simple	Yes
ACME	Leng et al., 2017	Global	Soil moisture target	SW/GW	No restriction	Prescribed	Yes
CLM4.5	Leng et al., 2013; Leng et al., 2014; Leng et al., 2015; Thiery et al., 2018; Thiery et al., 2020	Global	Soil moisture target	SW and virtual (GW may be activated)	No restriction (restricted by natural stock if GW activated)	Prescribed	Yes
ModelE2-R GISS	Puma and Cook, 2010; Cook et al., 2015; Singh et al., 2018	Global	Prescribed	SW and virtual	No restriction	Simple	Yes

Table 1.2: Representation of irrigation in large LSMs (continuation).

Model	Reference	Domain	Irrigation demand	Water source	Irrigation supply	Water allocation	Coupling to GCM
MAT-HI/HiGW-MAT	Hanasaki et al., 2008a; Pokhrel et al., 2012; Pokhrel et al., 2015	Global	Soil moisture target	SW and virtual (GW may be activated)	No restriction (aquifer depletion represented if GW activated)	Simple	No
VIC	Haddeland et al., 2006	Regional (South-east Asia and USA)	Soil moisture target	SW, reservoirs	Restricted by available water	Simple	No
ORCHIDEE-CROP	Yin et al., 2020	Regional (China)	Target value according to irrigation technique	SW/GW	Restricted	Simple	No
ISBA-SURFEX_v8.1	Druel et al., 2022	Regional (USA)	Soil moisture target	Virtual	No restriction	No	No
CLM5	Felfelani et al., 2021	Regional (USA)	Soil moisture target	SW/GW	No restriction (aquifer depletion represented)	Prescribed	No

for longwave radiation (Gascoin, 2009). Turbulence fluxes, corresponding to the sensible and latent heat fluxes, will also be calculated according to the evolution of surface characteristics like the roughness length (Blyth et al., 2021). When the LSM is run in online mode, it will pass upwelling short and longwave radiations, and the turbulent fluxes to the atmospheric model, playing the role of lower boundary of the atmospheric model.

The different experiments and strategies will depend on the scientific objectives and the scientific questions to be answered. For example, prescribing the atmosphere allows diagnosing the parameterization of the model and having an insight on errors or missing processes (Vuichard and Papale, 2015), but using an online simulation allows evaluating the joint interaction of the land surface and the atmosphere when there are changes in the parameterization or the inclusion of new processes (Seneviratne et al., 2013). This relationship between the research question and the scientific strategy is important to validate the use of the offline or online mode.

1.3.4 Synthesis on the representation of hillslope flow and irrigation within ORCHIDEE LSM

We have already mentioned that we will use the ORCHIDEE LSM as the modeling tool (section 1.3.1). Therefore we add a note on the representation of the interaction between groundwater, soil moisture and the atmosphere in ORCHIDEE. While the LSM represents groundwater dynamics in a rather simple way (Ngo-Duc et al., 2007), by default ORCHIDEE does not represent the interaction between groundwater, soil moisture and the atmosphere, nor the effect of topography within a grid-cell. An attempt to couple ORCHIDEE to TOPMODEL was shown in Ringeval et al., 2012. The coupling redistributed the soil moisture at the subgrid scale, and the performance of the coupling was tested by comparing offline simulations against observed river discharge and observed areas of inundated areas. Results underlined the difficulties of reproducing the observed variables but also the potential to simulate wetland areas in the LSM.

More recently, a first attempt to show the effect of a shallow water table in an online simulation with the LMDZ atmospheric model was described in Wang et al., 2018, but water table depth was prescribed. A simple representation of topography and hillslope flows was introduced in ORCHIDEE by including a lowland fraction, as reported in Tootchi, 2019. The lowland fraction was prescribed with a global map of wetlands area (Tootchi et al., 2019), and was tested offline at regional scale. ORCHIDEE and the new representation of hillslope flows were then used in online simulations in Arboleda Obando et al., 2022. The analysis focused on the effect of hillslope flows on the evolution of hydroclimatic variables under future climate change. Results showed a mitigation of drying trends in areas where precipitation was supposed to decrease due to climate change. In addition, warming was slightly reduced at global scale.

Now we will add a note on the inclusion of irrigation in ORCHIDEE. The first experiment

with the IPSL modeling framework is described in Boucher et al., 2004. The experiment included coupled simulations, but the land surface was represented by a bucket model, and the irrigation was prescribed, with no other consideration. The first inclusion of irrigation in an offline simulation is described in Rosnay et al., 2003. The irrigation demand is represented by an evaporative demand and a static crop coefficient, since plant development is not considered. In addition, the water source includes both the river streamflow and the aquifer, but it withdraws the water from the river on a priority basis. A third feature is the restriction of water supply according to the available water in the natural reservoirs.

The effect of plant development on irrigation demand was included in Guimberteau et al., 2012b, by estimating the potential plant transpiration under stress-free conditions. This experience uses online simulations by coupling ORCHIDEE to LMDZ, and maintains features from the Rosnay et al., 2003 module, such as water sources, the prioritization of rivers for water withdrawal and the restriction of water supply based on water availability. In addition water adduction from neighboring grid cells was disabled in the simulations due to the coarse simulation resolution. Recently, a version of ORCHIDEE that describes crop phenology and growth called ORCHIDEE-CROP included a new irrigation module (Yin et al., 2020). The new module represents flood and paddy irrigation techniques, to separate rice from no-rice irrigation. For the flood technique, irrigation demand is estimated using a soil moisture deficit approach, while for paddy, the demand is estimated with a paddy water level deficit. The experiment uses offline simulations in China, with and without water supply restrictions based on available water. If water supply is restricted, the module uses the same sources of water and withdrawal prioritization than in Rosnay et al., 2003. It should be noted that none of the experiments considered additional water supply constraints, such as environmental or infrastructural constraints, other than the total water availability in natural reservoirs.

1.4 Specific goals and thesis outline

In this chapter, we have shown scientific evidence suggesting that hillslope flow driven by topography, and irrigation activities, play a key role in the surface - atmosphere continuum as well as in continental hydrology. However, impacts and feedbacks of these two landscape drivers with the atmosphere are not well understood at large scale, due to simplification or lack of representation in land surface models, and limitations in observed datasets.

To advance the understanding of the interaction between each particular landscape driver with the atmosphere, and disentangle their individual effect on the water cycle, this research seeks to answer the following questions:

Q1. What is the impact/feedback of hillslope flow on present and future climate, for both mean and extreme values?

Q2. What is the impact of irrigation on land surface fluxes in present climate, for mean values?

The scientific strategy relies on the ORCHIDEE land surface model in offline mode and coupled to the LMDZ model, the atmospheric model of the IPSL Climate Model. We present the general structure of ORCHIDEE, and the main equations controlling evaporative fluxes and soil physics in chapter 2. We present as well some details on the way ORCHIDEE is coupled to the atmospheric model, and what are the technical difficulties to include new processes in ORCHIDEE. In Chapter 3 we present a new ORCHIDEE version that represents hillslope flow. Then, in order to respond to Q1, we show the modeling results of hillslope flow effects on hydroclimatic variables under climate change (as published in Arboleda Obando et al., 2022). We also present an analysis on the effect of hillslope flow on the evolution of temperature and rainfall extremes.

Chapter 4 presents a new irrigation scheme in the ORCHIDEE land surface model, that can be used at global scale, and that includes the use of new global datasets on water allocation. This scheme is then used to answer to Q2, focusing on the effects on land surface fluxes, but also on the effects on continental hydrology, and on the possible reduction of modeling biases for irrigation volumes, evapotranspiration, leaf area index, river discharge and total water storage anomalies. Finally, chapter 5 presents the main conclusions that respond to the stated questions, and discusses the limitations of these conclusions. This chapter also presents the main scientific perspectives for each landscape driver from a modeling point of view, and explores some possibilities for including both landscape drivers within a single version of ORCHIDEE in the future, and how to use this proposed version in online mode.

Chapter 2

The ORCHIDEE land surface model

2.1 General structure and input data

Here we describe ORCHIDEE version 2.2, which served as the basis for the introduction of the new irrigation module. But please note that the version that served as the basis for the introduction of the slope flows corresponds to ORCHIDEE 2.0. Both versions (ORCHIDEE 2.0 and ORCHIDEE 2.2) are very close to the version used for CMIP6 (Boucher et al., 2020; Cheruy et al., 2020). Version 2.2 includes a correction for negative soil water and down-regulation, and an improvement for the coupling of CO_2 with the LMDZ atmospheric model. ORCHIDEE 2.2 also includes minor bug fixes, and new adaptations to new supercomputers.

We also note the identification of each code revision. In the case of ORCHIDEE 2.0, the original code corresponds to revision r5164, and the changes introduced to represent the new hillslope flow representation are shown in chapter 3. In the case of ORCHIDEE 2.2, the original code corresponds to revision r7619, and the changes introduced to include the new irrigation scheme are shown in chapter 4. Finally, we outline that the representation of the processes described in this chapter remains the same or very close for both versions, for ORCHIDEE 2.0 and ORCHIDEE 2.2.

We also note here the contributions for the representation of each process inside the model. For hillslope flow, the module was in part tested in offline mode in the Seine river basin by Tootchi, 2019, and this version was already been used to run online simulations under future climate. In the case of the irrigation module, it is based on some of the characteristics from Yin et al., 2020, but a large part of the developments are original to this thesis project, and the new scheme was then tested during this thesis.

2.1.1 Overview

The model ORCHIDEE (for: ORganizing Carbon and Hydrology In Dynamics EcosystEm) is the land component of the IPSL climate model (Boucher et al., 2020). It describes the fluxes of mass (of water and carbon mainly), momentum and heat between the surface and

the atmosphere, and the carbon dynamics of the terrestrial biosphere.

ORCHIDEE is based on two main modules: the SECHIBA surface parameterization, and the STOMATE representation of photosynthesis, carbon allocation and phenology, as depicted in Fig. 2.1-a. ORCHIDEE can simulate the vegetation distribution with the dynamic global vegetation model (DGVM) LPJ, or it can be prescribed by annual maps (Krinner et al., 2005). For this study, the prescription of vegetation distribution is preferred, but activating the carbon parameterization. This strategy allows evaluation of the effect of landscape drivers on hydrology and vegetation dynamics (Wang et al., 2018).

While SECHIBA simulates the fast hydrological and energy flows, STOMATE represents the slower response of vegetation (Krinner et al., 2005). The hydrological module includes natural processes such as evaporation and transpiration, soil moisture dynamics and radiative fluxes (see Fig. 2.1-b) on the same time scale as the climate model, i.e. 15 to 30 minutes (Wang et al., 2018; Cheruy et al., 2020). The carbon module represents photosynthesis, stomatal conductance and plant phenology, carbon allocation and soil carbon dynamics on a daily time scale (Krinner et al., 2005). The hydrological module exchanges energy and water information with the carbon module and in return obtains leaf area index (LAI) values and canopy dynamics, which is important in partitioning evapotranspiration fluxes (Tafasca et al., 2020).

2.1.2 Representation of vegetation and soil

In ORCHIDEE, surface is represented as a rectangular grid cell. The vegetation is represented as a mosaic of a certain number of plant functional types (PFT), which borrow part or all the parameter values from a look-up table of metaclasses (MCTs) (Alléon, 2022). In the latest version of ORCHIDEE used for CMIP6, the PFT number is up to 15, and the number of MCTs is 13 (Tafasca, 2020). The 15 PFTs are: bare soil, tropical broadleaf evergreen, tropical broadleaf raingreen, temperate needleleaf evergreen, temperate broadleaf evergreen, temperate broadleaf summergreen, boreal needleleaf evergreen, boreal broadleaf summergreen, boreal needleleaf deciduous (for forest-type PFTS), temperate natural grassland (C3), natural grassland (C4), crops (C3), crops (C4), tropical natural grassland (C3) and boreal natural grassland (C3) (`https://orchidas.lsce.ipsl.fr/dev/lccci/orc_15pft.php`). ORCHIDEE version 2.2 does not have a specific crop phenology and harvest module, and considers that crops PFTs share the same values with grassland-type PFTS, with changes on some parameters, like vegetation height, leaf albedo, maximum leaf area index, and parameters controlling photosynthesis. A new development including a generic crop phenology has been tested in Wu et al., 2016, and is called ORCHIDEE-CROPS. This version was also used to test a new irrigation module at regional scale in China, with explicit representation of different irrigation techniques (Yin et al., 2020).

The soil column is discretized in layers of increasing thickness with depth, 11 by default, but the number of layers can be changed according to needs (Rosnay et al., 2002; Campoy

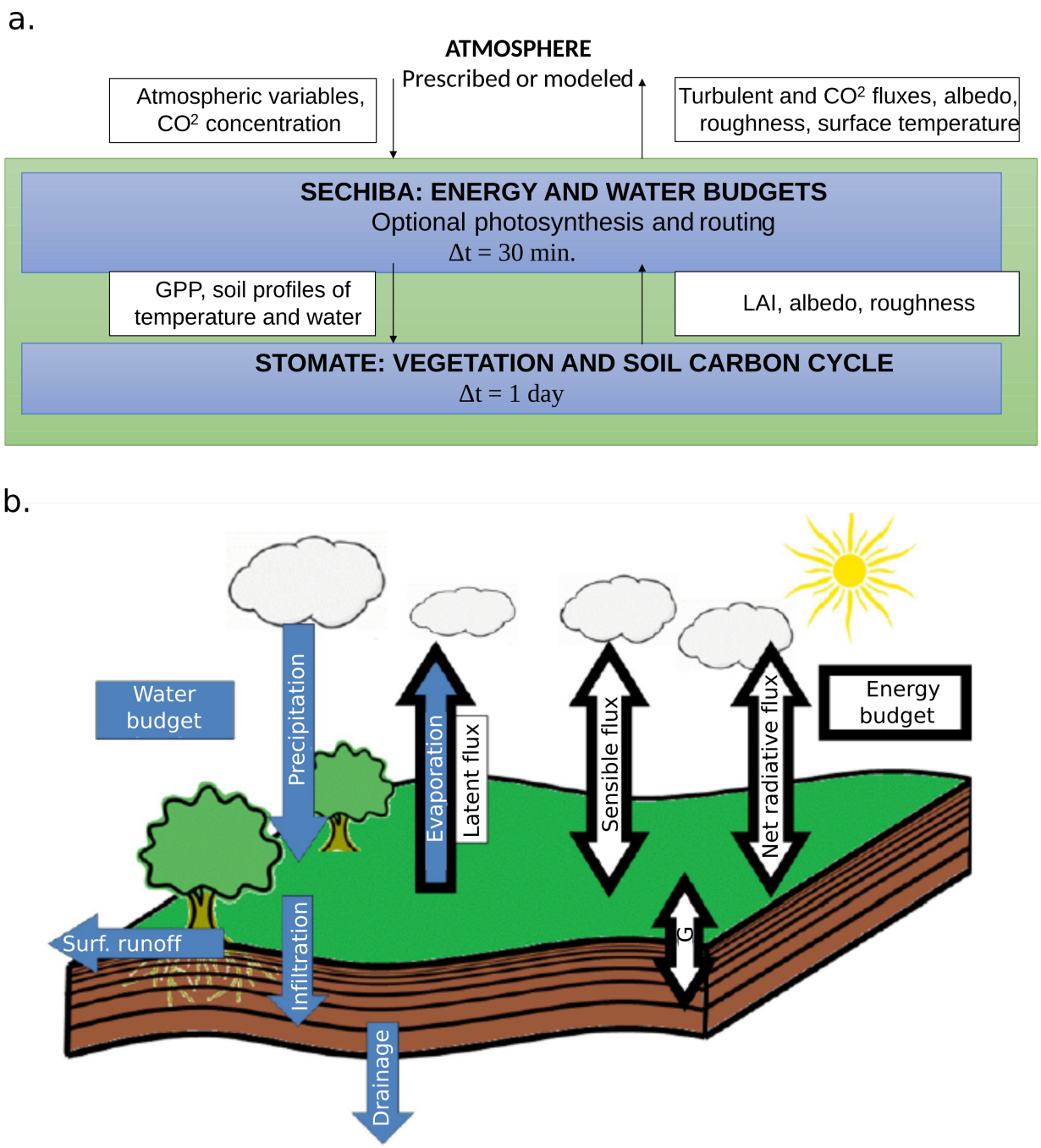

Figure 2.1: Basic structure of ORCHIDEE, depicting SECHIBA and STOMATE coupling. Diagram based on Krinner et al., 2005 and https://orchidee.ipsl.fr/about-orchidee/ with some simplifications (a). GPP mean gross primary production, LAI means leaf area index. Main processes included in ORCHIDEE, water fluxes in blue and energy fluxes in white (b), taken from Campoy et al., 2013. G represents the groundwater flux.

et al., 2013). Each pixel takes soil parameters based on Carsel and Parrish, 1988, depending on the dominant USDA soil texture class, according to a soil texture map. Soil texture is assumed uniform within the gridcell, but saturated hydraulic conductivity decreases with depth, as introduced by D'Orgeval, 2006. The texture map from Zobler, 1986 was retained

for CMIP6, but it is possible to use another soil texture map (see Tafasca et al., 2020).

To organize vegetation heterogeneity, the PFTs are arranged in independent soil columns (see an example in Fig. 2.2), each soil column with its own water balance, but with a single energy balance for the entire grid cell. By default, the number of soil colums is set to three, one for the bare soil, another for the forest-type PFTs, and the third for the crops and grasses PFTs (Tafasca, 2020). This separation into three soil columns prevent depletion of soil moisture by forest-type PFTs, with a deeper root system. The inclusion of new processes may lead to changes in the vegetation-soil discretization, for example in (Yin et al., 2020) to represent irrigation in China. There is no horizontal interaction between soil columns.

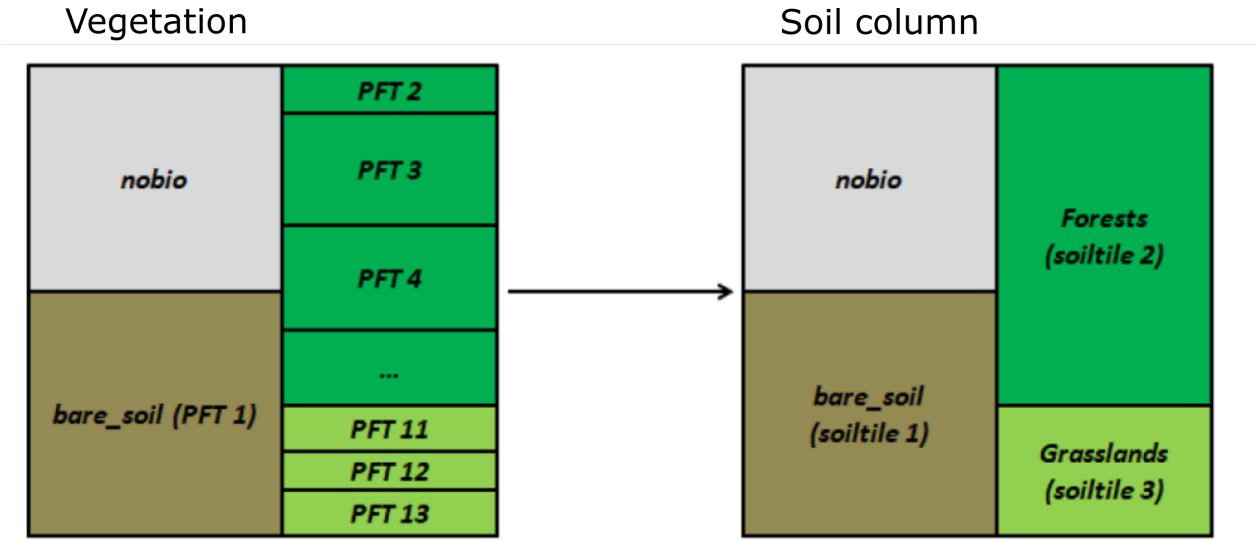

Figure 2.2: Division of the grid-cell into PFTs on the right, and correspondence of PFTs to soil columns. Color represents the areas within the same soil column. The nobio fraction corresponds to surfaces like ice, free water, cities, etc. (Ducharne et al., 2018). Figure taken from Alléon, 2022 with small modifications for simplification

2.1.3 Input data

ORCHIDEE needs two types of input data to run: data describing the land surface at global scale, and the meteorological forcing:

- Descriptive data: ORCHIDEE needs at least seven maps describing the surface. Firstly, ORCHIDEE needs the maps that describe the spatial vegetation distribution, i.e. the fraction of each PFT inside every grid-cell (Krinner et al., 2005). To calculate the soil hydraulic properties, the model needs a soil texture map (Tafasca, 2020), and to restrict the reinfiltration of surface runoff it needs a slope map (D'Orgeval, 2006). Routing needs at least three maps, the basin map, attributing an unique ID to each basin, the flow direction map, and a map of the topographic index (Ngo-Duc et al.,

2007). Additional processes may need additional input maps, e.g. representation of floodplains, irrigation areas or hillslope flow.

- Meteorological data: ORCHIDEE needs eight meteorological variables to run (see Table 2.1 for a summary, following Tafasca et al., 2020). If the LSM runs in coupled mode (Campoy, 2013), the atmospheric model exchanges information with the LSM every time step (for ORCHIDEE and LMDZ for example, the time step is 15 minutes). If ORCHIDEE runs in offline mode, the datasets typically provide the information in larger time-steps of 3 to 6 hours. ORCHIDEE disaggregates them into a time step of 30 minutes. (Mizuochi et al., 2021).

In the next sections we present details in the representation of vegetation and soil, especially in the strategy to represent the surface heterogeneity. Then we explore the mathematical representation of the water and energy budgets. Two main fluxes are shown in detail: the evapotranspiration flux to the atmosphere, and the vertical soil water diffusion. Next, the routing module that simulates the transport of water through watercourses is presented.

Table 2.1: Atmospheric variables used as input in ORCHIDEE.

Name	**Description**	**Units**
Ta	Air temperature at two meters	K
Qa	Air specific humidity at two meters	$kg.kg^{-1}$
W	Wind speed at 2 meters	$m.s^{-1}$
Psurf	Atmospheric pressure	Pa
SWdown	Downwelling shortwave radiation	$W.m^{-2}$
LWdown	Downwelling longwave radiation	$W.m^{-2}$
Pr	Rainfall	$kg.m^{-2}.s^{-1}$
Ps	Snowfall	$kg.m^{-2}.s^{-1}$

2.2 The energy and water balance of the land surface

2.2.1 Energy balance

For the energy balance, ORCHIDEE takes into account the downwelling and upwelling radiative terms, then estimates the change in surface temperature, and divides the available energy into different processes, using for most cases the updated surface temperature in each time step (D'Orgeval, 2006; Wang et al., 2016). The calculation of the net radiation in the surface is the difference between upward and downward radiation (see equation 2.1).

$$R_n = SW + LW\downarrow - LW\uparrow \tag{2.1}$$

Here, R_n is the net radiation, SW and LW represent the shortwave and longwave radiation respectively, and the arrows represent the direction (upward and downward), all terms in W/m^2. In the case of shortwave radiation, i.e. radiation coming from the sun, the net energy depends on the albedo α_{sw} , which controls the radiation that is reflected back to the atmosphere (see equation 2.2).

$$SW = SW \downarrow .(1 - \alpha_{sw}) \tag{2.2}$$

The albedo value is computed by ORCHIDEE according to snow and vegetation dynamics. Upward longwave radiation, i.e. radiation emitted by the surface depends on the surface temperature, according to the Stefan's law (see equation 2.3).

$$LW \uparrow = \epsilon.\sigma.T_{surf}^4 \tag{2.3}$$

Here ϵ is the surface emissivity, σ is the Stefan's coefficient in $W/(m^2.K^4)$ and T_{surf} is the surface temperature in K.

The net radiation in the surface is partitioned in ORCHIDE into at least four processes. This corresponds to the energy budget at the surface, and includes the latent and sensible heat fluxes, the ground heat flux and the energy stored by photosynthesis (see equation 2.4).

$$R_n = H_S + H_L + H_G + H_{photo} \tag{2.4}$$

Here H_S and H_L corresponds to the sensible and latent heat fluxes respectively, H_G is the ground heat flux, and H_{photo} is the chemical energy stored by photosynthesis, but neglected here (Alléon, 2022), all terms are in W/m^2.

The calculation of latent and sensible heat fluxes is based on similarity theory (Moene and Dam, 2014). For this, the gradient between the surface and the near atmosphere is used (see equations 2.5 and 2.6).

$$H_S = \rho.\vec{V}.C_d.Cp.(T_{surf} - T_{air}) \tag{2.5}$$

$$H_L = \beta_{ET}.[\lambda\rho.\vec{V}.C_d(q_{surf} - q_{air})] \tag{2.6}$$

Here, ρ is the air density, $\vec{V}$ is the horizontal wind, C_d is the drag coefficient and may be expressed as $1/(r_a.\vec{V})$, the aerodynamic resistance and the wind speed respectively (D'Orgeval, 2006, more details on the land-atmosphere coupling in section 2.4.2), Cp is the specific heat of the air, λ is the latent heat of vaporisation (or sublimation), T_{surf} is the surface temperature, T_{air} is the air temperature at 2 meters, q_{surf} is the saturated surface moisture, q_{air} is the saturated moisture at two meters, and finally β_{ET} is the resistance coefficient to the potential evaporation (Cheruy, 2018). We will go into the calculation of β_{ET} in more detail in section 2.3.1.

The last term of the energy balance is the ground heat flux, which relies on the description of the vertical temperature gradient (Cheruy, 2018; Alléon, 2022), and is expressed in equation 2.7.

$$H_G = -\kappa \frac{\partial T}{\partial z} \tag{2.7}$$

Where κ is the soil thermal conductivity ($Wm^{-1}K^{-1}$), T is the soil temperature (K) and z is the depth. These thermal properties depend on water content and soil texture (Ducharne et al., 2018).

The computation of the surface temperature and the corresponding saturated air moisture needs the use of a coupled numerical scheme, because the surface (represented in a coupled model by ORCHIDEE) is the lowest boundary of the atmospheric model, but at the same time interacts with the the lower atmosphere and changes its properties (Cheruy, 2018). The general interface within ORCHIDEE couples the radiation and the land surface schemes using an implicit coupling (Polcher et al., 1998). We will add some details on this coupling in section 2.4.2.

2.2.2 Water balance

At the land surface, ORCHIDEE partitions the total precipitation P, which includes rainfall and snowfall, into R_{TOT} total runoff (i.e. surface runoff and drainage to groundwater), ET the evapotranspiration, and the change in time of land water stock W (see equation 2.8 and Fig. 2.3).

$$\frac{\partial W}{\partial t} = P - R_{TOT} - ET \tag{2.8}$$

The total water stock W includes different reservoirs that are fed by precipitation. The first one is the stock of water intercepted by the vegetation canopy, the second one is the soil, and the third one is the snowpack (Campoy, 2013; Tafasca, 2020).

We will focus on the change of water stock in the soil, refered as W_s in equation 2.9. Changes in soil moisture are the result of effective precipitation reaching the soil surface. Effective precipitation corresponds to rainfall that does not refill the vegetation canopy, to the throughfall falling from the canopy, and to snowfall that melts. These effective terms are referred as P_e for rainfall and N_e for snowfall. Then the effective precipitation is partitioned into the bare soil evaporation E_g^c, the surface runoff R_s, and the infiltration I. This means that $P_e + N_e = E_g^c + R_s + I$. We note here that the bare soil evaporation is the result of different processes. When the water on the surface cannot supply the bare soil evaporation, some water is taken from the soil.

Some other processes must be taken into account to estimate the change of water stock in the soil. The first one is the water uptake from the roots, that corresponds to the plant transpiration E_t^c. The second is the deep drainage D, the flow reaching the bottom of the

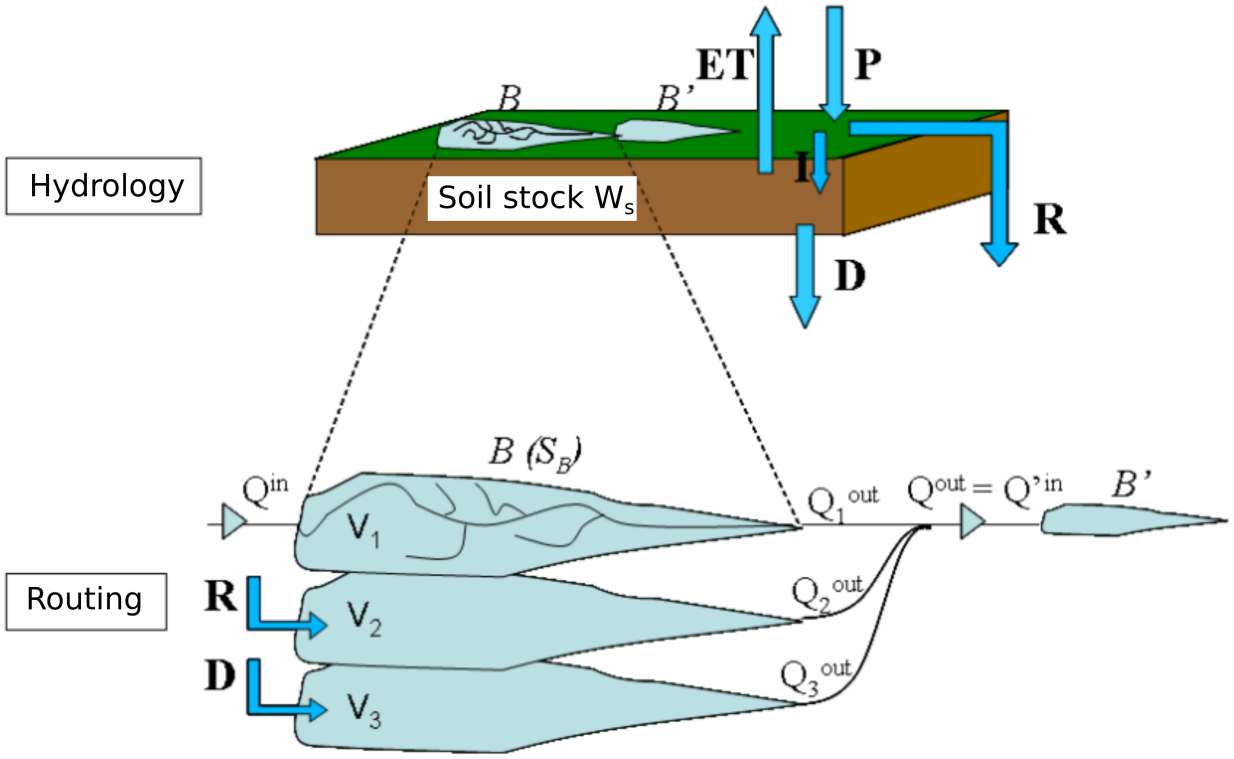

Figure 2.3: Main hydrology processes represented in ORCHIDEE, and link to runoff routing. The hydrology module computes the partitioning of precipitation into infiltration and surface runoff, and then into evapotranspiration and deep drainage. In the routing module, there are successive basins (B,B', etc) defined by surface area S_B. Each basin has three reservoirs, river reservoir V_1 receives flow from upstream. Surface and subsurface runoff reservoirs V_2 and V_3 receive surface and drainage fluxes from the soil column. Water flows out of each reservoir (Q_i^{out}, i =1,2,3) to the next reservoir (Q'_{in}). Figure taken from chapter 5 of D'Orgeval, 2006 with small changes.

soil column, which follows a free-drainage condition equal to $D = q_N = K(\theta_N)$, where $K(\theta_N)$ is the hydraulic conductivity in the bottom. Representation of changes of water stock in the soil is shown in equation 2.9.

$$\frac{\partial W_s}{\partial t} = I - E_g^c - E_t^c - D \tag{2.9}$$

Infiltration is calculated on the basis of a time-splitting procedure with a wetting front that saturates the soil layers (D'Orgeval, 2006), like a piston. When precipitation rate exceeds the infiltration capacity, excess infiltration will be converted to surface runoff. The infiltrated water will then be redistributed into the soil column (see section 2.3.2) while the surface runoff may reinfiltrate in flat areas (see D'Orgeval, 2006 and Tafasca, 2020 for more details.)

Finally, the evapotranspiration term is also partitioned into four subfluxes (see equation 2.10), and apart from bare soil evaporation includes transpiration E_t^c, canopy losses E_i^c and

snow sublimation E_s^c (Tafasca, 2020), with the term c indicating the grid-cell value.

$$ET = E_g^c + E_t^c + E_s^c + E_i^c \tag{2.10}$$

As the term $\lambda.ET$ in the water balance corresponds to H_L in the energy balance, the computation of its subfluxes as a function of water availability and modulated by the latent heat of evaporation, directly impacts the surface energy balance (Moene and Dam, 2014).

2.3 Representation of selected processes

2.3.1 Evapotranspiration

Evapotranspiration follows a classical bulk aerodynamic approach, with four fluxes: sublimation, interception loss, bare soil evaporation and transpiration. Each of the fluxes are limited by different resistances, as described in D'Orgeval, 2006; Guimberteau, 2010; Alléon, 2022. The actual evapotranspiration ET is calculated from a potential evaporation E_{pot} (see equation 2.11), and a stress function β_{ET} (see equation 2.6), following the same equations for the latent heat flux in the energy balance (compare to equation 2.6). D'Orgeval, 2006 introduced a correction for E_{pot} according to Milly, 1992.

$$E_{pot} = \rho.\vec{V}.C_d(q_{surf} - q_{air}) \tag{2.11}$$

$$ET = \beta_{ET}.E_{pot} \tag{2.12}$$

We already showed the ET partitioning in equation 2.10. As ORCHIDEE computes an effectively vegetated fraction per PFT, the bare soil evaporation comes from the non-vegetated fraction, and interception loss and transpiration come from the effectively vegetated fraction (Tafasca, 2020). For computation of the energy balance, these values are aggregated at the grid-cell scale.

Moreover, every term has its own stress function β_{ET}, which limits the local value of bare soil, interception and transpiration loss to the potential rate, and results in the mean value of actual evapotranspiration. If we neglect snow sublimation and floodplains evaporation for simplicity, the equation used to compute the stress function from its components is written in eq. 2.13 (Ducharne et al., 2018).

$$\beta_{ET} = (A_v(\beta_2 + \beta_3) + A_g\beta_4)/A_L \tag{2.13}$$

Where β_2, β_3 and β_4 are the individual stress functions on interception loss, transpiration and bare soil evaporation respectively, and A_v, A_g and A_L are the fractions of vegetated fraction, bare soil fraction, and total land area, respectively (Ducharne et al., 2018).

Beta for canopy interception loss

The beta value for canopy interception loss depends on the volume of water in the canopy I_k. The canopy can evaporate at a potential rate, only limited by aerodynamic resistance and an empirical structural resistance. If there is not enough water, the potential rate is reduced to I_k (see equation 2.14).

$$\beta_2 = \min\left(\frac{I_k}{E_{pot}}, \frac{I_k}{I_k^{max}} \frac{1}{1 + \frac{r_{struct}}{r_a}}\right) \tag{2.14}$$

Where I_k is volume of water intercepted in the canopy and I_k^{max} is the maximum volume of water that can be intercepted in the canopy, r_{struct} is the structural resistance, and r_a is the aerodynamic resistance as described in 2.6.

When canopy losses are reduced by the availability of water, the vegetation will start to transpire right after, so an additional term is needed. This term is called β_{23} (see equation 2.15)

$$\beta_{23} = max(0, \beta_{2,pot} - \beta_2) \tag{2.15}$$

Here, $\beta_{2,pot}$ is the second term of the right hand in equation 2.14.

Beta for transpiration

Transpiration depends on the stomatal conductance, which controls the leaf resistance. This stomatal conductance is directly dependent on soil moisture. If there is not enough water, transpiration will become zero (see section 2.3.2). β_3 is computed according to equation 2.16.

$$\beta_3 = \left(1 - \frac{I_k}{I_k^{max}}\right) \frac{1}{1 + \frac{r_a + r_{leaf}}{r_a}} + \min\left(\beta_{23}, \frac{I_k}{I_k^{max}} \frac{1}{1 + \frac{r_a + r_{leaf}}{r_a}}\right) \tag{2.16}$$

Where r_{leaf} is the leaf resistance, following (D'Orgeval, 2006; Alléon, 2022). Note here that the second right term corresponds to the transpiration after canopy losses are reduced by the availability of water.

Beta for bare soil evaporation

The flux of the bare soil evaporation is calculated using a supply/demand approach, assuming it can proceed at potential rate, unless water becomes limiting (See eq. 2.17).

$$\beta_4 = \min\left(\frac{Q_{up}}{E_{pot}}, 1 - \beta_2 - \beta_3\right) \tag{2.17}$$

Where Q_{up}^c is the maximum amount of water that can be extracted from the soil column (see section 2.3.2 for more details). The second term $1 - \beta_2 - \beta_3$ represents the condition that actual evaporation cannot be higher than the potential evaporation. In the latter case, ORCHIDEE gives priority to the canopy loss and transpiration (D'Orgeval, 2006).

2.3.2 Soil hydrology

ORCHIDEE relies on a one-dimension Fokker-Planck equation to represent unsaturated soil water flow (Rosnay et al., 2002; D'Orgeval, 2006; Campoy et al., 2013; Campoy, 2013). To do so the Richards equation (equation 2.18) uses a relationship between the hydraulic conductivity and diffusivity (equation 2.19) in function of the soil moisture.

$$\frac{\partial\theta(z,t)}{\partial t} = \frac{\partial}{\partial z}\left(D(\theta)\frac{\partial\theta(z,t)}{\partial z} - K(\theta)\right) - S(z,t) \tag{2.18}$$

$$D(\theta) = K(\theta)\frac{\partial h(\theta)}{\partial\theta} \tag{2.19}$$

Where $\theta(z,t)$ is the soil moisture at depth z (in $m^3.m^{-3}$), t is time, $D(\theta)$ is the hydraulic diffusivity in function of soil moisture (in $m^2.s^{-1}$), $K(\theta)$ is the hydraulic conductivity in function of soil moisture (in $m.s^{-1}$), $S(z,t)$ is the sink term due to transpiration (in $m^3.m^{-3}.s^{-1}$), and $h(\theta)$ is the matric potential (in m).

Unsaturated values of hydraulic conductivity and diffusivity follow Mualem and Van Genuchten (Genuchten, 1980; Mualem, 1976; Ducharne et al., 2018), and the parameter values are based on (Carsel and Parrish, 1988). More details in the mathematical implementation in D'Orgeval, 2006 and in Ducharne et al., 2018. In addition, from D'Orgeval, 2006 there are some modifications of the saturated hydraulic parameter. It follows an exponential decay with depth, but a decrease towards the soil surface to account for the presence of roots (D'Orgeval, 2006; Ducharne et al., 2018).

The model first calculates the change in soil moisture due to infiltration (see D'Orgeval, 2006 for more details in the implementation) and assumes a free drainage condition in the bottom (Campoy et al., 2013).

Control of bare soil evaporation

The variable Q_{up} in equation 2.17 is calculated at the end of each time step by a dummy integration to prevent mass conservation violation. The model may assume that the first layer does not contribute to evaporation, to limit the water flux and prevent soil moisture values under the residual soil moisture limit (Ducharne et al., 2018). An additional control exists when the soil moisture values in the top soil layers are under the wilting point. It is also possible to activate a soil resistance to constraint the soil evaporation but this option is not used in this work.

Control of transpiration

Transpiration sink term in equation 2.20 depends on the soil moisture profile and the root density profile. The root density $R(z)$ is assumed to decrease exponentially with depth z (see equation2.18) and depends on a decay factor c according to the PFT.

$$R(z) = exp(-cz) \tag{2.20}$$

With this assumption, it is possible to calculate a relative root density per layer (see

equation 2.21).

$$n_{root}(i) = \frac{\int_{\Delta z} R(z)}{\int_{z=0}^{z=2} R(z)} \tag{2.21}$$

Where $n_{root}(i)$ is the relative root density in layer i, following the fraction of the root density in layer Δz compared to the total soil column (from $z = 0$ to $z = 2$ for a 2 meters soil column). Note that by construction, the sum of all $n_{root}(i)$ is equal to 1.

The relative root density and the soil moisture are used to calculate a stress factor by layer according to equation 2.22.

$$u_i = n_{root}(i) \max\left(0, \min\left(1, \frac{W_i - W_w}{W_{\%} - W_w}\right)\right) \tag{2.22}$$

Here u_i is the stress factor of layer i, W_i the total soil moisture content in layer i, W_w the wilting point soil moisture content and $W_{\%}$, the threshold that constrains transpiration, equal to $W_w + p\%.(W_c - W_w)$, with W_c the field capacity soil moisture content and $p\%$ a constant set by default to 0.8. Above this value $W_{\%}$, transpiration is maximal, while below this limit transpiration is restricted and can become zero if it reaches the wilting point of soil moisture.

2.3.3 Runoff routing

ORCHIDEE is able to simulate the horizontal fluxes of water through river channels (Polcher, 2003; Ducharne et al., 2003). The transfer scheme routes drainage and runoff through three reservoirs (see the link between hydrology and routing in Fig. 2.3). Each reservoir has its own residence time, and they represent fast flow (surface fluxes), slow flow, and streamflow. The fast and slow reservoirs transfer water to the streamflow, while this latter receives water from upstream and interacts with downstream reservoirs. Further descriptions of the routing scheme are in Ngo-Duc et al., 2007 and Guimberteau et al., 2012a.

The representation of horizontal flows allows to include other processes linking the river and its watershed, such as flooding, ponding (not activated in this thesis), and irrigation withdrawals from groundwater and surface water. But note that the default structure of the routing scheme, with local flows directly feeding the river channel, does not represent the interaction between fast and slow reservoirs and the atmosphere through the soil surface. This means that this structure does not represent soil moisture redistribution led by hillslope flows. We will present the chosen representation of hillslope flow and irrigation in the corresponding chapter 3 and chapter 4 respectively.

The water that is transferred from each reservoir, Q_i^{out}, depends on the water stocked in reservoir i, V_i, and a value $\tau_i = k.g_i$ (see equation 2.23).

$$Q_i^{out} = \frac{V_i}{\tau_i} \tag{2.23}$$

Here, k in m corresponds to a topographic index, proportional to the grid-cell longitude and inversely proportional to the slope, and g_i is a constant for the reservoir i (Ducharne et al., 2003) in $daym^{-1}$. We use here parameters values from Ngo-Duc et al., 2007, i.e. 3.0, 25.0 and 0.24 $10^{-3}m^{-1}day$ for fast, slow and stream reservoirs, respectively, estimated empirically for the Senegal River. These values were then generalized for all the basins of the world, and results are reported to be acceptable for many larger rivers (Ngo-Duc et al., 2005).

2.4 LMDZOR, the land-atmosphere component of the IPSL climate model

2.4.1 General overview of LMDZOR

The land-surface-atmosphere component of the IPSL climate models is called LMDZOR. LMDZOR couples the ORCHIDEE LSM to the atmospheric model LMDZ6A (Hourdin et al., 2020). The revision of LMDZ6A used for this thesis corresponds to r3608. To represent the ocean, LMDZOR needs inputs of sea surface temperature (SST) and of sea ice content (SIC) to prescribe the ocean conditions.

LMDZ6A is an enhanced version that includes the new physics package, and was first tested for CMIP5 as LMDZ5B (Hourdin et al., 2013). LMDZ6A includes a complete re-thinking of the parameterization of turbulence, convection and clouds, and a more careful tuning of the model free parameters, as described in Hourdin et al., 2020. The new LMDZ6A physics includes a small-scale representation of turbulence, boundary layer convection represented with a thermal plume model, a new representation of deep convection and clouds, representation of aerosols and aerosol-cloud interactions, and an improved radiative scheme. There are also some changes on the boundary layer representation that we present in the next section in some more detail.

2.4.2 General interface between ORCHIDEE and LMDZ

Within the boundary layer, the estimation of meteorological variables at the surface boundary in LMDZOR is based on the Monin-Obukhov similarity theory, which proposes a relationship between mean gradients and a scaling parameter (Cheruy, 2018). LMDZORC uses the bulk stability functions proposed by Louis, 1979. These stability functions are determined experimentally and depend on the Richardson number (buoyancy production ratio and shear production ratio, see Moene and Dam, 2014) and roughness height ratio (actual height and roughness height ratio). They allow to estimate the values of drag coefficients for momentum, heat and moisture. It is worth noting that recently, a dynamic roughness height computed for each PFT based on the leaf area index was included in ORCHIDEE (Cheruy et al., 2020).

The interface between the atmospheric model and the LSM uses an implicit coupling scheme to compute the vertical atmospheric diffusion, using the turbulent surface fluxes,

as noted above. The numerical scheme calculates some atmospheric coefficients within the planetary boundary layer top-down to the surface. Then using those atmospheric coefficients and the heat fluxes, it calculates the surface temperature and the air temperature in the atmospheric layers from bottom to top. To close the energy balance at the surface and calculate the surface temperature and surface static energy, ORCHIDEE uses a sensitivity analysis for the current time step (Polcher et al., 1998). We note that the coupling between the atmosphere and the LSM includes two different schemes: turbulent diffusion and ground heat diffusion, and a forcing: the net radiation. The boundary layer scheme provides the atmospheric variables over the surface and the relationship with fluxes as well as the the drag coefficients, while the land surface model provides the turbulent fluxes, the albedo, and the surface roughness heights (Cheruy, 2018).

Finally, it should be noted that ORCHIDEE uses a simple flux-aggregation approach to couple the subgrid-scale land surface fluxes with the atmosphere (Polcher et al., 1998). This means that the different soil columns in the LSM "see" a single atmosphere condition. But we add that there are many possible strategies for coupling heterogeneous land fluxes to the atmosphere (Vrese et al., 2016b; Vrese and Hagemann, 2018). The subgrid scale variability may be coupled using a statistical representation, or in the case that a discrete representation of land surface heterogeneity is preferred, the mathematical representation may use a "parameter-aggregation" approach, a "simple flux-aggregation" approach (as ORCHIDEE does), and finally an explicit representation of the mixing process (Vrese et al., 2016b).

2.5 Inclusion of new processes inside ORCHIDEE

In this final section, some data on the ORCHIDEE code is given, and a personal reflections is made on the difficulties in including new processes within ORCHIDEE. This technical aspect of the research work is fundamental to take into account the limitations of the representation, as well as to understand the feedback mechanisms within the model.

ORCHIDEE is a complex model, with a complex code. Currently, it represents more than 80 Fortran files, with around 61.000 code lines and 43.000 comments lines. The structure of the code is modular. This means that we have a main routine that calls subroutines, exchanging input and output information. The main routine is sechiba.f90, which calls in a precise order all the other subroutines. The general order at each time step is as follows (see also Fig. 2.4 for the exchange of information between modules):

1. Call for the β_{ET} parameter value, based on water stocks at the end of the preceding time step from hydrol.f90.

2. Call for the energy balance module enerbil.f90, calculating ET and its subfluxes

3. Call for the soil hydrology module hydrol.f90, which updates the water stocks and the β_{ET} parameter value

4. Call for surface variables module condveg.f90, which updates surface parameters like emissivity or albedo

5. Call for soil thermodynamics module thermosoil.f90, which accounts for heat diffusion through the soil, with thermal parameters depending on soil moisture

6. Call for routing module routing.f90.

7. Call for slow processes included in STOMATE (file stomate.f90), and others like vegetation distribution in slowproc.f90.

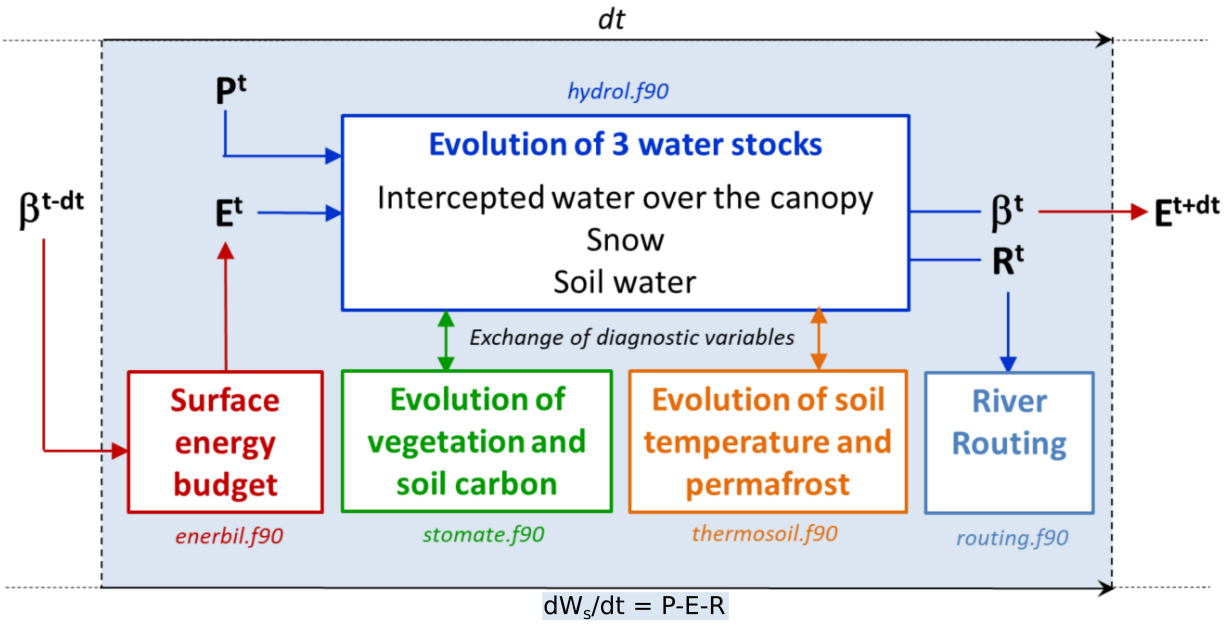

Figure 2.4: General structure of the ORCHIDEE code for a single time step dt. W_s is the water stock in the soil, β is the evapotranspiration resistance β_{ET}, E is the actual evapotranspiration, P is the precipitation, and R is the total runoff. Indices t-dt, t, and t+dt correspond to previous, current and subsequent time step. The figure links the processes to the name of the .f90 fortran module within de code. Figure taken from the ORCHIDEE training material, https://forge.ipsl.jussieu.fr/orchidee/attachment/wiki/GroupActivities/Training/cours_orchidee_jan2022_ducharne_wiki.pdf.

Including new processes within this structure, or improving already existing processes, is a task that needs some preparation beforehand. To this end, three questions are proposed here after the personal experience of working with the ORCHIDEE code, to guide the technical coding work:

1. Where should the new parameterization be included? This question is related to the position of the new parameterization inside the code flow.

2. Which are the input and output variables that must be included in the new process? Not only which variables, but also where they are calculated.

3. What is the interaction between the new outputs and other processes included inside the model? It means that new outputs may become inputs for other processes.

This simple framework based on three questions is intended to simplify the inclusion of new modules, or the improvement of existing ones. In addition, in cases where the new process is complex, it is best to break it into several sub-processes and apply the three questions to each of them. Thus, for the landscape drivers we are interested in, we can be able to understand the variables that affect the mathematical representation of the new process within ORCHIDEE, and what is the feedback from the new process on those variables. This clearness can also help in the coding-testing-debugging-testing process, to ensure the adequacy of the results.

2.6 Chapter conclusions

In this section we presented the ORCHIDEE land surface model. We showed how the surface heterogeneity is represented, and what is the input data needed to run the model. Then we presented the energy and water balance as estimated inside ORCHIDEE, and how are represented some processes of interest, linked to land surface fluxes, soil hydrology and continental hydrology. Finally, we focused on the LMDZOR, the land-atmosphere component of the IPSL climate model, that couples ORCHIDEE LSM to LMDZ atmospheric model. As a final personal reflection, we showed some ideas for the technical work of coding new processes inside ORCHIDEE. All these elements are important for the forthcoming chapters, where we will depict results on the effect of the inclusion of the two landscape drivers within ORCHIDEE.

Chapter 3

Effect of hillslope flow on the evolution of hydroclimatic variables

3.1 Introduction to the chapter

This chapter includes a paper recently published in Earth's Future (Arboleda Obando et al., 2022). We add part of the supplementary information in section 3.2.3.2 to include the comparison of the simulations with observed products. Addition of part of the supplementary information is the only change compared to the original paper, the rest of the supplementary information is in annex A.

In the first part of this chapter (section 3.2) we show the representation of hillslope flow within ORCHIDEE (section 3.2.2.1) and the numerical design of coupled simulations for present and future climate (section 3.2.2.2). Then we show the effect of hillslope flow on the long-term evolution of hydroclimatic variables under climate change (section 3.2.3.3). Furthermore, the assessment includes the analysis of long-term trends at global scale and at regional scale, using a simple climate classification based on the aridity index and mean air temperature (section 3.2.3.5).

In the second part (section 3.3) we show an additional analysis on the effect of hillslope flow in the evolution of climate extreme values for near-surface temperature and precipitation. To assess the effect of hillslope flow, we use simple indices to calculate the intensity and frequency of extreme events, as defined by a relative threshold based on quantiles. We end with some conclusions in section 3.4.

3.2 Influence of hillslope flow on hydroclimatic evolution under climate change

Pedro Felipe Arboleda Obando [1,3], Agnès Ducharne[1,3], Frédérique Cheruy[2,3], Anne Jost[1,3], Josefine Ghattas[3], Jeanne Colin[4], Camille Nous[1,3]

1 Laboratoire METIS (UMR 7619, Sorbonne Université, CNRS, EPHE), Paris, France, 2 Laboratoire de Météorologie Dynamique (UMR 8539, Sorbonne Université, CNRS), Paris, France, 3 Institut Pierre Simon Laplace (FR 636, Sorbonne Université, CNRS), Paris, France, 4 Centre National de Recherches Météorologiques (UMR 3589, Météo-France, CNRS, Université Fédérale de Toulouse), Toulouse, France

Abstract We analyzed the influence of hillslope flow on projections of climate change by comparing two transient climate simulations with the IPSL climate model between 1980 and 2100. Hillslope flow induces a reorganization and increment of soil moisture (+10%), which increases evapotranspiration (+4%) and precipitation (+1%) and decreases total runoff (-3%) and air temperature (-0.1°C) on an annual average over land for 1980-2010 when compared to simulation not representing hillslope flow. These changes in land/atmosphere fluxes are not homogenous and depend on regional climate and surface conditions. Hillslope flow also influences climate change projections. On average over land, it amplifies the positive trend of soil moisture (+23%), evapotranspiration (+50%) and precipitation (+7%) and slightly attenuates global warming (-1%), especially for daily maximum air temperature. The role of hillslope flow in supporting surface/atmosphere fluxes is more evident at a regional scale. Where precipitation is projected to decrease, hillslope flow is shown to attenuate the related declines in evapotranspiration, precipitation, and total runoff, regardless of aridity conditions and mean air temperature. Where precipitation is projected to increase, hillslope flow amplifies evapotranspiration enhancement but attenuates the increase in precipitation and total runoff. Warming is generally attenuated, especially in semiarid and cold areas, and humid and warm/temperate regions, but the signal is weak. These results demonstrate the role of hillslope flow in enhancing water and energy fluxes between the surface and the atmosphere. They also suggest that including hillslope flow in climate models would weaken the projected intensification of hydrological extreme events.

3.2.1 Introduction

There is strong evidence that soil moisture plays a critical role in the evolution of climate (Seneviratne et al., 2010). For instance, at the seasonal scale, the GLACE project (Koster et al., 2006) revealed that soil moisture anomalies in the Northern Hemisphere, the Sahel and equatorial Africa can heavily affect seasonal values of precipitation and temperature (Koster, 2004). In Europe, soil moisture plays a role in the northward propagation of Mediterranean drought and in the occurrence of extreme summertime temperatures (Zampieri et al., 2009; Quesada et al., 2012); pre-existing dry soil conditions are a necessary prerequisite for the

occurrence of heat waves (Perkins, 2015; Horton et al., 2016). In the United States, irrigation-induced changes in soil moisture could help explain part of the modeling bias in summer temperature and precipitation (Al-Yaari et al., 2019; Barlage et al., 2021).

Further efforts in the GLACE-CMIP5 project analyzed the feedbacks of climate change and land-atmosphere coupling. Early results revealed that the projected decrease in soil moisture would result in a stronger decrease in evapotranspiration and precipitation and a higher increase in temperature at the end of the twenty-first century (Seneviratne et al., 2013). Other results pointed to feedback between decreasing soil moisture and land surface temperature, relative humidity and precipitation, thus explaining an increase in aridity under climate change (Berg et al., 2016). By the end of the twenty-first century, in some regions, decreasing trends in soil moisture due to climate change can also lead to further increases in the intensity, frequency and duration of temperature extremes and in dry precipitation extremes (Lorenz et al., 2016).

For land-atmosphere coupling, knowledge gaps exist regarding the effect of topography heterogeneity on energy and water fluxes between land and atmosphere. The topographic gradient induces a hillslope flow of surface water and groundwater between the upland area and the lowland valley (Fan et al., 2019), which can create a wetter riparian wetland (Fan and Miguez-Macho, 2011). The role of groundwater is especially important for hillslope flow, because groundwater is the largest continental reservoir (Gleeson et al., 2016), and its slow flow influences a longer soil moisture memory in areas with shallow water tables (Cuthbert et al., 2019; Gleeson et al., 2011; Martínez-De La Torre and Miguez-Macho, 2019; Martinez et al., 2016a; Martinez et al., 2016b). In water-limited regions, wetter soil induced by groundwater increases evapotranspiration (ET) (Fan et al., 2019; Maxwell and Condon, 2016). Higher ET directly affects surface water and energy budgets and can lead to increased precipitation as response from the atmosphere (Lo and Famiglietti, 2011; Wang et al., 2018).

Modeling is a good option for disentangling the link between hillslope flow and land-atmosphere fluxes. Coupling a land surface model (LSM) to a general circulation model (GCM) allows us to explore the evolution of the land and atmospheric components at the global (Wang et al., 2018) and regional scales (Fan et al., 2007; Anyah et al., 2008; Campoy et al., 2013). In LSMs, the representation of groundwater storage and its contribution to river discharge is now commonly included, with multiple approaches from a simple reservoir to physically-based representations with water table dynamics (Gleeson et al., 2021). If implemented at a high enough spatial resolution, the latter approaches allow one to explicitly simulate hillslope flow and its influence on soil moisture heterogeneities, but they remain very rare in climate models, and only in regional ones (Anyah et al., 2008; Furusho-Percot et al., 2019). In coarse resolution LSMs classically coupled to atmospheric models, hillslope processes remain a challenge (Clark et al., 2015). Most attempts make use of the TOPMODEL formalism (Beven and Kirby, 1979; Band et al., 1993), either in a diagnostic mode (Gedney and Cox, 2003), or with a full coupling of subgrid water table depth distribution with the ones of soil moisture, runoff and ET (Walko et al., 2000; Koster et al., 2000; Ducharne et al., 2000).

These models, however, may overestimate the moistening of soils by capillary fluxes from the water table, as it is assumed to always be shallow in TOPMODEL (Gascoin et al., 2009; Beven et al., 2021). Interactions with deeper groundwater systems can also be described in climate models, usually via 1D capillary fluxes to the soil, which overlooks the modulations by small scale (subgrid) topography. The most comprehensive description of groundwater-soil moisture interactions in a global climate model is presently offered by the ISBA-CTRIP LSM (Decharme et al., 2019)), combining 2D horizontal groundwater flow between grid cells with vertical capillary rise in the fraction of each grid-cell with the lowest elevation. Therefore, the feedback of hillslope flow on climate change projections is not clear. Climate change, especially warming, is expected to have an impact on groundwater recharge and storage (Smerdon, 2017; Markovich et al., 2016; Wu et al., 2020). Such changes in groundwater storage and hillslope flow may support higher ET rates in transition zones between wet and dry climates for some time, but not indefinitely (Condon et al., 2020). However, the evidence provided is regional, and the modeling efforts overlook dynamical interactions with the atmosphere. Because land-surface coupling has an impact on the projection of climate change, the reorganization of soil moisture induced by hillslope flow may play a role in projections of some hydroclimatic variables on a global scale. Here, we present evidence of the influence of hillslope flow on global climate change projections of hydroclimatic variables. We contrast the results of two transient land-atmosphere simulations for the period 1979-2100, one of which uses the default land surface representation of the ORCHIDEE LSM (section 3.2.2.1, ORCHIDEE-REF), while the other includes a novel subgrid hillslope flow parameterization (section 3.2.2.1, ORCHIDEE-HSL). As described in section 3.2.2.2, we use LMDZOR, the coupled land-atmosphere component of the IPSL-CM6 climate model from the Institut Pierre Simon Laplace (Boucher et al., 2020; Cheruy et al., 2020). First, we focus the analysis on the historical period (1980-2010) to explore the effects of hillslope flow on yearly and seasonal average values in terms of both sensitivity and realism against observations (section 3.2.3.1). We then explore the effect of hillslope flow on climate change trends, which we call hillslope flow modulation. To calculate the hillslope flow modulation, we first estimate the long-term trend for each simulation during the twenty-first century; then the trend of the difference of the two simulations at the global scale in section 3.2.3.3; and finally, the spatial distribution of the hillslope flow modulation in section 3.2.3.4. To further analyze hillslope flow modulation at the regional scale, we use a simple climate classification inspired by the Köppen-Geiger and Thornthwaite classifications (Beck et al., 2018; Feddema, 2005) in section 3.2.3.5. The latter allows for defining which regions are prone to hillslope flow modulation and what is the type of modulation in these areas. In section 3.2.4, we discuss the main limitations of our results, and we close in section 3.2.5 with the main conclusions and perspectives.

3.2.2 Materials and methods

3.2.2.1 Description of the land surface model

ORCHIDEE-REF

ORCHIDEE (ORganizing Carbon and Hydrology in Dynamic EcosystEms) is a process-based model that describes the fluxes of mass, momentum and heat between the surface and the atmosphere (Krinner et al., 2005). The version used here as a reference (called ORCHIDEE-REF in the following) corresponds to version 2.0, included in the IPSL-CM6 climate model for CMIP6 simulations and described in Cheruy et al., 2020, Boucher et al., 2020, and Tafasca et al., 2020. Here, we summarize the main characteristics of the model. In section 3.2.2.1-ORCHIDEE-HSL, we summarize the hillslope flow parametrization.

In each grid cell, vegetation is represented by a mosaic of up to 15 plant functional types (PFTs), including bare soil. Each PFT is characterized by a set of parameters (Boucher et al., 2020; Mizuochi et al., 2021), and fractions are described by the LUHv2 dataset (Lurton et al., 2020). Plant phenology is controlled by the STOMATE module, which couples photosynthesis and the carbon cycle and computes the evolution of the leaf area index (LAI) (Krinner et al., 2005). It means that CO_2 influences plant growth and phenology. PFTs are grouped into three soil columns according to their physiological behavior: high vegetation (forest, eight PFTs), low vegetation (grasses and crops, six PFTs) and bare soil. A separate water budget is calculated independently for each soil column, in order to prevent forest PFTs from depriving the other PFTs of soil moisture but within each soil column, the uptake of water for transpiration considers the root distribution of the corresponding PFT (Rosnay et al., 2002). In contrast, the energy balance is calculated for the whole grid cell (Boucher et al., 2020).

Evapotranspiration is represented by a classical bulk aerodynamic approach with four subfluxes: snow sublimation, interception loss, bare soil evaporation and transpiration. The first two proceed at potential rates and originate from the snow-covered area and from the PFT fraction effectively covered by foliage. Bare soil evaporation is limited by upward water diffusion. Transpiration originates from the PFT fractions effectively covered by foliage, with no intercepted water, and is controlled by stomatal resistance, which depends on soil moisture and vegetation parameters.

Vertical soil water flow is represented by a 1-D Richards equation (Figure 3.1-a) coupled to a mass balance (Rosnay et al., 2002), and soil depth is set to 2 meters, here discretized into 22 layers to finely model lower layers implicated in drainage (Campoy et al., 2013; Wang et al., 2018). Surface infiltration is limited by the hydraulic conductivity of surface layers and is represented by a sharp wetting front based on the Green and Ampt model (Tafasca et al., 2020; D'Orgeval et al., 2008). The resulting increase in top soil moisture is delivered to the Richards redistribution scheme as a boundary condition, while the lower one consists in free drainage equal to the hydraulic conductivity of the deepest node. Lateral fluxes between

cells are neglected (Rosnay et al., 2002; Campoy et al., 2013).

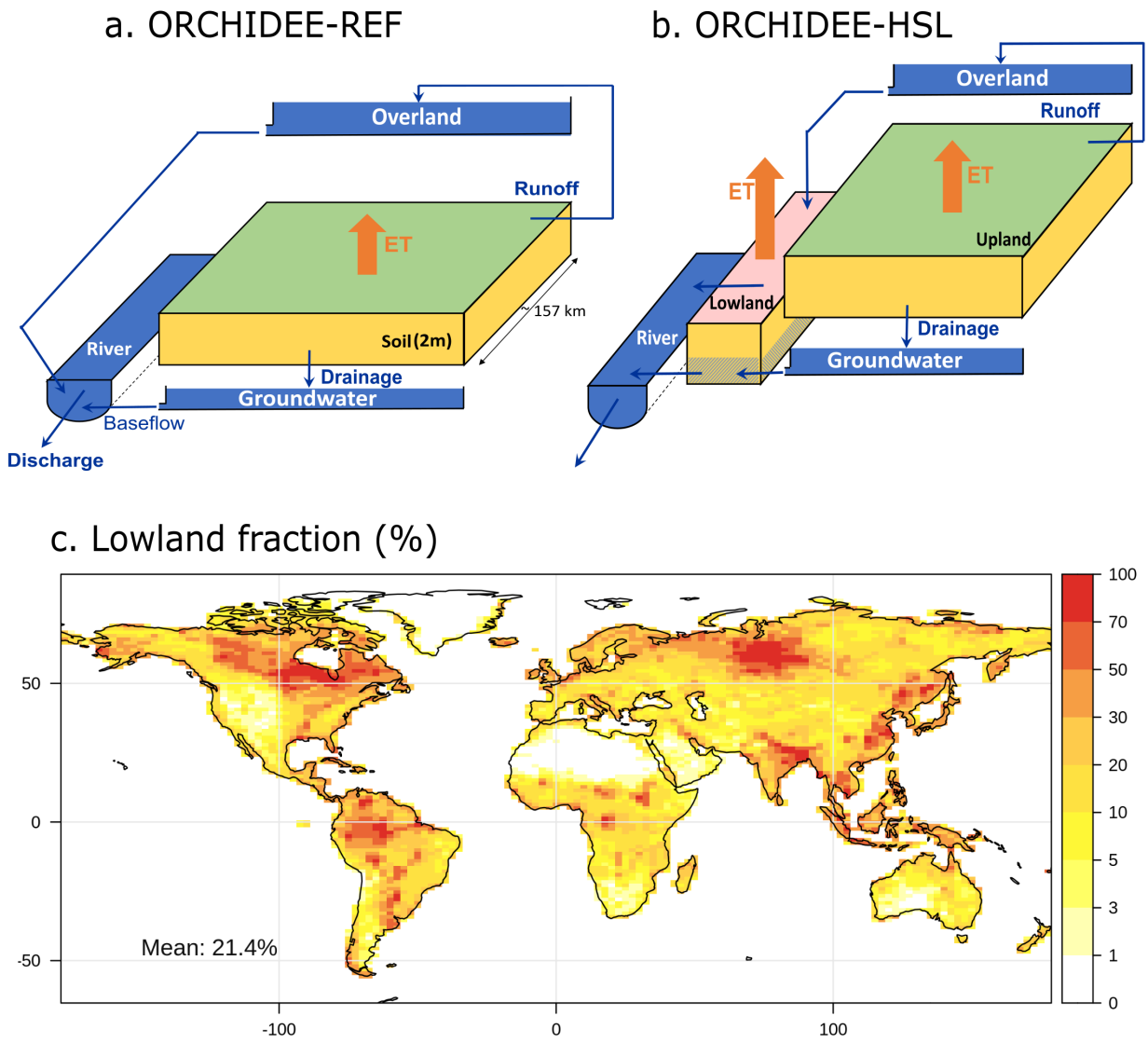

Figure 3.1: Schematization of the main hydrological fluxes in ORCHIDEE-REF (a) and ORCHIDEE-HSL (b), blue arrows represent surface and subsurface flows, orange arrows represent fluxes to the atmosphere. Map of lowland fraction from Tootchi et al., 2019 interpolated to ORCHIDEE resolution (c), corresponding to 2.5 x 1.3 degrees grid size.

Soil is assumed to be homogeneous inside every grid cell and represented by the dominant USDA soil texture, as taken from the Zobler, 1986 map. Soil parameters are a function of the soil texture, following Carsel and Parrish, 1988, while the unsaturated values of hydraulic conductivity and diffusivity depend on soil moisture using the Van Genuchten-Mualem model (Mualem, 1976; Genuchten, 1980). Even if the soil texture is assumed to be uniform inside every grid cell, the saturated hydraulic conductivity decreases with depth, following D'Orgeval et al., 2008.

The routing scheme (Figure 3.1-a) transfers surface runoff and drainage from land to the ocean through a cascade of linear reservoirs (Ngo-Duc et al., 2007; Guimberteau et al.,

2012a). Each grid cell is split into subbasins according to a flow direction map based on the work of Vörösmarty et al., 2000, enhanced over the polar regions by Oki et al., 1999 with a resolution of 0.5°. Every subbasin includes three reservoirs (Fig. 3.1-a), corresponding to groundwater, overland storage, and stream storage, with decreasing residence times (Ngo-Duc et al., 2007). The groundwater reservoir collects drainage from the soil column, while the overland reservoir collects surface runoff. There is no feedback from these two reservoirs on soil moisture. In particular, there is no capillary rise from the groundwater reservoir, so that groundwater cannot influence the atmosphere through the soil column. These two reservoirs are internal to each subbasin, and they both feed the stream reservoir, which also collects streamflow from the upstream subbasins, hence contributing to large-scale routing across subbasins and grid cells.

Eventually, the surface energy and water budget are computed at the same time step as the atmospheric model, i.e., 15 minutes. We impose the same time step on the routing scheme for consistency with ORCHIDEE-HSL. In contrast, the carbon and plant phenology processes in STOMATE are solved with a daily time step.

ORCHIDEE-HSL

ORCHIDEE-HSL describes the effect of hillslope flow along topography at the subgrid scale. To this end, it introduces a "lowland" fraction, which buffers the flow between the upland fraction and the river system (Figure 3.1-b) and has its own water budget, while the remaining "upland" fraction behaves like the soil of the entire grid cell in the reference version. Surface runoff and drainage replenish overland and groundwater reservoirs, which now feed the lowland fraction instead of the stream reservoir, but if there is no lowland fraction within the grid cell, overland and groundwater flows pass directly to the river, as in ORCHIDEE-REF. The lowland fraction can thus be seen as a topographically driven riparian wetland (Fan and Miguez-Macho, 2011), fed by the convergence of both surface water and groundwater, with a potentially higher evapotranspiration than the upland fraction. It is worth noting that this approach is equivalent to the use of the representative hillslope concept (Fan et al., 2019; Swenson et al., 2019), and is suitable for large-scale modeling efforts with redistribution at subgrid scale, but not for high resolution simulations, for which intercell flow (2D or even 3D) is necessary (Felfelani et al., 2021; Markovich et al., 2016).

In contrast to many LSMs describing topographically driven wetlands with a variable area, such as in TOPMODEL (Beven and Kirby, 1979; Band et al., 1993), we suppose here for simplicity that the lowland fraction remains constant in a grid cell, and only its soil moisture changes with time. In this framework, the lowland fraction is prescribed from a 500-m resolution global-scale wetland map recently designed for this purpose (Tootchi et al., 2019). It combines open-water and inundation imagery and high-resolution groundwater modeling (Fan et al., 2013) and is interpolated to the ORCHIDEE resolution according to section 3.2.2.2 (Figure 3.1-c).

Even if some vegetation types may be favored/prevented in lowland areas, this is overlooked due to the lack of guiding rules to do otherwise (Fan et al., 2019). Therefore, the lowland fraction has the same PFT composition as the upland fraction (and as the full grid cell in the reference configuration). A given PFT, however, undergoes weaker water stress in the wetter lowland fraction, which therefore produces higher transpiration and a higher LAI. Bare soil evaporation is also enhanced by the higher soil moisture in the lowland fraction.

In this fraction, the overland flow from the upland fraction is added to throughfall and snowmelt. Depending on soil moisture and hydraulic conductivity, the resulting amount of water can either infiltrate into the soil or produce surface runoff, which directly flows to the river. The flow from the groundwater reservoir is injected at the bottom of the soil column, which is supposed to be impermeable to vertical drainage, so that the deep layers can gradually saturate, thus forming a water table that drains horizontally to the stream reservoir as baseflow. The water table is practically defined as the top of the uppermost saturated soil layer when starting from the impermeable soil bottom. If the whole soil column becomes saturated, the excess water will add to surface runoff and flow into the river (Tootchi, 2019). The soil depth is kept at 2 m in the lowland fraction, and it is discretized into 22 layers (with increasing height from 1 mm in the top layer to 12.5 mm in the 8th layer and all layers below) to accurately simulate the water table depth and the overlying soil moisture gradients and resulting water fluxes according to the Richards equation (Campoy et al., 2013). This discretization is also imposed for consistency in the upland fraction and in the full grid cell of ORCHIDEE-REF.

Baseflow Q_{base} $[mm/s]$ to the streams comes from the lowland fraction. Following Darcy's law, it originates from the saturated layers below the water table, and is given by a solution of the long-term linearized Boussinesq equation at the catchment scale (Tootchi, 2019; Brutsaert, 2005) in equivalent water depth:

$$Q_{base} = \sum_{i=wtl}^{22} q_i = E_F * \frac{\pi^2}{4} * \frac{\Delta h}{B} * \frac{1}{B} * \sum_{i=wtl}^{22} \Delta z_i * K_i \tag{3.1}$$

Where E_F $[-]$ is the exchange factor multiplied by $\frac{\pi^2}{4}$, which accounts for variations of hydraulic conductivity along horizontal direction, anisotropy and riverbed clogging, based on water table shape (Brutsaert, 2005). The term $\frac{\Delta h}{B}$ corresponds to the mean gradient along hillslopes in the lowland fraction. It depends on Δh $[L]$, the height of water table above the bottom of the soil column, i.e. 2 meters depth, and on B $[L]$, the mean aquifer breadth from the streams to the divides. This term is equal to $\frac{1}{2*\delta}$, where δ $[L^{-1}]$ is the drainage density in the lowland fraction, assumed here to be the same as in the entire grid cell by lack of specific information. The term $\Delta z_i * K_i$ corresponds to the layer transmissivity, dependent on the layer thickness Δz_i $[L]$ and the layer hydraulic conductivity K_i $[L/T]$. Finally wtl is the layer that contains the water table.

Both higher values of the exchange E_F factor and of the drainage density δ increase the

baseflow rate: the former because it retains water in the lower zone for a shorter period, and the latter because it decreases the width of the aquifer, which facilitates the flow towards the river. In our simulation, E_F is set equal to 1, and δ is set to $0.535\,10^{-3}\ m^{-1}$, the average over the Seine river basin based on the global δ map of Schneider et al., 2017a.

3.2.2.2 Coupled simulation and experiment setup

The ORCHIDEE LSM is coupled to the LMDZ6A atmospheric model (Hourdin et al., 2020), as embedded in the IPSL-CM6A-LR climate model (Boucher et al., 2020). This land-atmosphere coupled model is often referred to as LMDZOR (Cheruy et al., 2020). Here, the resolution of LMDZOR is defined by 144 x 143 points in longitude and latitude, which correspond to 2.5 x 1.3 degrees, respectively, and by 79 vertical levels. The sole difference in our simulations compared to the IPSL-CM6A-LR setup is that land cover is kept constant and representative of the early 21st century conditions (year 2000) and permafrost is turned off. It should be noted that these simulations exclude irrigation.

Two coupled simulations using LMDZOR were run for the period 1979-2100: the REF simulation, with no lowland representation, and the HSL simulation, which includes the sub-grid representation of hillslope flow through a lowland fraction (section 3.2.2.1-ORCHIDEE-HSL). Spin up was conducted for each simulation to reach storage equilibrium. The SST/SIC forcing datasets consist of bias-corrected values from a fully coupled (land-ocean-atmosphere) simulation by the CNRM-CM6-1 (Voldoire et al., 2019) climate model against observed data. The simulation was performed for ScenarioMIP (Tebaldi et al., 2021) under historical and SSP5-8.5 radiative forcing. The radiative forcing was set differently for historical (1979-2014) and future (2015-2100) periods: historical corresponds to observed values, while future corresponds to the shared socioeconomic pathway (SSP) SSP5-8.5 (O'Neill et al., 2016)), selected to obtain a strong climate change signal.

3.2.3 Results

3.2.3.1 The impact of hillslope flow on historical climate

In this section, yearly and seasonal mean values for the period 1980-2010 were compared for both simulations. The statistical significance of the mean difference between both simulations was assessed at each pixel with two sided Student's t test at the confidence level of 5%.

Figure 3.2 shows the difference between REF and HSL simulations for annual averages covering the historical period (1980-2010). Hillslope flow increases soil moisture (SM) almost everywhere (Figure 3.2-a), except in arid and semiarid areas where there are fewer lowland fractions and changes are not detected by the statistical test. Evapotranspiration (ET) is also enhanced (Figure 3.2-b), but the increase is limited to moisture-limited regions (Seneviratne et al., 2010). Precipitation (P) increases, but the increment is weak and clustered in a few hotspots (Figure 3.2-c). In particular, the inclusion of hillslope flow does not change the zonal

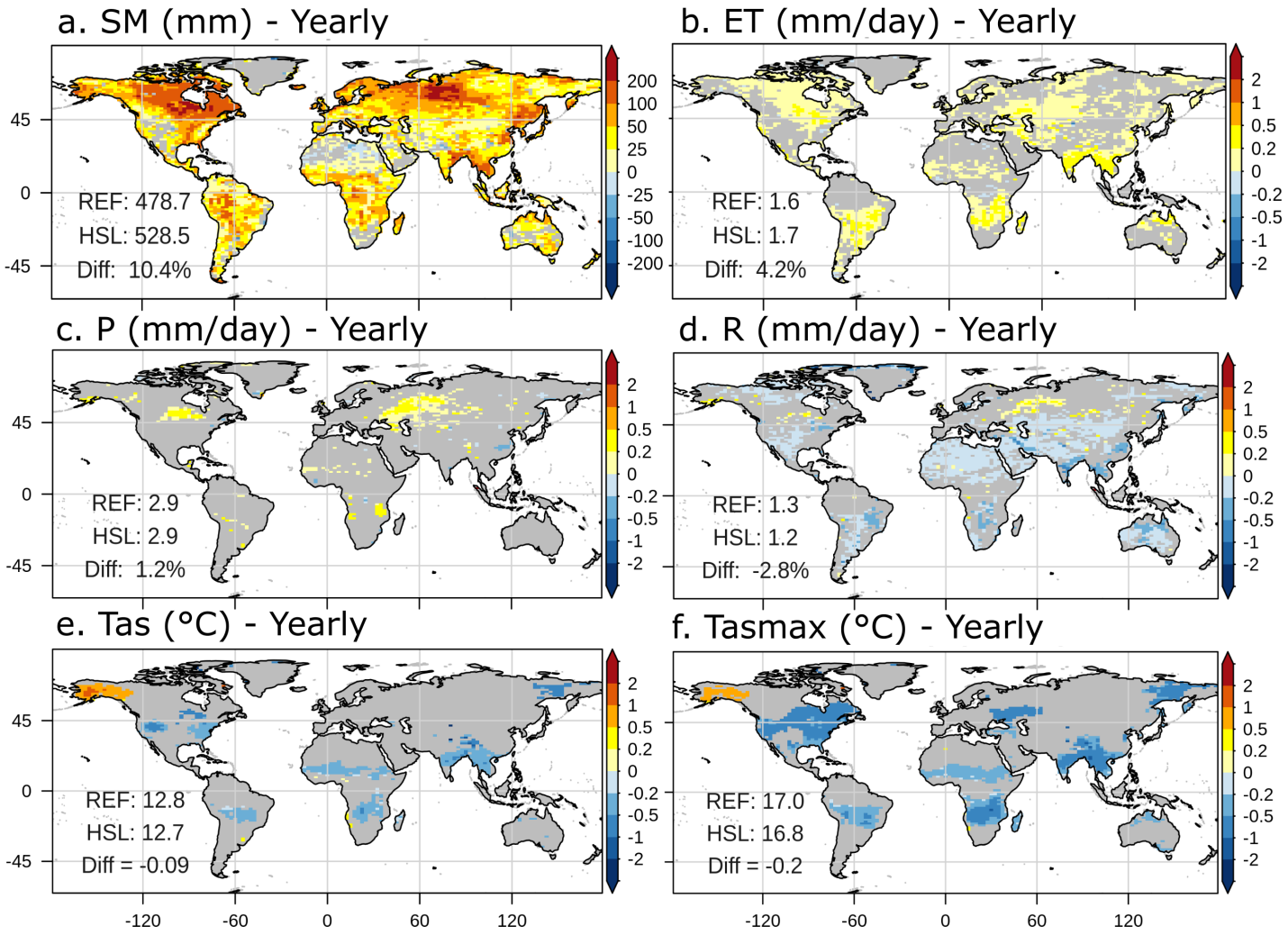

Figure 3.2: Change in mean yearly values between HSL and REF for the period 1980–2010: (a) SM, (b) ET, (c) P, (d) R, (e) Tas, (f) Tasmax. Statistical significance of the mean differences is tested at each point with a Student test (p = 0.05). The areas with insignificant changes are left gray.

distribution of P (Figure 3.4-a) or the positive P bias against observed data (for yearly and seasonal values), especially in the tropics. This bias impacts ET values (Figure 3.4-b), which tend to be excessive in the tropics as well (see section 3.2.3.2). In areas with a positive P bias, hillslope flow does not enhance ET, as these regions are not water-limited but energy-limited, so there is no coupling between SM and ET (Seneviratne et al., 2010).

Total runoff (R) decreases in most zones (Figure 3.2-d) as a result of ET enhancement, except in areas where P increases (R will increase if the P rise is greater than the ET rise). Mean air temperature (Tas, Figure 3.2-e) cools down as a result of increased ET, with the exception of Alaska, where it increases, most likely linked to internal variability of the model. The cooling down signal is weak, -0.09 °C over land, and the correlation between ET enhancement and Tas cooling does not necessarily fit well (for instance, in the northwestern USA, the Siberian Far East, or the Caucasus). The average daily maximum temperature

(Tasmax) shows a stronger cooling in magnitude over a wider area than Tas (Figure 3.2-f). The impact on the Tasmax is linked to the cooling effect of ET and to changes in the soil thermal inertia (Cheruy et al., 2017). The control that soil moisture exerts on thermal inertia may explain the greater impact on the Tasmax compared to Tas, as well as an increase in the average daily minimum temperature (Tasmin, Figure A.2). The increase in Tasmin as a result of wetter soil is due to a reduction in both surface temperature variability and nocturnal soil cooling.

Figure 3.3 a-d shows the differences between both simulations for boreal summer. During JJA, the ET increase is stronger than for yearly values (Figure 3.3-a), with higher values in both the Northern and Southern Hemispheres. The statistical test does not detect any change in areas such as India (where there is an increment in yearly means), and there is a decrease in some tropical areas (for example, the northern Amazonian basin) owing to a reduction in downwelling radiation at the surface, which is consistent with the results from Wang et al., 2018. The P increment is also stronger during JJA (Figure 3.3-b), especially in the Sahelian band, even if P decreases in small areas (such as in the Democratic Republic of Congo). R decreases (Figure 3.3-c) following increases in ET, except in areas where the P rise counteracts the ET rise (for example, in the transition areas between the Sahel and the wetter southern areas) or where ET decreases (north of South America). Tasmax cooling is stronger during boreal summer as well (Figure 3.3-d) and fits well with areas where ET is enhanced, with the exception of the Siberian Far East and North China, where cooling down and ET enhancement do not match.

Comparisons of monthly climatological values are shown for Southern Hudson Bay (SHB, Figure 3.3-e) in Canada and for Sahelian Sudanese Band (SSB, Figure 3.3-f) in Africa. Both regions correspond to different latitudes, seasonality and climates, but both show an increase in ET and air cooling by the inclusion of hillslope flow at yearly scales. Monthly values with detectable differences according to the t test and 5% confidence are marked by a shaded column. In both regions, there is an increase in ET during the wetter months (July in SHB, August in SSB), but in SSB, the test detects a change during the driest months, indicating that hillslope flow keeps sustaining ET. For both regions, increases in ET do not translate into a change in the shape but rather into a change in the ranges of the ET curve. In SHB, changes in P occur during the wettest months, while in SSB, the statistical test detects changes in June but not in August when the peak takes place, even if the peak value slightly increases. These results are consistent with (Wang et al., 2018; Lo and Famiglietti, 2011), who state that a shallow water table affects the intensity and extent of rain belts and enhances local convection but does not affect the main P patterns. For SHB, the increase in P may be due to positive feedback between ET and P from increased convection, while in SSB, the changes may be due to enhanced Hadley circulation and poleward movement of the rain belts (which also explains local decreases in P during boreal winter, see Figure A.1).

R shows larger changes between the two regions. In SHB, the R peak is higher and occurs earlier due to hillslope flow. In SSB, R decreases during the dry season and increases during

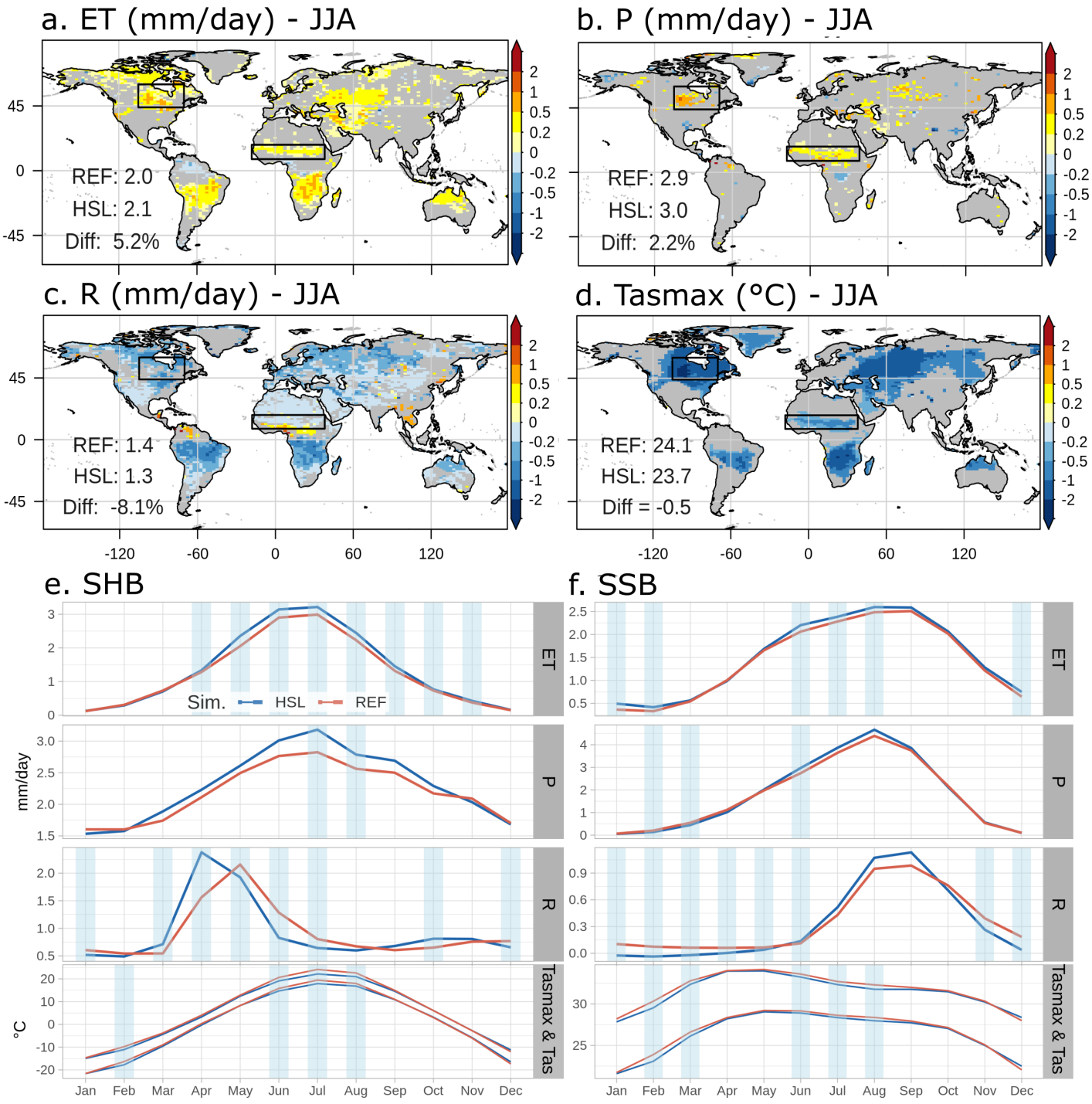

Figure 3.3: Same as Figure 3.2 but for (a) ET, (b) P, (c) R, (d) Tasmax, and boreal summer (JJA) mean values. Regional monthly multiyear values of ET, P, R, Tas and Tasmax for Southern Hudson Bay, SHB (e) and Sahelian Sudanese Band, SSB (f) for 1980-2010. Statistical significance of the mean differences was tested for each month with Student's t test (p = 0.05). Months with significant changes are shaded in blue. In the Tasmax & Tas caption, the top blue and red lines correspond to Tasmax.

the wet months, but the statistical test only detects changes during the dry season and not changes during the peak runoff months. In both regions, the decrease in R is linked to ET enhancement, which leaves less water to runoff, but for the case of SHB, the decrease is partially counteracted by an increase in P. Changes in R peak timing are explained by the characteristics of the lowland fraction. Since the lowland fraction does not have drainage, it can become saturated by groundwater flow and infiltration more easily. If the lowland becomes saturated, all excess water will then become surface runoff and will flow directly to the river. This means that the lowland fraction may produce surface runoff sooner, with a larger peak. For the air temperature, cooling is mostly observed, but it does not occur with the same intensity all the time. Sometimes, this decrease occurs in conjunction with increases in ET (although higher ET does not necessarily impact temperature, for example, during the hottest months in SHB). In others, it is not due to changes in ET but rather to changes in thermal inertia due to increases in SM (for example, in February in SHB or March in SSB).

The above changes in the regional hydrology are consistent with the results obtained by Tootchi, 2019 based on offline simulations in the Seine River basin (Northern France, temperate humid climate). This author also illustrates the sensitivity of the hillslope parametrization to soil depth and the exchange factor E_F (Equation 3.1), and to the extent of the lowland fraction: when the latter increases from 5 to 75% in the Seine River basin, annual mean SM and ET increase by 21 and 6% respectively, while annual mean R decrease by 24%.

3.2.3.2 Comparison of simulations with observed products of precipitation and evapotranspiration

Comparison of zonal bias in Cheruy et al., 2020 (Figure 4) with zonal means from our simulations and from observed data (Figure 3.4-a) shows that inclusion of the lowland fraction does not change the bias on zonal precipitation values, especially for areas between -30 and 20° of latitude. This is consistent with Mizuochi et al., 2021, which compares results from an offline simulation and from a coupled with "nudging" simulation. This bias on P comes from impacts of atmospheric and land surface components in the simulation. In general, ORCHIDEE-HSL has slightly stronger precipitation rates in tropical areas (see for example 3.4-a, JJA values), which indicates a slightly stronger bias.

For evapotranspiration (Figure 3.4-b), bias is less important than for P, because it benefits from the improvement on the downward SW bias (Cheruy et al., 2020). In any case, ET bias is higher between -30 and 20°, overlapping the area where P bias is higher. A strong P rate induces a strong coupling between available energy and ET, preventing any ET enhancement due to hillslope flow. The presence of the lowland fraction induces a stronger ET especially in mid latitude, which could help to improve ET bias in some areas. For example, offline simulation in Mizuochi et al., 2021, Table 3, shows a negative ET bias of -0.231mm/day, while inclusion of hillslope flow could enhance ET, reducing the global bias. The cooler temperature

in HSL simulation, due to the evaporative cooling, can improve warm bias during summer in the northern hemisphere, as shown in Figure 5 in Cheruy et al., 2020 for simulation 6Actrl and AMIP and here for HSL in Figure 3.4.

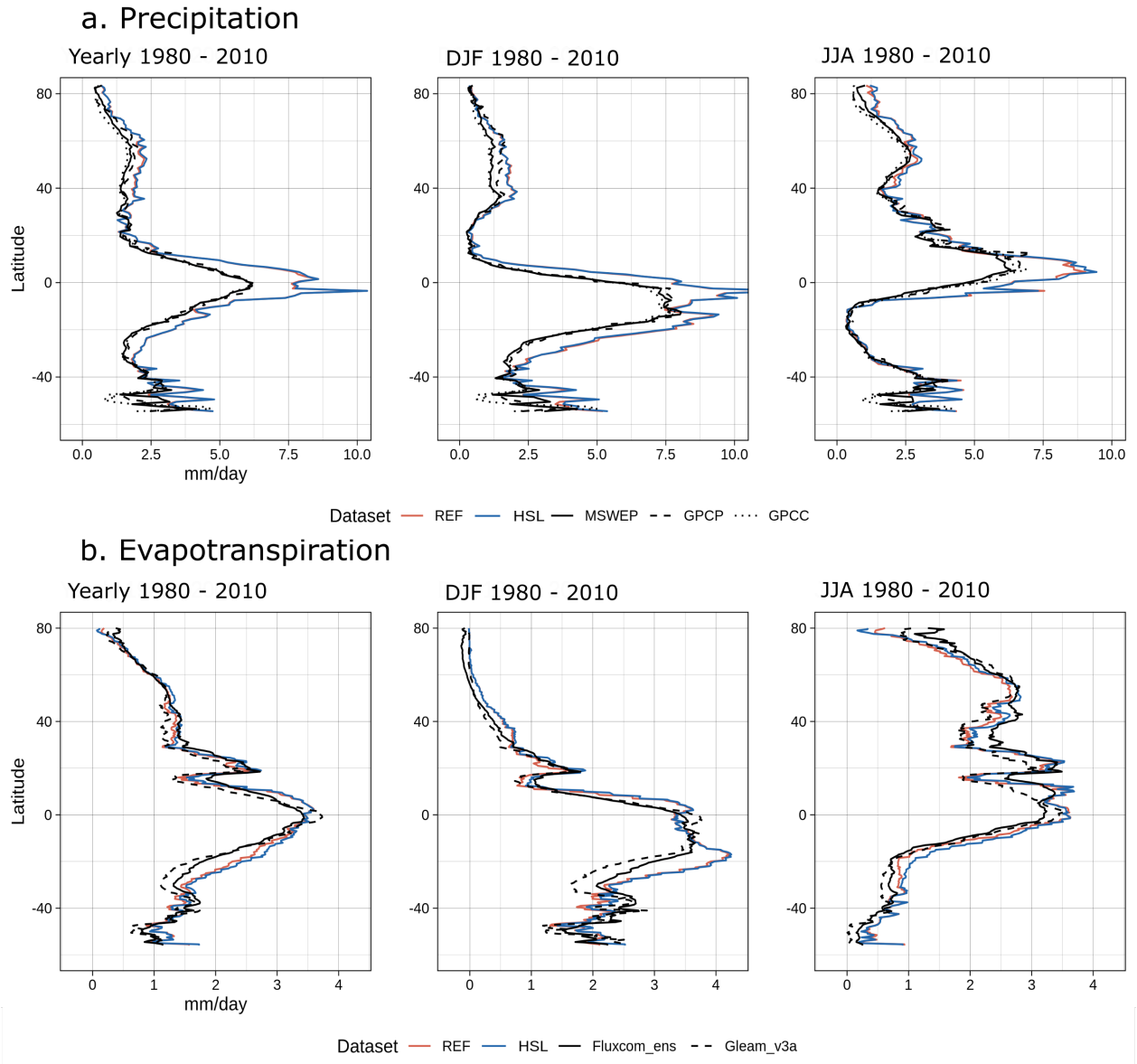

Figure 3.4: Zonal means of precipitation (a) and evapotranspiration (b) using simulations and observed datasets, for yearly, DJF and JJA and period 1980-2010. Reference datasets are MSWEP (Beck et al., 2017), GPCP (Adler et al., 2018) and GPCC (Schneider et al., 2017b) for precipitation, and Fluxcom (Jung et al., 2019) and Gleam v3 (Martens et al., 2017) for evapotranspiration.

3.2.3.3 Global influence of hillslope flow on climate change projections

Global trends

In this section, and hereafter, long-term trends (1980-2100) were computed using Sen's Kendall slope estimator, a nonparametric method, robust enough against outliers (Sen, 1968; Burn and Hag Elnur, 2002; Perkins and Alexander, 2013). The slope was computed for each simulation and also for the difference between them to isolate the effect of hillslope flow on the climate change trend. The statistical significance of the trends was tested with the Mann-Kendall tau test at the confidence level of 5%.

Figure 3.5 shows the land average time series between 1980 and 2100 for both simulations and the difference between HSL and REF (Diff. in the figure). Linear long-term trends are calculated for the three time series. REF simulation includes the effect of climate change, HSL includes the effect of climate change and hillslope flow, and Diff. isolates the effect of hillslope flow on the projection. The spatial distribution of climate change (calculated as the difference between averages in future, 2070-2100, and in historical, 1980-2010) is shown in Figures A.3 and A.4 for REF. The simulation demonstrates the main characteristics of climate change: global warming and increment of the water cycle (more P, ET and R), but with regional increases of aridity (drier soil, less P, ET and R), for example, in Southern Europe and the Mediterranean area (with a stronger and wider increase of aridity during boreal summer).

The REF simulation shows strong warming for the Tasmax (Figure 3.5-a) as a result of climate change (+6.2 °C per century), but when considering climate change and hillslope flow (HSL simulation), warming is slightly less important (+6 °C per century). The trend of the difference (Diff.) between HSL and REF is negative because hillslope flow slows down warming and is detected by the statistical test. The Diff. trend indicates the magnitude and direction of the hillslope flow impact in the long term. Additionally, the trend of the difference (-0.08 °C per century) does not exactly match the differences between HSL and REF trends (-0.2 °C) as a result of numerical errors in the slope calculation induced by nonlinearity, but these errors are generally small.

For ET (Figure 3.5-b), the rate is enhanced by climate change (+0.02 mm/day/century), and it increases faster if the hillslope is included (+50.5% faster). For the case of yearly P (Figure 3.5-c), climate change increases P at the end of the century (+0.35 mm/day/century), and hillslope flow amplifies the increment of P, i.e., P trend increases faster (+6.9% faster). During the boreal summer, ET decreases (-0.03 mm/day/century) due to climate change (Figure 3.5-d), but hillslope flow opposes this trend by enhancing ET and attenuating the reduction (-39.2%).

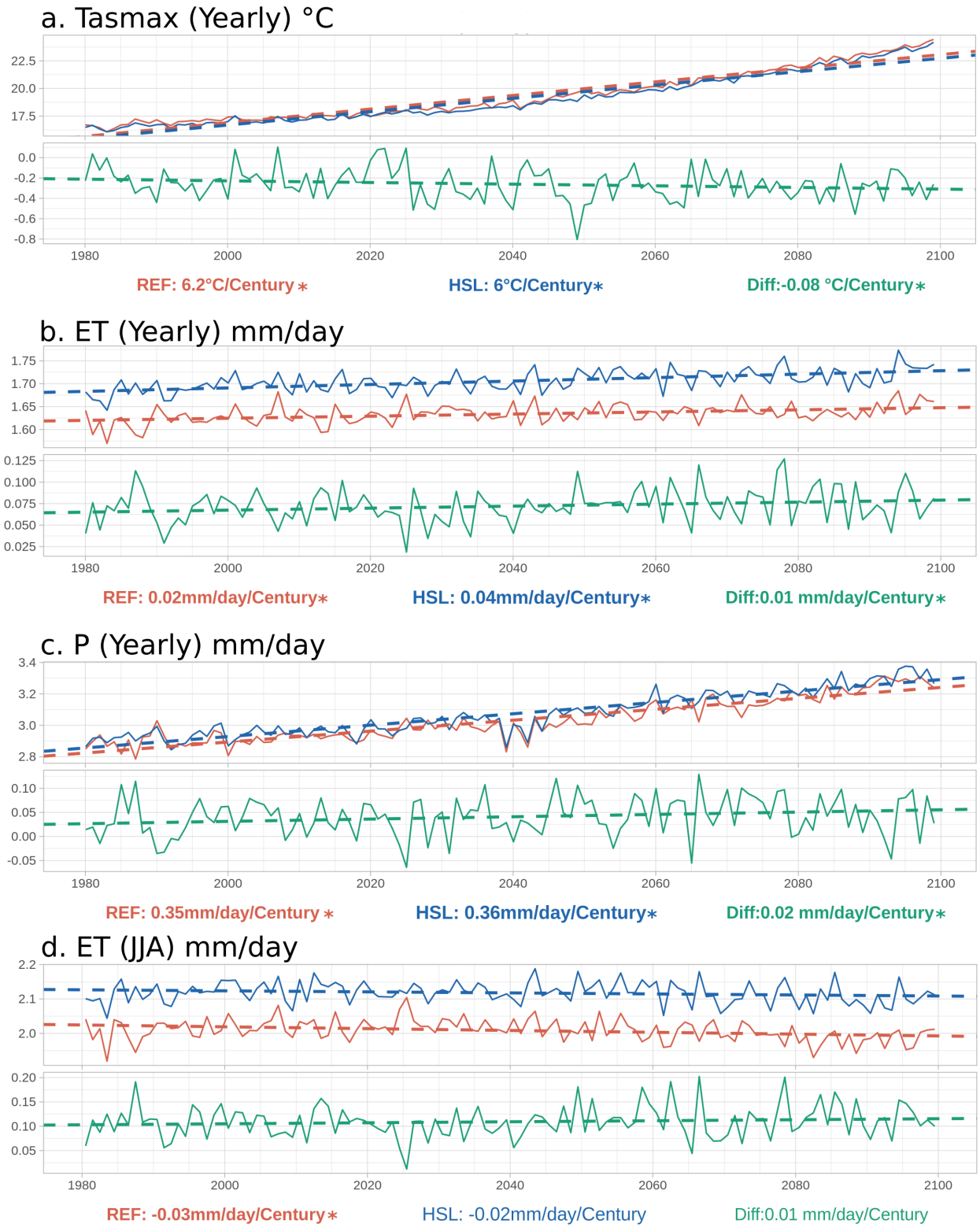

Figure 3.5: Global land average for both simulations, and difference between them, for the period 1980–2100, for daily max. temperature (a), evapotranspiration (b), and precipitation (c), at yearly scale, and evapotranspiration (d) for boreal summer. The statistical significance of the trend was tested with a Mann-Kendall test (p = 0.05). Significant trends are written in bold with an *. Diff. corresponds to the trend of the difference between HSL and REF.

Hillslope flow modulation

With respect to the climate change trend (REF simulation), the isolated effect of hillslope flow on long-term trends (HSL-REF time series, Diff. slope in Figure 3.5) can adequately reflect the influence of hillslope flow on the evolution of a variable. This influence is referenced here as hillslope flow modulation and is defined in Table 3.1-b. A single color is associated with each of the possible combinations of the hillslope flow effect and climate change trend, and we use this color matrix in further analysis. When the trend increases/decreases more rapidly, i.e., REF and Diff. slopes have the same sign, we speak of amplification. When the trend increases/decreases more slowly, i.e., the REF and Diff. slopes have different signs, we speak of attenuation. Finally, if the REF and HSL trends have opposite signs, indicating that the hillslope flow counteracts climate change, we speak of an inversion. A significant modulation means that the HSL-REF trend is significant according to the Mann-Kendall tau test at 5%.

We show the modulation of hillslope flow in climate change trends in Table 3.1-a for global land average values at yearly and seasonal scales. Each variable presents the slope of climate change and the color of the hillslope flow modulation. The percentage corresponds to the ratio of the Diff. slope (HSL-REF time series) to the climate change slope (REF simulation). It indicates the magnitude and direction of hillslope flow modulation compared to climate change impact. For the case of SM, hillslope flow amplifies a positive trend for yearly values (+24%), as well as for ET (+51%) and P (+7%), while the R increase is attenuated. Sensible heat flux (SHF) rise is attenuated. For air temperature, we observe a small reduction in warming for the Tasmax, Tas and Tasmin but it is only detected by the statistical test for the Tasmax (-1.3%).

These modulations may change at the seasonal scale, for example, during boreal summer (JJA) for SM and ET. The enhanced water storage in the lowland fraction at all times leads to amplified SM and ET increases in boreal winter and on an annual average, and helps counteract the decrease of these variables that is induced by climate change in boreal summer. Such an increased soil moisture memory, by means of water redistribution at the landscape scale, increases the resilience of water resources and land surface fluxes to enhanced droughts caused by climate change. Another example of modulation inversion at the seasonal scale compared to the annual scale is found for R, Tas and Tasmin. These variables all exhibit positive long-term trends whichever the season, which are usually attenuated but in boreal autumn (SON). For Tas and Tasmin these seasonal amplifications are small and insignificant, unlike the one of R which continues in boreal winter, and is probably related to the higher soil moisture in the lowland fraction, favoring runoff in the rainy season, as noted in the historical period (section 3.2.3.1).

Table 3.1: Trends of global land average values for 1980-2100 and hillslope flow modulation in % (a) and matrix of hillslope flow modulation with respect to climate change (C.C.) trend and corresponding color (b). The statistical significance of the trend was tested with a Mann-Kendall test (p = 0.05). Significant trends are written in italic bold.

a.

Season	Variables	SM mm/Cent.	ET mm/day/Cent.	P mm/day/Cent.	R mm/day/Cent.
Yearly	C.C. Trend	***8.0***	***0.02***	***0.3***	***0.3***
	Modulation	***23.6%***	***50.5%***	***6.9%***	3.0%
DJF	C.C. trend	***14.1***	***0.05***	***0.5***	***0.4***
	Modulation	2.6%	-2.0%	1.0%	***8.8%***
MAM	C.C. trend	***15.6***	***0.05***	***0.3***	***0.4***
	Modulation	-0.07%	***41.1%***	2.1%	***-11.2%***
JJA	C.C. trend	-1.5	***-0.03***	***0.1***	***0.1***
	Modulation	***-279.3%***	-39.2%	11.5%	0.2%
SON	C.C. trend	***3.0***	***0.02***	***0.4***	***0.4***
	Modulation	***112.0%***	***91.5%***	***10.1%***	***13.2%***
Season	Variables	Tasmax °C/Cent.	Tas °C/Cent.	Tasmin °C/Cent.	SHF W/m^2/Cent.
Yearly	C.C. trend	***6.2***	***6.4***	***6.9***	***4.2***
	Modulation	***-1.3%***	-1.2%	-1.1%	-4.5%
DJF	C.C. trend	***5.9***	***6.6***	***7.4***	***2.0***
	Modulation	-1.6%	-1.7%	-1.5%	3.9%
MAM	C.C. trend	***5.4***	***5.7***	***6.2***	***3.8***
	Modulation	***-3.9%***	***-3.6%***	***-3.0%***	***-11.4%***
JJA	C.C. trend	***6.6***	***6.6***	***6.7***	***6.6***
	Modulation	-0.9%	-0.8%	-0.8%	-2.0%
SON	C.C. trend	***6.6***	***6.8***	***7.2***	***4.3***
	Modulation	-0.02%	0.2%	0.5%	-6.0%

b.

	Negative CC	Positive CC
Amplification	Negative HSL-REF	Positive HSL-REF
Attenuation	Positive HSL-REF	Negative HSL-REF
Inversion	Positive HSL-REF	Negative HSL-REF

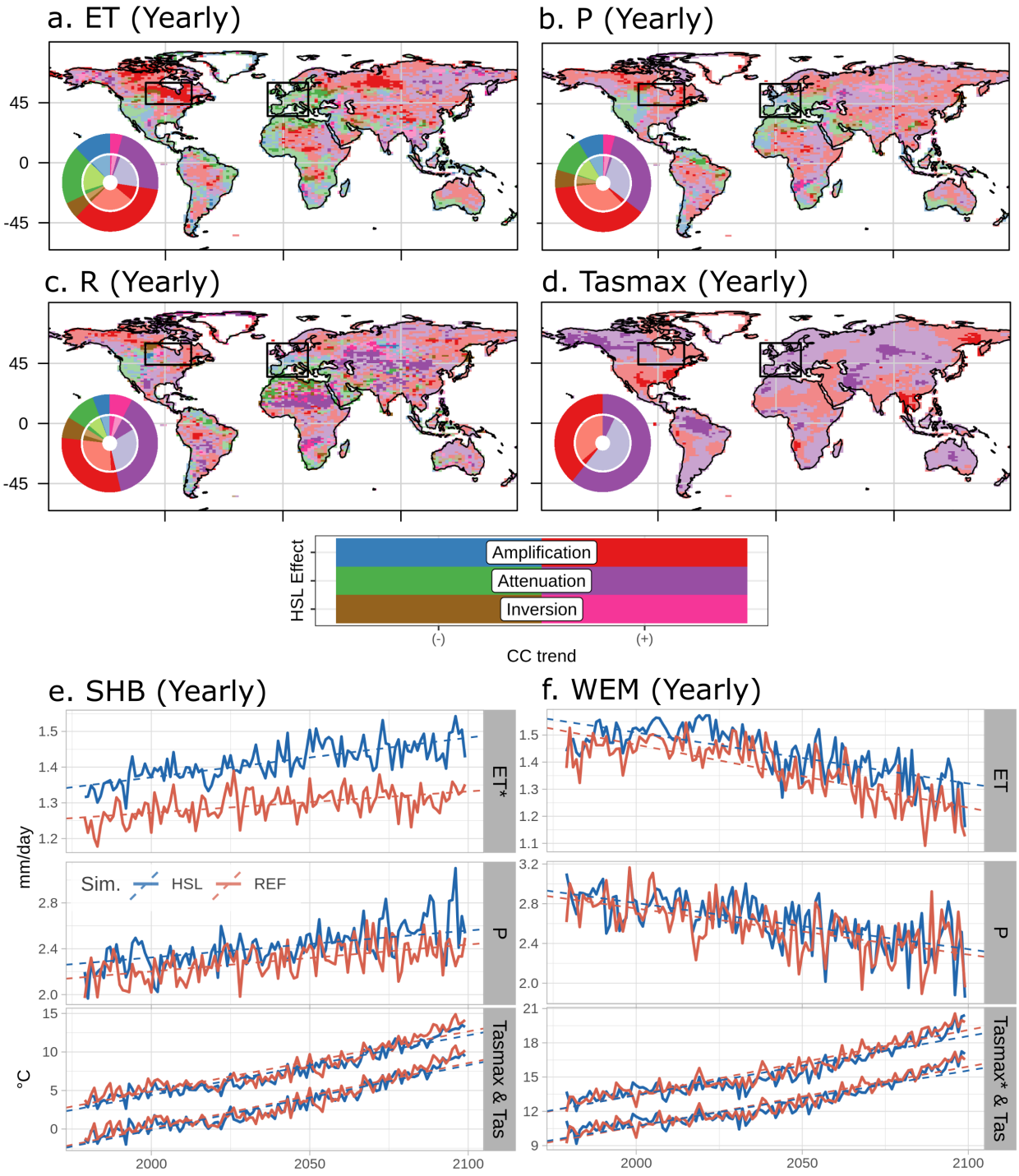

Figure 3.6: Spatial distribution of hillslope flow modulation in yearly mean values for period 1980–2100, ET (a), P (b), R (c) and Tasmax (d). The areas with insignificant changes in hillslope flow modulation have transparent colors. Doughnuts show the distribution of hillslope flow modulation (outer circle) and the corresponding partitioning of the significant & insignificant modulation (inner circle). We use a Mann-Kendall test ($p = 0.05$). The table below the maps define the modulation types and corresponding colors. Regional annual average values of ET, P, and Tas & Tasmax in Southern Hudson Bay, SHB (e) and Western Europe and the Mediterranean, WEM (f) for 1980-2100. Statistical significance of the modulation was tested with a Mann-Kendall test ($p = 0.05$), and significant trends are shown by a * in the vertical titles. In the Tasmax & Tas panel, the top blue and red lines correspond to Tasmax.

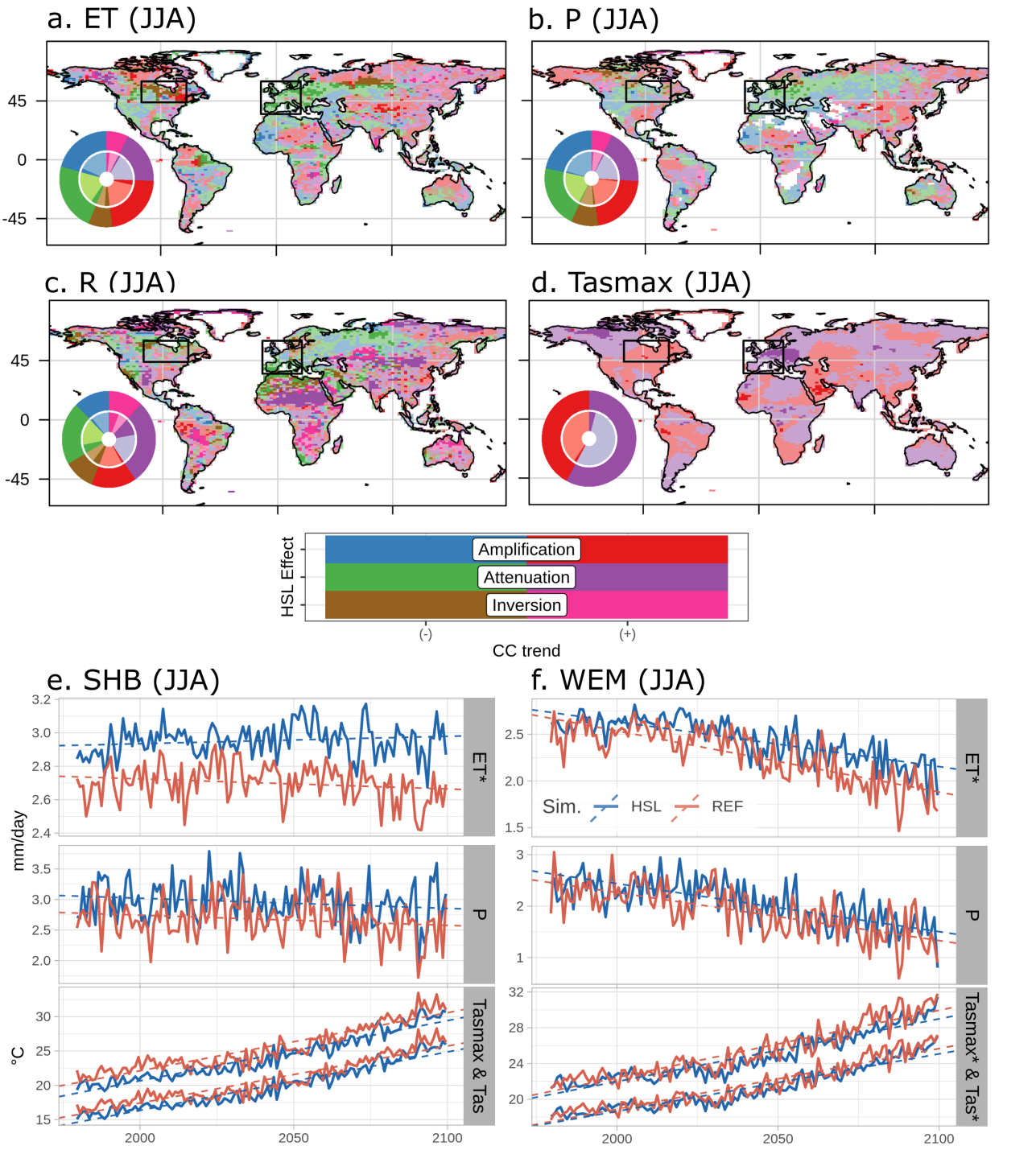

Figure 3.7: Same as Figure 3.6 in boreal summer (JJA) mean values for 1980–2100. In panel b, areas in white have very low JJA precipitation over the entire period, which prevents extracting a trend.

3.2.3.4 Spatial distribution of hillslope flow modulation on climate change projections

Many areas show an amplification of ET increase due to hillslope flow (red color, Figure 3.6-a), particularly in the Northern Hemisphere, especially in areas with high lowland fraction (e.g., in Southern Hudson Bay and Central Siberia, detected by the statistical test). Other areas show a reduction in ET decline (green color, like Eastern Europe), although their detection by statistical tests is less frequent. P presents a similar modulation distribution (mostly amplification of P increases or attenuation of P declines, Figure 3.6-b), but in this case, the hillslope flow modulation is undetected in most cases by the statistical test. Geographically, the type of ET and P modulation seems to agree with each other. For instance, attenuation of a decline (in green) is seen for both variables in Southern Europe and California. Amplification of an increase (in red) also matches, (in Northern Australia and the Amazonian basin).

For yearly values of R (Figure 3.6-c), attenuation/amplification of an increase (purple and red color, respectively) are the most frequent modulations. The modulation of hillslope flow on R appears to depend on both the magnitude and direction of ET and P modulations. For example, in North Africa, a slower reduction in R (green color) matches with a slower reduction in ET (which should accelerate the R reduction) and a slower reduction in P (which should slow down the R reduction if it is greater than changes in ET). For the case of yearly Tasmax (Figure 3.6-d), we observe mostly a slowing down of warming (purple color) rarely detected by the test. The statistical test also detects an acceleration of warming (red color) (for instance, in the USA South Atlantic, (SA USA), Figure A.7). In general, slower warming (purple) occurs in areas where ET increases faster (red color) or decreases slower (green color). Faster warming seems to match slower ET increases (purple color), such as in Southeast Asia. However, in other regions, this agreement does not match.

During the boreal summer, the distribution of hillslope flow modulation shifts for ET (Figure 3.7-a), and attenuation of ET declines becomes more common (green color, e.g., in Eastern Europe). The inversion of the negative trend of ET (i.e., hillslope flow counteracts the signal of climate change from negative to positive, brown color) is also important in the Northern Hemisphere . For P (Figure 3.7-b), changes in the modulation distribution are similar to ET but again are mostly undetected by the statistical test. For R (Figure 3.7-c), attenuation of increases (purple) is still the most common modulation, but the attenuation of R decline (in green) and the inversion of positive trends to negative (in magenta) occur more often during JJA and are more likely to be detected by the statistical test. The type of modulation for R appears to remain dependent on ET and P changes, but changes in the timing and intensity of the R peak due to the presence of the lowland fraction may also affect seasonal trends. The modulation distribution during boreal winter is similar to those of yearly means for R, with the exception of Northern Russia (Figure A.5).

For the Tasmax, (Figure 3.7-d) hillslope flow still slows down warming (purple color)

during the boreal summer, but the statistical test detects this modulation almost exclusively in the Northern Hemisphere. For JJA means, attenuation of ET declines or amplification of ET increases (green and red colors, respectively) seem to fit well with areas where warming slows down (in Europe), while amplification of ET declines and attenuation of ET increases (blue and purple colors, respectively) agree with warming acceleration. Sensible heat flux also depicts similar modulations in some regions (Figure A.6). During winter, slower warming is still the main hillslope flow modulation, but the statistical test mostly detects warming acceleration, probably linked to long-term trends of thermal inertia, following modulations on SM (Figures A.5 and A.6).

In SHB (Figure 3.6-e), ET increases more rapidly due to hillslope flow (modulation detected by the statistical test). This increase in ET does not cause a change in the P projection (although P remains higher throughout the period when hillslope flow is included). The air temperature projection does not change either (although the HSL simulation continues to show lower values). In the case of Western Europe and Mediterranean, WEM (Figure 3.6-f), ET decline is slower (but the statistical test does not detect the modulation). This attenuation of ET decline does not agree with an attenuation of P decline, but it slows down air temperature warming (especially for the Tasmax, whose modulation is detected by the statistical test).

During the boreal summer in SHB (Figure 3.7-e), the ET trend inverts (from negative to positive) due to hillslope flow (the modulation is detected by the statistical test). The change in the ET trend does not attenuate the P reduction and does not slow down warming, but HSL simulation consistently presents higher values for P and lower values for Tas and Tasmax. Surprisingly, we detected an acceleration of warming in SHB during boreal summer, despite the increase in ET, but the hillslope flow modulation in this case is small and undetected by the statistical test. In WEM (Figure 3.7-f), ET decline is slower (modulation detected by the statistical test). The attenuation does not attenuate P decline, but it slows down warming, and modulation is detected for both the Tas and Tasmax.

3.2.3.5 Influence of hillslope flow modulation on regional climate projections

Climate classification for regional analysis

To further analyze whether climate characteristics have an impact on hillslope flow modulation, we separated regions based on a simple climate classification. This classification is based on the use of a moisture factor and a thermal factor, following Feddema, 2005. The aridity index (AI) and mean annual air temperature (MAT) are chosen as moisture and thermal factors, respectively, since they are continuous variables and are simple to calculate from the outputs of climate models. We do not consider a seasonality factor or the use of other variables, as other classifications, for the sake of simplicity. The objective is to reproduce the main features of other climate classifications, such as the Köppen-Geiger classification (Beck

et al., 2018) and revised Thornthwaite classification (Feddema, 2005).

Both the aridity index and the mean air temperature are calculated for the reference period 1980-2010 from the REF simulation (Figure 3.8 a-b). The aridity index AI is computed following the World Atlas of Desertification (Cherlet et al., 2018), i.e., $AI = P/PET$, P is the annual mean precipitation, and PET is the annual mean potential evapotranspiration. To compute the potential ET from the model's outputs, we follow Greve et al., 2019 and Milly and Dunne, 2016, which calculate $PET = 0.8R_N/\lambda$, with R_N being the net radiation at the surface and λ being the latent heat of vaporization.

We classify AI into three groups: arid (A), semiarid (SA) and humid (H), for $AI < 0.35$, $0.35 < AI < 1.125$ or $AI > 1.125$, respectively. MAT is classified into four groups: subpolar (SP), cold (c), temperate (t) and warm (w) for $Tas < -5$, $-5 < Tas < 7$, $7 < Tas < 20$ and $Tas > 20$ °C, respectively. We group all the grid cells from the subpolar group into a single class, SP, regardless of the value of AI. For the remaining cells, class is the result of merging AI and MAT groups, except for arid Group A, which is considered a single class. The resulting classification is shown in Figure 3.8-c. The inclusion of the effect of climate change on the water cycle is important, as there is evidence that it can take different trajectories even within the same climatic region, as in West Africa (Gaetani et al., 2020). To include the long-term effects of climate change on aridity, we divide the classes according to their long-term trend in P for the period 1980-2100. P+ is added to the class code if the trend is positive or P- if it is negative (P- is marked as * in Figure 3.8-c) even when the P trend is not detected by the test, except for subpolar (SP) and humid cold (H-c) because negative P trends rarely occur in these areas. Finally, to isolate the effect of proximity to the ocean, we consider an additional class called "Coastal", which corresponds to grid cells with a fraction of land less than 50%.

The final classification includes 9 classes where the P trend is not considered and 15 classes where it is considered (Figure 3.9). The climate classification captures the main features of the Köppen-Geiger classification, as calculated by Beck et al., 2018, and the revised Thornthwaite classification by Feddema, 2005, but there are biases and mismatches linked to the positive P bias detected in the tropics and midlatitudes. For instance, the climate classification does not capture the arid region of Central Australia well due to a wet bias, while the semiarid areas of India and the Sahel are too large. The use of HSL simulation to calculate the classification produces a similar distribution, with small regional differences (in Australia and northern high latitudes, Figure A.8), because the inclusion of hillslope flow does not drastically alter the distribution of P and ET biases.

Hillslope flow modulation at regional scale

For ET and P (Figure 3.9 a-d), we observe that hillslope flow attenuates the reduction of yearly means due to climate change for all classes with P- (P reduces due to climate change). For ET, attenuation of yearly decline ranges from 6 to 67%, and for P, it ranges from 16 to

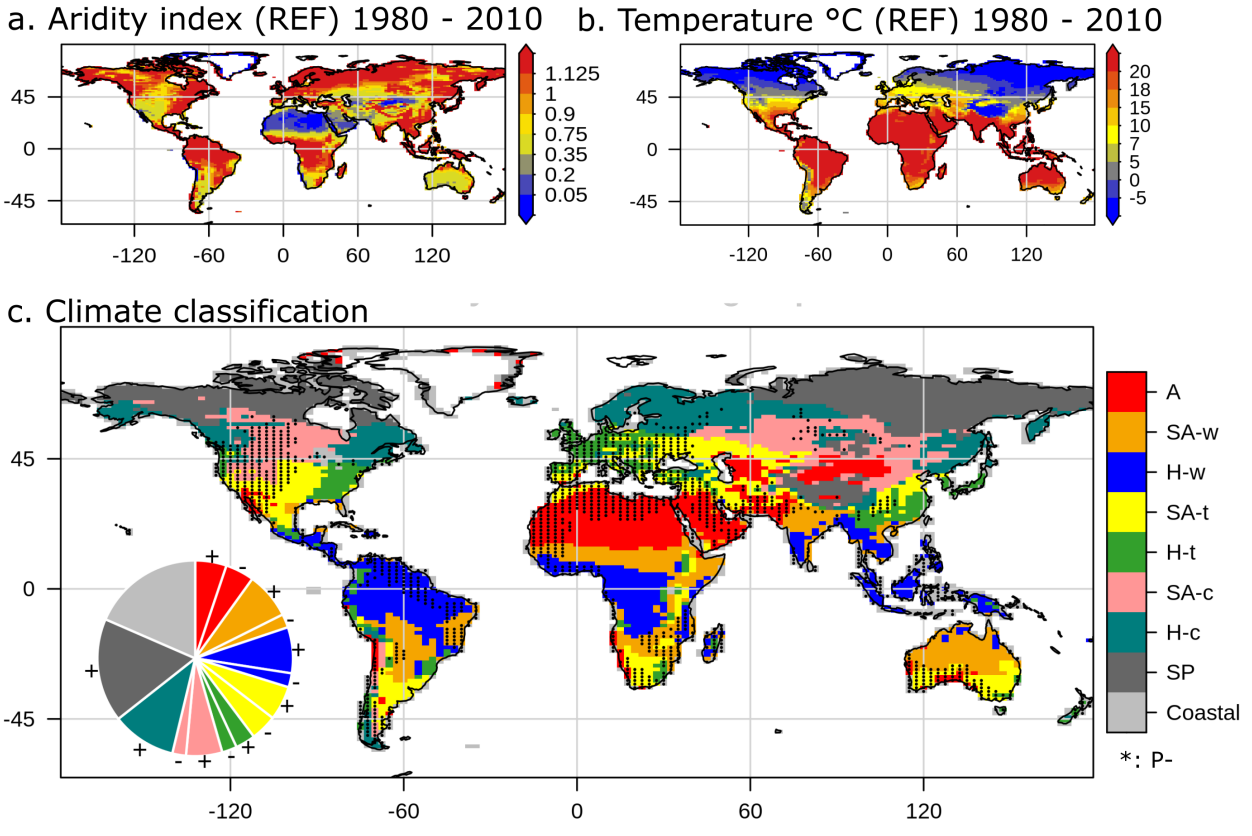

Figure 3.8: Aridity index (a) and mean temperature (b) from REF simulation for the period 1980–2010. Simple climatic classification from both variables (c). Areas with negative P trends (P-) for the period 1980-2100 are stippled. The piechart shows the distribution of climate classes, separated among positive and negative P trends under climate change (identified by + and -). Climate classes correspond to arid (A), semiarid and warm (SA-w), humid and warm (H-w), semiarid and temperate (SA-t), humid and temperate (H-t), semiarid and cold (SA-c), humid and cold (H-c), and subpolar (SP). Refer to the text for definition of each class.

48%. During summer, we observe the same modulation with the exception of arid areas (A P-), which amplify the reduction of both ET and P, and humid warm areas (H-w P-), where ET increase is enhanced. Some of these modulations are detected by the statistical test, and they match well with attenuation of SM decline and attenuation of SHF increase (Figure A.9).

When P increases due to climate change, hillslope flow mostly enhances ET increment (except for humid temperate, H-t P+, where reduction is attenuated, but absolute trend values are small). In the case of P, hillslope flow mostly attenuates the P increase (except for humid temperate, H-t P+, where the increase is amplified) in part because P is already higher during the historical period, so the P rate increases slower. Finally, classes subpolar (SP) and humid cold (H-c) show an amplification of both ET and P increase, and for the case of class H-c, modulation is detected by the statistical test. During summer, ET and P do not present a single type of modulation in areas where P increases (P+), but humid cold

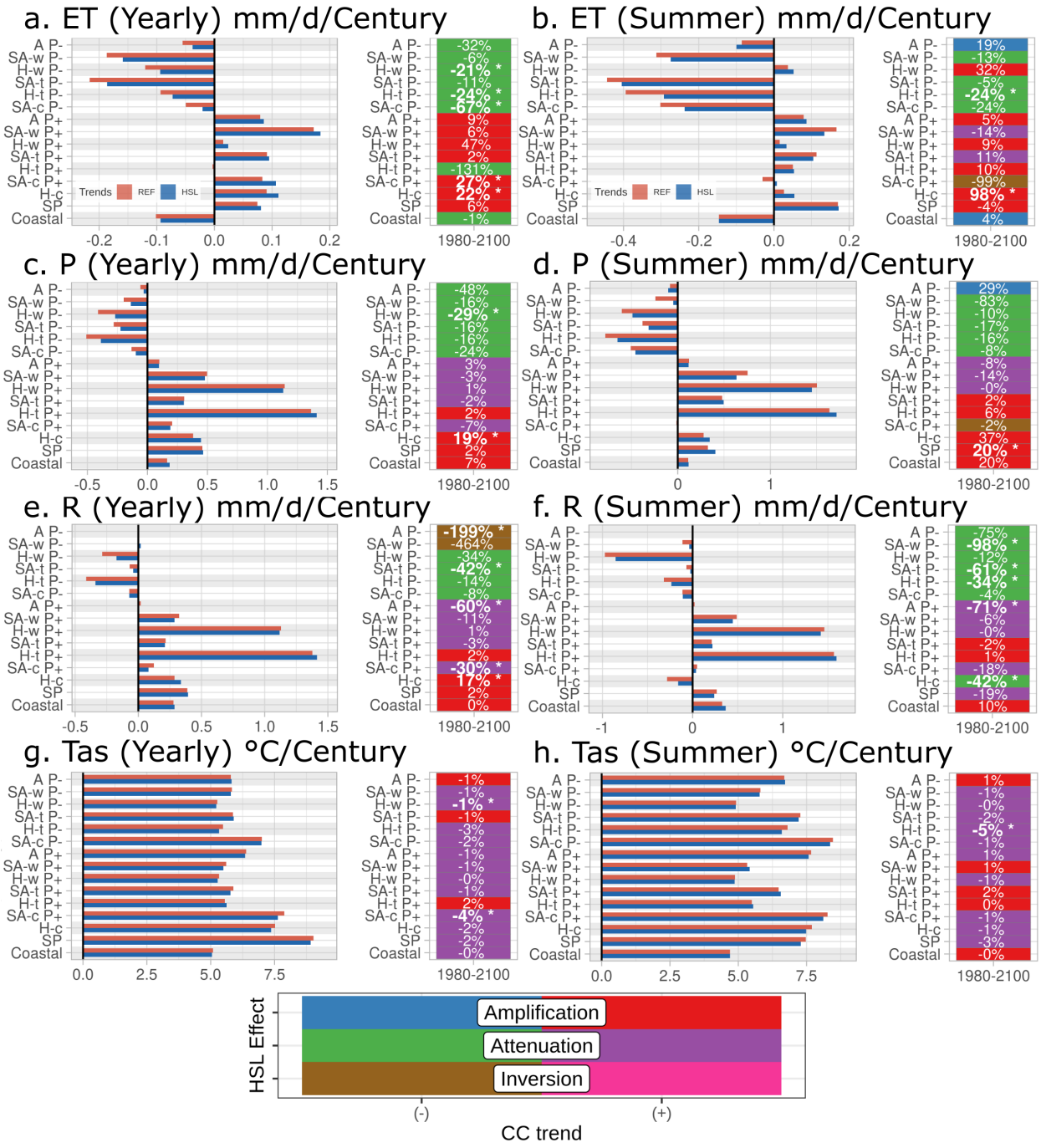

Figure 3.9: Trends of regional average grid cells according to climatic classes in 1980-2100 for REF and HSL, and hillslope flow modulation in % for (a, c, e, g) yearly values, (b, d, f, h) summer values. Summer is defined as JJA for northern grid cells and DJF for southern grid cells. Variables are (a, b) ET, (c, d) P, (e, f) R and (g, h) Tas. Statistical significance of the hillslope flow modulation was tested with the Mann-Kendall test ($p = 0.05$). Significant hillslope flow modulations are written in bold with an *, and the color of the cell corresponds to the modulation type as shown at the bottom. The percentage of modulation is calculated as for table 3.1-a. Climate class names are the same as Figure 3.8.

(H-c) areas present an enhancement of ET increase (+98%), and the subpolar (SP) class has an amplification of P increase (+20%), both detected by the statistical test.

For R, classes with P decrease due to climate change (P-) and have a reduction in negative trends (from -8 to -42%), with the exception of arid (A P-) and semiarid warm (SA-w P-) classes, which have an inversion from negative to positive R trends (but absolute values are small, even if modulation is detected for A P-). For summer means, R declines are attenuated for all classes with P-. For classes with P+, R increase is attenuated, except for humid temperate (H-t P+) class, following results for P. Summer values also closely follow results for P, except for semiarid temperate class (SA-c P+) which present an attenuation of an increase, humid cold (H-c) which reduces the R decline, and subpolar (SP), which attenuates R increase. Arid regions and semiarid/humid cold areas have detectable modulations according to the statistical test.

Tas shows a slowing of the yearly warming trend for almost every class, except for arid and semiarid temperate, with P decline due to climate change (A P- and SA P-), and humid temperate with P increase (H-t P+). These modulations agree with those of Tasmin, but for the Tasmax, the single class with acceleration of warming is humid temperate with an increase in P (H-t P+, Figure A.9). During summer, acceleration of warming becomes more common for Tas (for the Tasmax as well, Figure A.9), but the sole detectable modulation by the statistical test is attenuation of warming, for yearly and summerly values.

These regional scale analyzes show that, where climate change decreases P rates, hillslope flow attenuates the relatedSM and ET declines, and the subsequent P and R declines. In regions where P increases, in contrast, hillslope flow amplifies the resulting increases of ET while it attenuates the ones of P and R. Eventually, hillslope flow is shown to weaken the projected intensification of hydrological extreme events. Our regional results also confirm the weak attenuation of warming found at the global scale.

3.2.4 Discussion

This study presents two coupled simulations with a single model; thus, our results may be affected by spurious effects due to internal model variability. In addition, our model represents the effect of groundwater on soil moisture and topography-driven subgrid variability in a very simplified way, with many shortcomings, including the lack of dynamics in both land use and the extension of lowland humid areas, and the lack of PFT differences in lowland and upland areas. All this forces us to consider these results as qualitative indicators of potential first order effects.

Our results can be summarized by Figure 3.10-a on historical land average values for the main affected variables. In our simulations, hillslope flow increases SM, ET and P at the global scale and reduces R, except in areas where the increase in P is greater than that in ET. Both offline and online studies show the same impact for SM, ET and R if groundwater-SM interaction is activated, and online simulations present an increase in the P rate as well.

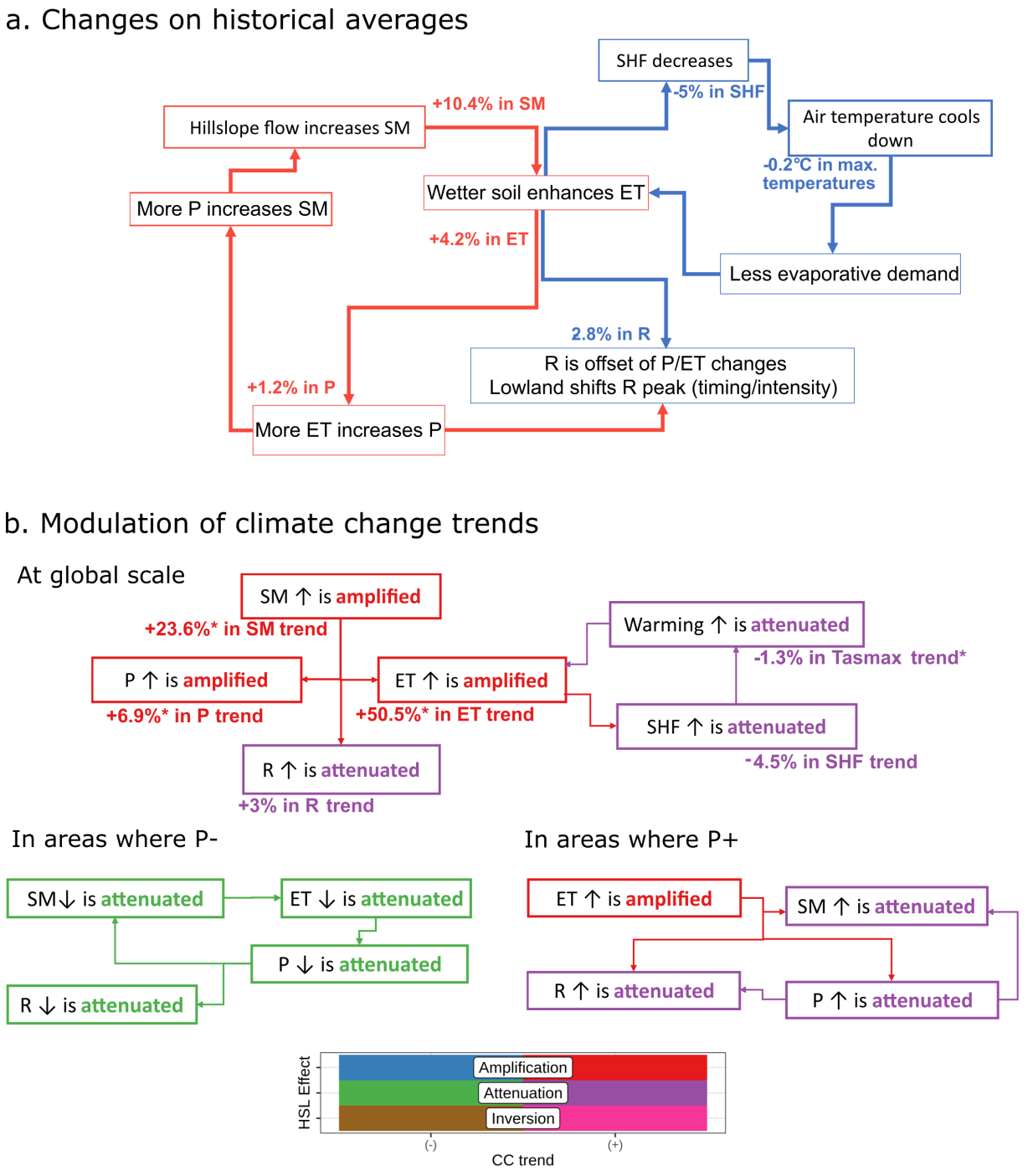

Figure 3.10: Schematic of main impacts. Summary of the main impacts and feedbacks due to the inclusion of hillslope flow during the historical period (a). Red color refers to an increase, blue color to a decrease. Summary of the main hillslope flow modulations at the global and regional scales (b). Colors from the table of hillslope flow modulation are used for the arrows and percentage corresponds to modulation at global scale.

Likewise, a study using LMDZOR with prescribed water table depths of one meter (Wang et al., 2018) shows the same effects for SM, ET and P but with higher impact due to unrealistic water tables. The decrease in SHF and air temperature in our simulations (Figure 3.10-a), due to enhanced ET, is also observed in online studies. For the air temperature, we detected a stronger effect on a larger area for Tasmax than for Tas when comparing HSL and REF. This effect has been observed in coupled simulations when irrigation is included (Thiery et al., 2017).

To assess whether our results carry some generality, we compare them with other assessments of groundwater impact on land surface fluxes, i.e., offline simulations by Koirala et al., 2014; Decharme et al., 2019; Miguez-Macho et al., 2007, and near-surface climate, i.e., coupled land-atmosphere simulations by Lo and Famiglietti, 2011; Leung et al., 2011; Anyah et al., 2008.

Among the models compared here, only ORCHIDEE-HSL and ISBA-CTRIP (Decharme et al., 2019) include a representation of subgrid variability. Other modeling approaches, such as MAT-GW (Koirala et al., 2014) and CLM3.5 (Lo and Famiglietti, 2011), assume a capillary rise over a flat grid cell. Models that do not account for subgrid heterogeneity may show stronger effects than those with subgrid variability. For example, ET enhancement in MAT-GW is higher (9%) than its reference simulation compared to the enhancement in ORCHIDEE-HSL (4.2%) and in ISBA-CTRIP (1.1%). In any case, the effects on land surface fluxes and near-surface climate are consistent in direction across all the studies.

Other limitations in our results for land average values are related to modeling choices. First, we prescribe a static lowland fraction with many uncertainties (Tootchi et al., 2019), but this fraction is likely to be dynamic, according to the concept of variable contributing area (Beven and Kirby, 1979). Second, the deactivation of permafrost may induce a stronger signal in high latitude regions, as permafrost can hinder effective hillslope flow (Sergeant et al., 2021). Finally, we overlook losing streams; their inclusion could lead to lower ET rates in our simulations if the water table depth is below the soil column (Brunner et al., 2011; Rashid et al., 2019), especially in flat semiarid areas and/or where extensive groundwater pumping takes place (Jasechko et al., 2021), but they can also contribute to higher ET rates if the stream sustains a shallow water table Miguez-Macho et al., 2007.

For future climates, comparing our results is more difficult. To our knowledge, there are no studies that analyze the effect of hillslope flow and groundwater-SM interaction over long-term trends under climate change. Some studies assess the effect of climate change on groundwater storage, for instance, in Wu et al., 2020 for key mid-latitude aquifers with CESM-LE and CLM4.0. The coherence of our results with other studies for land average values is especially important because the former makes our analysis for future climate more robust.

Figure 3.10-b summarizes the modulations of long-term climate change trends by hillslope flow. At the regional scale, the modulation of ET trends depends strongly on the sign of P changes with climate change, which is overlooked in the offline climate change impact

assessment of Condon et al., 2020 with an integrated surface-groundwater hydrologic model over the contiguous United States. Hillslope flow attenuates climate change trends of all other hydrological variables. Therefore, it has the potential to partially alleviate the intensification of droughts projected by current climate models (Cook et al., 2018; Douville et al., 2021) and already ongoing (Padrón et al., 2020). It can also attenuate the projected runoff increases in regions and seasons with increased P. These regional attenuations contrast with the amplifications that dominate the global scale response of hydrological variables (but R). It is noteworthy that these global scale amplifications, like the attenuation of global warming in our simulations, contradict the conclusions from the GLACE-CMIP5 experiment. In this framework, Berg et al., 2016 show that, on average over land, land-atmosphere feedbacks amplify anthropogenic warming and attenuate the subsequent increases of P and ET, therefore amplifying aridity (P/PET) increases. These contrasted results at regional and global scales show the need to develop process-based understanding of climate change interactions with the water cycle.

For air temperature, we observe that hillslope flow slightly attenuates warming at both scales(Figure 3.10-b) due to amplification of ET increase and attenuation of SHF increase. However, in some areas (Figure 3.9), we observe a small amplification of warming for the HSL simulation, which is difficult to explain. In arid regions, faster warming might be the result of decreasing rates of ET. Elsewhere, accelerating warming occurs even if there is an inversion of ET trend from negative to positive, for example, in the South Atlantic area of the USA (SA USA, Figure A.7). This warming amplification could be linked to changes in net radiation at the surface, as has been reported in coupled simulations with irrigation (Thiery et al., 2017) for areas far away from irrigated regions.

Some modeling choices could limit our results for hillslope flow modulation on climate change trends. The first is the activation of permafrost, which could have an impact on the speed and strength of climate change trends in high latitude areas (Sergeant et al., 2021). The second is overlooking losing streams, which may become more common in the future due to widespread water table decline (Graaf et al., 2019), and could prevent any impact on ET by the disconnection between groundwater and the lowland fraction. The third is land use change, which is not included in our simulation and has a complex relationship with groundwater, land surface fluxes, and climate (Zipper et al., 2019).

3.2.5 Conclusions

This study analyzes the influence of hillslope flow on mean climate and climate change projections. It relies on a new parameterization of subgrid-scale hillslope flow in the ORCHIDEE LSM and compares two transient coupled land-atmosphere simulations under historical and strong climate change scenarios. The impact on projections is split into mean values and long-term trends for several hydroclimatic variables (P, ET, R, SHF and air temperature).

During the historical period, the redistribution of water along topography by hillslope flow

increases SM, especially in the Northern Hemisphere, and it enhances water exchanges from the surface to the atmosphere (+4.2% in ET) and from the atmosphere to the surface (+1.2% in P). ET enhancement occurs mostly in transition areas and during dry seasons, while the P response is mainly due to local convection (as in Canada) and poleward movements of rain belts (as in the Sahel-Sudan band). As a result, R tends to decrease (-2.8%), except in areas where there is a strong P increase. The presence of the lowland fraction may also lead to changes in the R peak in some regions (such as Southern Hudson Bay). On the other hand, ET enhancement shifts the energy partitioning by decreasing SHF, which cools down the near-surface atmosphere. The effect is weak for Tas (-0.1 °C) but is stronger and wider for Tasmax (-0.2 °C). Finally, as a result of the SM increase and subsequent changes in soil thermal inertia, Tasmin can increase regionally in central Africa and some areas of the Amazonian basin.

For long-term trends over the twenty-first century, climate change is the leading driver, but hillslope flow can modulate climate change effects. Globally, hillslope flow enhances the increase in both P and ET and slightly slows global warming. At the regional scale, when climate change decreases P rates, hillslope flow attenuates the decline in both ET and P. This effect of hillslope flow occurs in all regions, regardless of regional aridity and mean temperature. Seasonally, hillslope flow modulation could persist, as in the Western Europe and Mediterranean region, WEM. Furthermore, because it attenuates most regional P declines, hillslope flow also attenuates the related R decrease. In contrast, when climate change increases P rates, hillslope flow enhances the increase in ET and attenuates the increase in both P and R. However, modulation at the seasonal scale may be different, depending on regional changes. Regional warming is slower when hillslope flow is included, but the signal is weak for yearly and seasonal mean values and is stronger for the Tasmax than for the Tas.

Eventually, the areas most prone to modulation of climate change trends by hillslope flow are humid areas, either warm like tropical South America and West Africa, temperate like Western Europe, or cold like Canada and northern Europe. Semiarid and cold areas (such as the northern Great Plains in North America) and humid and warm/temperate regions (such as tropical South America and Western Europe) are prone to slower warming than elsewhere when hillslope flow is included.

Our results highlight the role of hillslope flow in sustaining land surface-atmosphere water fluxes. This attenuating role (except for ET increases where P increases due to climate change) suggests that the inclusion of hillslope processes would weaken the projected intensification of droughts and aridity. The effect of hillslope flow on regional projections also suggests an attenuation in the evolution of extreme temperature events such as heat waves (Mu et al., 2021), and in hydrological extreme events. To our knowledge, only a few models include the effects of groundwater on soil moisture in CMIP6: CESM2 and its LSM CLM5 (Danabasoglu et al., 2020; Lawrence et al., 2019), NorESM2, which uses CLM5 (Seland et al., 2020), E3SM-1.1, which includes CLM4.5 (Golaz et al., 2019), and CNRM-CM6-1 with its

LSM ISBA-CTRIP (Voldoire et al., 2019; Decharme et al., 2019). Our results and their implications call for including or improving the representation of hillslope flow and the related groundwater storage in LSMs such as ORCHIDEE and for incorporating these processes into state-of-the-art climate change projections.

3.3 Effect of hillslope flow on the evolution of climate extremes

Here we present a brief description of the approaches to define and identify an extreme value of temperature and precipitation. Then, we analyze the influence of hillslope flow on extreme values of maximum air temperature (Tasmax) and precipitation (P) for the two simulations used in section 3.2. The analysis presented here uses daily data from both transient simulations. Recall that simulation REF does not include hillslope flow representation, while HLS include hillslope flow. We compare frequency and intensity for the historical period (1980 - 2010) and for the future (2070-2100).

3.3.1 How to identify temperature and precipitation extremes

Identification of temperature and precipitation extremes needs the use of indices. Those indices will allow then to classify a value as "extreme" according to certain conditions. How to calculate the index, and which are the conditions to consider a value as "extreme" depends on the goal of the index.

We identified three main approaches in the literature. First one is based on the work of the ETCCDI, it uses relative calendar-day thresholds based on quantiles, and are calculated for a reference period (Zhang et al., 2005; Zhang et al., 2011). ETCCDI indices have been used for assess the trends of frequency and intensity of extreme values at global and regional scale (Alexander et al., 2006; Bitencourt et al., 2020) and understand the role of soil moisture on projected extreme values (Lorenz et al., 2016).

The second uses a single relative threshold based on quantiles. In this case the goal is to compare the effect of a single process, for example understand the effect of irrigation on frequency of heat extremes (Thiery et al., 2017; Thiery et al., 2020), understand the relationships and biases on heat stress extremes (Brouillet and Joussaume, 2019; Zhao et al., 2015) or analyse the link between heat extremes in northern Europe and rainfall in southern Europe (Quesada et al., 2012).

Finally, the third one considers absolute thresholds. For example, we may find the number of days under 0°C or over 25°C, or the number of days with precipitation larger than 10mm (Lorenz et al., 2016). The main problem with absolute thresholds is it may prevent the comparison of information spatially, since the defined threshold may be rare at one point and normal at another. Temporarily, the same problem arises, during a period of the year one

event may be normal, and rare in another moment (Perkins, 2015). But this approach may be important in sector-specific assessment (Horton et al., 2016).

3.3.2 Indices for frequency and intensity of climate extremes

We use two metrics to quantify the influence on intensity and frequency:

1. The difference of quantiles between both simulations. This index allows to assess the impact on intensity of extreme events, and is shown in equation 3.2. The differences of quantiles Δq, uses values q^p_{HLS} and q^p_{REF} corresponding to the quantiles from simulation HLS and simulation REF respectively, with and exceedance probability p.

$$\Delta q = q^p_{HLS} - q^p_{REF} \tag{3.2}$$

2. The PR index. It allows to analyse the impact on frequency, and is shown in equation 3.3. The PR index uses P_{REF}, the probability of exceedance of the quantile q_{ref} in simulation REF, for example 0.05 for the 95th percentile, and $P^{q_{ref}}_{HLS}$, the probability of exceeding the same quantile q_{ref} but in the simulation HLS. If PR is greater than 1, the value is more likely to occur, if PR is lesser than 1, the value is less likely to occur.

$$PR = \frac{P^{q_{ref}}_{HLS}}{P^{q_{ref}}_{REF}} \tag{3.3}$$

While the quantile difference gives an idea of the change in intensity, the PR value measures the change in frequency. We use three quantiles to evaluate the effect of hillslope flow: q_{90}, q_{95} and q_{98} i.e. values with a probability of exceedance of 10%, 5% and 2% for both Tasmax and P.

3.3.3 Results

Figure 3.11 shows the effect of climate change alone (simulation REF), i.e. future (Fut, 2070 - 2100) against historical (Hist, 1980 - 2010) for both . We observe a general warming, which is slightly more important for quantile q_{95} and q_{98} (Figure 3.11-a), and an increase in frequency (Figure 3.11-b) which according to the simulation REF becomes higher for the quantile q_{98} (4.5 times for q_{90} against 15.1 times for q_{98}).

For the case of precipitation, we observe an increase of extreme values, but there are regions where the values decrease (for instance the Mediterranean and USA West Coast). PR ratio for P also shows that extreme values in areas like the Sahara might become less frequent, while in others like the Amazon basin are likely to become more frequent. Global average PR values indicate a higher frequency for all quantiles.

Results in temperature may be explained by global warming, and the differential impact that this warming has on extremes (Perkins, 2015). For the case of P, it is the result of a

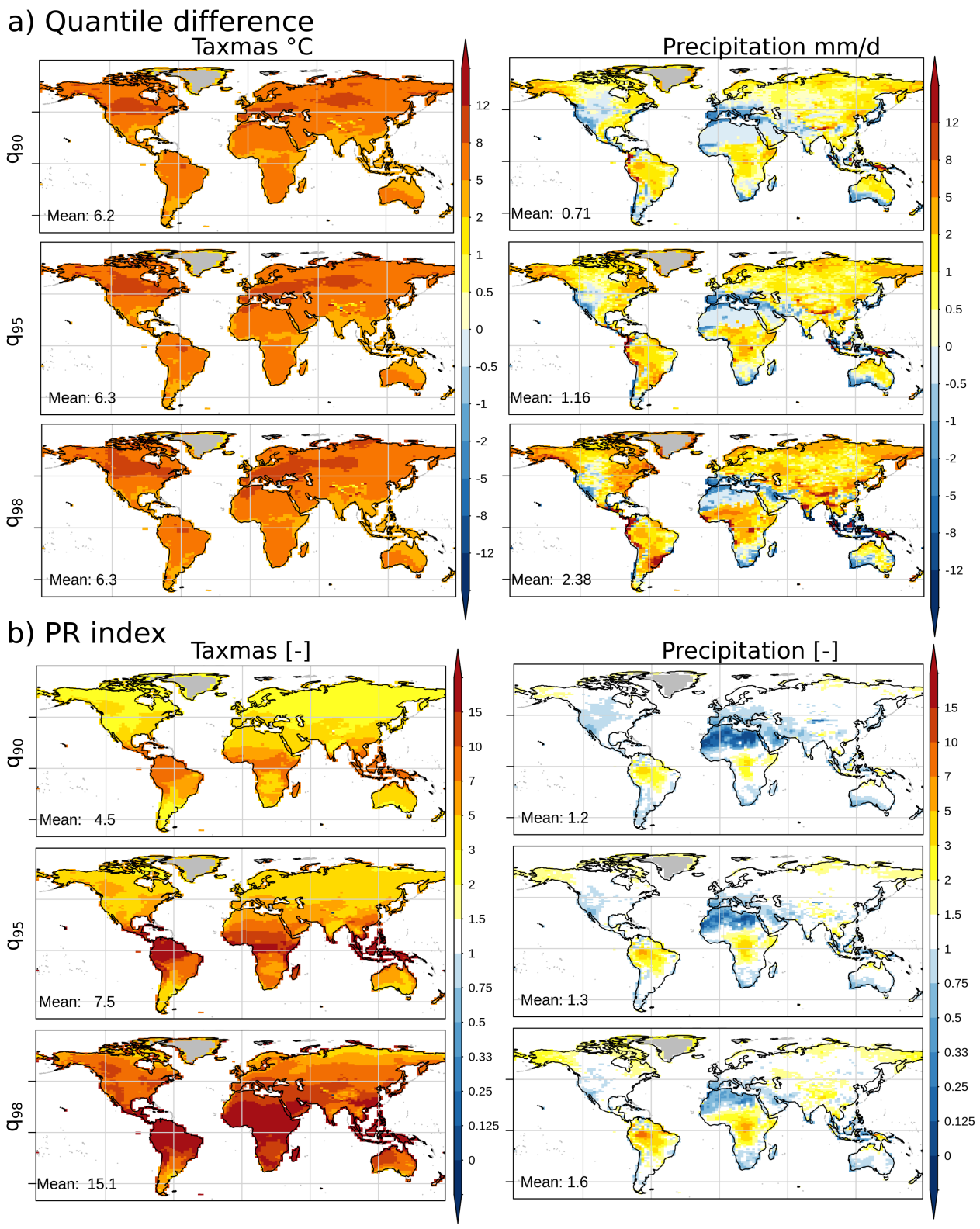

Figure 3.11: Difference of quantiles (a) and PR index (b) between future (2070-2100) and historical (1980-2010), REF simulation, for maximum air temperature Tasmax (first column) and precipitation P (second column).

strengthening of the water cycle as a result of air warming and the corresponding increase in water vapour content (Dunn et al., 2020). It can be linked to seasonal strengthening of mechanisms like "wets get wetter" and more intense local convection. In any case, the effect of climate change on precipitation is weaker than for temperature. These results are coherent with the scenario SSP5-8.5 used in both simulations, as well as general patterns of projected increases in extremes (see for instance Figure SPM.6 in AR6, IPCC, 2021).

Figure 3.12 shows the effect of hillslope flow, i.e. differences between HSL and REF simulations, in quantile difference for historical and future periods (i.e. with future climate change and hillslope flow modulation), while Figure 3.13 shows the PR ratio. We observe that, for Tasmax in 3.12-a, temperature values cool down, and cooling is slightly more important for the more extreme quantile, with the exception of some mostly arid areas, like the small areas in the Sahara, Australia and central USA. This cooling down is maintained in the future, with a similar pattern, but becomes slightly stronger for q_{90} and slightly weaker for q_{98} compared to the historical period.

Precipitation in Figure 3.12-b presents stronger values for all quantiles in the present and future, when we assess the effect of hillslope flow. In the future, the effect of hillslope flow increases, especially for the most extreme values, but the spatial distribution of the signal continues to be noisy and heterogeneous.

For frequency, Tasmax extreme values (Figure 3.13-a) are likely to become less frequent as a result of hillslope flow, for historical and future periods. But this effect is slightly weaker for q_{98} in the future, when we compare it to the historical period. In addition, the spatial distribution present some changes, for instance in central Africa and central North America.

For precipitation (Figure 3.13-b), hillslope influence is less important, with global average values of PR ratio near 1 (which means that the frequency does not change). Spatially, there is a strong effect in North Africa, which leads to less frequent extreme precipitation for both quantiles q_{90} and q_{95}, but this effect disappears for q_{98}. This pattern is similar in the future, with some regional differences between historical and future periods

Our results suggest that hillslope flow has an important cooling effect for extreme temperature, which also decreases extreme temperature frequency. For precipitation, the results are difficult to assess, but they suggest an increase in intensity, and a small influence on frequency, which may be important at the regional scale.

The results urge us to estimate other indexes such as those proposed by the ETCCDI. This would allow us to evaluate other characteristics of the extreme values, and to compare with other data sets for the historical period, in order to validate. They also suggest the need to assess the influence on frequency, intensity and duration of heatwaves, using the framework from Perkins and Alexander, 2013 and Russo et al., 2015, as the effects seem stronger for higher Tasmax quantiles.

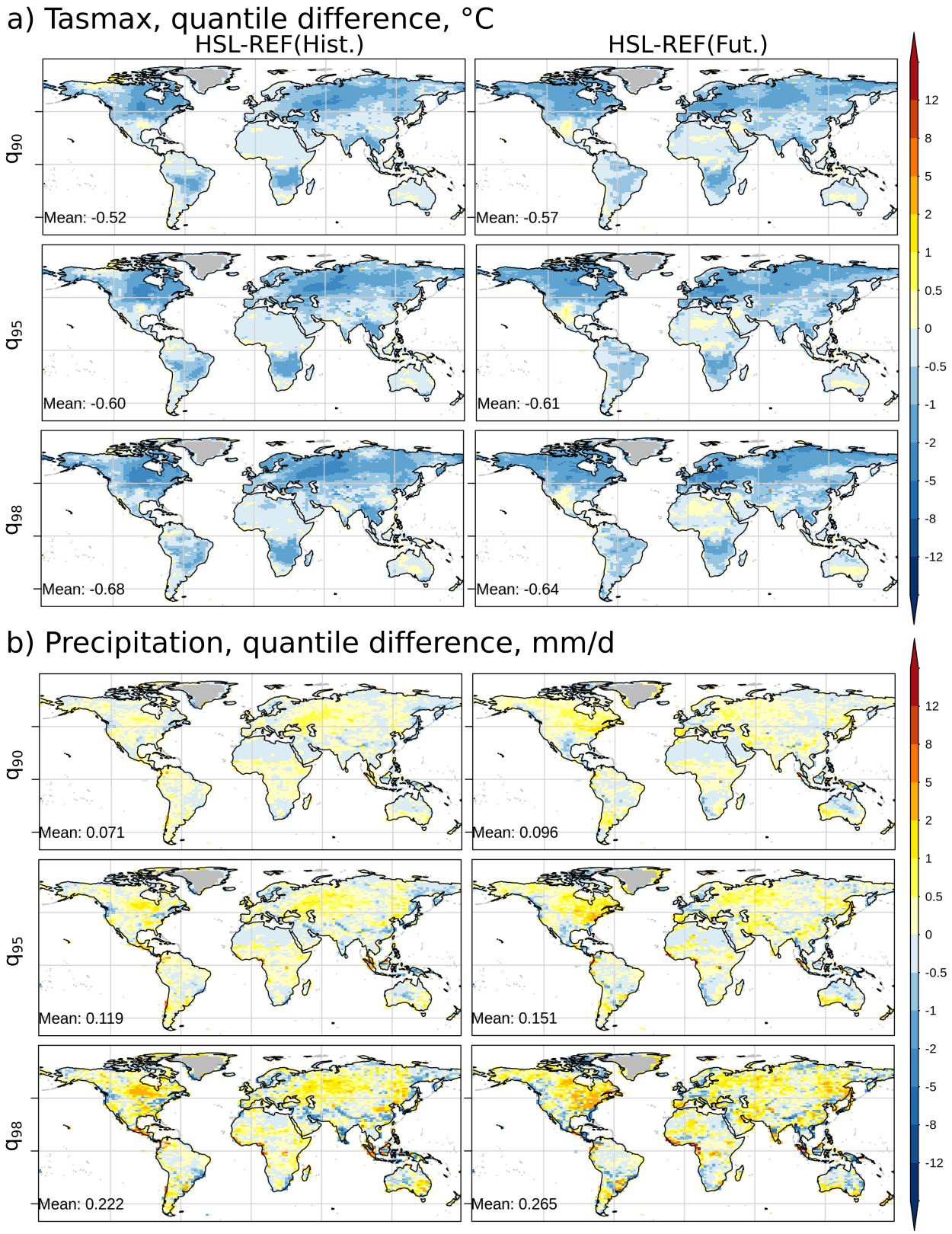

Figure 3.12: Difference of quantiles for historical (1980-2010, first column) and future (2070-2010, second column) period, between HSL and REF simulations, for maximum air temperature Tasmax (a) and precipitation P (b).

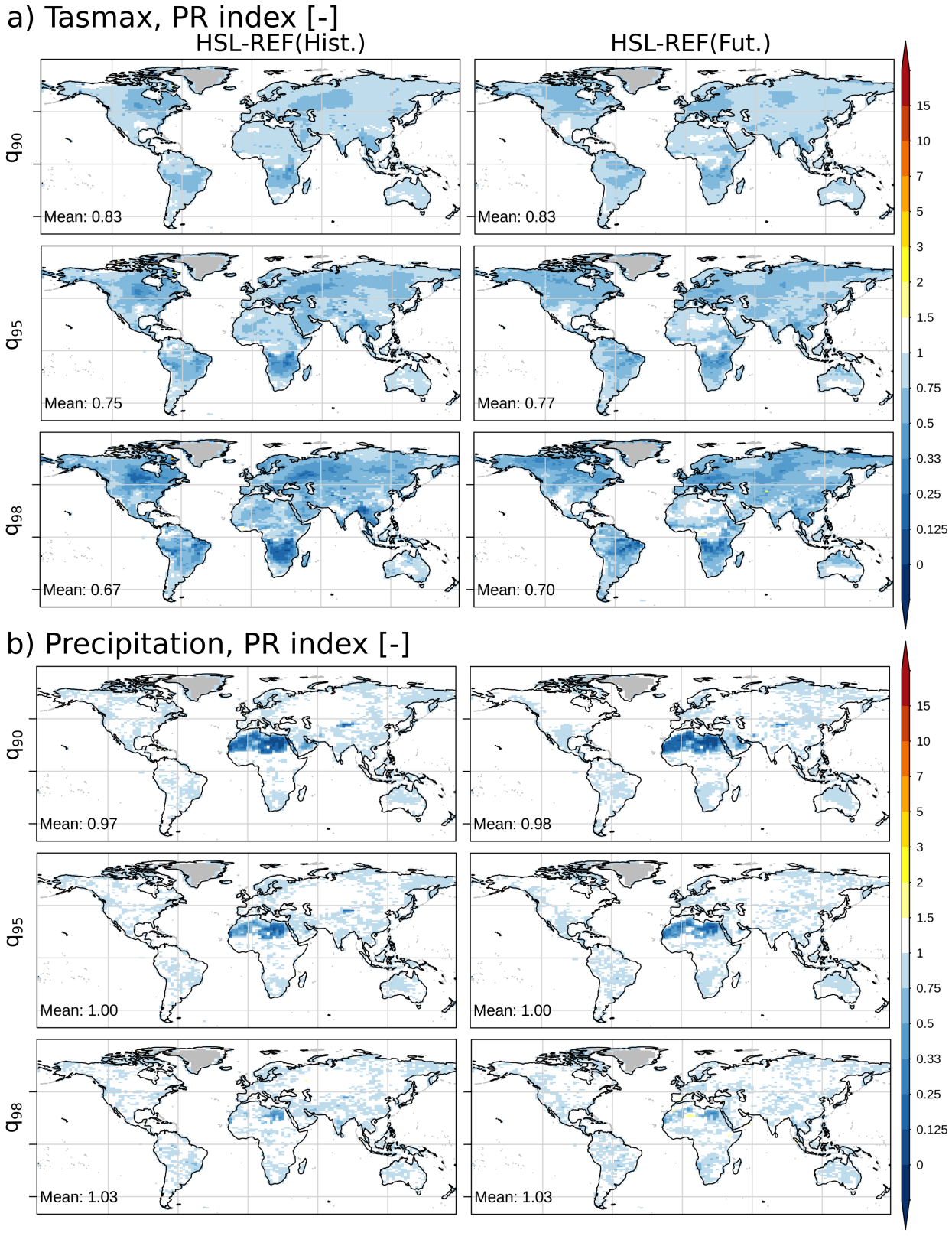

Figure 3.13: PR index for historical (1980-2010, first column) and future (2070-2010, second column) period, between HSL and REF simulations, for maximum air temperature Tasmax (a) and precipitation P (b).

3.4 Chapter conclusions

In this section we show a simple parameterization to represent hillslope flow at subgrid scale within ORCHIDEE. We use this hillslope-flow representation in a transient simulation, coupling ORCHIDEE and LMDZ under future climate change (period 1980-2100), and we compare the outputs to a reference simulation with no hillslope flow.

The results show an effect on average values under the near-present climate, with an increase of soil moisture, evapotranspiration, precipitation, and decrease of air temperature and total runoff. The effect of hillslope flow is also observed in the evolution of hydroclimatic variables, with an amplification of positive trends of soil moisture, evapotranspiration and precipitation, and attenuation of warming. But this amplification at global scale hides a different role according to the trend of precipitation. In areas with negative precipitation trends, hillslope flow attenuates the declines of evapotranspiration, precipitation and runoff, regardless of aridity conditions and mean air temperature. In areas with positive precipitation trends, hillslope flow amplifies evapotranspiration but attenuates precipitation and runoff. And warming is in general attenuated, but signal is weak.

We also explored the effects of hillslope flow on the evolution of extreme values of precipitation and maximum air temperature. The results suggest a significant cooling of the intensity of extreme temperatures, while their frequency decreases. In the case of precipitation, the effects on intensity are difficult to assess, but suggest an increase in extreme values, while the effect on frequency is weak, with some exceptions on a regional scale. In the future, the effects of hillslope flow on the intensity and frequency of temperature extremes should be maintained, but with slight changes in spatial distribution. The analysis does not allow us to define whether the decrease in the intensity and frequency of extreme temperatures due to inclusion of hillslope flows is related to local climatic conditions, or whether local climate does not play an important role in the modulation of hillslope flow effects.

These results encourage the inclusion of a better representation of hillslope hydrology within land surface models, as it has an effect in projected changes on hydroclimatic variables, and on some characteristics of extreme events. For the current representation of hillslope flow within ORCHIDEE, additional improvements are still possible, for instance the inclusion of losing streams and the explicit representation of the water table depth, to simulate the disconnection between groundwater and surface when the water table becomes deeper. Finally, here we assessed the effect of hillslope flow on climate with no human intervention, but in reality, there are many areas where hillslope flow and anthropic activities (like irrigation) occur at the same time. If irrigation is sustained by groundwater, this activity could reduce or prevent the hillslope flow, i.e. we could observe an "inter-processes interference". So far, it is not understood which could be the effect of irrigation (with mostly rapid water flows) on the link between groundwater and the atmosphere sustained by hillslope flow (with mostly slow water flows). To answer this latter questions, hillslope flow processes and irrigation activities should be included in a single version of the ORCHIDEE LSM.

Chapter 4

Introduction of a new irrigation scheme in ORCHIDEE, and effects on global and continental hydrology

4.1 Introduction to the chapter

This chapter includes a section (section 4.2) in paper format, to be rewritten and submitted to Geoscientific Model Development (supplementary information in annex B).

In the first part of this chapter, we present a new irrigation scheme to be used at global scale, the results of a sensitivity analysis and parameter tuning (section 4.2.2), and the numerical design we used for the experiment (section 4.2.3). Then, we show the estimates of irrigation at global scale and a comparison against observed datasets (section 4.2.4.1). In addition, we present the effect of including irrigation within ORCHIDEE on the mean values of some water and energy variables (section 4.2.4.3).

The following sections present the relationship between landscape descriptors and modeling biases of evapotranspiration, leaf area index, and irrigation (section 4.2.4.5), the assessment of the spatial distribution of the modeling bias for evapotranspiration and leaf area index (section 4.2.4.6) and the comparison to observed values of total water storage anomalies and river discharge (section 4.2.4.7).

Second part of the chapter adds a comparison of irrigation estimates with observed values in France (section 4.3) and finally, we end with some conclusions (section 4.4).

4.2 Validation of a new global irrigation scheme in the ORCHIDEE land surface model

Pedro F. Arboleda-Obando[1], Agnes Ducharne[1], Zun Yin[2], Philippe Ciais[3]
1 METIS, Sorbonne University, 2 Geophysical Fluid Dynamics Laboratory, Princeton University, 3 LSCE, Université de Versailles Saint-Quentin-en-Yvelines

Abstract Irrigation activities are important for sustaining food production, and account for 70% of total global water withdrawals. In addition, due to increased evapotranspiration, these activities have an impact on hydrology and climate. In this paper we present a new irrigation scheme within the LSM ORCHIDEE. We perform a sensitivity analysis and a simple parameter tuning to set the parameter values, and match the observed irrigation rates, assuming uniform parameter values over land. With the scheme and the tuned parameter values, we compare the bias of simulated irrigation versus reported data, and we identify that some areas in India, in China, and in Africa, concentrate the errors in irrigation rate estimates. The comparison with observed products show that including the new irrigation scheme within ORCHIDEE reduces the negative bias of ET, but exacerbates the positive bias of the LAI except for the intensively irrigated areas, where irrigation reduces a negative LAI bias. Irrigation does not have a large impact on the representation of TWSA, but decreases river discharge values, in some cases significantly, although this does not necessarily lead to a better representation of discharge dynamics. The spatial distribution of the irrigation bias and the comparison with landscape descriptors datasets shows a relationship between irrigated rice and the errors in the irrigation estimate, and suggests that the scheme could be improved by explicitly representing paddy irrigation. Also, that some other anthropogenic processes could help to reduce part of the irrigation bias, and to increase the model performance to simulate TWSA and discharge dynamics. These results encourage the use of coupled simulations to explore the joint evolution of climate, water resources, and irrigation activities.

4.2.1 Introduction

The practice of irrigation, which seeks to increase crop yields by reducing plant water stress (Siebert and Döll, 2010; Klein Goldewijk et al., 2017), supports about 43% of the world's food production on about 20% of arable land (Siebert and Döll, 2010; Grafton et al., 2017). The beneficial effects of irrigation on food production, and population and economic growth, have dramatically pushed the increase of irrigated areas during the 20th century, from 28 Mha in 1850 to 276 Mha in 2000 (Klein Goldewijk et al., 2017; Siebert et al., 2015). As a consequence, by the year 2000, irrigation accounted for 70% of the total water withdrawn (between 2657 and 3594 km^3/year). The consumptive water use, i.e. the part of the withdrawn water that actually evapotranspires, represents half of that volume (between 1021-1598 km^3/year,

around 1.7% of total continental evapotranspiration of 75.6x10^3 km^3/year according to Jung et al., 2019), and represents around 90% of the total consumptive water use by human activities (Pokhrel et al., 2016; Döll et al., 2012; Hoogeveen et al., 2015).

Water abstraction and the increase in evapotranspiration have a direct impact on the water and energy balances, and on surface and subsurface hydrology (Döll et al., 2012; Taylor et al., 2013; Vicente-Serrano et al., 2019). The atmosphere also reacts to these changes on land surface fluxes, for example with regional increases/decreases in rainfall rate, or decreases in temperature extremes (Lo and Famiglietti, 2013; Guimberteau et al., 2012b; Cook et al., 2015; Puma and Cook, 2010; Al-Yaari et al., 2019; Thiery et al., 2020), and irrigation has been identified as a source of error in some key variables of the water cycle in ORCHIDEE LSM (Mizuochi et al., 2021). Thus, it was recently shown that climate models better capture historical trends in evapotranspiration if they account for irrigation and its expansion, although the resulting cooling effect is too strong if irrigation is not limited by water availability (Al-Yaari et al., 2022). Finally, with the acceleration of climate change, the demand for irrigation water is likely to increase, not only by expansion of the irrigated area, but also by an increased demand for irrigation (Wada et al., 2013). All these impacts and effects have promoted the inclusion of irrigation inside land surface models (LSMs), which represent the continental branch of the hydrologic cycle in the earth system models (Pokhrel et al., 2016).

To represent irrigation, any modeling scheme must answer three questions: When to irrigate, how to irrigate, and how much to irrigate (Pokhrel et al., 2016). In global hydrology models (GHMs) developed to assess water resources availability and use, irrigation requirement by the plant is equal to the consumptive use (i.e water that evaporates), and is commonly computed as the difference between evapotranspiration with no irrigation, and a crop-specific potential evapotranspiration, PET (Siebert and Döll, 2010; Mekonnen and Hoekstra, 2011; Wada et al., 2014; Hanasaki et al., 2018; Chiarelli et al., 2020). Total water withdrawal also considers delivery losses (losses during conveyance) and return flows, i.e. water that returns to the river channel or the groundwater recharge. Return flows are related to the irrigation efficiency, and can be calculated with empirical ratios or specific rules according to the irrigation method (Rost et al., 2008; Jägermeyr et al., 2015). Not all models calculate total water withdrawal, but the advantage of calculating the withdrawn volume is that it allows comparison and validation with datasets of reported values, for example the FAO AQUASTAT dataset (Frenken and Gillet, 2012).

In addition, some GHMs have also included an explicit representation of the water supply, i.e. surface, groundwater, and adduction from non-local reservoirs (Döll et al., 2012) as well as non-sustainable groundwater (Wada et al., 2012). Other models have included a representation of water allocation, i.e. the rules of water use per source, based on the global inventory of the areas equipped for irrigation by water source (Siebert et al., 2010). The water allocation rules can also take into account an environmental flow requirement that may limit the actual irrigation rate (Hanasaki et al., 2008a).

LSMs may use a different approach to estimate the irrigation requirement. A few LSMs use a value of potential evaporation or potential transpiration, to estimate irrigation for a generic crop type (Rosnay et al., 2003; Guimberteau et al., 2012b). This approach, however, is not often used in LSMs, because they do not deduce evapotranspiration (ET) from daily PET input data, but from the direct solution of the surface energy balance at an hourly or sub-hourly time step, so there is a consistency issue between empirical PET formulas and potential ET rates in LSMs (Barella-Ortiz et al., 2013). Other LSMs use independent irrigation estimates directly as input data (Lo and Famiglietti, 2013; Cook et al., 2015). A third approach in LSMs and some GHMs estimates water requirements by calculating a deficit, for example, a soil moisture deficit between actual soil moisture and a target (Haddeland et al., 2006; Hanasaki et al., 2008a; Leng et al., 2014; Pokhrel et al., 2015; Jägermeyr et al., 2015), and triggers irrigation if soil moisture drops below that target. Note that the first approach (potential evaporation) estimate an irrigation requirement, while the second and third approaches includes the return flows but excludes the delivery losses.

Regarding the water supply, the LSMs have limitations on the representation of the water source. For instance, some models do not include groundwater pumping, but a virtual reservoir representing fossil groundwater (Ozdogan et al., 2010; Leng et al., 2014; Pokhrel et al., 2012). As a result, available water does not constrain the actual water withdrawal, but in some cases an explicit representation of water table depletion is included (Pokhrel et al., 2015; Leng et al., 2017; Felfelani et al., 2021). The latter is important in areas like the US high plains, or India. Some models include water supply by reservoirs (Haddeland et al., 2006; Pokhrel et al., 2012), but adduction of non-local surface water is usually not included due to model resolution (Guimberteau et al., 2012b). In addition, LSMs represent water allocation by using simple prioritization rules, withdrawing first from surface water and then from groundwater or the virtual reservoir, without estimation of a minimum environmental flow in rivers. Some models have included most explicit rules (Leng et al., 2015; Leng et al., 2017) using the global inventory from Siebert et al., 2010, or local information in regional experiments (Felfelani et al., 2021). For water application, there are some models that include different irrigation methods (Leng et al., 2017) but typically water is simply applied to the soil surface. These simplifications allow to assess the effect of irrigation on climate by coupling the LSM to an atmospheric model (Puma and Cook, 2010; Lo and Famiglietti, 2013; Guimberteau et al., 2012b; Lo et al., 2021), but they restrict the use of LSMs to evaluate the effect of irrigation on water resources.

One example is the ORCHIDEE LSM (Krinner et al., 2005), which represents the continental branch in the IPSL Earth System Model, ESM (Boucher et al., 2020). The first attempts used a potential evaporation approach to estimate irrigation requirement (Rosnay et al., 2003; Guimberteau et al., 2012b) and assess the impacts of irrigation on land surface fluxes and climate. This irrigation scheme includes an explicit representation of water supply from surface and groundwater, but adduction from non-local reservoirs was disabled. Water allocation is based on simple rules and may limit the actual irrigation volume if the supply

reservoirs are depleted. More recently, a model with a crop phenology module, ORCHIDEE-CROP, included an improved irrigation scheme that was tested in China (Yin et al., 2020). Water supply and allocation rules are maintained, but the scheme represents two irrigation methods according to the crop type: flood and paddy irrigation. These improvements allowed to assess the effect of irrigation on water resources at regional scale.

Here, we present evidence on the effect of including irrigation to reduce modeling biases in some key variables like evapotranspiration and leaf area index, but also river discharge and total water storage dynamics. We describe a a new irrigation scheme that restrain irrigation according to water supply, and that includes environmental restriction to water withdrawal, water allocation rules based on the facility to access the water reservoirs, and adduction of water from non-local water sources (section 4.2.2.2). To set the parameter values, we use short simulations and perform a sensitivity analysis and a simple parameter tuning, to match observed irrigation rates (section 4.2.2.3). With these parameter values, we compare irrigation estimations from the model with observations (section 4.2.4.1) and assess its variability due to changes on parameter values and input maps (section 4.2.4.2). Then, we analyse the effect of irrigation in modeling land surface fluxes and in vegetation dynamics (section 4.2.4.3 and 4.2.4.4). We add a factor analysis using classes of irrigated fractions and the corresponding values of bias in section 4.2.4.5. Then, we compare our results with observed values of evapotranspiration (ET) and leaf area index (LAI) in section 4.2.4.6, and to observed datasets of total water storage anomalies (TWSA), and discharge in section 4.2.4.7. We discuss the results in 4.2.5 and we show the main conclusions and perspectives in 4.2.6.

4.2.2 Model description

4.2.2.1 ORCHIDEE v2.2

ORCHIDEE describes the fluxes of mass, momentum, and heat between the surface and the atmosphere (Krinner et al., 2005). Here we use version 2.2, which is close to the version used for CMIP6 (corresponding to 2.0). Version 2.0 has been largely described in many papers (Cheruy et al., 2020; Boucher et al., 2020; Tafasca et al., 2020) and version 2.2 (here used under revision r7619) only adds a few minor bug corrections. We summarize the main characteristics of the model that mediate in the simulation of irrigation.

In each grid cell, vegetation is represented by a mosaic of up to 15 plant functional types (PFTs), including generic C3 and C4 crops, as well as generic C4 grasses, and tropical, boreal and temperate C3 grasses. The PFTs fractions are described by the LUHv2 dataset (Lurton et al., 2020), and each PFT is characterized by a specific set of parameters, applied to same set of equations (Boucher et al., 2020; Mizuochi et al., 2021). Plant phenology is controlled by the STOMATE module, which couples photosynthesis and the carbon cycle and computes the evolution of the leaf area index (LAI), all these processes depending on CO_2 atmospheric concentration (Krinner et al., 2005).

A specialized version of ORCHIDEE has been proposed by (Wu et al., 2016) to better describe temperate crops, with phenology thresholds based on accumulated degree days after sowing date, improved carbon allocation to reconcile the calculations for leaf and root biomass and grain yield, and nitrogen limitation related to fertilization. It was not used in this work by lack of ubiquitous parameters at global scale, so that C3 and C4 crops are simply assumed to have the same phenology as natural grasslands, but with higher carboxylation rates and adapted maximum possible LAI (Krinner et al., 2005).

Roots constitute an important link between the carbon and the water balance. In each PFT, root density decreases exponentially with depth, and the parameter that controls the decay is PFT-dependent. It is worth noting that the root density profile is constant in time and goes down to the bottom of the soil column, set at 2 m, but forest PFTs have much denser roots than crop and grass PFTs, especially in the bottom part of the soil (Wang et al., 2018). The resulting root density profile is combined with the soil moisture profile and a water stress function to define the water stress factor of each PFT on transpiration (Tafasca et al., 2020) and to estimate the water uptake for transpiration (Rosnay et al., 2002).

Evapotranspiration is represented by a classical aerodynamic approach and is composed of snow sublimation, interception loss, bare soil evaporation (E), and transpiration (T). The first two proceed at a potential rate, while bare soil evaporation is limited by upward diffusion of water through the soil, and transpiration is controlled by a stomatal resistance, which depends on soil moisture and vegetation parameters. The vegetation types are grouped into three soil columns according to their physiological behavior: high vegetation (eight forest PFTs), low vegetation (six PFTs for grasses and crops), and bare soil. While the energy balance is calculated for the whole grid cell (Boucher et al., 2020), a separate water budget is calculated independently for each soil column, in order to prevent forest PFTs from depriving the other PFTs of soil moisture.

Vertical soil water flow is represented by a 1-D Richards equation coupled to a mass balance, and lateral flow between cells and soil columns is neglected (Rosnay et al., 2002; Campoy et al., 2013). Here, soil depth is set to 2 meters, and discretized into 22 layers here to finely model lower layers implicated in drainage. Infiltration is simulated as a sharp wetting front based on the Green and Ampt model (Tafasca et al., 2020; D'Orgeval et al., 2008). The resulting increase in top soil moisture is redistributed by the Richards equation. The bottom boundary condition assumes free drainage, equal to the hydraulic conductivity of the deepest node. The saturated hydraulic conductivity decreases with depth, but roots increase the hydraulic conductivity near the surface (D'Orgeval et al., 2008). Soil parameters are a function of soil texture (Tafasca et al., 2020), and the spatial distribution is taken from the Zobler, 1986 map.

A routing scheme transfers surface runoff and drainage from land to the ocean through a cascade of linear reservoirs (Ngo-Duc et al., 2007; Guimberteau et al., 2012a). Each grid cell is split into sub-basins according to a 0.5° flow direction map. Tree reservoirs are considered inside every sub-basin, representing groundwater, overland, and river reservoir, and each one

presents a distinct residence time (Ngo-Duc et al., 2007). The groundwater reservoir collects drainage from the soil column, while the overland reservoir collects surface runoff. Both reservoirs are internal to each subbasin and flow to the stream reservoir, which also collects streamflow from the upstream basins and contributes to large-scale routing across subbasins and grid cells. Note that there are two surface reservoirs, overland representing the headwater streams, and river reservoir representing large rivers.

The water and energy budgets and the routing scheme are computed at the same 30-minute time step, while the carbon and plant phenology processes in STOMATE are solved with a daily time step.

4.2.2.2 Irrigation scheme

The irrigation scheme (Figure 4.1) is based on the flood irrigation representation from Yin et al., 2020, but it includes some changes in the parameterization to run at global scale. The flood irrigation technique is chosen for global simulations, as it is the most used technique for irrigation activities (Jägermeyr et al., 2015; Sacks et al., 2009).

Firstly, the scheme defines a root zone depth in the crop- grass soil column, based on the cumulative root density (CRD), ranging from 0 at the soil surface to 1 at the soil bottom: the root zone comprises all soil layers with a CRD below a user-defined threshold, $Root_{lim}$. When the threshold is set to 0.9, the root zone includes 90% of the root system. For a 2-m soil column with 22 layers, and an exponential root density decay of 4 (default value for crops and grasses in ORCHIDEE), this threshold defines a root zone depth of 0.5 m, encompassing 10 soil layers.

We can then define a soil moisture deficit D [mm] in the root zone, as the sum of the difference between actual soil moisture and a soil moisture target, in all layers of the root zone:

$$D = \sum_{i \in Rootzone} \max(0, \beta\, W_i^{fc} - W_i), \tag{4.1}$$

where W_i and W_i^{fc} (both in mm) are the actual and field capacity soil moisture in soil layer i, respectively, and β is a user-dependent parameter that controls the target value. To prevent irrigation when there is not plant development, for example during winter, we set the deficit D to zero if all crops and grasses are below a certain LAI threshold, LAI_{lim}.

The irrigation requirement I_req [mm/s] is calculated as:

$$I_{req} = f_{irr}\ \min(D/\Delta t, I_{max}), \tag{4.2}$$

Where f_{irr} is the fraction of irrigated surface [-] in the grid cell, defined by a map of irrigated fractions. The map that prescribes the irrigated fraction may change every year, but note that we do not separate the irrigated area into a separate soil column. I_{max} is a user-defined maximum hourly irrigation rate [mm/h]. This threshold is used to avoid

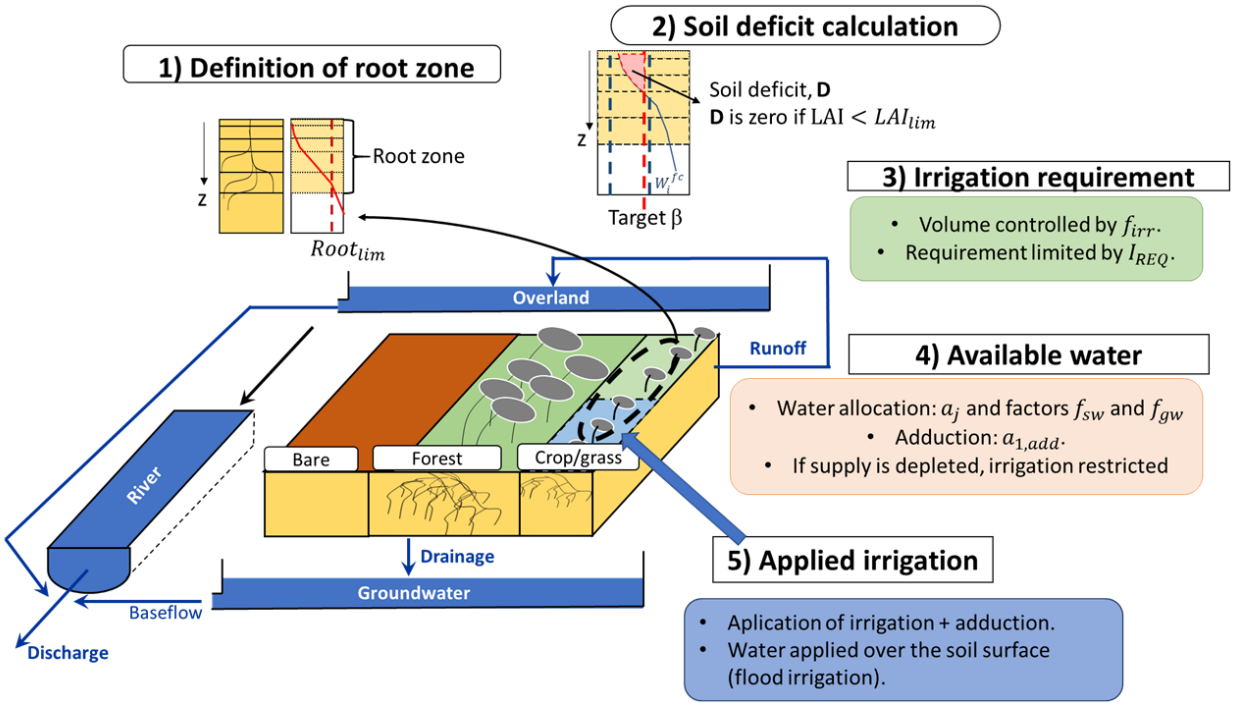

Figure 4.1: ORCHIDEE model and new irrigation scheme. See text for explanation of parameters

excessive runoff production when the deficit is large, because the scheme assumes that the requirement will be fulfilled in the next time step, and the actual irrigation rate applied to the soil surface could exceed the infiltration capacity of the soil. The effective irrigation (I, see below) is uniformly applied over the crops and grasses soil column. Therefore, care is taken inside the model so that the irrigated fraction is not greater than the crops and grasses soil column. In cases when the fraction of irrigated area is smaller than the fraction of soil column, irrigation will eventually be applied over a larger area than the actually irrigated surface. The difference in size could result in a larger fraction of irrigation water actually evaporating than in reality, and could lead to an overestimation of the evapotranspiration increase, especially in areas that are energy-controlled (Puma and Cook, 2010).

Irrigation can be withdrawn from the three routing reservoirs, but the effective water availability, A_w [mm], also depends on the facility to acess surface water and groundwater, and it can be reduced to preserve environmental flows:

$$A_w = f_{sw}\,(a_1\,S_1 + a_2\,S_2) + f_{gw}\,a_3\,S_3. \tag{4.3}$$

In this equation, S_j [mm] is the volume storage in each routing reservoir, with index j equal 1, 2 and 3 for the stream, overland, and groundwater reservoirs, respectively. To prevent from complete depletion of these reservoirs, which all feed streamflow and support aquatic ecosystems, we mimic an environmental flow regulation by reducing the available volume owing to a user-defined parameter a_j, between 0 and 1. It is set here to 0.9 for all

three reservoirs, such as to keep at least 10% of the available water at each time step. The facility to irrigate from surface water reservoirs (S_1 and S_2) and groundwater reservoir (S_3) is accounted for by factors f_{sw} and f_{gw}, also ranging between 0 if the reservoirs cannot be used and 1 if they are fully accessible. In the present application, these factors represent the fraction of irrigated areas that are equipped for irrigation with surface and ground water, respectively, following the global map of Siebert et al., 2010. This map assumes that a grid-cell is either equipped for groundwater irrigation or for surface water irrigation, so $f_{sw} + f_{gw} = 1$, but this is not mandatory, and f_{sw} and f_{gw} could also be made dependent on water table depth, on water, food, or energy prices, or on public regulations. Note that this global map is based on available information from national census reports, and only for a reference year, so it could contain errors due to lack of information. We do not consider irrigation from non-conventional sources.

Eventually, the actual irrigation I [mm/s] is estimated at each time step by comparing I_{req}, i.e. the demand, to water availability A_w [mm], i.e. the supply:

$$I = \min(A_w/dt, I_{req}). \tag{4.4}$$

If we assumed that water abstraction Q_j from each reservoir is simply proportional to available water in each of them, it would be given by the following equations, the sum of the three right-hand side terms being equal to I:

$$\frac{dS_1}{dt} = -Q_1 = -\frac{f_{sw}\, a_1\, S_1}{A_w}\, I \tag{4.5}$$

$$\frac{dS_2}{dt} = -Q_2 = -\frac{f_{sw}\, a_2\, S_2}{A_w}\, I \tag{4.6}$$

$$\frac{dS_3}{dt} = -Q_3 = -\frac{f_{gw}\, a_3\, S_3}{A_w}\, I \tag{4.7}$$

But we chose to implement an additional constraint for surface water withdrawals, which are withdrawn from the stream reservoir (corresponding to large rivers) in priority. This new constraint leads to define the revised set of equations, where the total surface water availability is $A_{sw} = f_{sw}\,(a_1\, S_1 + a_2\, S_2)$:

$$\frac{dS_1}{dt} = -Q_1 = -\min\left(\frac{A_{sw}}{A_w}\, I\,,\ \frac{f_{sw}\, a_1\, S_1}{\Delta t}\, I\right) \tag{4.8}$$

$$\frac{dS_2}{dt} = -Q_2 = -\min\left(\frac{A_{sw}}{A_w}\, I - Q_1\,,\ \frac{f_{sw}\, a_2\, S_2}{\Delta t}\right) \tag{4.9}$$

$$\frac{dS_3}{dt} = -Q_3 = -\frac{f_{gw}\, a_3\, S_3}{A_w}\, I \tag{4.10}$$

The sum of Q_1, Q_2, and Q_3, still equals I. Note that for Q_1 and Q_2, first terms inside the

min function assure that surface water is withdrawn in priority from the stream reservoir.

When $I_{req} - I > 0$, i.e. there is a deficit and the water supply cannot satisfy the irrigation demand, the scheme may adduct water from the neighboring grid cell with the largest streamflow volume . The choice of water adduction was introduced in Guimberteau et al., 2012b, but was disabled due to the coarse modeling resolution. Here we use a similar parameterization, but we add a user-defined parameter to take into account the facility to access distant river reservoirs:

$$\frac{dS_{1,add}}{dt} = -Q_{1,add} = -\min\left(I_{req} - I\,,\ \frac{a_{1,add}\,S_{1,add}}{dt}\right) \tag{4.11}$$

In this equation, water adduction $Q_{1,add}$ from the largest river reservoir in the neighboring grid cell $S_{1,add}$, will depend on the facility of access represented by the factor $a_{1,add}$. This factor can range between 0 if there is no adduction, and 1 if the distant river reservoir is fully accessible for water adduction.

The irrigation water, $I + Q_{1,add}$, is finally added at the soil surface for infiltration, thus resembling a flood or drip irrigation technique. We note that irrigation is not restricted to an optimal period during the day nor to limitations on the duration of irrigation, but may be triggered at any moment. It may lead to an overestimation of evapotranspiration (Ozdogan et al., 2010). We do not represent dams operation in this simulation, even if they play an important role to modulate the temporal dynamics of surface water and assure a water supply for irrigation in many large river basins (Pokhrel et al., 2016; Hanasaki et al., 2008a).

4.2.2.3 Sensitivity analysis and parameter tuning

Shorter tests (23 simulations plus a single simulation with no irrigation, to estimate the increase of evapotranspiration) were run to assess the sensitivity of the irrigation rates at the global scale to different parameter values, using GSWP3 as meteorological forcing, and the LUHv2 from Hurtt et al., 2020 to prescribe the irrigated surfaces (see Section 4.2.3.2). All the tests were run with the same initial conditions and three years run (1998 - 2000), and a comparison of irrigation and ET increase values was performed for the year 2000. By using the last year, we reduce the effect of the common restart file on the simulation outputs. A brief description of each parameter as well as the unit, range, and values used in the sensitivity analysis is shown in table 4.1.

Reference values were chosen based on preliminary tests (not shown). The preliminary tests performed with a-priori values showed an underestimation of irrigation rates at global scale, so the reference values that were used in the sensitivity analysis were intended to maximize the irrigation rate. We change the value of one parameter at a time (once-at-a-time screening, see Mishra, 2009; Song et al., 2015) and then we observe its effect on the irrigation rate and on the increase in evapotranspiration. We tried to include the full range of parameters, but it is worth noting that in some cases, values were restricted to ensure an expected behavior. In the case of β, we set values around 1.0 (target equal to

the field capacity soil moisture) as it seems a plausible target for flood irrigation, but note that values higher than 1.4 or lower than 0.6 are possible (highest target is the saturated soil moisture, lowest target is zero). For adduction, we set parameter values under 0.2 (20% of streamflow available for adduction at every time-step), which seem high enough to represent water adduction in large river basins. In the case of the LAI limit and I_{max}, the upper value was selected a-priori.

Table 4.1: Parameters of the irrigation module, brief description, range and values used in the sensitivity analysis. Values in bold correspond to the reference value. Note that, for parameter A_i, the three reservoirs share the same value.

Parameter	**Description**	**Unit**	**Range**	**Values**
β	Controls the soil moisture target, equal to $\theta_{fc} * \beta$	Fraction, no units	[0-∞]	0.6, 0.8, **0.9**, 1.0, 1.2, 1.4
a_j	Controls the fraction in reservoir available for irrigation, the complement being the fraction left for ecosystems	Fraction, no units	[0-1]	0.1, 0.5, **0.9**, 1.0
$a_{1,add}$	Controls the fraction in stream reservoir available for adduction	Fraction, no units	[0-1]	0.0, **0.05**, 0.1, 0.2
I_{max}	Maximum irrigation rate per hour	mm/h	[0-∞]	0.5, 1.0, **3.0**, 5.0, 7.0
$Root_{lim}$	Defines if a soil layer is part of the root zone	Cumulated relative root density	[0-1]	0.0, 0.5 **0.9**, 1.0
LAI_{lim}	Minimum LAI in crops and grasses PFTs to trigger irrigation	m^2/m^2	[0-∞]	0.0, **0.1**, 0.3, 0.5, 1.0

Figure 4.2 shows that β is the parameter with the strongest effect on the global mean irrigation rate, followed by the cumulated root density threshold $Root_{lim}$, I_{max}, and the fraction of stream storage available for adduction $a_{1,add}$. The fraction of water storage left for the ecosystems (called Environmental in the figure, a_j) has a more limited effect, suggesting that in many irrigated areas, there is enough water to fulfill the irrigation requirements. Finally, the LAI limit, LAI_{lim}, to trigger irrigation has a weaker effect than the other parameters. In the case of ET increase (Fig. 4.2), the sensitivity to the different parameters is similarly hierarchized, although the magnitude is not necessarily the same.

For β, we explore in more detail its behavior to set a value. Note that we use the chosen reference values for the other parameters. We compare the irrigation rate estimated by ORCHIDEE in the short tests with the observed irrigation from Sacks et al., 2009 (Fig. 4.3). When comparing the volume at global scale (km^3 for the year 2000, Fig. 4.3-a) we observe

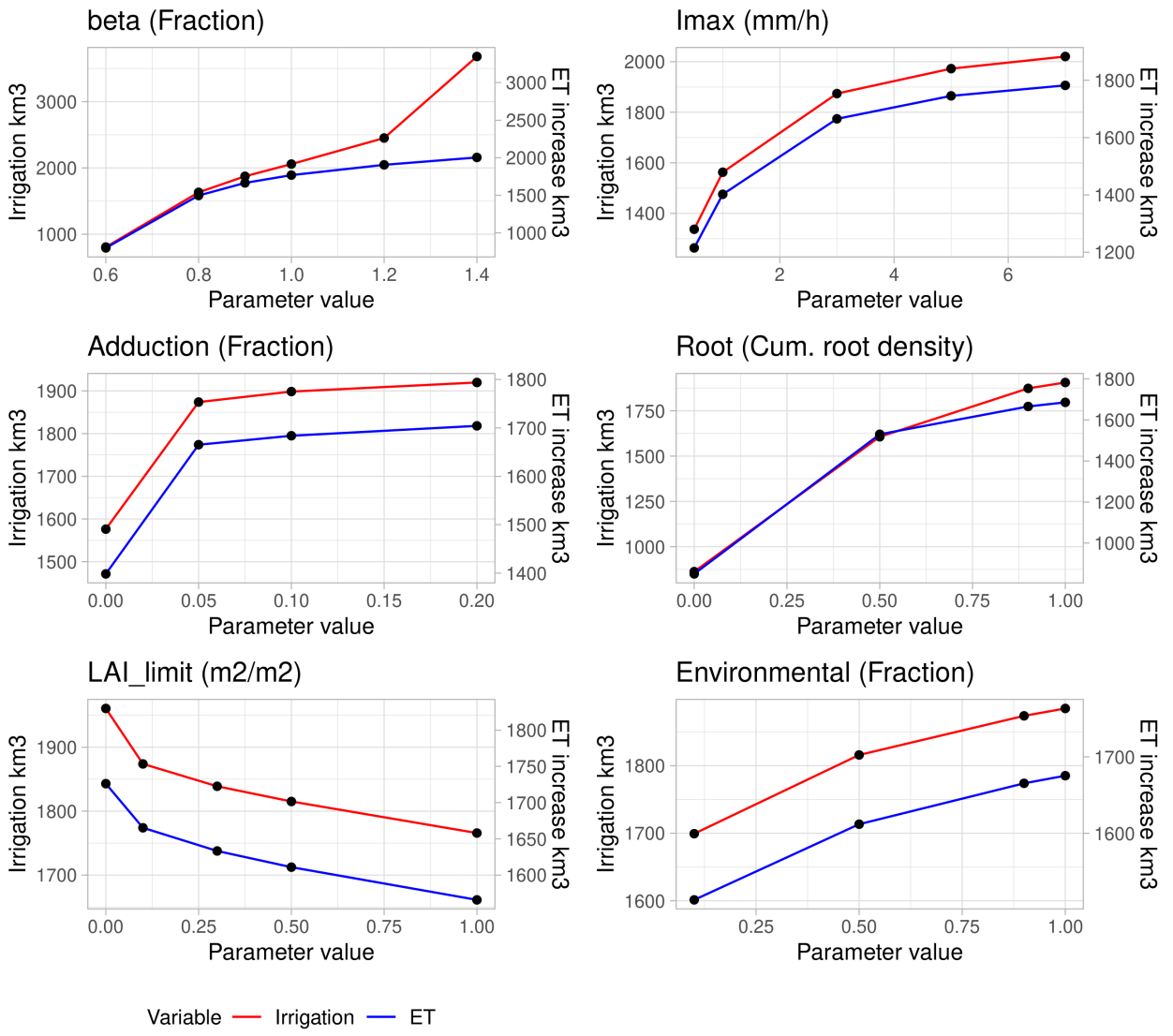

Figure 4.2: Sensitivity of global irrigation volumes and increase of evapotranspiration (km^3) to changes in parameter values, for the year 2000 using short simulations. Secondary y-axis correspond to ET increase values. Note that the y-axis scales differ between parameters.

that a value of 1.2 maximizes the irrigation and minimizes the irrigation bias. When we assess the distribution of bias using grid-cell values (Fig. 4.3-b) we observe that for β equal to 0.8, 0.9, or 1, the bias distribution is centered around 0, while it starts to move to higher values for 1.2 and 1.4.

When we define the β value that minimizes the irrigation bias at a grid-cell scale (Fig. 4.3-c) we observe mostly two classes of area, the first with values of 1.2 and 1.4 (for instance in China and north India) and the second with values of 0.6. The corresponding bias of the β value is used in Fig. 4.3-d to build a composite map of irrigation bias. The resulting bias (called multi in Fig. 4.3-a and b) shows an underestimation of irrigation volume, but a better spatial distribution than the other simulations. These results suggest that the β parameter should have at least two values, 1.4 in areas of China, India and USA, and 0.6 in

the rest of irrigated areas. For simplicity here and as a tradeoff between the underestimation of irrigation volume and the spatial distribution of bias, we choose to set β to 0.9. We use the reference values for the other parameters, as the reference values maximize the irrigation rate.

After this analysis we underline three points. First, this process does not correspond to a proper calibration, as the number of simulations is low and the observed data is sparse. The objective of this process is to identify key parameters and reduce the underestimation of irrigation by tuning the parameter values. Second, although the once-at-a-time method is suitable given the computational cost of running an ORCHIDEE simulation, it also has drawbacks and limitations in its analysis (Song et al., 2015), for instance its qualitative nature, and lack of quantification of individual interaction between parameters. Third, we use the LUHv2 map, which represents the areas actually irrigated, AAI (a lower value than the areas equipped for irrigation, AEI, which is used in other datasets). We do not consider the effect of input data uncertainty in this analysis, but we will asssess the effect of changing input data in long simulations.

4.2.3 Numerical design

4.2.3.1 Simulation set-up

ORCHIDEE is run at global scale in offline mode. We run the model for the period 1970 - 2013, but we leave the first 10 years as warm-up, and we focus our analysis on the period 1980 - 2013. We use the GSWP3 (Hurk et al., 2016) as meteorological forcing (`http://hydro.iis.u-tokyo.ac.jp/GSWP3/`) with a resolution of 0.5 degrees. Here we prescribe the irrigated surfaces in transient mode, i.e. irrigated surfaces may change every year, based on the Historical Irrigation Dataset (HID) from Siebert et al., 2015 and on Land Use Harmonization 2 (LUHv2) dataset. HID presents a map every 10 years before 1980 and every 5 years after at 5 arcmin resolution, and for each year, we use the nearest map in time to avoid data interpolation, LUHv2 presents a map every year with a 0.25 degrees resolution (Hurtt et al., 2020).

The performed simulations use uniform parameters over land, and are summarized in Table 4.2. As a reference, we use a simulation with no irrigation, called NoIrr. The simulation Irr_NoTuned includes irrigation, with the HID maps as input, and a-priori parameter values. This latter simulation does not consider the conclusions from the sensitivity analysis, and for instance does not activate irrigation withdrawal from the overland reservoir and adduction.

We run additional simulations to assess the uncertainty of irrigation rates in the irrigation scheme and assess the influence of the most sensitive parameters, according to the sensitivity analysis. We analyze the effect of the irrigated areas by using another set of input maps, from the LUHv2 dataset. The main difference between the HID and LUHv2 maps is that HID prescribes the area that is equipped for irrigation (AEI), while LUHv2 prescribes the

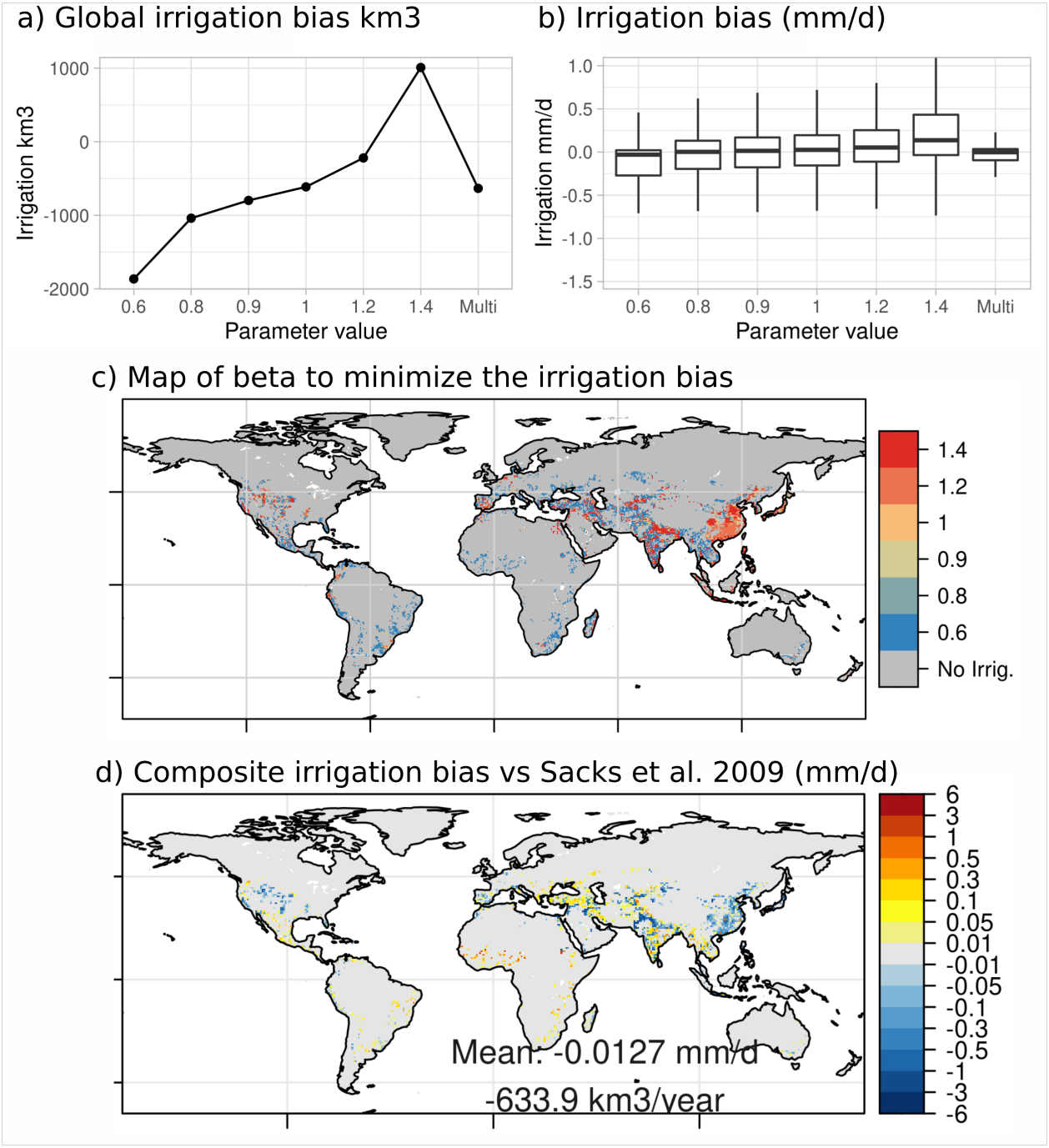

Figure 4.3: Calibration of β value with Sacks et al., 2009 dataset as observed value, using outputs from the short simulations. Calibration of β value using global irrigation volumes in km^3 (a) and boxplot using grid-cell bias in mm/d (b). Map of β to minimize the irrigation bias, according to the short simulations (c) and composite map of irrigation bias according to the calibrated β value in mm/d (d). Multi simulation in a) and b) correspond to the bias of the composite map shown in (d).

area that is actually irrigated (AAI). As a result, the HID dataset has a greater irrigated surface (3.0 $10^6 km^2$ for HID, 2.5 $10^6 km^2$ for LUHv2 at global scale).

The comparison of simulations Irr and Irr_LUH aims at assessing the effect of large

differences in input irrigated areas on irrigation rates. We also assess the impact of the desactivation of adduction in our scheme, and finally, we assess the effects of changes in β (with simulations Irr_NoTuned, Irr, and Irr_Beta) and I_{max} parameter values.

Table 4.2: Simulations with inputs and parameter values. In brackets, the units of the parameter, [-] means that the parameter corresponds to a fraction and does not have a unit. In bold the change in parameter values respecto to the Irr simulation.

Simulation	**Irrigation**	**Irrigated surfaces**	β [-]	a_j [-]	I_{max} **[mm/h]**	**Adduction [-]**
NoIrr	**No**	–	–	–	–	–
Irr_NoTuned	Yes	HID	**1.0**	**0.9,0.0,0.9**	**1.0**	**0.0**
Irr	Yes	HID	0.9	0.9,0.9,0.9	3.0	0.05
Irr_LUH	Yes	**LUHv2**	0.9	0.9,0.9,0.9	3.0	0.05
Irr_NoAdd	Yes	HID	0.9	0.9,0.9,0.9	3.0	**0.0**
Irr_Beta	Yes	HID	**0.75**	0.9,0.9,0.9	3.0	0.05
Irr_Imax	Yes	HID	0.9	0.9,0.9,0.9	**1.0**	0.05

4.2.3.2 Validation datasets and other datasets used on the analysis

The validation of the new irrigation scheme and its effect on the model bias is focused on five variables: evapotranspiration, leaf area index, discharge, irrigation withdrawal and total water storage anomalies. We also use two landscape descriptors datasets to look for correlations between model bias and landscape characteristics.

Evapotranspiration - We use two datasets: the first product is Gleam v3.3a, which combines satellite-observed values of soil moisture, vegetation optical depth, and snow-water equivalent, reanalysis of air temperature and radiation, and a multisource precipitation product (Martens et al., 2017). The second dataset is Fluxcom (Jung et al., 2019), which merges Fluxnet eddy covariance towers with remote sensing and meteorological data using machine learning algorithms. Here we use the RS+METEO products that combines eddy covariance and meteorological information from reanalysis datasets, specifically the averages of RS+METEO WFDEI and RS+METEO CRUNCEP_v8, to cover the analysis period.

Leaf area index - We use the LAI3g dataset (Zhu et al., 2013) climatological values for the period 1983-2015. This dataset uses a neural network algorithm and satellite observations of the Normalized Difference Vegetation Index (NDVI) 3g.

River discharge - We use monthly data from the Global Runoff Data Centre (GRDC, https://www.bafg.de/GRDC-/EN/Home/homepage_node.html) in 14 large basins with strong irrigation activities. We choose the station nearest to the river mouth that also has data available for the study period.

Irrigation water withdrawals - We use two datasets: first, we compare the simulated irrigation rates with values from the FAO-AQUASTAT database (https://www.fao.org/aquastat/en/) reported in Frenken and Gillet, 2012 for irrigation volumes around 2000. AQUASTAT is based on reported values at the country scale, so it does not inform on seasonal values or their spatial distribution. In countries with a lack of information, data is completed using modeling outputs to estimate the plant requirement, especifically GlobWat, and country-level ratios of irrigation efficiency to calculate the irrigation water withdrawal (Hoogeveen et al., 2015). While the plant requirement corresponds to the increase of evapotranspiration, the irrigation water withdrawal is the volume that is abstracted from the natural reservoirs, and includes the losses and return flows.

We also use the information of irrigation water withdrawal around the year 2000 from Sacks et al., 2009. This reconstruction uses national-level census data, primarily from AQUASTAT and state-level information in the US and province-level in China, with maps of croplands by crop type, areas equipped for irrigation, and climatic water deficit. The result is a gridded map with a resolution of 0.5 degrees.

It should be noted that both data sets are subject to errors and uncertainties in their estimation. In the case of reported values, there may be errors or inaccuracies in reporting, while the modeling estimates or reconstruction map depend on the assumptions used. However, in general they provide an order of magnitude of irrigation water use at regional, continental and global scales.

Total water storage anomalies - We compare the total water storage anomalies (TWSA) from our simulations with three different monthly products of TWSA based on GRACE (Gravity Recovery and Climate Experiments) observations based on global mascon solutions, that are suitable for hydrologic applications (Scanlon et al., 2016): CSR (Save et al., 2016), GRC Tellus, called here TELLUS (Watkins et al., 2015) and NASA GSFC (Loomis et al., 2019). CSR has a spatial resolution of 0.25 degree, while TELLUS and NASA GSFC have a resolution of 0.5 degrees. As the differences between products at the large river basin scale are small, we use the average value of both three products. All the products cover the period from april 2002 to the end of the simulation in 2014.

Other landscape descriptors datasets - To perform a comparison with independent landscape descriptors (see below, section 4.2.3.3) we use the fraction of irrigated rice from MIRCA2000 (Portmann et al., 2010) and the Global Reservoir and Dams dataset, GRanD (Lehner et al., 2011).

4.2.3.3 Data processing and analysis

We aggregate and interpolate all the observed data to the 0.5 degrees spatial resolution of the ORCHIDEE simulations. For ET, we mask Gleam and the simulated data according to Fluxcom, which does not cover all the continents, so all the comparisons are made over the same grid cells with available information. For LAI, we exclude grid-cells with no data

in LAI3g from the analysis. We compare grid cell values and zonal average values. The statistical significance of the mean difference between observed and simulated time series is assessed with a Student's t-test at the 5 % significance level.

We use the simulated discharge from the grid cell that best matches the watershed area upstream of the discharge station. In addition, we only use time steps with data available from observations, so that both time series agree. For TWSA, we compare observed and simulated basin averages. As ORCHIDEE gives the total water storage (TWS) value, we normalize the time series with the mean value of the NoIrr simulation for the period 2002-2008, the same as the observed products. In this way, the effect of irrigation over TWS is observed in the time series.

In addition to direct comparison at the grid cell, zonal or basin scale, we performed a factor analysis to reveal relationships between modeling bias and landscape descriptors. We used the fraction of irrigated areas around 2000 from HID, as well as the fraction of irrigated rice from MIRCA2000, both interpolated to the ORCHIDEE resolution. We defined six classes for both factors, following (Mizuochi et al., 2021):

1. Class 1: 0%
2. Class 2: 0 to 5%
3. Class 3: 5 to 10%
4. Class 4: 10 to 20%
5. Class 5: 20 to 50%
6. Class 6: 50 to 100%

We also performed a comparison between basin-scale irrigation bias and the capacity of dams used for irrigation within the basin, according to GRanD.

4.2.4 Results

4.2.4.1 Validation of irrigation water withdrawals

Irrigation from Irr simulation is estimated at 0.049 mm/d (2452.5 $km^3/year$) around the year 2000 (Fig. 4.4-a). This estimation is in the lower part of other studies which range between 2465 and 3755 $km^3/year$ and is lower than AQUASTAT estimation of 2672 $km^3/year$ around the year 2000 (Pokhrel et al., 2016). The results suggest that the proposed scheme is adequate to simulate the reported estimations of irrigation despite the underestimation (-8% than the 2672 $km^3/year$ from FAO around 2000 by Frenken and Gillet, 2012). We note that this estimate is also higher than that of the old irrigation scheme of Guimberteau et al., 2012b, but the scheme proposed here can still benefit from a more robust parameter tuning.

The groundwater irrigation rate in the Irr simulation is 0.0184 mm/d (917.3 km3/year) around the year 2000 (Fig 4.4-b). This estimation is in the medium range of estimation from other studies, which ranges from 570 to 1708 km3/year (Pokhrel et al., 2016). Some of these studies, however, include non-renewable groundwater extraction (e.g., Wada et al.,

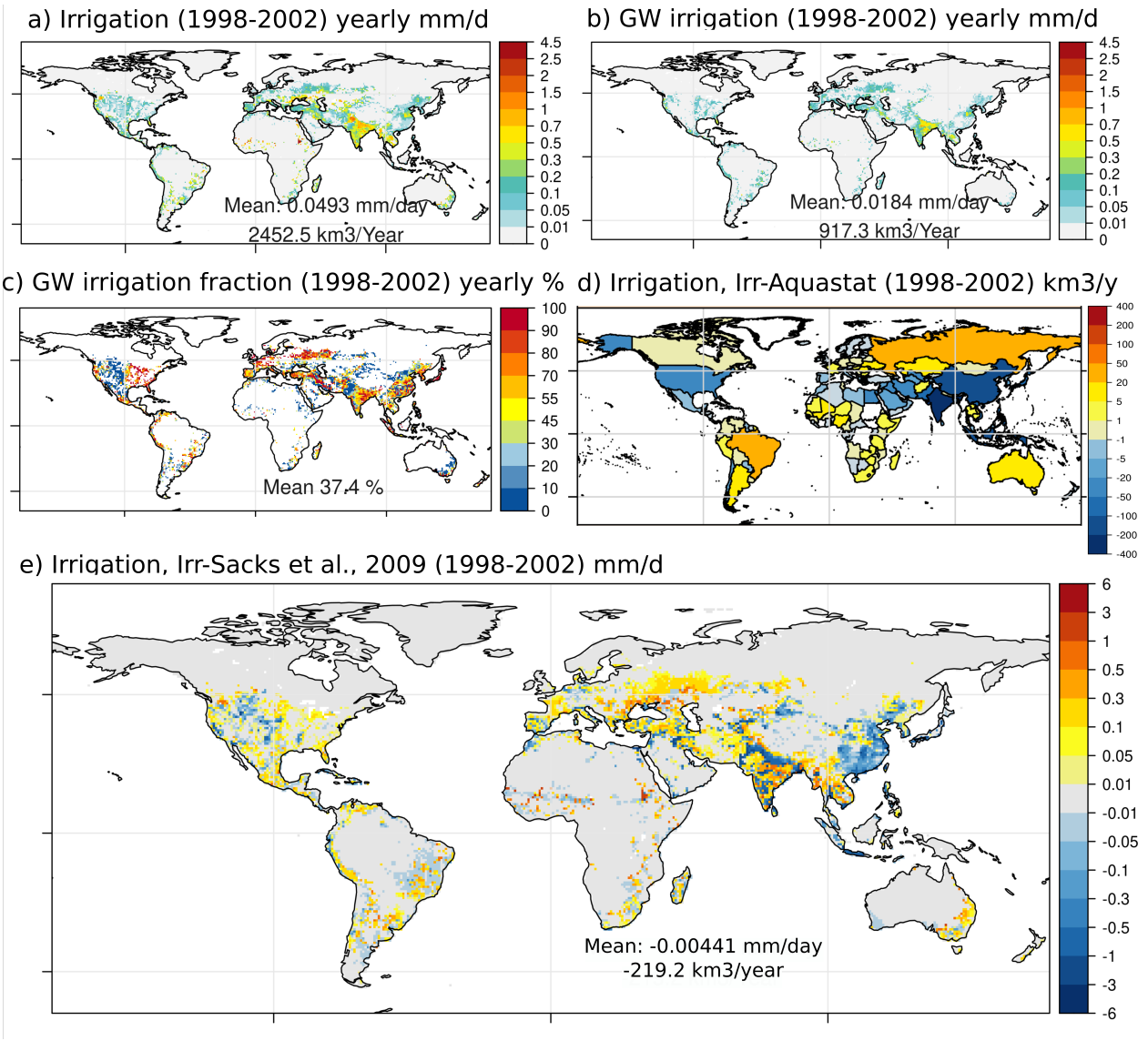

Figure 4.4: Total water withdrawal for irrigation in the Irr simulation, yearly average for 1998-2002 (a), groundwater irrigation withdrawn for irrigation, yearly average for 1998-2002 (b), fraction of groundwater abstraction to the total water withdrawal for irrigation in irr simulation, yearly average for 1998-2002, areas in blank do not have irrigation activities, (c), difference in water withdrawn for irrigation between Irr (yearly average, 1998 - 2002) and AQUASTAT values (Frenken and Gillet, 2012) at country level in km3/year (d), difference in water withdrawn for irrigation between Irr (yearly average, 1998 - 2002) and dataset from Sacks et al., 2009 (e).

2012), which could indicate an overestimation of groundwater extraction in ORCHIDEE. In our scheme irrigation is constrained water offer, whereas for simulations with non-renewable groundwater, the offer does not constrain the irrigation rate. The fraction of groundwater use for irrigation to the total water withdrawal for irrigation (Fig. 4.4-c) is lower in our simulation (37.4%) when compared to the simulation of Döll et al., 2012 (42% of groundwater fraction of total withdrawal), even though both studies use the same map of areas equipped

for irrigation with surface and groundwater from Siebert et al., 2010. The main difference between both experiments (this study and Döll et al., 2012) is that the prescribed map of areas equipped for irrigation by water source, affects the water demand in Döll et al., 2012, whereas it affects the water supply in the ORCHIDEE irrigation scheme. This feature of the ORCHIDEE parameterization also explains regional differences in the groundwater irrigation fraction between the two studies.

At the country-scale, Fig. 4.4-d shows that the irrigation module underestimates water withdrawals in the main hotspots of irrigation, i.e. India, China, and the USA, while the strongest overestimation per m^2 of area equipped for irrigation occurs in Africa (see Figure B.2). Such reduced contrasts between highly and weakly irrigated countries (see Fig. B.1-a) could indicate a limitation of the module to represent local irrigation strategies, as our scheme uses uniform values for all the parameters. Comparison with the estimation from Sacks et al., 2009 support this result (-0.004 mm/d, -219.2 km3/y, Fig. 4.4-e) and allows us to identify the areas where the irrigation bias is the strongest. In India, the Indus basin presents a strong underestimation, as well as in the Northern part of the Ganges-Brahmaputra basin. In China, there is a more widespread underestimation. That is also the case in the west part of the US Great Plains. The other regions present in general an overestimation of irrigation withdrawals, which is especially important in some small areas in Africa, in Eastern Europe and north to the Caspian sea, and in some areas of central Asia (see original data from Sacks et al., 2009 in Fig. B.1-b).

4.2.4.2 Variability of the irrigation rates due to parameter values and input data

The global annual irrigation volumes (Fig. 4.5-a) show a large uncertainty across the simulations due to changes in the parameter values (for instance, -24.7% between Irr_NoTunned and Irr). The parameter set used in the Irr simulation manages to increase the irrigation rate and to markedly reduce the irrigation bias when compared to the Irr_NoTuned simulation. Also, a positive trend in the annual irrigation volume is observed in all simulations. It is caused by the increase in irrigated area, observed in both HID and LUHv2 datasets (see simulations Irr and Irr_LUH). The irrigated area has been identified by Puy et al., 2021 as the main driver of irrigation water withdrawal, and the increase of the prescribed irrigated area in the simulations explains in part the positive trend in the irrigation rate. The other part of the positive trend could be explained by the differences in the parameter values (for instance simulations Irr and Irr_beta).

Based on the mean annual values (Fig. 4.5-c), the β parameter has the largest effect on the mean irrigation rate (-22.3% when β decreases from 0.9 to 0.75), followed by the change of input map from HID to LUHv2 (-19.7%), a lower I_{max} (-16.5%) and, finally, no adduction (-15.7%). From a spatial point of view, the overall reduction in irrigation due to the above changes is not homogeneous and large areas may even display an increased irrigation rate.

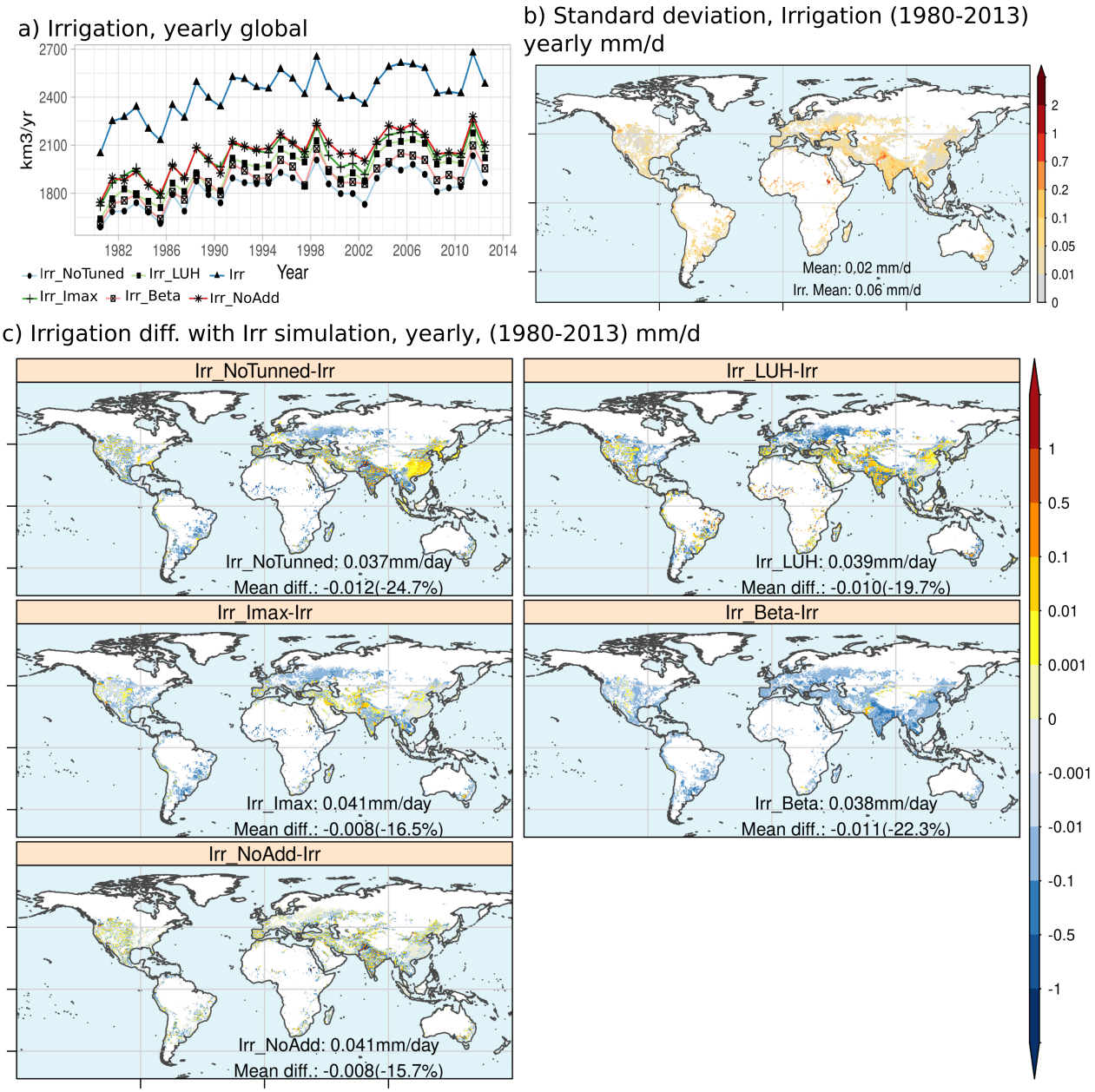

Figure 4.5: Time series of globally averaged irrigation rates simulated by ORCHIDEE (a). Map of the standard deviation of mean irrigation rates from all simulations in mm/d (b). Maps of mean difference between Irr simulation and others, for the period 1980 - 2013 in mm/d (c). Blank areas correspond to grid-cells with no irrigated areas

The exception is the β parameter, which shows an overall reduction in irrigation with a lower parameter value, except in the Indus basin. The Indus river basin is a region that depends on both surface and groundwater for irrigation, and the irrigation demand is one of the most important worldwide (Laghari et al., 2012). In Irr_Beta, a lower β induces a reduction of water demand in the upper areas of the Indus river basin, increasing the river discharge downstream. More surface water supply in the middle and lower parts of the basin can increase irrigation in these areas, even if the water demand also decreases, because the

irrigation deficit i.e. the difference between demand and supply, is still high despite the demand reduction. We advance here that the propagation of water supply through the river system can explain part of the heterogeneity in the response to parameter changes.

The standard deviation of the pluri-annual mean irrigation across all the simulations with irrigation from table 4.2 (Fig. 4.5-b) highlights the areas where the model's estimations are the most variable. We identify the Indus river basin, as well as irrigated areas near the upper and lower Nile rivers, and areas near the Black sea. Other areas with strong irrigation activities like China do not show a high standard deviation, which illustrates a less important variability of the estimation from the ORCHIDEE model. But we note that the coefficient of variation, the ratio of the standard deviation and mean (see Fig. B.2), is in fact much more homogenous. So far, we cannot explain the differences in the spatial distribution of the standard deviation and of the coefficient of variation, but we advance that is probably due to the use of global parameter values.

4.2.4.3 Effect of irrigation on water and energy balance

The activation of irrigation from NoIrr to Irr induces an increase of ET in the irrigated areas, as expected (Fig. 4.6-a). The increase is small on an annual global scale (0.04 mm/d) but is stronger on average in the irrigated areas (0.2 mm/d, +38%). In some areas in Pakistan and India, ET increases by more than 1 mm/d. The increase of ET (or consumptive use) corresponds to 2094 km^3/yr at the global scale, which is higher than the other estimations, ranging between 1098 and 1598 km3/year around the year 2000 (Pokhrel et al., 2016). This overestimation in ET increase is explained in part by an increase of bare soil evaporation that is slightly larger than the increase of the crop transpiration (Fig. B.3-a and Fig. B.3-b respectively). The similar increase of both subfluxes suggests that the ET increase may be overestimated by the model, as a large part is supported by bare soil E, while in reality, the irrigation management tries to reduce this non-beneficial flux. Changes in ET also induces changes in other energy variables, as well as in surface temperatures (see Fig. B.3).

Irrigation also induces an increase in soil moisture (Fig. 4.6-b) but the effect is much weaker than for ET, even in irrigated areas (7.6 mm, +2%). For total runoff and drainage, the increase is small (Fig. 4.6-c and Fig. 4.6-d) and focused on some areas in Egypt and East Europe. It indicates that irrigation inside ORCHIDEE does not induce a stronger recharge as reported by Döll et al., 2012. Besides, irrigation depletes part of the groundwater reservoir as a result of water abstractions, especially in the Caucasus and India (Fig. 4.6-e). The river reservoir is also depleted (Fig. 4.6-f), and in this case, the routing scheme propagates downstream the depletion induced by irrigation, for example in India (Ganges and Indus rivers) and in the Nile river.

The TWS integrates all these changes in a single value (Fig. 4.6-g). In areas with intensive surface water use (Indus river in India, or Upper Nile river in Africa, Fig. 4.4), the TWS increases as a result of water transfer from the river to the soil surface, except in grid cells

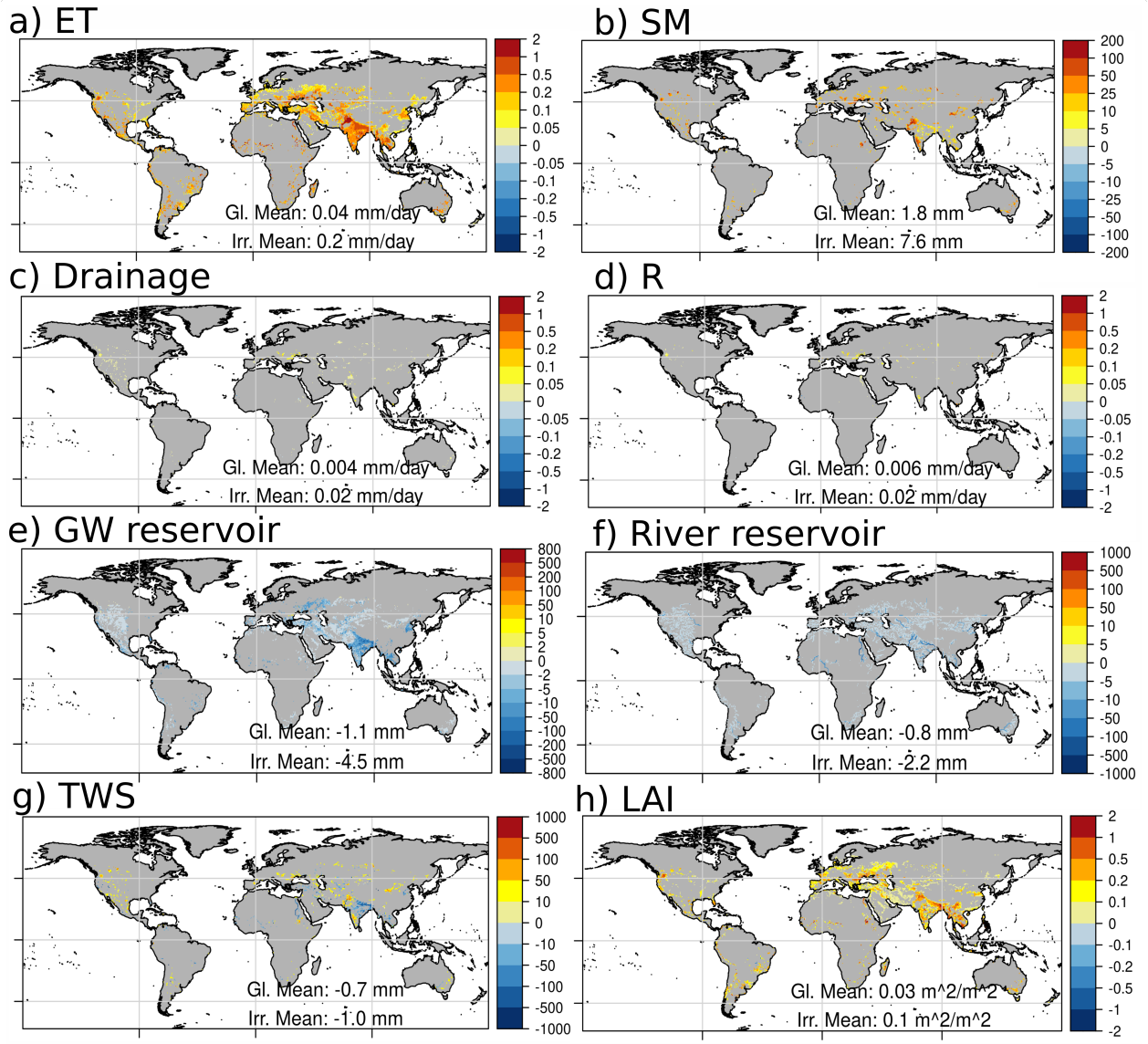

Figure 4.6: Yearly average difference for 1980 - 2013 between Irr and NoIrr of ET, mm/d (a), SM, mm (b), drainage, mm/d (c), total runoff, mm/d (d), groundwater reservoir, mm (e), river reservoir, mm (f), TWS, mm (g), and LAI, m/m (h). Statistical significance of the mean differences is tested at each point with a Student's test (p = 0.05). The areas with insignificant changes are left gray.

that drain an important upstream area, where the value decreases. In areas with intensive groundwater use (Ganges river basin in India, Eastern USA, Fig. 4.4), the TWS decreases with irrigation, or the change induced by irrigation is not statistically significant. Changes in water pathways and related residence times likely account for changes in TWS, due to shifts of some irrigation water from surface water to groundwater via soil moisture, or from groundwater to surface water (Graaf et al., 2014). It should be noted that, in our simulations, the mean residence time of soil moisture in irrigated areas goes from 267 days for NoIrr to 245 days for Irr. The decrease of the residence time when irrigation is enabled is linked to the rapid water transfer to the soil surface, and evapotranspiration increase. It is worth noting

that despite the change in mean residence time of soil moisture, the two values are higher than the mean residence time of river flows (a few days) and lower than that of groundwater (several months or even years) (Schneider, 2017). Finally, coherent with the increase in ET, and due to the reduction of water stress and increase of photosynthesis activity, we observe an increase in LAI in irrigated areas (Fig. 4.6-h).

4.2.4.4 Seasonal dynamics of water resources at a large river basin scale.

The seasonality of irrigation, and the moment the scheme trigger the irrigation, are also important to understand the effects of irrigation on hydrology variables. Monthly average values in four large basins (see considered large basins in Fig. B.5) with different climates and heavy irrigation activities (Fig. 4.7) show differences in the simulation of irrigation rates and in the effects on ET and LAI .

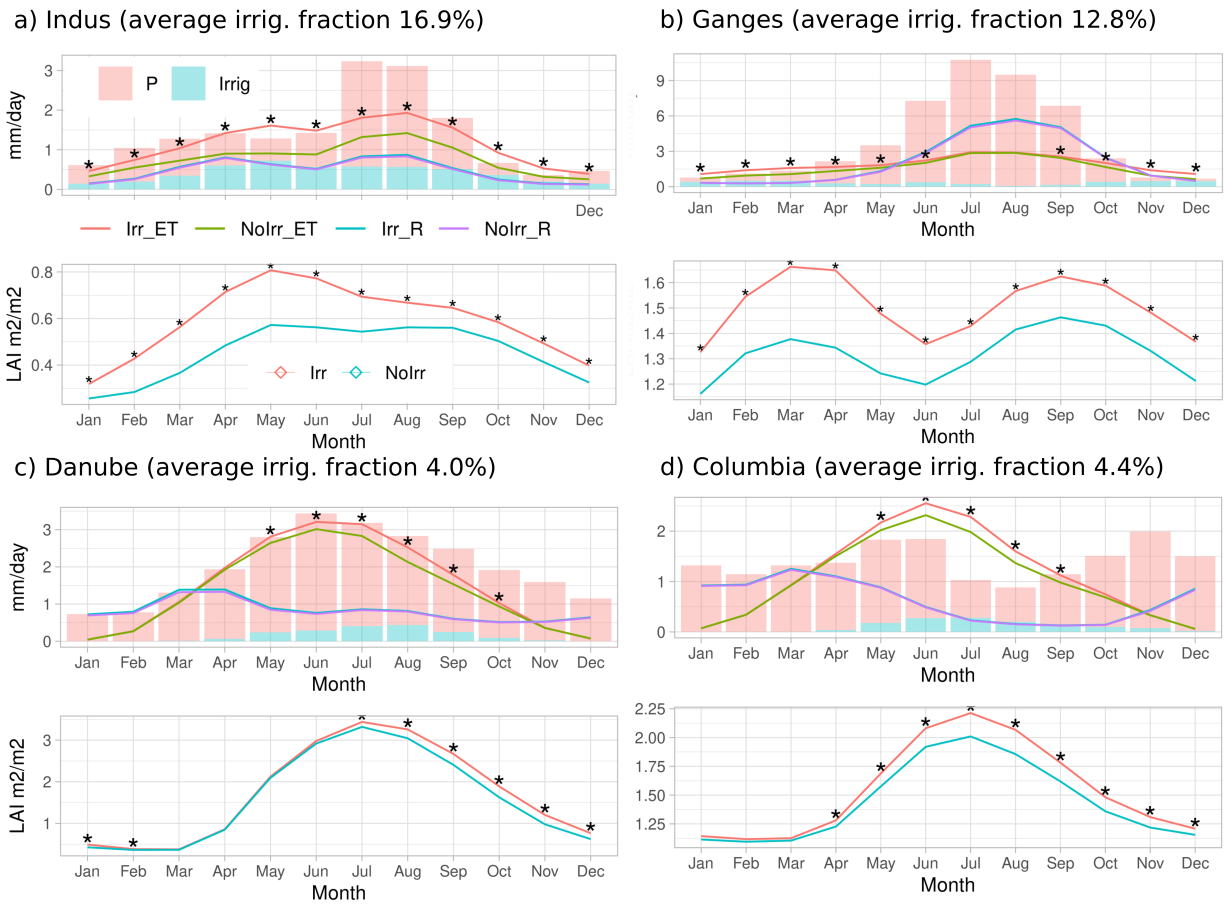

Figure 4.7: Average multiyear monthly values for period 1980-2013 at basin scale for Indus (a), Ganges (b), Danube (c), Columbia (d). The first row presents ET, R, P and irrigation values (mm/d), second row presents the mean LAI values (m2/m2), for both Irr and NoIrr simulations. Statistical significance of the modulation was tested with a t-student test (p = 0.05), and significant differences are shown by a * over the values from the Irr simulation.

The Ganges and Indus basins are located south of the Himalayan range (Fig. 4.7-a and

Fig. 4.7-b respectively). Both river basins have the highest irrigated fraction compared to the basin area (16.9% for the Indus on average for 1980-2013, 12.8% for the Ganges). But the Ganges basin has a higher rainfall rate than the Indus, although in both cases rainfall is strongly seasonal due to the monsoon. A larger irrigated surface and a higher water stress explains a larger irrigation rate in the Indus compared to the Ganges (also differences in water sources, see B.7). Moreover, while the peak irrigation period in the Indus basin runs from April to September, it starts in October and runs through April in the Ganges basin. Interestingly enough, and probably due to the size of both basins, irrigation rate is never zero, which does not seem realistic. In any case, it is worth to note that the Indus river basin has a rice-wheat system (Laghari et al., 2012), where rice is grown during the kharif (wet, summer) and wheat is grown during the rabi (dry, winter). Thus there are at least two irrigation periods along the year. This could indicate that the scheme partially captures the seasonality of the irrigation in the Indus basin, but we cannot support this hypothesis so far. Comparison of the simulation outputs with seasonal data reported within the basin could corroborate this hypothesis.

These differences in the irrigation seasonality affect differently the evapotranspiration. While in the Ganges, the increase in ET between the NoIrr and Irr simulation occurs from September to June, in the Indus the increase in ET is observed during all months of the year, but is more important between April and September. The increase in LAI is also visible in both basins when comparing NoIrr and Irr simulations. In the Indus basin, we observe a shift in the LAI peak in May, but irrigation increases LAI during all the months of the year. In the Ganges basin, in contrast, the activation of irrigation does not shift the LAI dynamics, but the increase in LAI is also observed during all the months. In both basins the LAI is higher even when the irrigation rate is at its lower.

On the other hand, we observe a different pattern in two temperate basins, the Columbia river basin in North America (4.4% of the basin area is irrigated on average for 1980-2013), and the Danube river basin in Europe (4% of the area basin is irrigated on average for 1980-2013) in Fig. 4.7-c and Fig. 4.7-d respectively. In both basins irrigation occurs from April to November, but is reduced to zero during winter. Consequently, ET is higher in the Irr simulation between May and September in the Danube and Columbia river basins. As for the LAI increase in the Irr simulation, it occurs from July to February in the Danube basin, and from April to December in the Columbia basin. Moreover, the increase in LAI is also delayed with respect to the irrigation peak and the increase in ET in both basins. Differences in LAI timing are probably related to differences in the distribution of PFTs. The results in temperate basins seem consistent with the main hypotheses of the scheme, i.e. that irrigation is not active during the boreal winter and is concentrated during the warmer months.

4.2.4.5 Factor analysis: correlation of modeling biases and landscape descriptors classes

Figure 4.8-a shows the bias of ET by class of irrigated fraction at grid-cell scale, when we compare ORCHIDEE simulations with Fluxcom dataset. It shows that the activation of irrigation reduces the ET bias in those areas with high irrigation fractions. For the comparison with Gleam in Figure 4.8-b, it shows that the activation of irrigation induces a positive bias in those areas with irrigation. When comparing absolute ET values by irrigation class (Fig. 4.8-c), we observe that NoIrr and Gleam are similar in all the classes except for 0 and All, i.e. no irrigated fraction and all grid cells. It means that the differences between NoIrr and Gleam comes from non-irrigated areas. This could suggest a limitation in Gleam to represent the effects of irrigation on ET rates as this product does not display an increase of ET in irrigated areas compared to non-irrigated ones. On the other hand, Irr and Fluxcom boxplots are similar for classes 10-20, 20-50, and 50-100. Thus, Fluxcom could be prioritized to assess the effect of irrigation on ET.

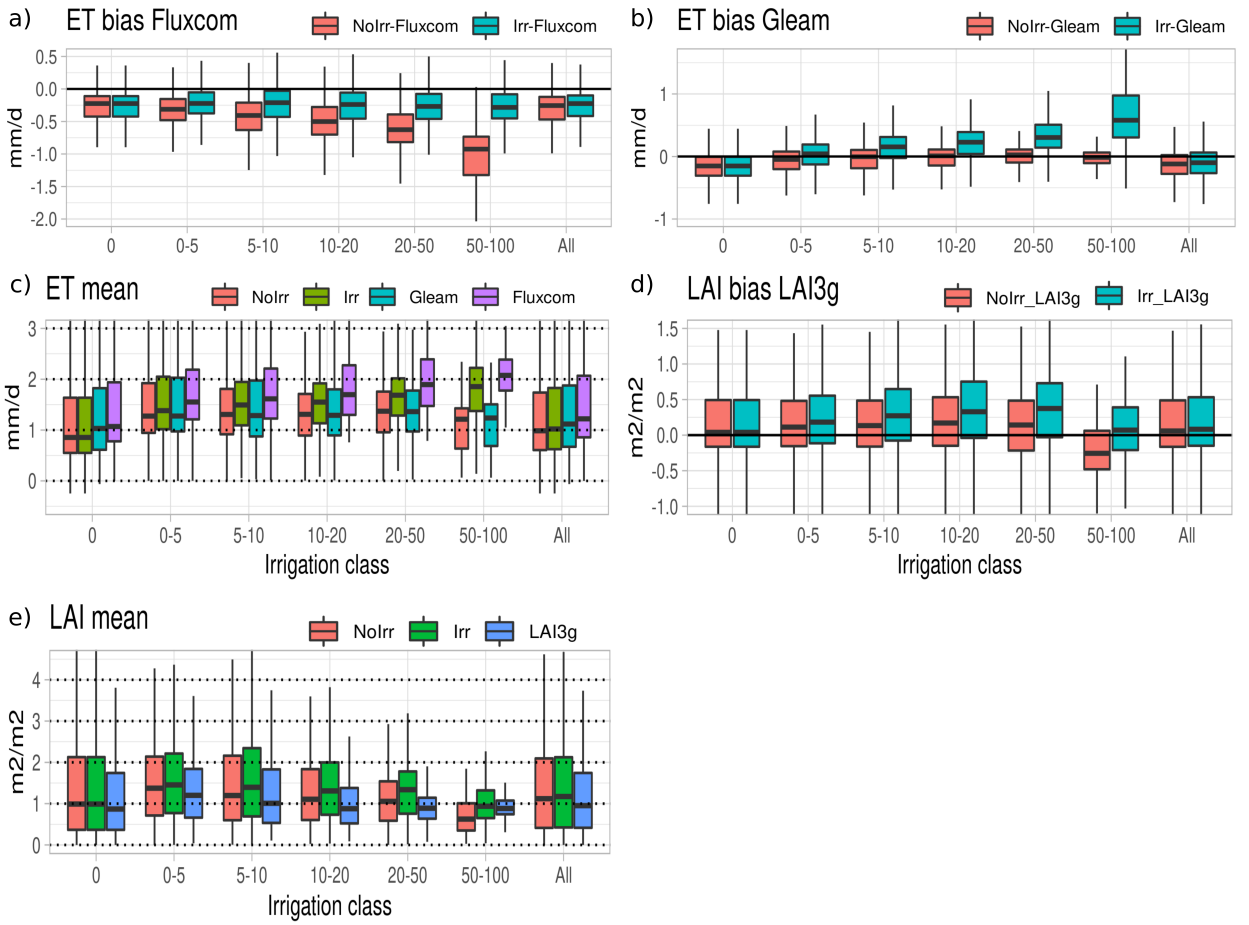

Figure 4.8: Factor analysis of ET bias with Fluxcom against irrigated fraction classes (a), and with Gleam (b). Mean ET values of simulations and observed products against irrigated fraction classes (c). LAI bais with LAI3g against irrigated fraction classes (d) and mean LAI values of simulations and observed product against irrigated fraction classes (e).

A similar analysis for the LAI bias and classes of irrigated fraction (Fig 4.8-d) shows an increase in the LAI difference between ORCHIDEE and LAI3g in the Irr simulation. Also, for all clases, the positive bias in the NoIrr simulation is exacerbated in the Irr simulation, except for the most intensively class (class 50-100), which reduces the negative bias when comparing NoIrr and Irr simulations. It is worth noting that the class 50-100, where irrigation is more important, is the single one with a negative bias in NoIrr, and this negative bias is partially reduced when irrigation activities. This is due to less water stress and thus more photosynthesis and biomass production, which is coherent with the decrease of ET bias for this class. When comparing absolute values between the simulations and the observed product (Fig. 4.8-e), we also observe that the boxplot spread of the boxplot is smaller for LAI3g than for the simulations, and that the spread is lower for classes with small irrigated fraction than for intensively irrigated classes. Activation of irrigation within ORCHIDEE does not significantly change the boxplot spread for any class.

For the irrigation bias, classes with a high fraction of irrigated paddy rice, (for instance class 20-50 or 50-100), exhibit a higher bias than classes with small fractions (Fig 4.9-a). The spatial distribution of irrigated paddy rice is concentrated in southeast Asia, within the most irrigated basins worldwide (see Fig. B.6). The ratio of irrigated fraction and the crop and grasses soil column fraction, exhibits the same behavior (Fig.Fig 4.9-b). The use of classes of irrigated fraction shows the same behavior as well (Fig 4.9-c). At the large basin scale (see values in Table B.2)), the irrigation bias also correlates well with the capacity of dams used for irrigation (Fig. 4.9-d) if we retire a single outlier corresponding to the Nile river basin (r value without the outlier is -0.55).

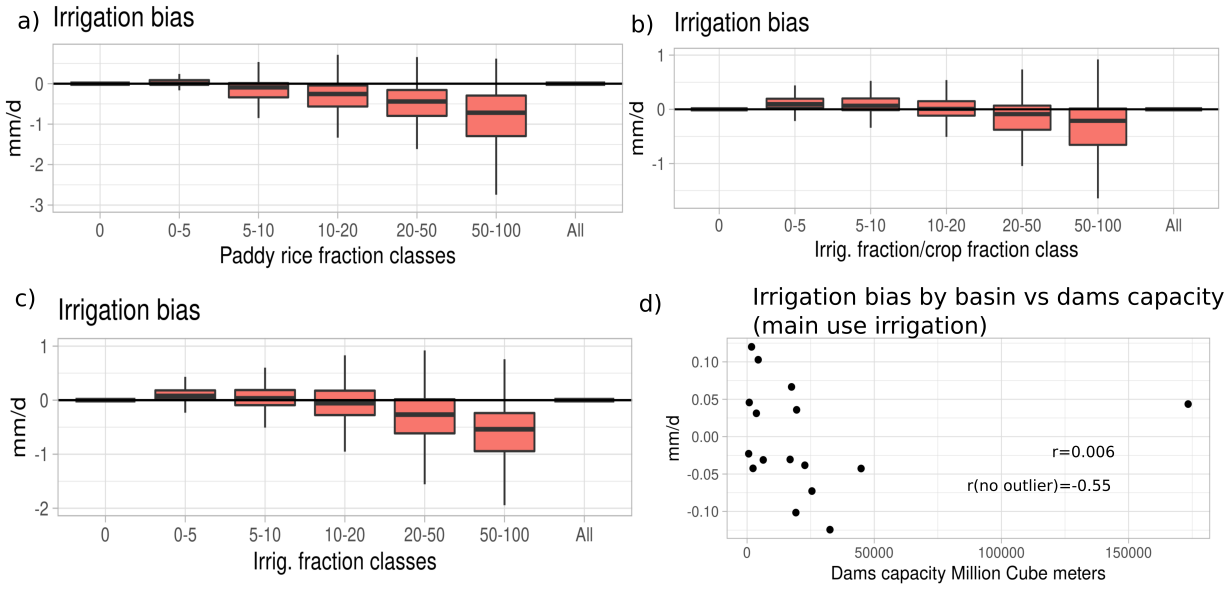

Figure 4.9: Factor analysis of irrigation rate bias with data from Sacks et al., 2009, against irrigated paddy rice classes (a), irrigated fraction of the soil column (b) and irrigated fraction of the grid cell (c). Basin average value of irrigation bias against dams capacity (d).

4.2.4.6 Spatial distribution of ET and LAI bias

The NoIrr simulation has a negative bias when we compare this simulation with both Fluxcom and Gleam datasets (Fig. 4.10-a and Fig. 4.10-b). In addition, the activation of irrigation in Irr does not correct this bias when compared with Fluxcom, and leads to overestimation when compared to Gleam. At the regional scale, conclusions concerning the effect of irrigation activation on ET bias depend on the observed product. For instance, in India, if we compare NoIrr and Irr with Fluxcom, the bias passes from negative to non-significant according to the statistical test in some areas, but when we compare the ORCHIDEE simulations with Gleam, the bias passes from non-significant to positive. In Southern China, there is an underestimation of ET for both simulations and for both products.

The average zonal values at yearly, boreal winter, and boreal summer periods in the irrigated areas (Fig. 4.10-c) confirm that both simulations NoIrr and Irr underestimate ET when compared to the observed products, with local exceptions. The underestimation is more important for FLUXCOM than for GLEAM. On the other hand, the activation of irrigation reduces the ET bias for Fluxcom (lead to overestination for Gleam). Seasonal effects do not change this general pattern, but the extension and localization of the bias reduction.

In the case of LAI, we observe that the NoIrr simulation has a positive bias when we compare it to the LAI3g dataset (Fig. 4.11-a) and that this positive bias increases in the Irr simulation, because irrigation enhances transpiration, thus photosynthesis and biomass production. In some areas of India, like the Indus river basin, the activation of irrigation may reduce a negative bias, but in general, the positive bias increases, for example in China.

The mean zonal values (Fig. 4.11-b) show that the LAI increase is mostly found in the northern hemisphere and in a small part of the southern hemisphere, roughly following the increase in ET. Seasonally, increases of LAI also are mostly found in the northern hemisphere. For example, in the boreal winter, just small latitudes in the southern hemisphere shows a statistically detected change due to activation of irrigation. This is probably led by the zonal distribution of irrigated areas, mostly concentrated in the northern hemisphere. Other factors like PFT distribution and local climate could also influence the small effect of irrigation on LAI in the southern hemisphere.

4.2.4.7 Effect of irrigation on TWSA and river discharge

We now focus on the average TWSA value at the basin scale (Fig. 4.12). Activation of irrigation induces small changes in TWSA, which is coherent with changes in TWS between both simulations (Fig. 4.6-e). For instance, we observe higher peaks and low values in Huang He when irrigation is activated, while in the Ganges and in river basin, low values are lower in the Irr simulation. The changes in water pathways and related residence times that explains changes in TWS between Irr and NoIrr (section 4.2.4.3), also could explain these changes in TWSA dynamics at large basin scale. Other basins, like the Nile river basin or the Amu-Darya, show little effect between both simulations.

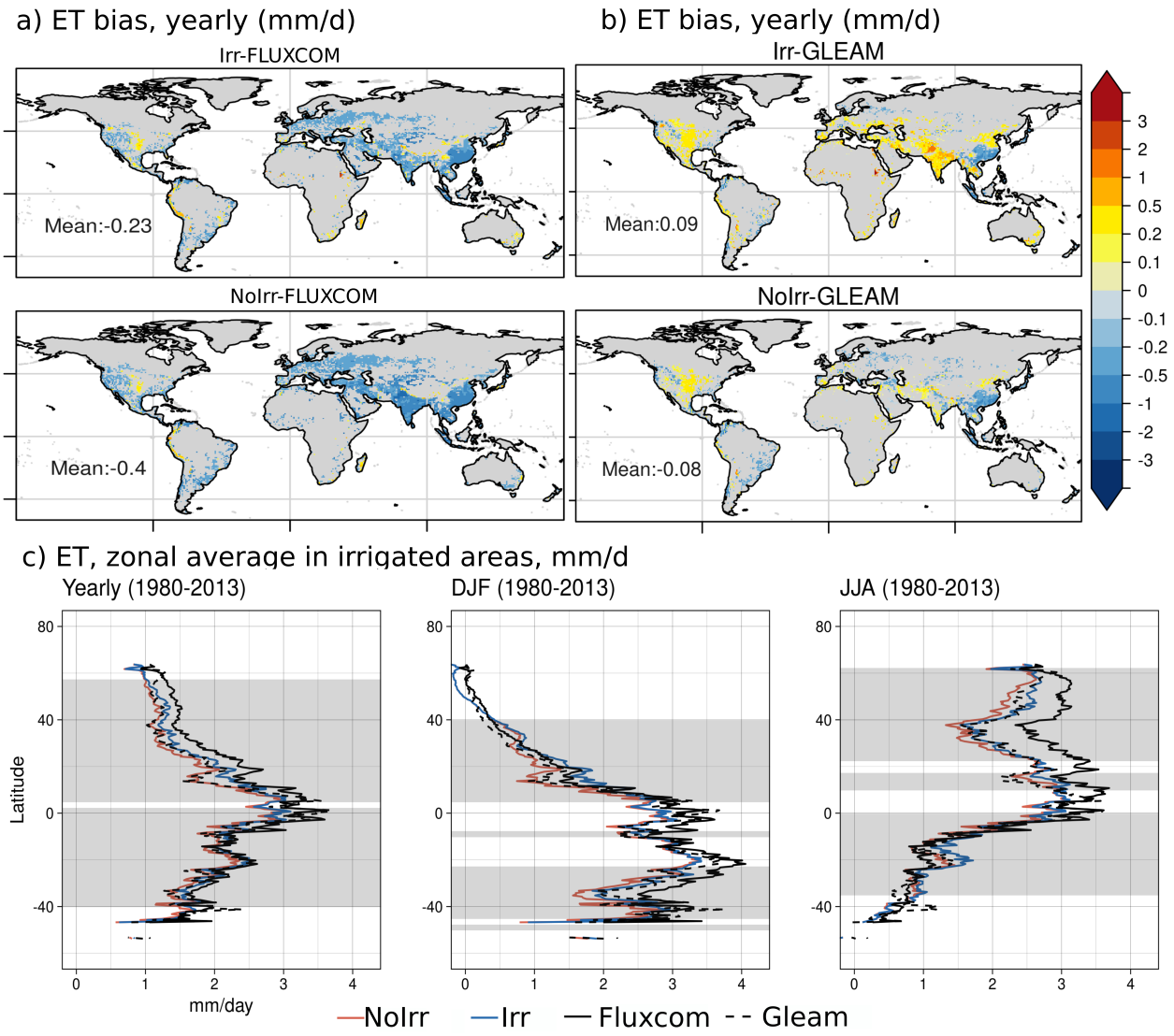

Figure 4.10: Difference of yearly average values for 1980 - 2013 between NoIrr and Irr simulations, and Fluxcom (a) and for NoIrr and Irr simulations, and Gleam (b) for ET in mm/d. Statistical significance of the mean differences is tested at each point with a Student's test (p = 0.05). The areas with insignificant changes or no irrigated fraction are left gray. Zonal average values of areas with irrigated fractions for yearly, boreal summer (JJA) and boreal winter (DJF) of ET for period 1980 - 2013 (c) in mm/d. Gray areas for zonal average values depict the latitudes with significant differences between Irr and NoIrr simulation, according to the Student t-test (p = 0.05).

On the other hand, ORCHIDEE does not capture the trends that are shown by GRACE data, even when irrigation is activated, for instance in Huang He, Colorado and Indus river basin. There are probably multiple causes for this limitation in ORCHIDEE simulations compared to GRACE: first, an underestimation of irrigation rates, which is coherent with the biases shown in Fig. 4.4 at country-level and grid-cell scale. Second, and related to the first cause, the lack of fossil groundwater abstraction in ORCHIDEE. As the irrigation scheme represents abstractions from shallow aquifers but not from fossil sources, the model

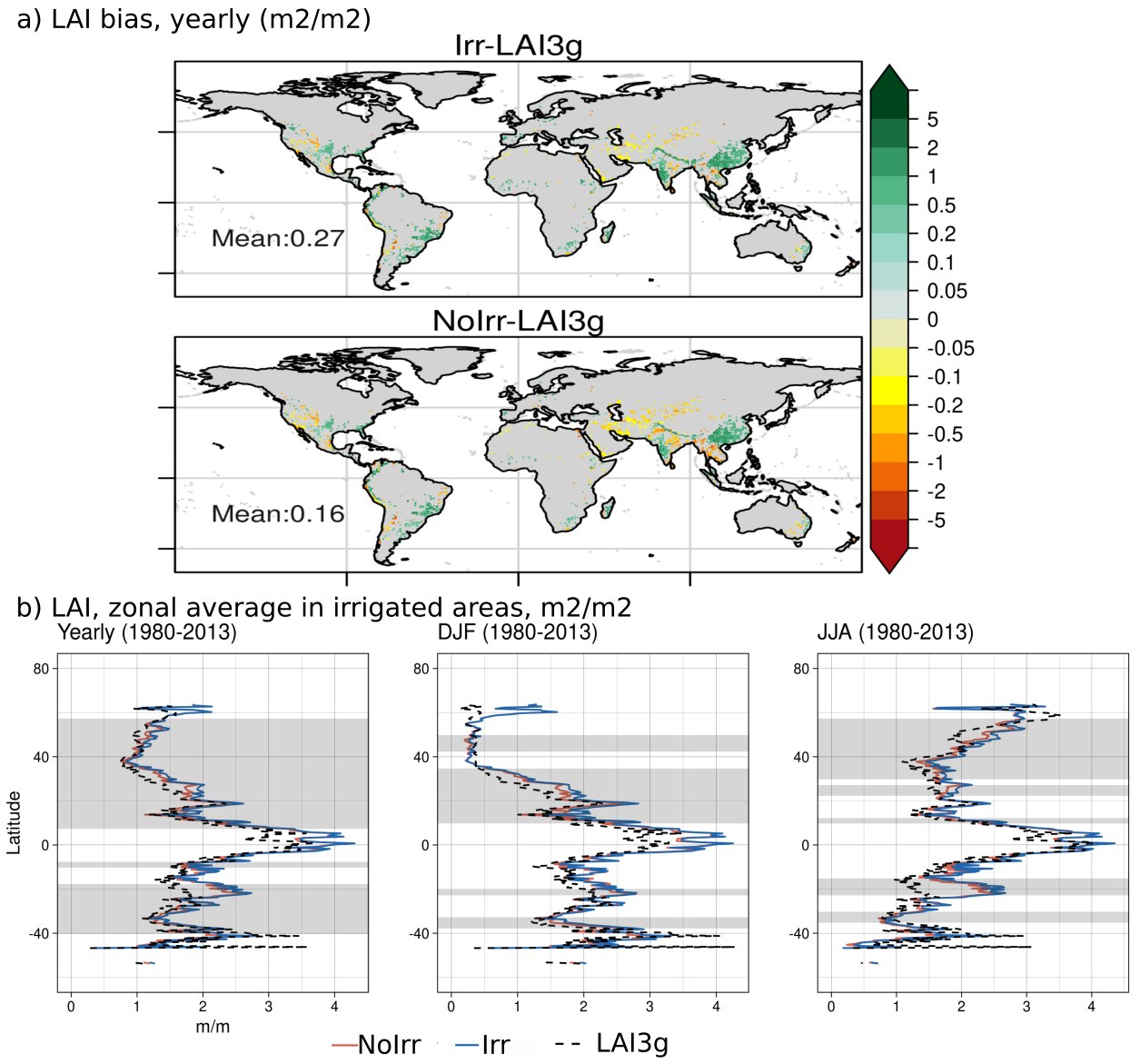

Figure 4.11: Difference of yearly average values for 1980 - 2013 between NoIrr and Irr simulations, and LAI3g (a) for LAI in m^2/m^2. Statistical significance of the mean differences is tested at each point with a Student's test (p = 0.05). The areas with insignificant changes or no irrigated fraction are left gray. Zonal average values of areas with irrigated fractions for yearly, boreal summer (JJA) and boreal winter (DJF) of LAI for period 1980 - 2013 (b) in m^2/m^2. Gray areas for zonal average values depict the latitudes with significant differences between Irr and NoIrr simulation, according to the t-student test (p = 0.05).

could restrain irrigation due to a supply shortage, thus could have problems fitting the negative trend in those areas with heavy groundwater use, as already reported by Yin et al., 2020 for China. Third, glacier loss misrepresentation in ORCHIDEE could explain part of the differences to observed negative trends in some basins, for instance in the Indus and Ganges basins, that depend on water flow from the Himalaya mountains (Rodell et al., 2018). Four, problems to estimate the water partitioning between water fluxes and water

stock in ORCHIDEE. This could explain part of the problems in both simulations to fit the positive TWSA from GRACE in the Murray river basin between 2010 and 2014, for instance, or the high peak in both simulations during 2007 in the Nile, higher than the value from GRACE. So far, we cannot explain to which extent each one of these causes participate in the misrepresentation of GRACE TWSA trends within ORCHIDEE.

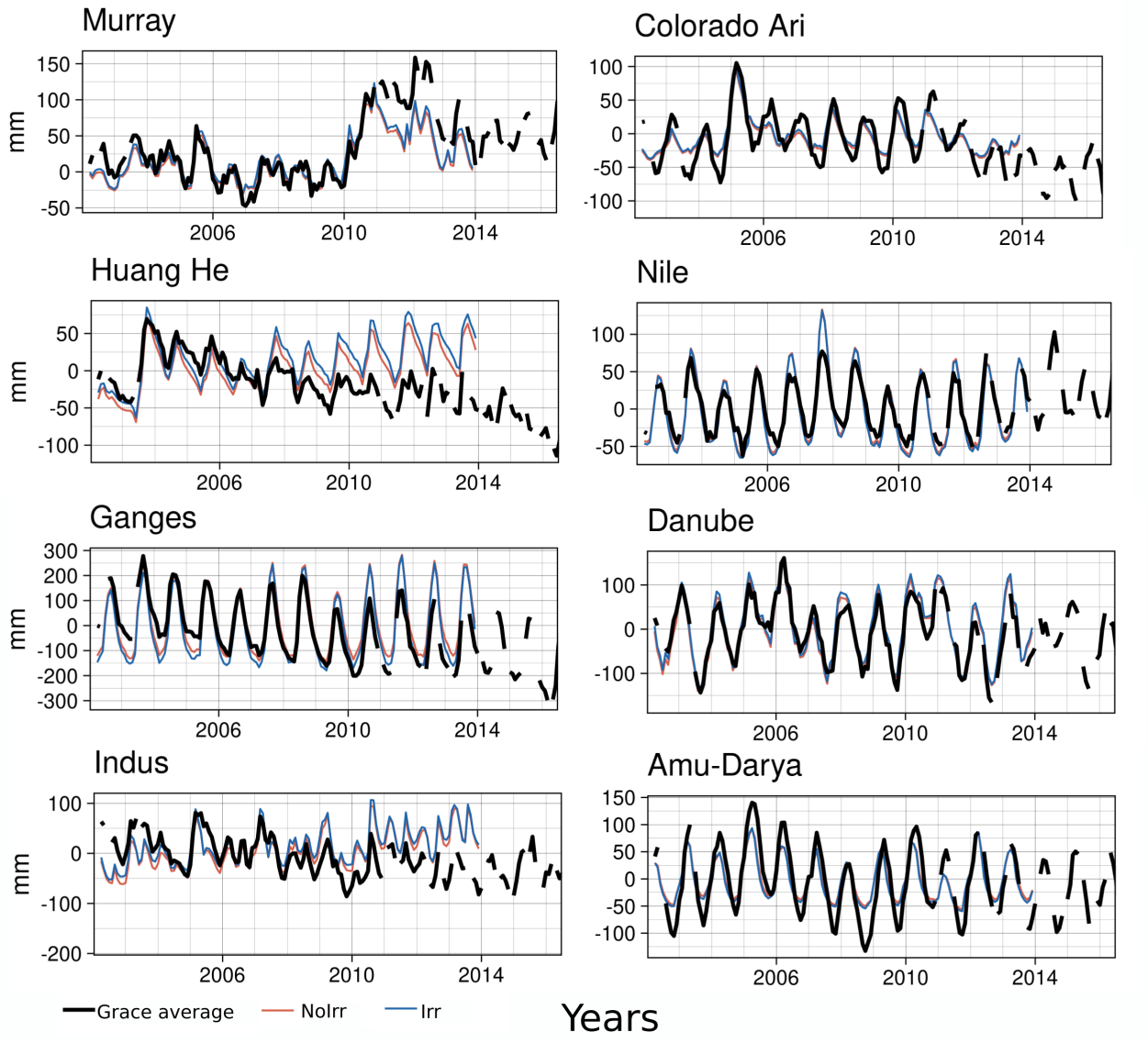

Figure 4.12: Comparison of TWSA between ORCHIDEE simulations and GRACE datasets in large basins with strong irrigation activities.

The correct simulation of river discharge (discharge stations used here in Fig. B.5) is another challenge in ORCHIDEE and other LSMs (Oki et al., 1999; Ducharne et al., 2003; Guimberteau et al., 2012a; Koirala et al., 2014; Cheruy et al., 2020) (Fig. 4.13). Irrigation plays an important role to reduce the average values when we compare NoIrr and Irr simulations (see for example the Nile, or the Indus rivers, these results are coherent with those from Graaf et al., 2014, metrics as annex in Table B.1). The main effect of irrigation over the seasonal variations is that peak discharge can occurs before in the Irr simulation, or that

decrease after the peak is more rapid and low values are lower in Irr than in NoIrr. These changes are due to triggering of irrigation during spring and summer, and the corresponding ET increase. This decrease runoff and depletes the river reservoir. It is worth noting that the Irr simulation does not necessarily reduce the discharge bias against GRCD data compared to the NoIrr simulation, with the exception of the Danube river. Multiple causes could explain the incorrect simulation of discharge dynamics in ORCHIDEE, even when irrigation is activated. For instance a wrong ET estimation, poor representation of snow dynamics, and the lack of representation of permafrost effect on discharge dynamics could explain part of these mismatches (Cheruy et al., 2020). Also, a lack of representation of other anthropogenic processes like dam management, and water withdrawal for other economic sectors and other uses could explain the differences in seasonal discharge dynamics between ORCHIDEE and observed data in some basins (Pokhrel et al., 2016).

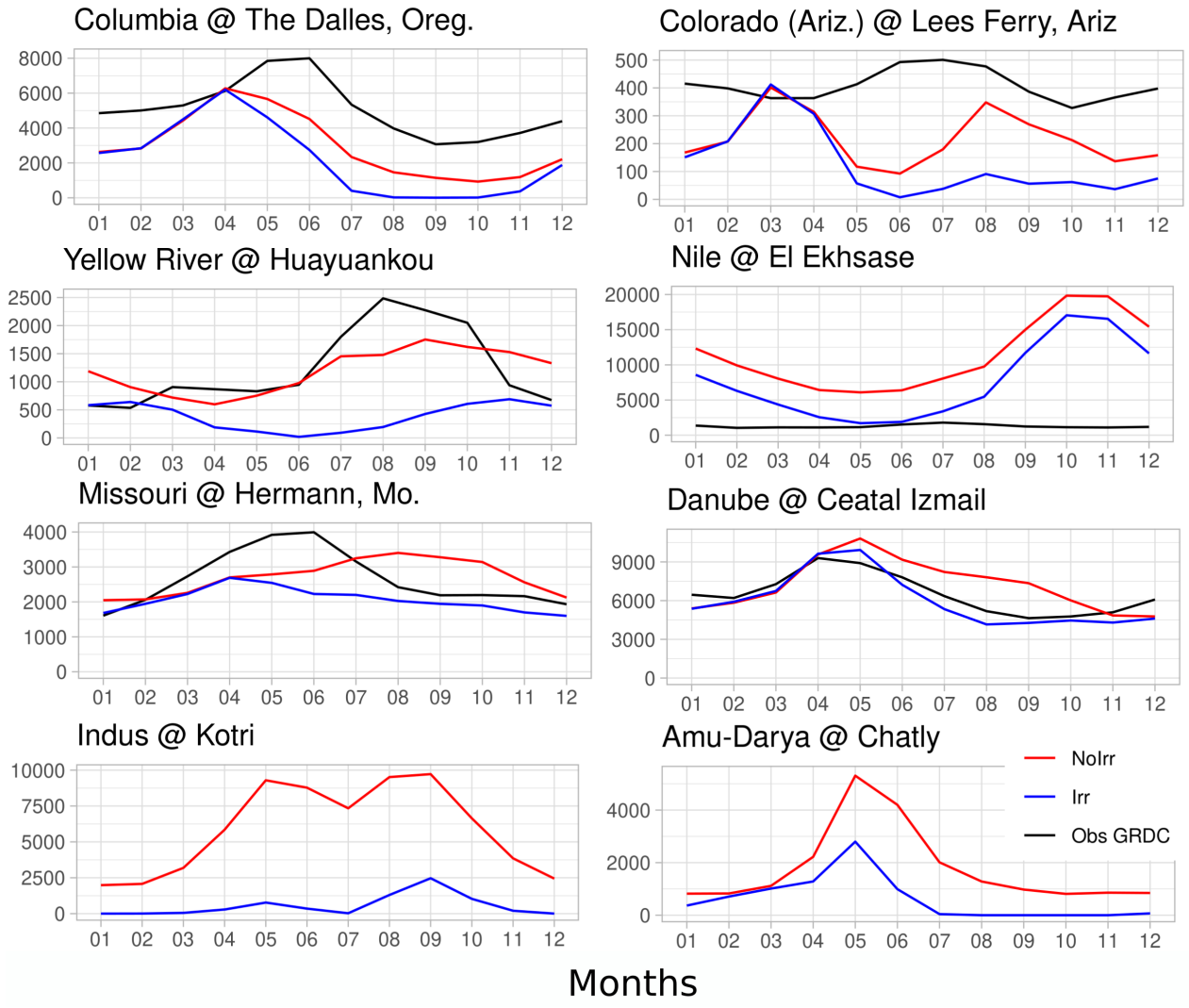

Figure 4.13: Comparison of observed and simulated river discharge in large basins with strong irrigation activities.

4.2.5 Discussion

In this study, we implement a new irrigation scheme inside the ORCHIDEE land surface model. The model estimates the irrigation water demand by calculating a soil moisture deficit. Besides, it constrains the actual irrigation rate by the available water supply. The water supply takes into account an environmental restriction, and the facility to access the water sources according to local infrastructure. Note that the environmental restriction is not a proper module to estimate environmental flow requirements, and other more robust approaches exist (for instance in Hanasaki et al., 2008a, providing monthly environmental flow requirements). Additional environmental requirements could reduce the surface water supply, thus the irrigation rate (Hanasaki et al., 2008b). For the facility to access the water sources, here we use two static factors based on local infrastructure, but note that water allocation is dynamic and can change according to water availability (Graaf et al., 2014) as well as economic and societal aspects (D'Odorico et al., 2020). The irrigation scheme also allows to represent the adduction of water from neighboring grid cells, which can be important in areas of China and India, where surface water use is important. The irrigation scheme seems to produce acceptable estimations of irrigation rates and surface and groundwater withdrawal volumes at the global scale, but it underestimates irrigation volumes in areas of China, India and the US (the most irrigated areas) while overestimates irrigation in some countries of Africa and South America.

Paddy rice irrigation could explain part of irrigation bias in southern Asia, as the paddy technique needs the inundation of the field and maintains a saturated soil at least during 80% of the crop duration (Vrese and Hagemann, 2018). The areas with a high irrigated paddy rice fraction also show a larger irrigation bias than areas with a low fraction. The LSM MATSIRO with an irrigation module, called MAT-HI and HiWG-MAT (Pokhrel et al., 2012; Pokhrel et al., 2015) already implemented an explicit representation of paddy rice irrigation, by setting a higher soil moisture target for rice than for other crops. An explicit paddy representation was also implemented in ORCHIDEE-CROP (Yin et al., 2020) at a regional scale. Setting an independent soil moisture target for rice also seems coherent with the sensitivity analysis and parameter tuning, that shows that β should have at least two values to optimize the irrigation estimation, one for areas in China and India, and one for other places.

In any case, the activation of irrigation leads to a reduction of the negative evapotranspiration bias, when we compare the simulations with the Fluxcom product. In the case of Gleam, we observe that the negative bias becomes positive for the simulations with irrigation. Furthermore, the Gleam values do not show large ET differences in the intensively irrigated areas compared to the areas with small irrigation fractions. This suggests that Gleam is not suitable for estimating irrigation rates in irrigated areas. On the other hand, irrigation seems to exacerbate the positive LAI bias, except for areas with intense irrigation activities. In those areas, the negative LAI bias with no irrigation is reduced when irrigation is activated. These results show the benefits of including an irrigation scheme to partially reduce some

modeling biases, especially in intensively irrigated areas.

The effect of irrigation on the ORCHIDEE estimations of TWSA is small, and mostly related to an increase of low values, especially in areas with an important groundwater supply. For discharge, activation of irrigation induces a reduction of river discharge. This reduction of discharge, due to surface water withdrawal, does not necessarily improve the model performance to fit observed values, with the exception of the Danube river basin. These results on TWSA and river discharge show that inclusion of irrigation alone does not necessarily fit simulated values of TWSA and discharge to observed products. Including additional anthropic processes could help to reduce these biases. For instance, as capacity of dams used for irrigation is correlated to the irrigation bias detected in section 4.2.4, including dam management could increase the water supply in some basins during dry months or years, then increasing the irrigation volume in those areas with a high irrigation demand. It could also have an impact on river discharge dynamics. Inclusion of fossil groundwater pumping could also help to represent TWSA trends in some areas.

It is worth noting that we did not compare the effect of irrigation in the bias of other hydrologic variables. The comparison of ORCHIDEE without and with irrigation showed an increase of bare soil evaporation as large as that of transpiration, and mostly small effects on runoff and recharge. Even if irrigation management tends to reduce the water that evaporates from bare soil or that returns to the environment (Koech and Langat, 2018; Gibson et al., 2019), results from Döll et al., 2012 show an increase of recharge due to irrigation in areas of India and China, while in areas of the US the results show an increase of surface water due to irrigation activities. This could be related to other limitations in the ORCHIDEE model, and might indicate some limitations in the irrigation scheme that need to be explored.

4.2.6 Conclusions

We implemented a global irrigation scheme within ORCHIDEE LSM, with a simple representation of environmental restriction, water allocation rules based on local infrastructure, and water adduction from non-local water reservoirs. We compared the irrigation estimates to reported values of irrigation withdrawal, and then we compared the outputs with and without irrigation to observed products of ET, LAI, TWSA and discharge. Our results underline the difficulties to represent irrigation on a large scale using simple schemes and limited information, but at the same time the results highlight the effect that the inclusion of irrigation can have in reducing some modeling biases in some areas, especially on ET.

The model could still benefit from improvements on parameter tuning by explicitly representing paddy rice irrigation, which could decrease irrigation bias in areas of southern Asia. Dam management representation could also reduce negative biases in some heavily regulated basins by increasing the water supply. These two aspects could change the spatial distribution of the ET and LAI increase within the model. For TWSA and discharge, the inclusion of other processes, like dam management or groundwater depletion could help to represent

observed seasonal dynamics and trends that the model is not currently able to represent. Besides, exploring the effect of irrigation in other hydrologic variables, and comparing this effect to observed datasets, could indicate unknown limitations in the scheme and within the ORCHIDEE model. Finally, as LSMs are commonly used in coupled mode with climate models and irrigation could have an impact on some atmospheric variables via changes on latent heat flux, these results also encourage the use of coupled simulations to explore the joint evolution of climate under the ongoing change (for past and especially future periods), water resources, and irrigation activities.

4.3 Simulation of irrigation in France

This section shows an analysis focused on France. We compare the trends of irrigated areas at the metropolitan France scale, and the volumes of withdrawn water for irrigation at the french department scale.

4.3.1 Validation datasets in France

We compare the datasets of irrigated areas used in the ORCHIDEE simulations (HID and LUHv2), and we add two more:

- GMIA5: This dataset (Siebert et al., 2005) shows both the area equipped for irrigation and the area actually irrigated at 5 arcmin resolution around the year 2005.

- Varenne de l'eau: This dataset (Agreste, 2010) provides the area actually irrigated at the communal level for the year 2010.

In the case of LUHv2 and HID, where there is only one variable (AEI or AAI) we use the conversion factors from the GMIA5 dataset to obtain the corresponding lacking variable. To compare the simulation of irrigation volumes in ORCHIDEE, we use reported values from the BNPE (La banque nationale des prélèvements quantitatifs en eau, https://bnpe.eaufrance.fr/), with reported values at the withdrawal point between 2008 and 2019. These withdrawal volumes are merged at the department scale, and then we use the department area to normalize the irrigation rate. This processing method allows to compare the irrigation volumes from BNPE with the average irrigation rates from ORCHIDEE at the department level, with no consideration of differences in the irrigated areas inside each administrative unit. As for AQUASTAT, BNPE dataset may include unaccuracies and errors on reported values, and is exposed to underestimation due to unreported withdrawals, as seem to be the case before 2012 (Oliveira, 2022).

4.3.2 Comparison of areas with irrigation activities

HID and LUHv2 datasets show a slow increase during the first part of the XX century, an important acceleration of both AEI and AAI after 1960, a peak around the year 2005, and a slight reduction afterwards (Fig. 4.14). The linear trend before 1960 is probably due to the lack of information, and the use of linear interpolation during this period to fill the missing data (Oliveira, 2022). Comparison with GMIA5 and Varenne de l'eau show some differences in the size of both variables for years 2005 and 2010, but in general the order of magnitude is the same for all datasets. But we remark that similarity in AEI and AAI at the country-level hides important spatial differences, as shown by Oliveira, 2022.

These differences may be important, as in the new scheme, the water demand is constrained by climate, soil and the prescribed irrigated fraction, but also by the local water supply in the three natural reservoirs (overland, river and groundwater). If the irrigated area is uncertain in magnitude, or if the spatial distribution of the irrigated surfaces is different between datasets, the corresponding values of water demand and water supply might be different, inducing changes in the simulation of irrigation rates. The prescription of the irrigated areas is one of the main sources of uncertainty inside the new irrigation scheme in ORCHIDEE and in other irrigation withdrawal estimations (Puy et al., 2021), and at the same time it is one of the most difficult to estimate at global and regional scale.

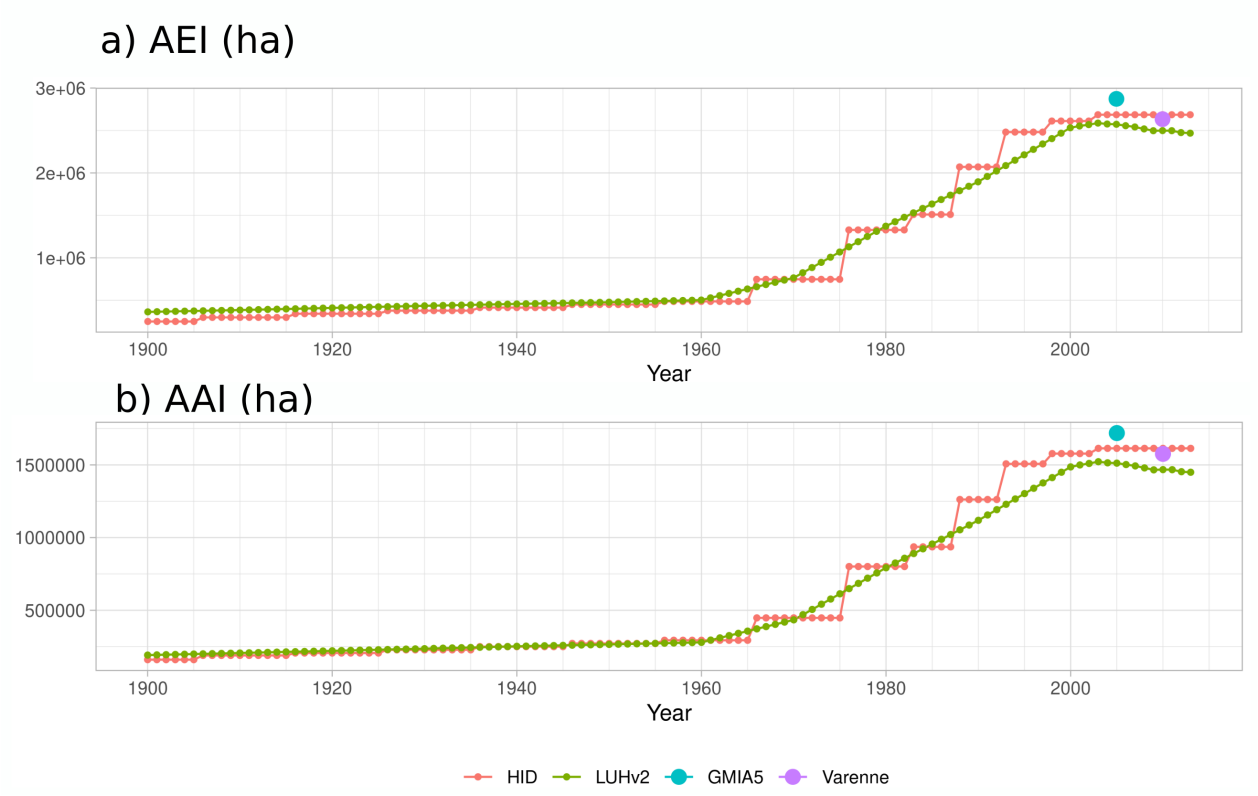

Figure 4.14: Temporal evolution of AAI and AEI in metropolitan France, period 1900-2020, in ha.

4.3.3 Validation of simulated irrigation in France

Comparison of irrigation shows a strong overestimation in ORCHIDEE compared to BNPE data (Fig. 4.15). This overestimation of the irrigation volume was already visible in the global scale comparison with AQUASTAT and Sacks et al., 2009 datasets. ORCHIDEE simulates a higher irrigation rate in administrative units where the reported values are lower by one order of magnitude. That is the case in the northern areas like Britanny, Normandy and Hauts-de France regions for Irr and Irr_beta simulations, or in southern areas for all simulations. The exception is the eastern region, where the overestimation in the ORCHIDEE simulation is less important, and is linked to the prescribed irrigated surface, which is smaller in both HID and LUHv2 datasets (Oliveira, 2022).

Other differences in simulations are linked to the differences in the prescribed information. Irr_LUH depicts large areas with no irrigation, which is not coherent with the BNPE dataset. Simulations Irr and Irr_beta, which use HID dataset to prescribe input data, present a larger number of departments with irrigation as the reported values, but overestimation is general in the two simulations.

The irrigation bias may have multiple causes: first there exist an important uncertainty in the spatial patterns of the areas equipped for irrigation or actually irrigated, according to the dataset used in the corresponding simulation. In France, the difference between HID and LUHv2 (which represent AEI and AAI respectively) is around 1 million hectares, and they depict different spatial patterns (Oliveira, 2022) but theoretically the model should use the AAI, which can change from year to year. Second, there may exist an underestimation of the reported values from BNPE, which could partially explain the large difference in some administrative units, but not the gap at national level (Oliveira, 2022). Third, the new irrigation scheme may fail to represent local irrigation strategies due to the use of a single global β value.

About the representation of local irrigation strategies, we observe that the simulation with a lower β, i.e. with a lower soil moisture target, induces a reduction on the irrigation bias, as already shown in section 4.2.2.3. It highlights the importance of a different β value to represent local irrigation strategies. Analysis of the calibration using some short simulations suggest that a value equal to 0.6 would reduce the bias and fit the simulation to the reported values. Some preliminary analysis in France (Oliveira, 2022) shows that irrigation in France is strongly dependent on the soil moisture target, and supports the modeling strategy to include a lower β in France and in other countries of similar characteristics.

4.4 Chapter conclusions

In this chapter, we introduced a new parameterization to represent irrigation at global scale within ORCHIDEE. The new module uses a simple soil moisture target approach, but is constrained by water supply from natural reservoirs to estimate the actual irrigation volume.

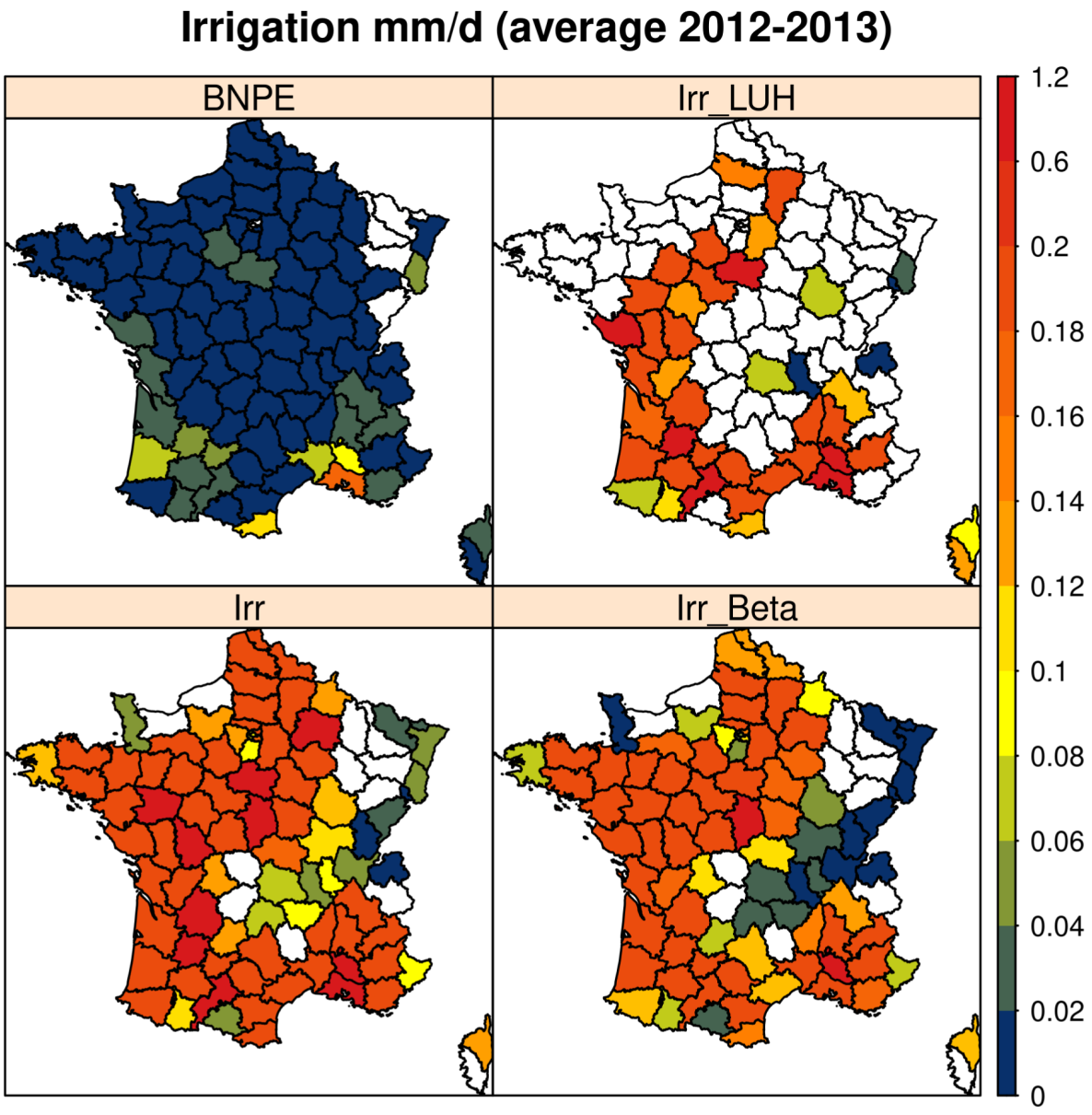

Figure 4.15: Comparison of BNPE irrigation withdrawals and ORCHIDEE irrigation withdrawals from Irr_LUH, Irr, and Irr_beta simulations at french department scale. Average values in mm/d for 2012-2013. BNPE volumes were normalized with the department area. White departments do not have any information in the BNPE dataset or have no irrigation in ORCHIDEE simulations.

Besides, the scheme includes a volume that must be left for the ecosystems (an environmental discharge) and allocates water according to the facility to access water sources, based on local infrastructure. To set-up an acceptable estimation of water withdrawal for irrigation, the parameter values were tuned by comparing irrigation estimates from short simulations to observed values.

The model simulates acceptable estimates of irrigation volumes. However, an explicit representation of paddy rice could help to decrease a negative bias in areas of India and China

and a positive bias in other regions of Europe, Africa and Latin America. The sensitivity analysis and calibration of the β parameters suggest the need for at least two distinct values of the soil moisture target to reduce the irrigation bias and fit observed datasets, and support the representation of paddy irrigation. It also could help to reduce the positive irrigation bias in France, where ORCHIDEE shows a general overestimation.

Directly linked to activation of irrigation in ORCHIDEE, we observe in our simulations an increase of ET and LAI values. Comparison with observed datasets shows that the irrigation scheme reduces part of the negative bias in ORCHIDEE for ET in irrigated areas. On the other hand, activation of irrigation seems to exacerbate the positive bias in LAI values, except for the most intensively irrigated areas, where the negative bias of LAI is reduced. No major impact was observed in TWSA as has been reported in the literature, probably due in part to the lack of representation of the fossil groundwater pumping. For discharge the impact is more important, and in all analyzed cases irrigation tends to decrease the average discharge value, but metrics show that including irrigation does not necessarily improve the representation of discharge dynamics in ORCHIDEE. This is probably due to lack of other processes, like dam management, which also have an impact on discharge dynamics, besides limitations in ORCHIDEE.

These results use offline simulation outputs, and they show that the proposed parameterization, even if simple and easy to use, simulates reasonably well the main characteristics of the irrigation patterns at global and regional scales. Furthermore, the inclusion of water adduction and the use of new information for water allocation (map of areas equipped for irrigation with surface and groundwater) help to contrain the simulated effects of irrigation on land surface fluxes and hydrologic variables. It encourages the use of the module in coupled simulations, in order to assess in detail the joint response of irrigation activities, water resources and climate. As part of these perspectives, a few LMDZOR (coupling between ORCHIDEE and LMDZ, the atmospheric model of the IPSL) simulations with this irrigation scheme are included in two projects currently in progress: IRRMIP, an irrigation model intercomparison project focused on the effect of irrigation and heat extremes in past climate, and BLUEGEM, which aim to explore the joint evolution of past and future climate, soil, groundwater and irrigation.

Chapter 5

Conclusions and perspectives

5.1 General conclusions on the effect of landscape drivers

The main objective of this work was to advance the understanding of the interaction between topographically driven hillslope flow and irrigation activities with the atmosphere, and to disentangle their individual effects on the water cycle. We refer to these two processes as landscape drivers, as each of them causes changes in landscape conditions and soil moisture (note that there are other landscape drivers). The goal of this work was summarized in the following two questions (chapter 1, section 1.4):

Q1. What is the impact/feedback of hillslope flow on present and future climate, for both mean and extreme values?

Q2. What is the impact of irrigation on land surface fluxes in present climate, for mean values?

In chapter 3 of this thesis we analyzed the impact and feedbacks of hillslope flow on present and future climate, answering question Q1. We took advantage of some of the work done in the IGEM (Impact of groundwater on earth system models)[1] project, during which a parameterization of hillslope flow was included in ORCHIDEE land surface model. The hillslope flow is represented by dividing the typical grid-cell in two fractions, an upland fraction and a lowland fraction. Both fractions can interact with the atmosphere, but the lowland fraction acts as a buffer between the upland fraction and the river network, and then is potentially wetter. We compared two coupled transient simulations using LMDZOR, the land-atmosphere component of the IPSL climate model, under climate change for 1980-2100, with and without hillslope flow. The main conclusions can be divided into two main parts: the effect on the mean values of hydroclimatic variables under historical climate, and the effect on the long-term trend of these variables under climate change.

[1] See more in https://www.metis.upmc.fr/~ducharne/gem/anr.php

Regarding the effect of hillslope flow on mean values, it induces a general increase in soil moisture. In areas where energy is available, the increase in soil moisture near the surface induces an increase in evapotranspiration and a reduction in runoff. In some areas, an increase in precipitation is observed as an atmospheric feedback and, in that case, runoff may also increase. As a direct consequence of increased evapotranspiration, or latent heat flux in energy terms, sensible heat flux decreases, and near-surface air temperature cools down. Finally, the additional water flow concentrated on a fraction of the grid induces an increase in leaf area index, as the plant has access to more water to ensure transpiration and photosynthesis. For extreme values, the hillslope flow induces a decrease in the intensity and frequency of maximum air temperature extremes, and a slight increase in the intensity of precipitation extremes, without major changes in frequency.

As for the effect of hillslope flow on the evolution of hydroclimatic variables under climate change, we observed that this landscape driver can induce an acceleration, attenuation or reversal of long-term trends under climate change. When precipitation decreases locally due to climate change, hillslope flow will attenuate the negative trend in soil moisture, evapotranspiration, precipitation and runoff, regardless of local climate. In areas where precipitation increases due to climate change, hillslope flow will amplify the positive trend in evapotranspiration and attenuate the positive trend in soil moisture, runoff and precipitation. In general, hillslope flow produces a slight reduction in warming. For extreme values of maximum air temperature, although the global-scale effects in intensity and frequency are close to those of the present, its spatial pattern changes. For precipitation extremes, the effect of hillslope flows on intensity is slightly larger in the future, and remains small with respect to frequency under present and future climate.

In chapter 4 of this thesis we analyzed the impact of irrigation on land surface fluxes in the current climate, answering question Q2. To enable the analysis, we introduced a irrigation scheme to be used at global scale, as part of the ongoing work of the BLUEGEM (Biosphere and Land Use Exchanges with Groundwater and soils in Earth system Models) project (see more information in section 5.2.2). The scheme estimates the water demand based on a soil moisture deficit against a user-defined target, and constrains the actual irrigation to water supply (including adduction from non-local river reservoirs). Besides, supply estimation includes a water volume left for ecosystems (environmental flow) and water allocation rules based on local infrastructure to access the natural reservoirs.

We performed a sensitivity analysis, then tuned the scheme parameters using short offline simulations and assuming uniform values over land. We tested the scheme with offline simulations at global scale, for the current climate (1980-2013). The scheme simulates acceptable estimates of irrigation volumes, when compared to reported values from AQUASTAT and to other modeling estimations (Pokhrel et al., 2016). However, we observed an important underestimation of irrigation rates in southern Asia and the US, while other areas in Europe, Africa and Latin America showed an overestimation. This seems coherent with the tuning process, which showed the need for at least two distinct soil moisture targets to reduce irri-

gation bias. The synthesis of the effects of including irrigation activities can be divided into two parts: effect on mean values in the current climate, and effect on modeling biases versus observed datasets.

When we compared the simulations without irrigation and with irrigation in ORCHIDEE, we observed that irrigation induces an increase in soil moisture and evapotranspiration. This is not surprising, since it is the ultimate goal of irrigation activities, to increase soil moisture and plant transpiration. We observed a decrease in sensible heat flux and surface temperature, as a direct consequence of higher evapotranspiration in the irrigated simulation. We also noticed an increase in leaf area index, since irrigation prevents part of the crop water stress, allowing photosynthesis and plant development. But irrigation requirements and the corresponding water withdrawals reduce natural reservoirs, i.e. groundwater and river discharge.

When comparing ORCHIDEE results and observed outputs, we observed that irrigation reduces the negative modeling bias of ET in irrigated areas. Conversely, in the case of leaf area index, irrigation exacerbates the positive modeling bias, except for the most intensively irrigated areas, where the negative LAI bias is reduced. In the case of large river discharge, irrigation decreases the value due to water withdrawals, however the activation of irrigation in ORCHIDEE does not necessarily improve the model's performance of discharge dynamics against observed values. Finally, in the case of total water storage anomalies, we observed a minor effect on mean and seasonal dynamics due to irrigation, while observed trends were not well captured by ORCHIDEE, even when irrigation was enabled.

We summarized the effects of each individual landscape driver studied in this thesis in four main conclusions. These effects remain mostly weak at global scale. The two first conclusions are related to the effect on mean values under present climate, while the two last conclusions are based on the effect on long-term trends under climate change. We underline that only the first conclusion was addressed for both hillslope flow and irrigation.

C1. Landscape drivers studied here maintain higher soil moisture and induce a higher evapotranspiration, when there is available energy. Even if the effect is weak for both landscape drivers at global scale, ET enhancement leads to changes in hydrological flows and water reservoirs, as well as in energy balance and vegetation dynamics.

C2. For hillslope flow, the response of the atmosphere may include a cooler air temperature and more precipitation, but note that the atmospheric response is not always observed, as it also depends on atmospheric circulation. The atmospheric response creates feedbacks with soil moisture, evapotranspiration and runoff variables.

C3. Hillslope flow modulates the evolution of hydrological variables under climate change. It attenuates negative trends of soil moisture, evapotranspiration and runoff in the areas prone to undergo a reduction in precipitation due to climate change, regardless of local aridity conditions and average annual temperature.

C4. The modulation of climate change effects on hydrological variables induces a modulation in the evolution of climate as well: we simulate an attenuation of global warming and a reduction of negative trends of precipitation. Evolution of climate will impact the evolution of hydrologic variables, for instance runoff and evapotranspiration.

In the case of hillslope flow effects, we should note that conclusions C1, C2, C3 and C4 are supported by the results of LMDZOR, which couples the LMDZ atmospheric model and ORCHIDEE LSM. The coupled simulations allow us to assess the climate response to new land surface conditions for both current and future conditions, but add atmospheric model biases and feedbacks that could affect our results and the corresponding analysis. Also, the hillslope flow representation used here includes first-order effects on land surface conditions, but there are other processes that can modulate these effects, and that were not included in the simulations. These limitations call to verify the generality of conclusions of this study with simulations from other models and with observed data sets when possible. We will discuss some possibilities and perspectives that are detached from these limitations in section 5.2.

For the case of irrigation, the results support conclusion C1, but we do not fully understand the effects on climate, as we used here offline simulations. The literature results suggest that irrigation has a weak but significant effect on historical climate, especially in intensively irrigated areas (Thiery et al., 2017; Al-Yaari et al., 2022). On the other hand, the models involved in these published studies do not constrain irrigation to the supply available from natural reservoirs, so the effect could be overestimated. In addition, it is not clear whether irrigation and its effects under future climate change are sustainable, or whether the overexploitation of water resources can induce a halt in the possible effects on the evolution of hydroclimatic variables. As for hillslope flow, we will discuss some perspectives detached from these limitations in section 5.2.

Finally, we have analyzed the effect of each landscape driver as an isolated process. In this sense, this thesis work has included: 1) the introduction of new processes in the ORCHIDEE model, 2) the testing of the new parameterization with offline simulations at regional and global scales, and 3) the analysis of coupled simulations using LMDZOR. In reality both processes occur at the same time, in many cases in the same regions, and both are partly sustained by groundwater. This could result in "inter-processes interference", i.e., that water withdrawal for irrigation, which in many cases is a rapid process, interferes with the rather slow hillslope flow. In that case, can groundwater depletion caused by irrigation stop both the increase in soil moisture and evapotranspiration? Could this slow or halt the effects of landscape drivers on the evolution of hydroclimatic variables? So far there is no evidence to answer this question. Thus, this limitation calls to introduce both processes in a single ORCHIDEE version, and we discuss some ideas to do so in subsection 5.2.1.3.

5.2 Perspectives

5.2.1 Developments in ORCHIDEE

5.2.1.1 Hillslope flow

The main conclusions and the limitations presented above open some interesting perspectives for the study of the effects of both landscape drivers. In the case of hillslope flow, the modeling framework could include some improvements in the parameterization. First, the inclusion of lowland dynamics, moving from a static lowland map to a dynamic lowland fraction as a function of local conditions, could help to assess the modulation of hillslope flow effects due to lowland dynamics. Including lowland dynamics in large-scale LSM is challenging, but the addition of an imposed drainage function at the bottom of the lowland fraction, following the results of Maquin, 2016 and the H2CS model, could be a starting point. We also mention Swenson et al., 2019 and the generalization of representative hillslopes (a concept close to the use of a lowland fraction as done in ORCHIDEE) in CLM5 as a further step in that direction, which could be reproduced in ORCHIDEE.

Second, we used here for simplicity uniform parameter values over land, such as the drainage density. A further step could be to consider the use of global maps, to include the modulation of hillslope flows due to local characteristics. For instance, Schneider et al., 2017b proposed a global drainage density map based on high resolution topography, lithology and climate, that could be used by ORCHIDEE. Some other models also use geomorphological relationships to obtain shape parameter values, for instance ISBA LSM (Vergnes et al., 2014). Thirdly, the improvement of vegetation representation by establishing links between the lowland fraction and some specific PFTs within ORCHIDEE could allow to include the subgrid heterogeneity induced by hillslope flows. And finally, the inclusion of additional processes with a direct impact on the effects of hillslope flow, such as stream losses and disconnection of groundwater from the surface, which can modulate part of the effects of hillslope flow at global and regional scale. This is particularly important in arid to semi-arid climates, where water tables are frequently fed by rivers (Graaf et al., 2019). In that sense, ISBA already represents river-aquifer interaction in some aquifer basins at global scale (Vergnes et al., 2014; Decharme et al., 2019). The inclusion of this type of process in ORCHIDEE could therefore be explored as well.

Another challenge is to compare modeling results, to validate the representation of hillslope flows as done in the model. In this sense, the inclusion of ORCHIDEE in the BLUEGEM[2] project opens up a wide range of possibilities. The BLUEGEM project aims to explore the joint evolution of groundwater, irrigation and climate in the recent past and in the future. The project plans to calibrate a high-resolution version of ORCHIDEE centered in France in offline mode, and including hillslope flow and irrigation activities. The regional-scale calibration process is also the opportunity to compare simulation results with observed and

[2]See more in https://www.metis.upmc.fr/~ducharne/bluegem/index.php

remotely sensed datasets. This would allow partial validation of the effects of hillslope flow on surface conditions and hydrology.

5.2.1.2 Irrigation

For irrigation, the results suggest that part of the irrigation bias could be explained by paddy rice irrigation. Thus, representing paddy could help to reduce the error on irrigation estimates. The sensitivity analysis and parameter tuning support the inclusion of paddy representation, as the model would need at least two different soil moisture targets to fit the observed irrigation rates: a higher target for some areas in China and India (two regions with important irrigated areas with paddy), and a lower target for other regions. Other improvements could include to represent irrigation as a separate soil column within ORCHIDEE, to better account for soil moisture dynamics. Explicit representation of crop phenology, taking advantage of the ongoing work to introduce a global crop module in ORCHIDEE (ORCHIDEE-CROP), could be necessary if the scientific questions are related to seasonal irrigation dynamics. Furthermore, inclusion of dams management could help to increase the irrigation rates by increasing the simulated water supply, and could help to improve the representation of discharge dynamics in ORCHIDEE in highly regulated basins (Yin et al., 2021; Zhou et al., 2021b). Finally, inclusion of fossil groundwater pumping and corresponding groundwater depletion could be important to represent some of the negative TWSA trends observed in GRACE, that ORCHIDEE in not currently capable to simulate, even when irrigation is activated. This could be considered by including an additional reservoir with no restriction on supply in some areas, following other LSMs (Pokhrel et al., 2016).

On the other hand, the lack of comprehensive observations has prevented a better understanding of the impact of irrigation on land surface flows and hydrology. Two projects open some perspectives to compare the model results to observed and modeled datasets. The first one is BLUEGEM project (see web page in section 5.2.1.1), and the calibration of a high-resolution ORCHIDEE version in France already mentioned above. As for hillslope flow, comparison of this modeling experiment with observed datasets could help to validate part of the effects of irrigation on surface conditions and hydrology. The other perspective is linked to the LIAISE[3] project. This project opens an interesting perspective to compare our results in offline mode to observed values. The LIAISE project seeks to better understand the impact of anthropization on the land-atmosphere-hydrology interactions, and the limitations of models to represent these aspects of the terrestrial water cycle in the semi-arid Iberian peninsula. One of the pillars of the project is based on campaigns to measure land surface fluxes and soil moisture in the Ebro basin (northern Spain) in irrigated and natural areas. Therefore, it could be interesting to compare offline ORCHIDEE simulations with irrigation at regional scale to the observed datasets of the LIASE project and to some of its modeling experiments. Comparison could focus on land surface fluxes, surface conditions

[3]See more in https://www.hymex.fr/liaise/index.html

and hydrologic flows.

5.2.1.3 Some ideas for including irrigation and hillslope flow in a single ORCHIDEE version

We already mentioned that, in reality, hillslope flows and irrigation activities may occur in the same regions, and that, as both of them are partly sustained by groundwater, it is not clear if water withdrawal for irrigation, which in many cases is a rapid process, could interferes with the rather slow hillslope flow. To try to respond to this question, we need to introduce both landscape drivers in a single ORCHIDEE version.

Currently, hillslope flow is represented in ORCHIDEE by including a lowland fraction (see Figure 5.1-a). This lowland fraction buffers groundwater and overland flows to the river channel, and can interact with the atmosphere. At the grid cell scale, the same 15 PFTs are used to represent the vegetation distribution in the upland and lowland fractions. It means that each PFT takes water from its corresponding upland column and from the single soil column representing the lowland fraction. In this context, the irrigated surface can be located in the crop and grasses soil column, and in the lowland fraction, so irrigation water would be applied to both fractions. It should be noted that crops and PFT grasses would not be the only vegetation types that access lowland soil moisture for transpiration. This means that additional water from irrigation activities would also be supplied to forest vegetation types and bare soil located in the lowland fraction.

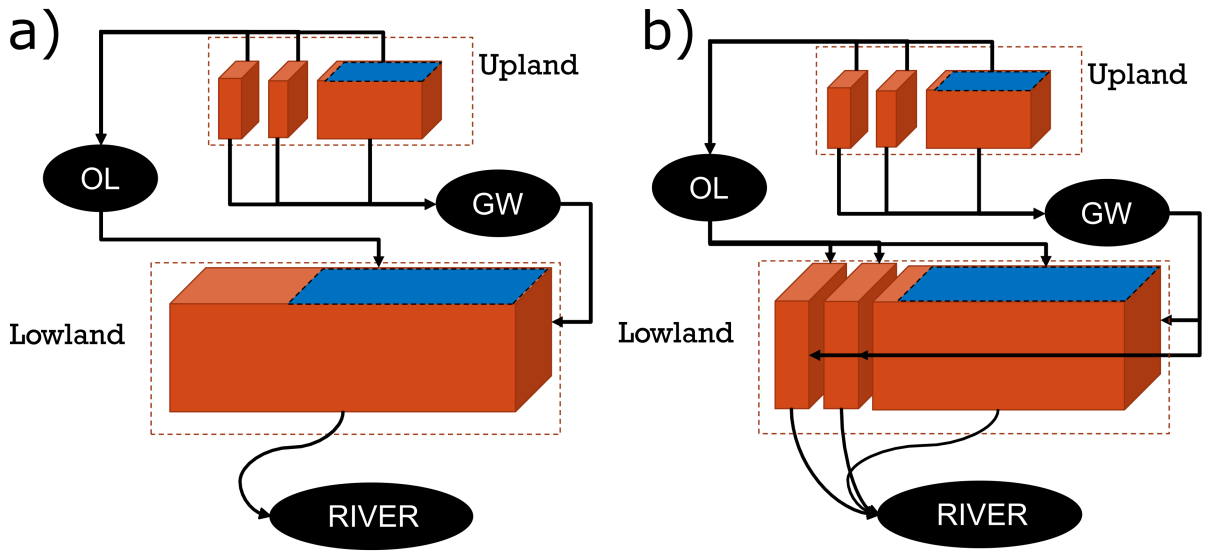

Figure 5.1: Schematic for an ORCHIDEE version with hillslope flow and irrigation. Current hillslope flow representation (a) and new hillslope flow representation (b). The surfaces in blue correspond to the irrigated area, while OL means overland and GW means groundwater reservoirs. Note that for a) there are just 15 PFTs, while for b) there are 30 PFTs.

To represent hillslope flow and include irrigation activities, we propose the following

changes (see Figure 5.1-b):

- To separate the lowland fraction in one or more soil columns, initially the same number as the upland fraction. Hillslope flow is represented as a flow from upland to lowland fraction through overland and groundwater reservoirs, as for the former representation. The flow that enters the lowland fraction is divided according to soil column fractions. This complexification into six soil columns allows to estimate in a finer way the soil moisture deficit in the upland and the lowland fraction.

- To duplicate the vegetation types from 15 to 30 PFTs, half for the upland fraction and half for the lowland fraction. In this way, the model can account for the differences in water stress and photosynthesis activity induced by hillslope flow at the subgrid scale for the same vegetation types.

- To link each lowland PFT to a single lowland soil column, following the organization in the upland fraction. Thus, a column of lowland soil column containing crops and grasses can be represented. It allows to concentrate the irrigation volume on the two soil columns of crops and grasses (one in upland and one in lowland fraction), preventing the irrigation of forest vegetation types and bare soil.

With this structure, the irrigation scheme can provide additional water to both upland and lowland crops. Initially, we propose to represent a single irrigation rate for the entire grid cell, regardless of the potentially higher soil moisture in the lowland fraction. More complex rules could be proposed, if the tests suggest an increase of the irrigation bias or unrealistic effects on land surface fluxes.

Note that in the scheme presented in figure 5.1-b, the source of water for irrigation comes from overland and groundwater reservoirs, which also support hillslope flows. If irrigation activities withdraw a large volume from overland or groundwater, hillslope flows to the lowland fraction may be diminished or prevented altogether, concentrating that volume of water in the upland and lowland soil columns with crops and grasses. It should also be noted that the proposed scheme would simulate three different water tables, one for each lowland soil column.

Finally, the new ORCHIDEE version proposed here opens some interesting perspectives for its use in coupled mode, that we explore in the next subsection.

5.2.2 Use in coupled simulations

We already stated above that in this thesis we do not fully understand the effects of irrigation on climate, as we used offline simulations. Thus, It seems natural to propose coupled simulations to understand the effect of irrigation (under historical climate). In this context, the LIAISE project (see web page as footnote in section 5.2.1.2) could open the possibility to confront our conclusions on regional atmospheric feedbacks induced by irrigation against

other simulations and observed datasets. The challenge of comparing modeling datasets from coupled simulations with observations could be addressed through the use of innovative bias correction methods (Krinner et al., 2020) and zoomed-nudged configurations (Campoy et al., 2013).

Another interesting perspective is the use of the IPSL climate model with ORCHIDEE and the irrigation scheme in IRRMIP (Irrigation Model Intercomparison Project). IRRMIP aims to understand the impacts of expanding irrigation during the last century on different sectors: water resources, climate, and agriculture, by comparing different coupled land surface-atmosphere systems. A first analysis will focus on climate extremes, especially heat extremes, which have implications for human health (Zhao et al., 2015). Also, the project envisages to compare results from the climate model community with both hydrological models and crop models, which could be important to assess the generality of some of the results.

Finally, the use of the IPSL climate model with an ORCHIDEE version including both hillslope flow and irrigation opens interesting perspectives within the framework of the BLUEGEM project (see web page in section 5.2.1.1). The project contemplates the use of factorial simulations with the IPSL climate model including ORCHIDEE and the CESM2 including CLM5 in coupled mode for 1900-2100. These factorial simulations seek to assess the fingerprint of groundwater-soil moisture interaction and irrigation on climate, water resources and soil carbon pools during the anthropocene. It could help to provide improved projections of global climate that includes the effect of groundwater and irrigation on climate. This is especially important for irrigation, since, as far as we know, there are no studies on the interaction of irrigation and climate under future climate change. In addition, the BLUEGEM project seeks to combine global simulations to local and regional knowledge and expertise (in two case studies, metropolitan France and Mekong river basin), in order to refine land use and irrigation scenarios, and to propose sustainable pathways for management strategies. It could help to assess the usefulness of global scenarios and projections at regional scales.

All these perspectives are extremely interesting, not only because they advance the understanding of the simulated effects of landscape drivers studied here, but also because they could allow us to confront our results with other modeling frameworks and, above all, with observed datasets and regional knowledge. The latter point is important, because, following conclusions from Gascoin, 2009, confrontation to observed data will always have the strangest power to both stimulate and to temper the scientific imagination.

Appendix A

Supporting Information for "Influence of hillslope flow on hydroclimatic evolution under climate change"

Introduction

This supplementary completes all the plots shown in section 3.2. Figures A.1 and A.2 includes the difference between HSL and REF simulations at yearly, boreal summer and boreal winter, in the historical period 1980-2010. Figures A.3 and A.4 show the difference between historical (1980 - 2010) and future (2070 - 2100) for the REF simulation at yearly, boreal summer and boreal winter values.

Figures A.5 and A.6 show the spatial distribution of hillslope flow modulation on climate change trends, for the period 1980 - 2100, with the same color code used in the paper. Figure A.7 shows regional yearly and boreal summer average values for a region in the USA South Atlantic (SA USA), for 1980 - 2100.

Figure A.8 shows the aridity index and mean annual air temperature from HSL simulation for 1980 - 2010, and the corresponding climate classification using HSL data. Finally, Figure A.9 shows the regional average trends and hillslope flow modulation for the period 1980 - 2100, and yearly/summer values.

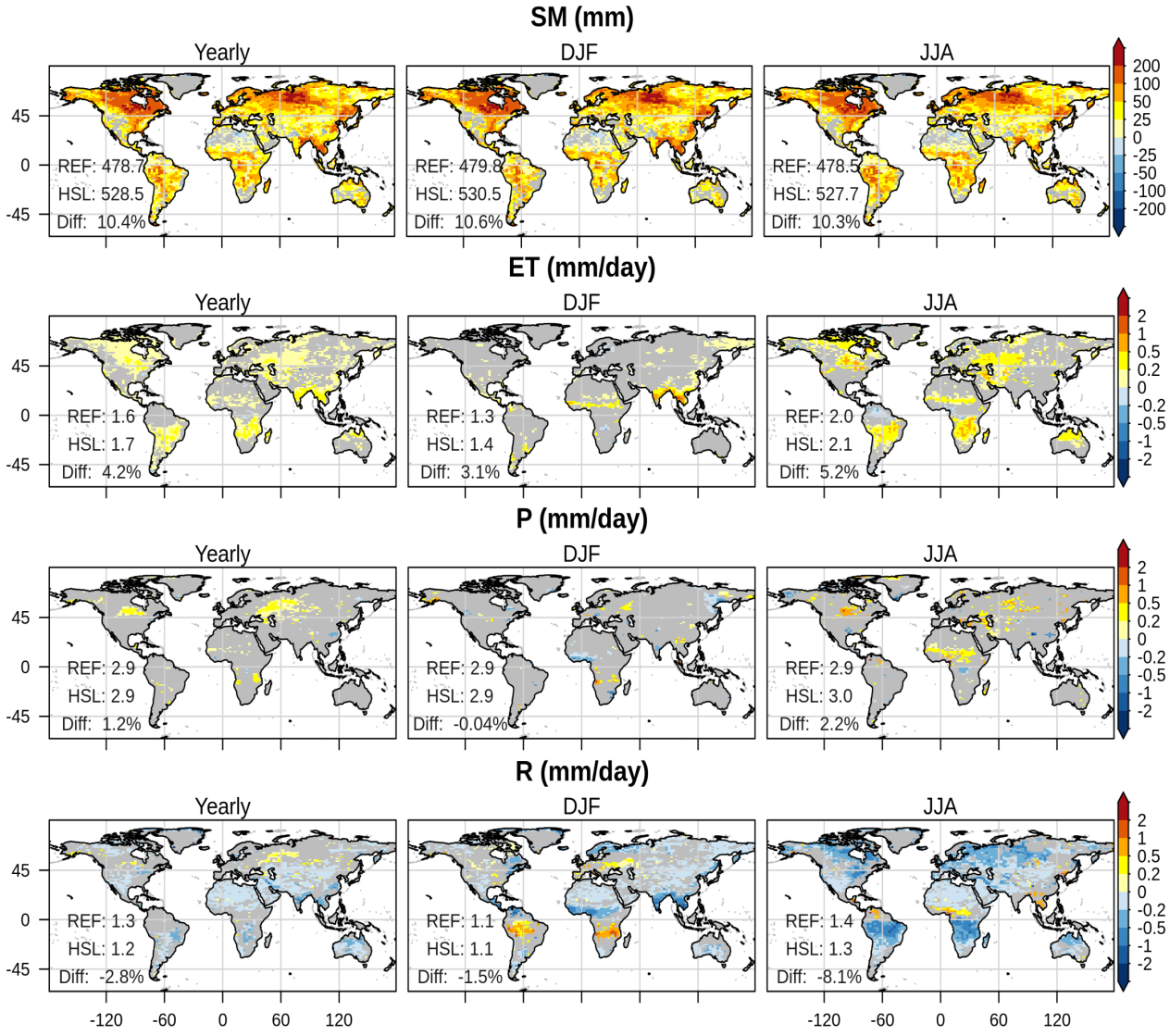

Figure A.1: Change on mean yearly, boreal winter and boreal summer values between HSL and REF, for period 1980 – 2010, for SM, ET, P and R. Statistical significance of the mean differences is tested at each point with a Student test (p = 0.05). The areas with insignificant changes are left gray

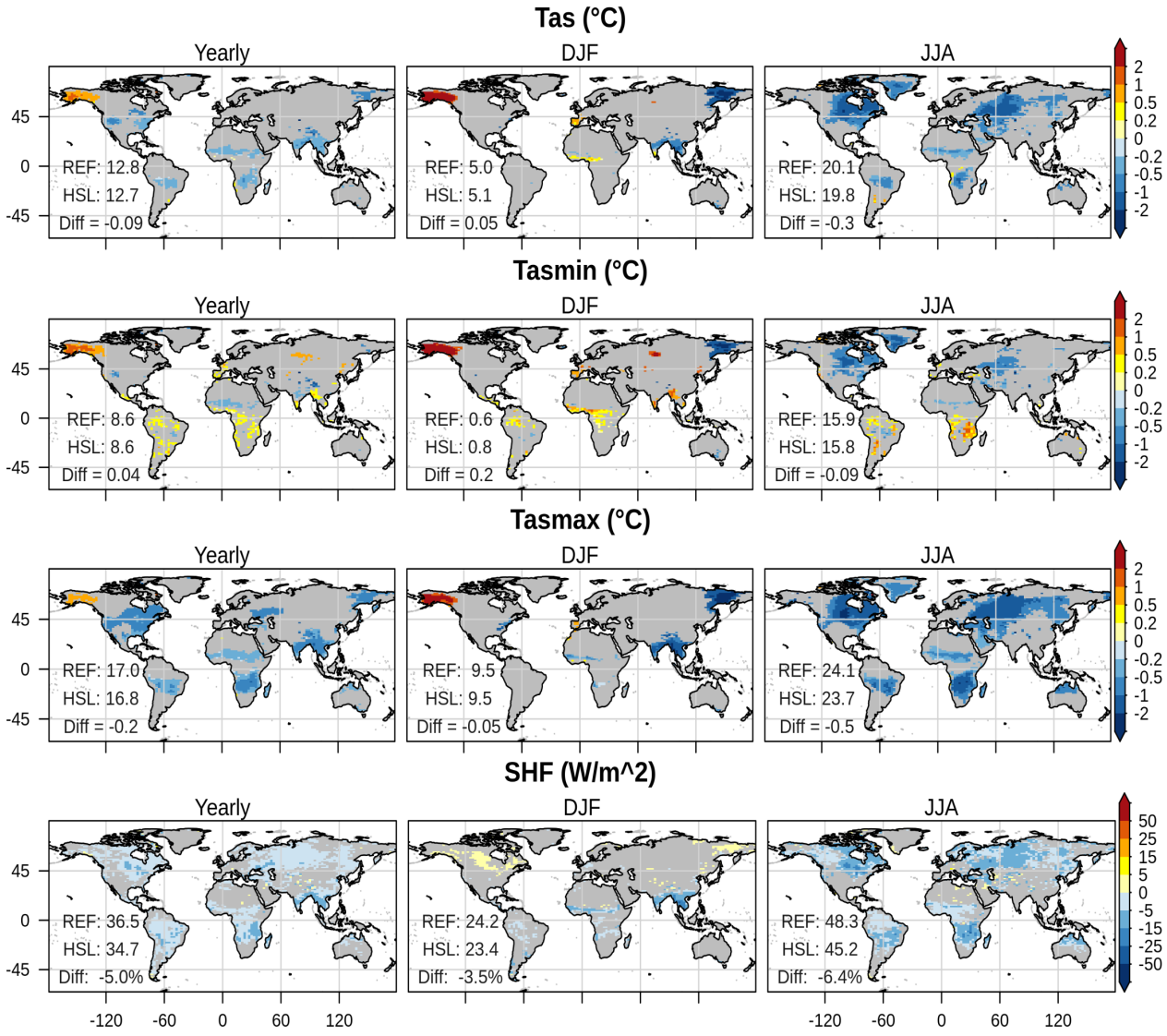

Figure A.2: Same as Figure A.1 but for Tas, Tasmin, Tasmax, and SHF.

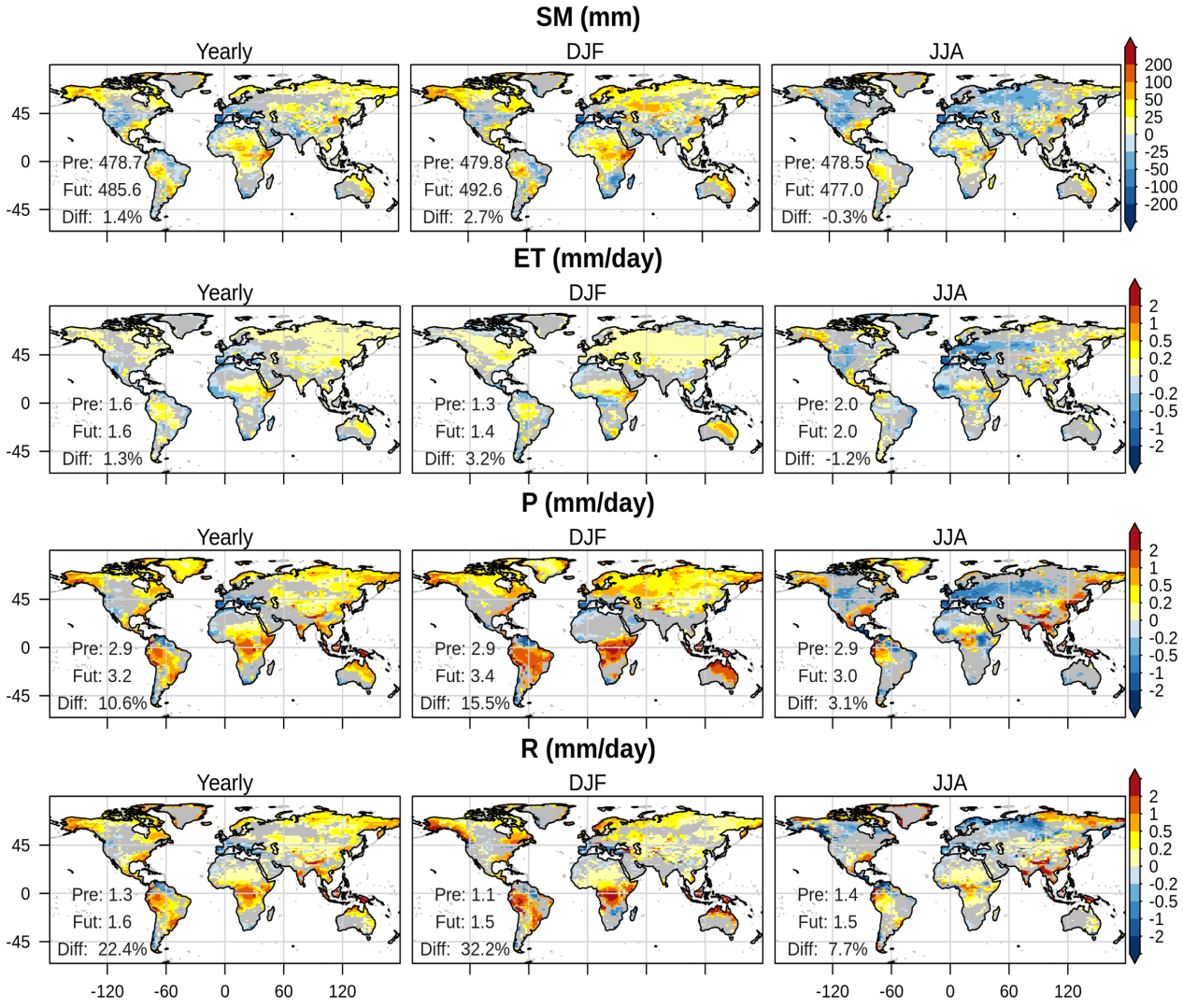

Figure A.3: Change on mean yearly, boreal winter and boreal summer values between periods 2070-2100 and 1980-2010 using REF simulation data, for SM, ET, P and R. Statistical significance of the mean differences is tested at each point with a Student test (p = 0.05). The areas with insignificant changes are left gray

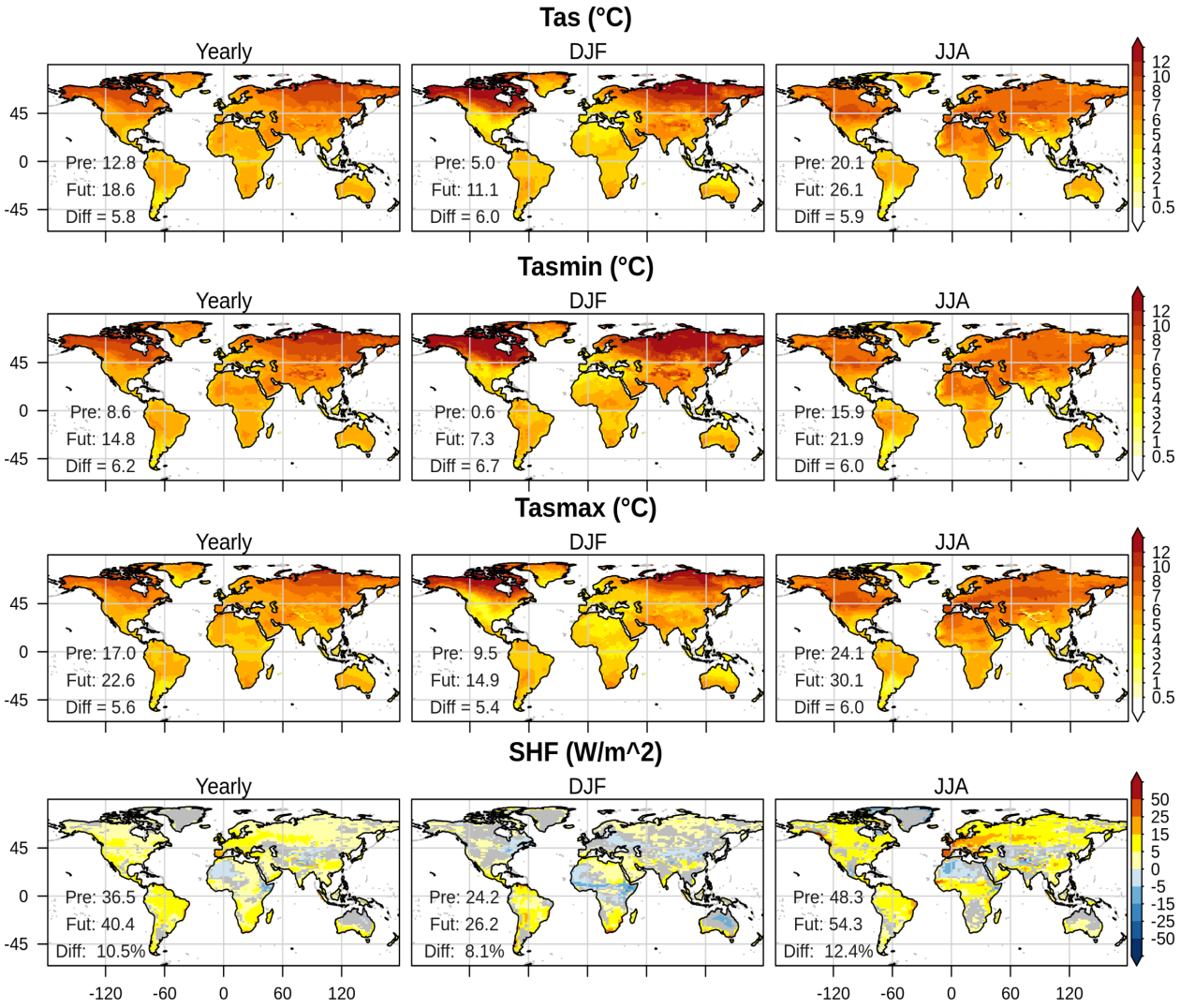

Figure A.4: Same as Figure A.3 but for Tas, Tasmin, Tasmax, and SHF.

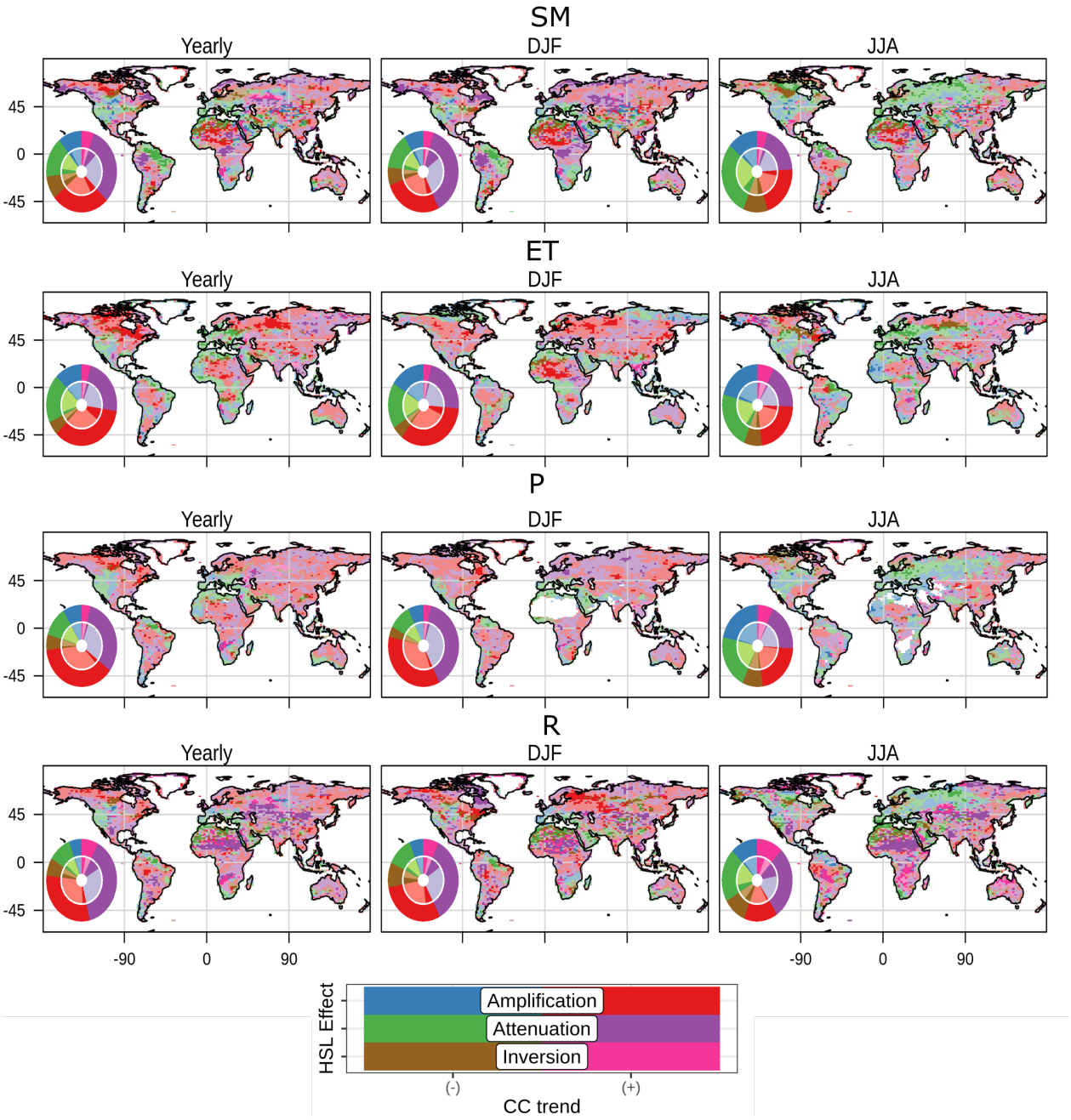

Figure A.5: Spatial distribution of hillslope flow modulation in yearly, boreal winter and boreal summer mean values for period 1980 – 2100, for SM, ET, P and R. Statistical significance of the trend is tested with a Mann-Kendall test (p = 0.05). The areas with insignificant in hillslope flow modulation have transparent colors. Doughnuts show the distribution of hillslope flow modulation (outer circle) and the corresponding partitioning of the significant & insignificant modulation (inner circle). We use a Mann-Kendall test (p = 0.05). The table below the maps define the modulation types and corresponding colors.

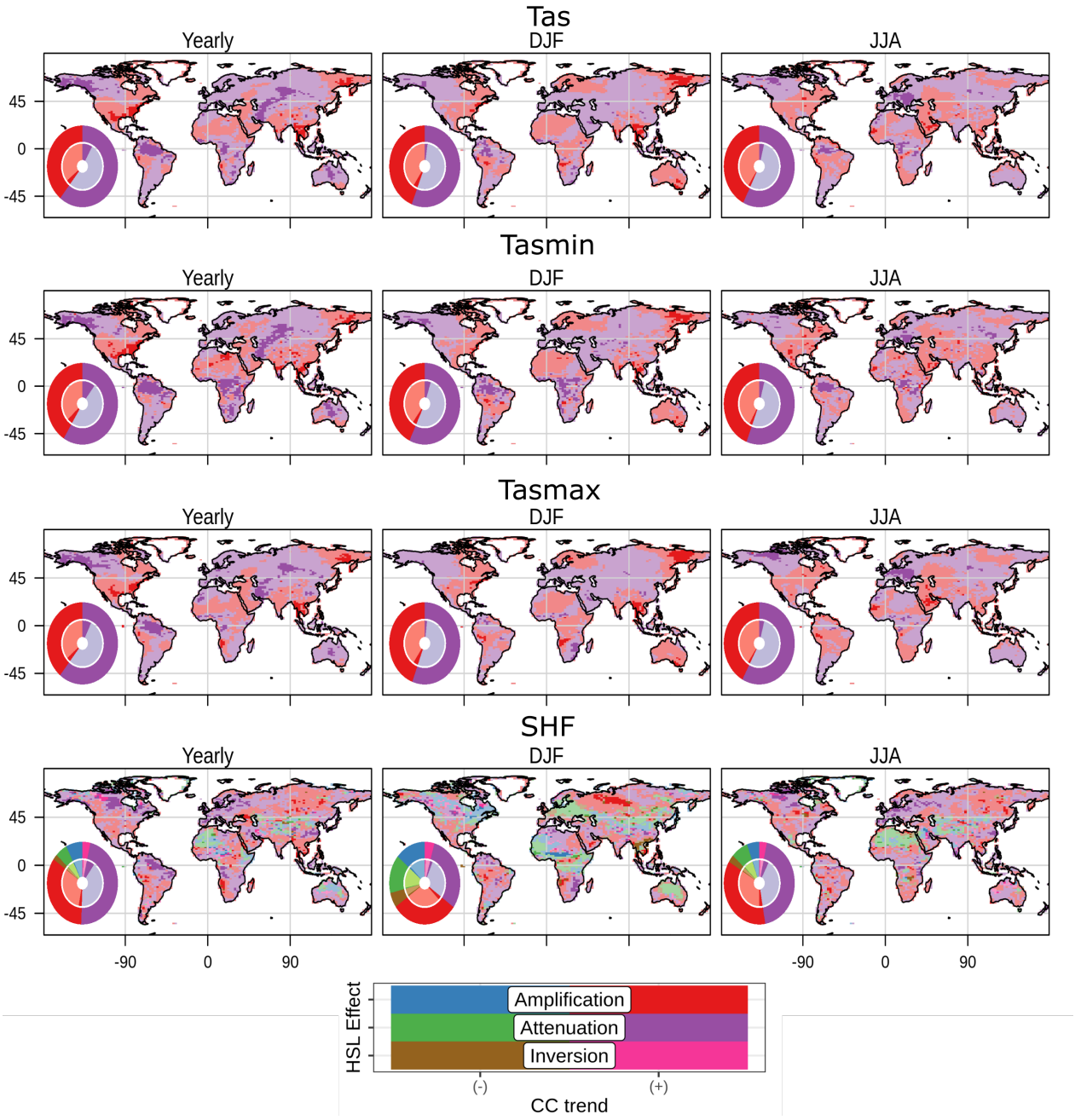

Figure A.6: Spatial distribution as Figure A.5 for Tas, Tasmin, Tasmax and SHF.

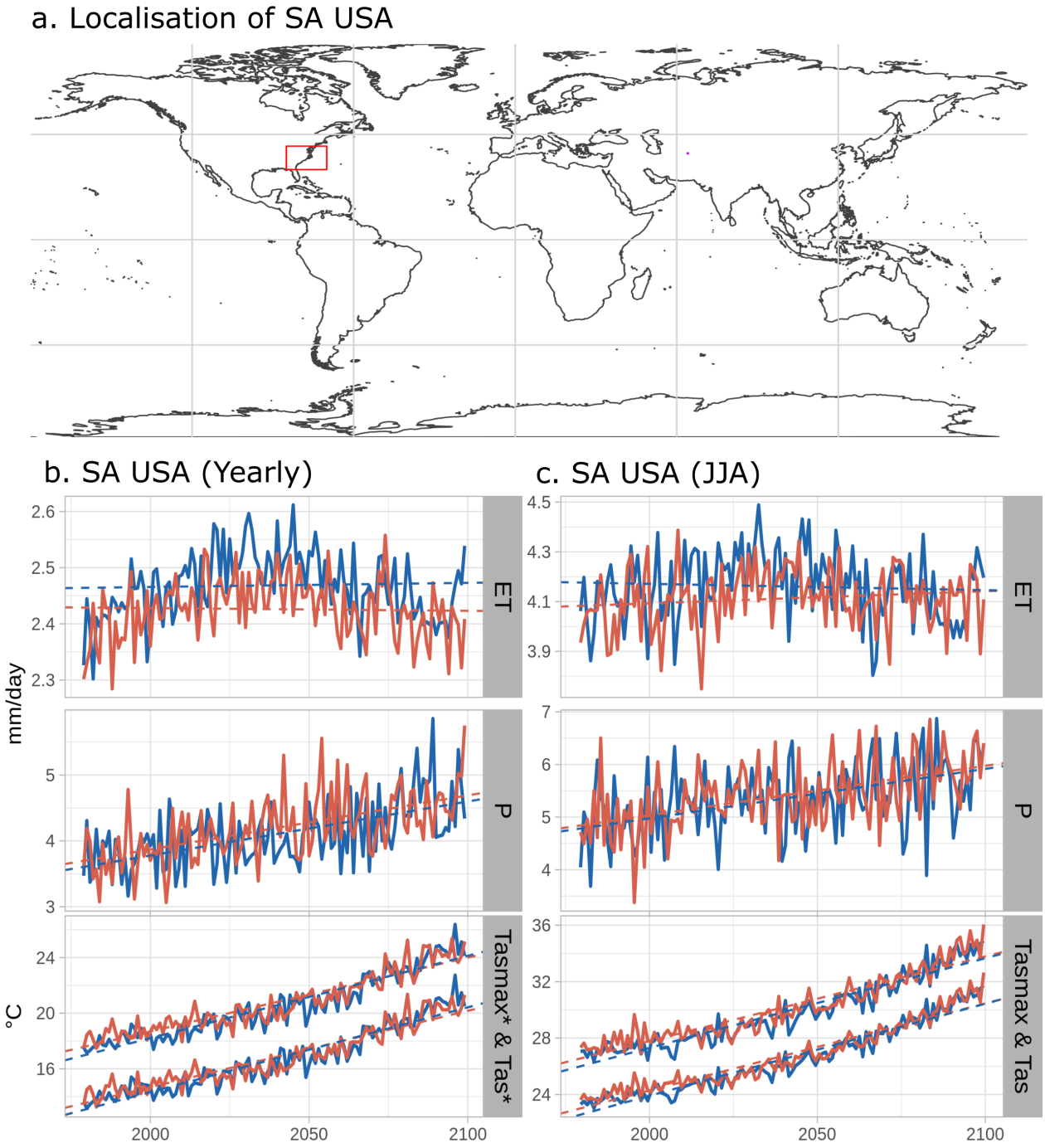

Figure A.7: Localization of USA South Atlantic (SA USA) (a), and regional average values of ET, P, Tas and Tasmax for yearly (b) and JJA means (c) for 1980-2100. Statistical significance of the modulation was tested with a Mann-Kendall test ($p = 0.05$), and significant trends are shown by a * in the vertical titles. In the Tasmax & Tas panel, the top blue and red lines correspond to Tasmax.

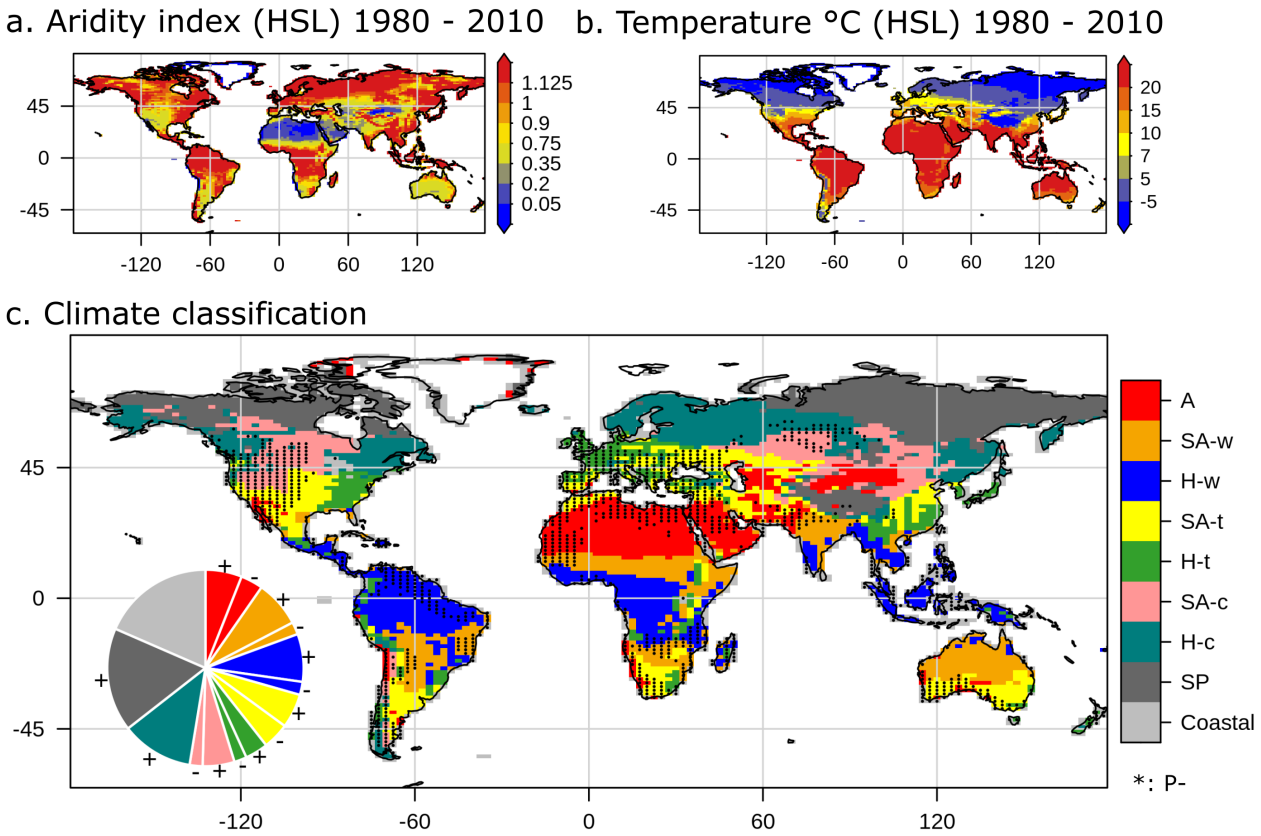

Figure A.8: Aridity index (a), and mean temperature (b) from HSL simulation for period 1980 – 2010. Simple climatic classification from both variables (c). Areas with negative P trends (P-) for the period 1980-2100 are stippled. The piechart shows the distribution of climate classes, separated among positive and negative P trends under climate change (identified by + and -). Climate classes correspond to arid (A), semiarid and warm (SA-w), humid and warm (H-w), semiarid and temperate (SA-t), humid and temperate (H-t), semiarid and cold (SA-c), humid and cold (H-c), and subpolar (SP). Refer to the text in the paper for definition of each class.

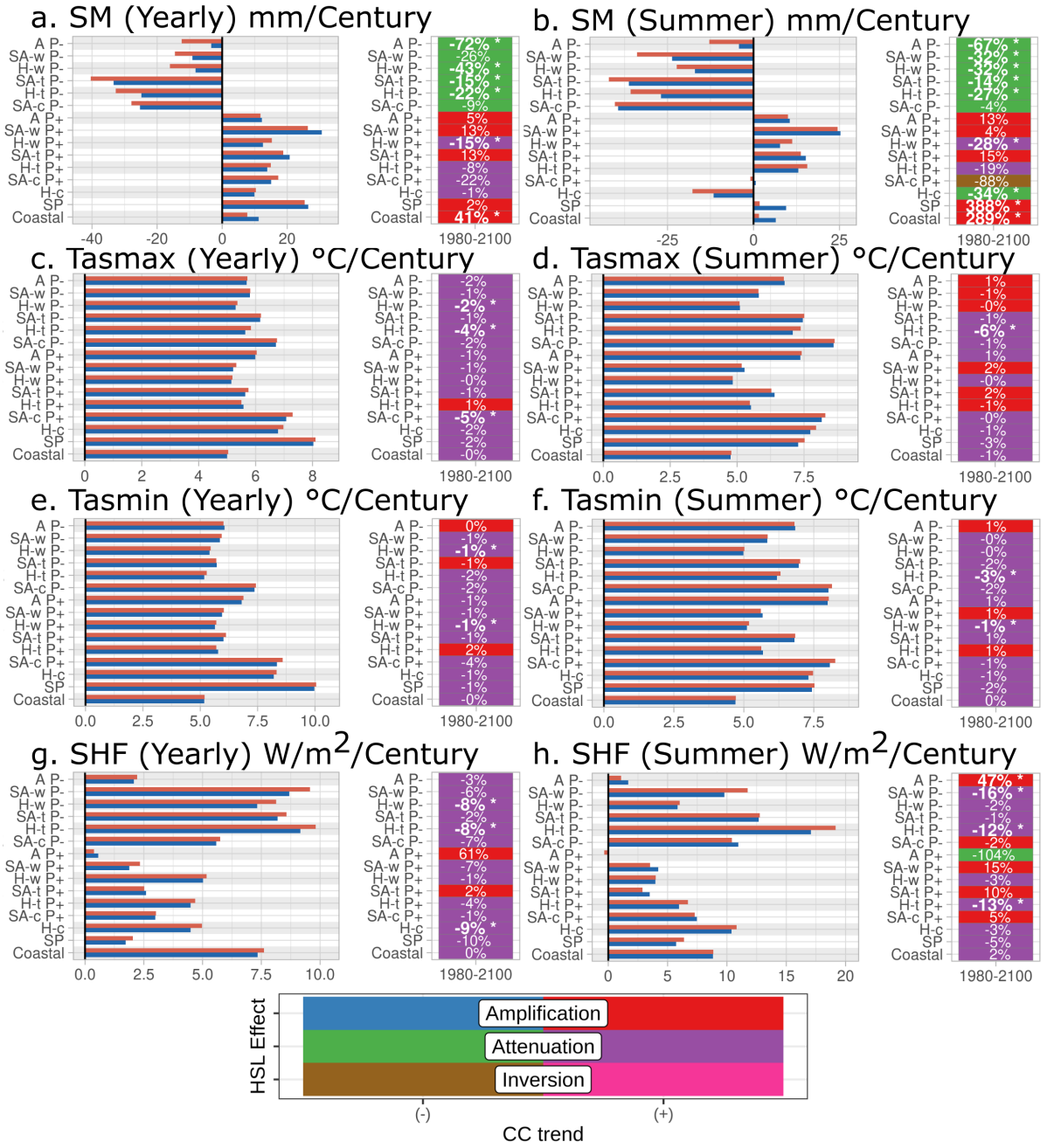

Figure A.9: Trends of regional average grid cells according to climatic classes in 1980 - 2100 for REF and HSL, and hillslope flow modulation in %, for (a, c, e, g) yearly values, (b, d, f, h) summer values. Summer is defined as JJA for northern grid cells and DJF for southern grid cells. Variables are (a, b) SM , (c, d) Tasmax, (e, f) Tasmin and (g, h) SHF. Statistical significance of the hillslope flow modulation was tested with the Mann-Kendall test (p = 0.05). Significant hillslope flow modulations are written in bold with an *, and the color of the cell corresponds to the modulation type as shown at the bottom. The percentage of modulation is calculated as for table 1 in the paper. Climate class names are the same as Figure A.8.

Appendix B

Supporting Information for "Validation of a new global irrigation scheme in the ORCHIDEE land surface model"

Introduction

This section completes the information shown in section 4.2. Figure B.1 shows volumes of water withdrawal for irrigation and of ET increase from ORCHIDEE and AQUASTAT for 1998-2002, as well as the irrigation rate from Sacks et al., 2009 while Figure B.2 shows information on the bias of irrigation rates, normalized by the are equipped for irrigation at country level, and the coefficient of variation of irrigation rates, using average irrigation rates simulations from table 4.2.

Figures B.3 and B.4 show difference between Irr and NoIrr for additional variables, including energy terms. Figure B.5 shows basins included in the analysis of the effect of the new irrigation module, and the corresponding discharge stations. Figure B.6 shows the fraction of irrigated paddy rice, with a focus on Southeast Asia.

Figure B.7 shows average monthly multiyear values for 1980-2013 for four chosen large basins. Finally, Figure B.8 shows the same information for the Seine river basin, with additional information on the source of water used for irrigation.

We also present two tables. Table B.1 shows goodness-of-fit metrics for ORCHIDEE discharge values and observed values from GRDC selected stations. We use four metrics: relative bias (equation B.1), the relative change of amplitude of average monthly values (equation B.2), the Pearson's correlation coefficient r (equation B.3, Helsel and Hirsch, 1992) and Kling-Gupta Efficiency KGE (equation B.4, Gupta et al., 2009; Kling et al., 2012).

$$B = \frac{\sum_{i=1}^{n} (S_i - O_i)}{\sum_{i=1}^{n} O_i}.100 \tag{B.1}$$

$$RelAmp = \frac{\max\left(S_j\right)_{j=1,12} - \min\left(S_j\right)_{j=1,12}}{\max\left(O_j\right)_{j=1,12} - \min\left(O_j\right)_{j=1,12}}.100 \tag{B.2}$$

$$r = \frac{\sum_{i=1}^{n}\left(S_i - \overline{S}\right).\left(O_i - \overline{O}\right)}{\sqrt{\sum_{i=1}^{n}\left(S_i - \overline{S}\right)^2}.\sqrt{\sum_{i=1}^{n}\left(O_i - \overline{O}\right)^2}} \tag{B.3}$$

$$KGE = 1 - ED = 1 - \sqrt{(r-1)^2 + (\sigma_s/\sigma_o - 1)^2 + (\mu_s/\mu_o - 1)^2} \tag{B.4}$$

Here S and O represents simulated and observed values, respectively, n represents the monthly values from the time-series, j represents one of 12 the months in a year, σ represents the stadard deviation, and μ represents the average value, with indices s and o indicating simulated or observed time series.

In table B.2 we show the sum of the capacity of dams used for irrigation. We also present the average values at large river basin for irrigated fraction and irrigated paddy fraction, and the bias of evapotranspiration and irrigation.

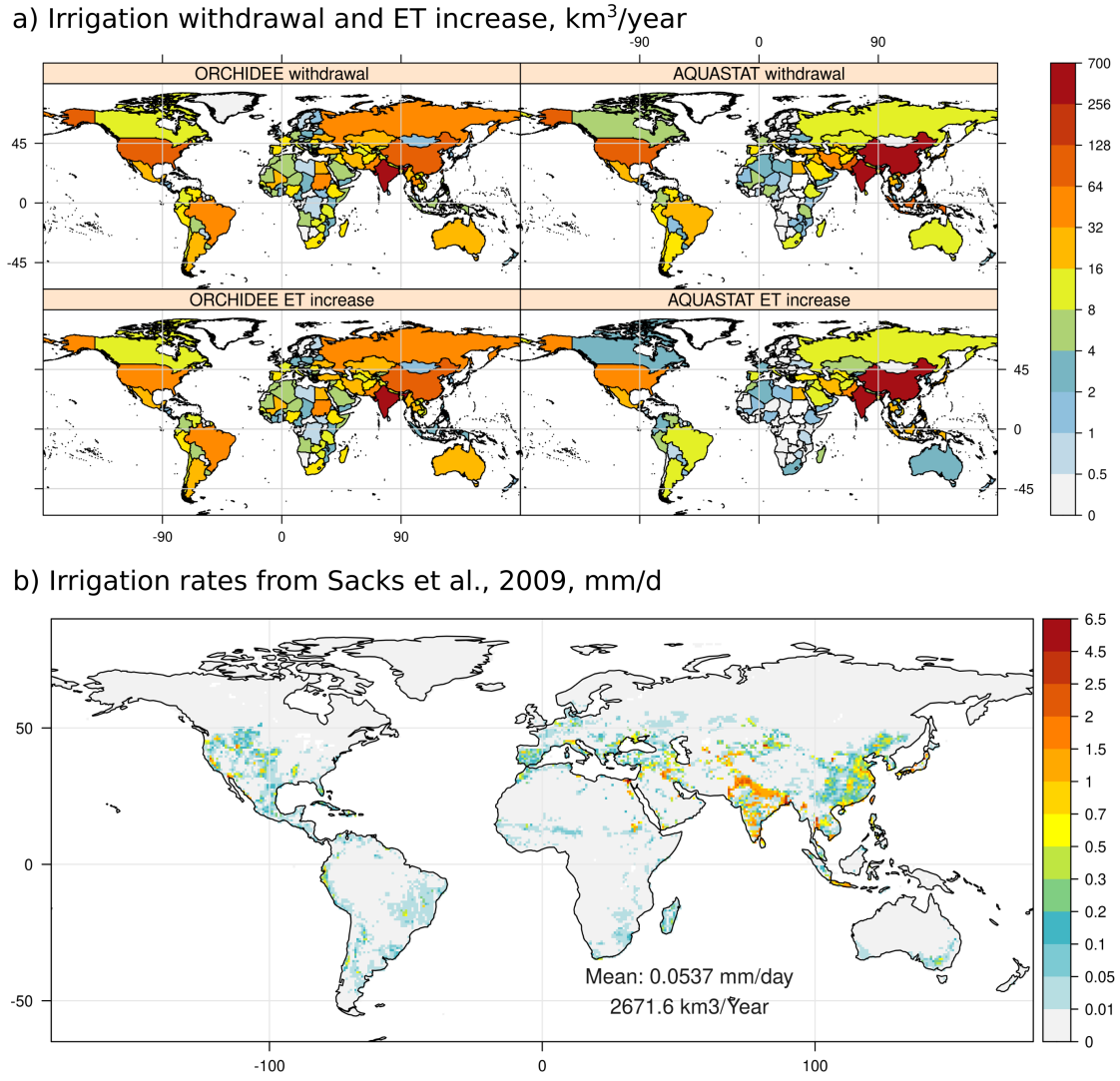

Figure B.1: Volumes of water withdrawal for irrigation and ET increase (called irrigation requirement in AQUASTAT dataset) by country from ORCHIDEE (Irr simulation, average value for 1998-2002), and AQUASTAT (value around 2000), in km^3/year (a). Irrigation rate from Sacks et al., 2009 for year 2000, mm/d.

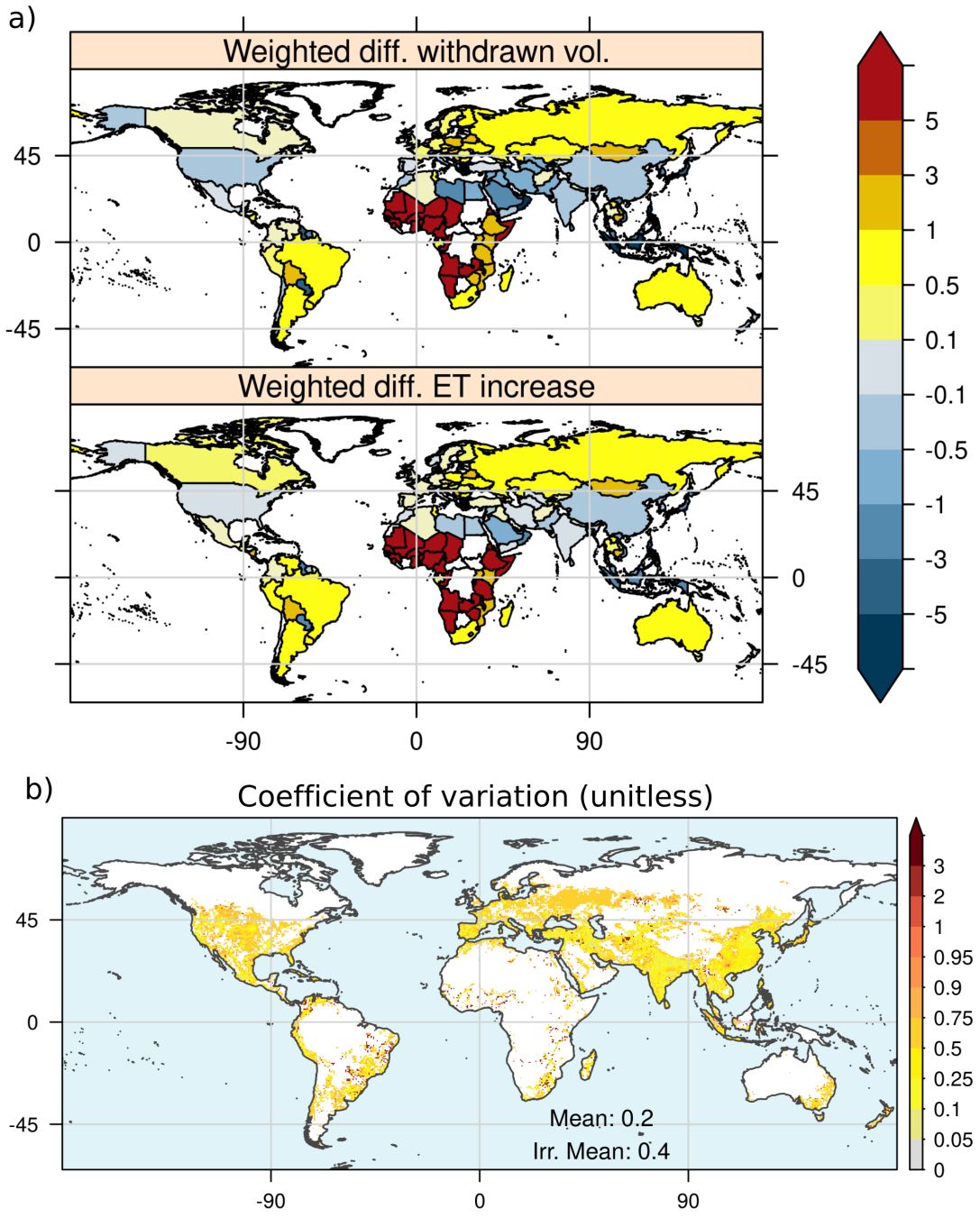

Figure B.2: Bias of irrigation between Irr (average value for 1998-2002) and AQUASTAT (value around year 2000), normalized by area equipped for irrigation by country, and difference of the increase of ET between Irr and AQUASTAT. Values in m3/m2. Coefficient of variation of irrigation rates (b). Average irrigation values of simulations from table 4.2. White correspond to grid-cells with no irrigated areas.

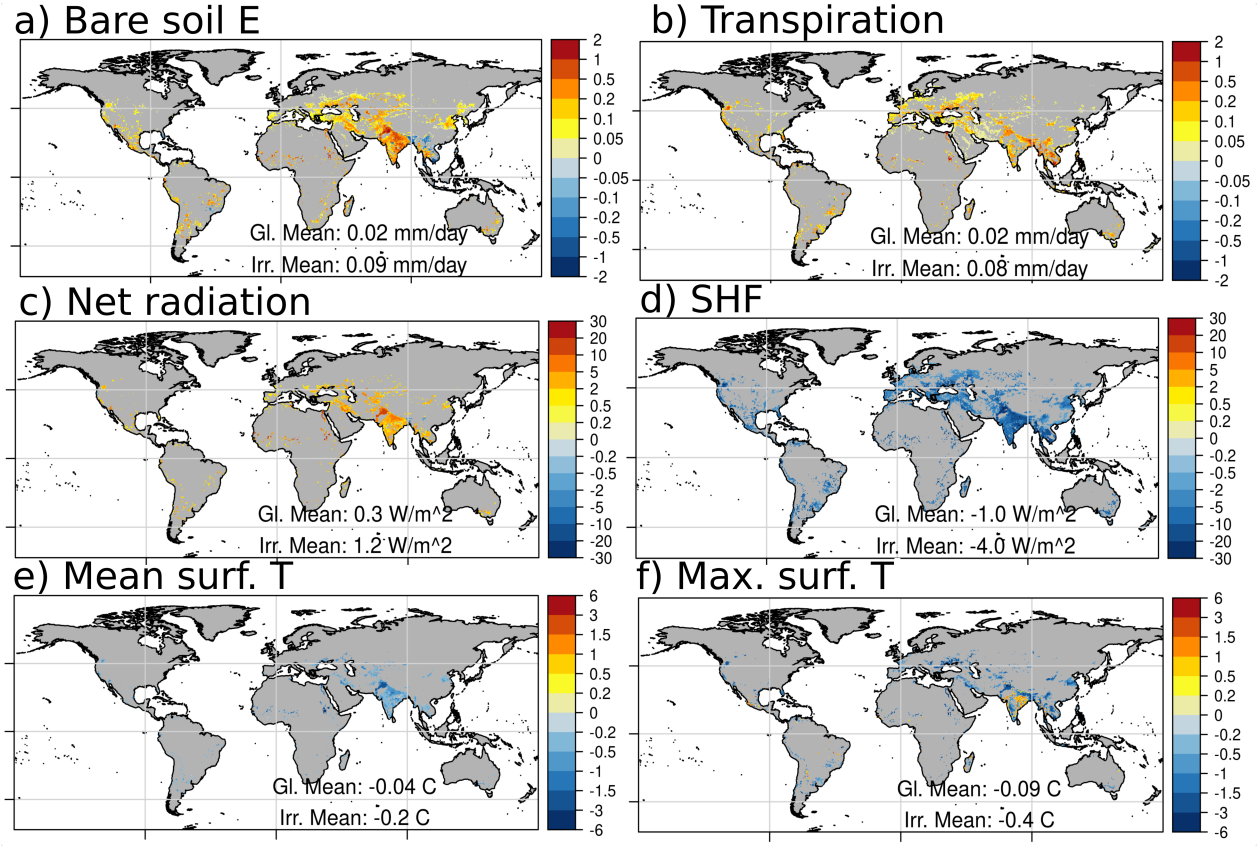

Figure B.3: Yearly average difference for 1980 - 2013 between Irr and NoIrr of bare soil E, mm/d (a), T, mm/d (b), net radiation W/m^2 (c), SHF, W/m^2 (d), mean surface temperature, °C (e), and max. surface temperature, °C (f). Statistical significance of the mean differences is tested at each point with a Student's test (p = 0.05). The areas with insignificant changes are left gray.

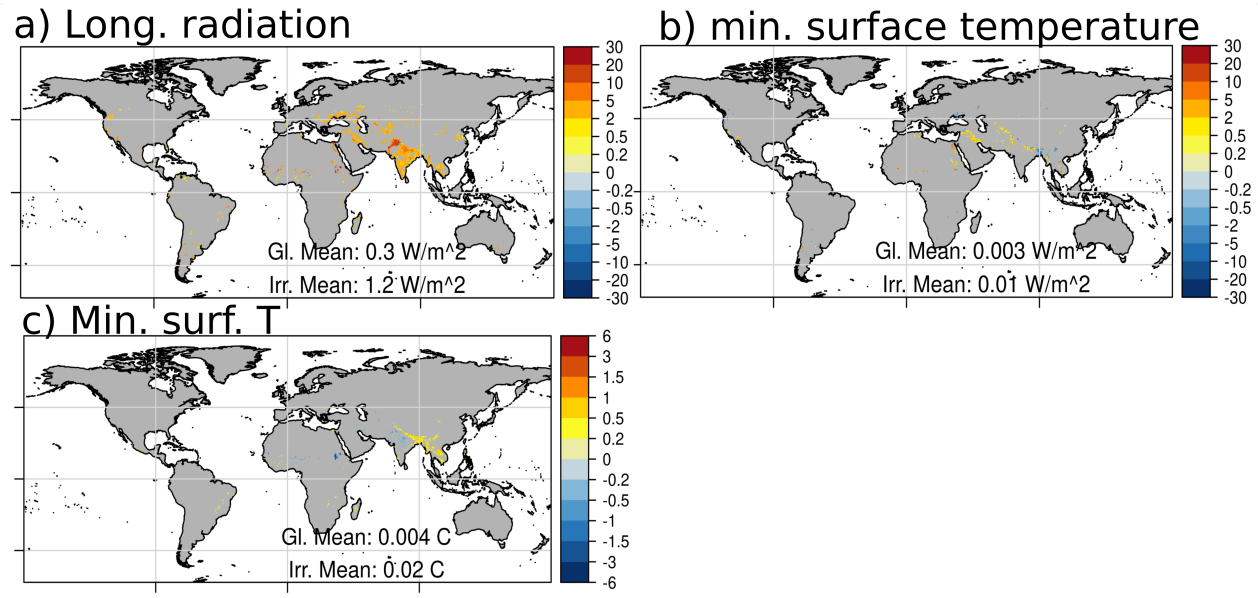

Figure B.4: Yearly average difference for 1980 - 2013 between Irr and NoIrr of net longwave radiation (a), net shortwave radiation (b), min. surface temperature (c). Statistical significance of the mean differences is tested at each point with a Student's test (p = 0.05). The areas with insignificant changes are left gray.

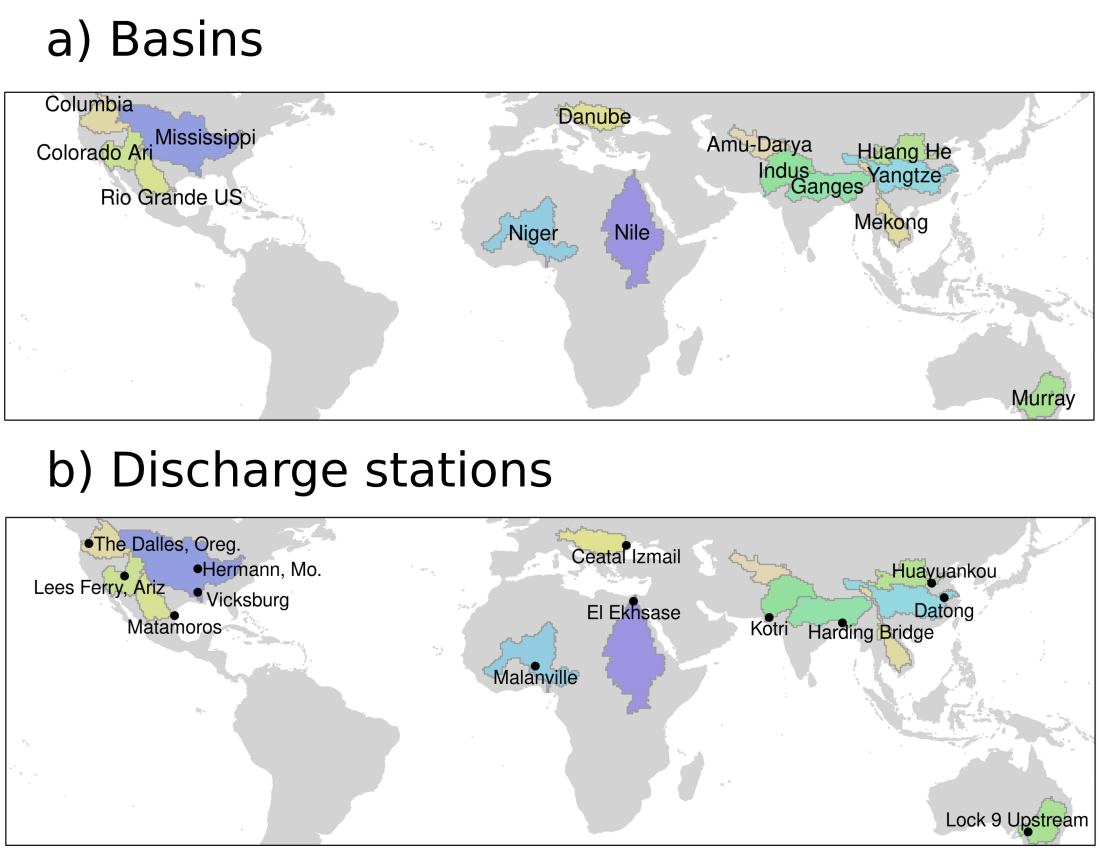

Figure B.5: Limits of large basins used in the regional analysis (a). Discharge stations used in the comparison with ORCHIDEE outputs (b).

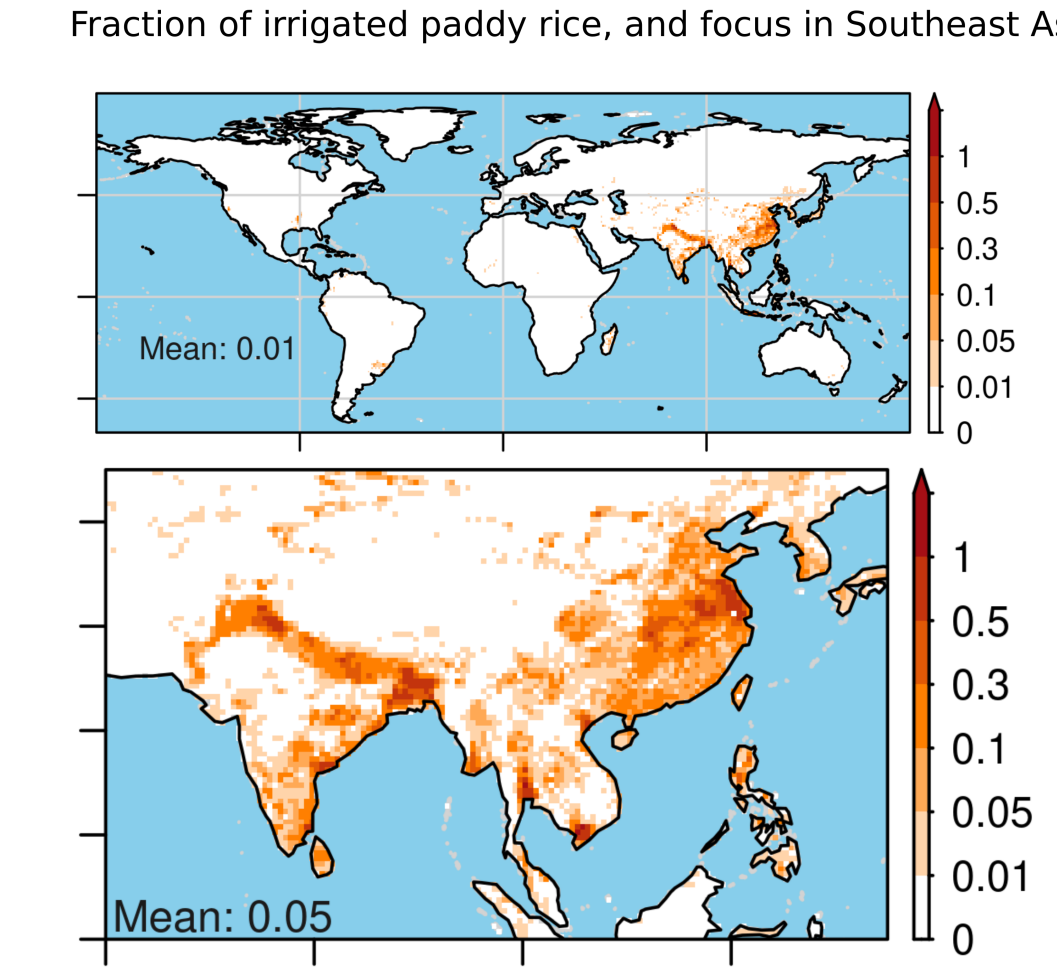

Figure B.6: Fraction of irrigated paddy rice, and focus on Southeast Asia. Data comes from MIRCA2000 (Portmann et al., 2010).

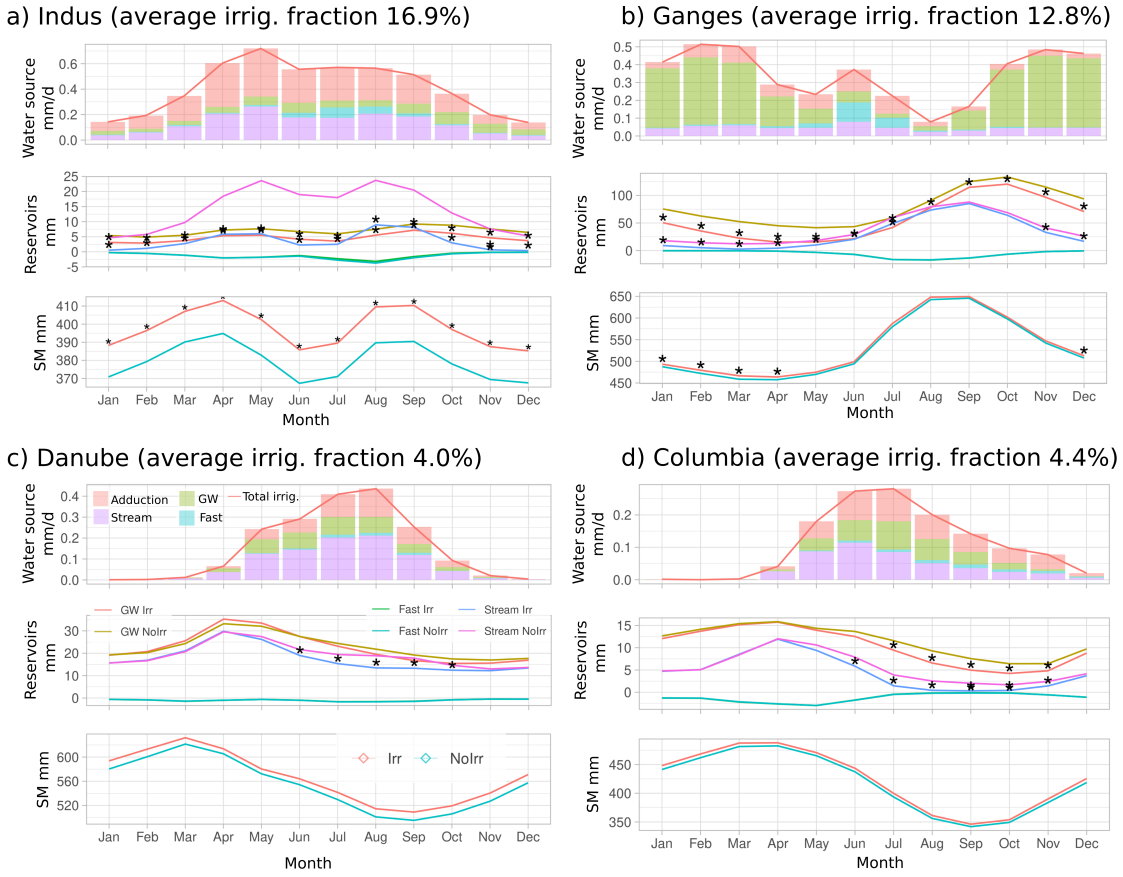

Figure B.7: Average multiyear monthly values for period 1980-2013 at basin scale for Indus (a), Ganges (b), Danube (c), Columbia (d). The first row presents water source for irrigation from Irr simulation in mm/day, the second presents the routing reservoirs in mm (values of fast reservoirs multiplied by -1 for display purposes), the third the soil moisture in mm, for both Irr and NoIrr simulations. Statistical significance of the modulation was tested with a t-student test (p = 0.05), and significant differences are shown by a * over the values from the Irr simulation.

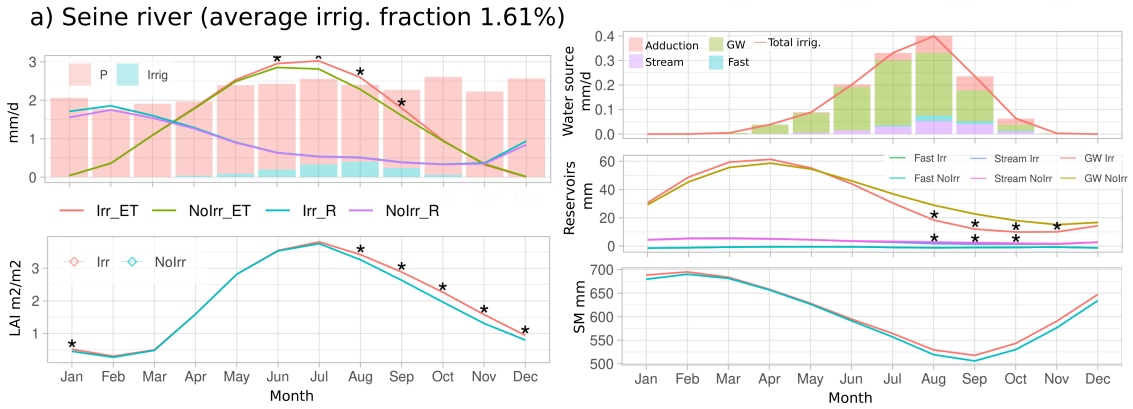

Figure B.8: Average multiyear monthly values for period 1980-2013 at basin scale for Seine river basin. In the first column, The first row presents ET, R, P and irrigation values (mm/d), second row presents the mean LAI values (m2/m2). In the second column, the first row presents water source for irrigation from Irr simulation in mm/day, the second presents the routing reservoirs in mm, the third the soil moisture in mm, for both Irr and NoIrr simulations. Statistical significance of the modulation was tested with a t-student test ($p = 0.05$), and significant differences are shown by a * over the values from the Irr simulation.

Table B.1: Goodness-of-fit metrics for ORCHIDEE discharge values and GRDC selected stations. RelAmpli stands for relative change on amplitude, r for Pearson correlation coefficient, KGE for Kling-Gupta efficiency.

	Metric	Irr-NoIrr(%)	Bias %		RelAmpli%		r		KGE	
ID	River@Station		NoIrr	Irr	NoIrr	Irr	NoIrr	Irr	NoIrr	Irr
1	Columbia @ The Dalles, Oreg.	-26.54	-41.43	-56.97	8.47	25.68	0.8	0.69	0.54	0.34
2	Colorado (Ariz.) @ Lees Ferry, Ariz	-42.35	-46.84	-69.36	78.69	134.17	0.08	0.01	-0.03	-0.21
3	Mississippi @ Vicksburg	-5.08	-7.23	-11.94	-54	-47.65	0.62	0.69	0.43	0.49
4	Missouri @ Hermann, Mo.	-24.08	2.24	-22.38	-43.27	-54.33	0.59	0.69	0.59	0.61
5	Rio Grande (MX) @ Matamoros	-81.43	6387.44	1104.72	8349.66	2306.7	0.12	0.13	-71.71	-17.76
6	Nile @ El Ekhsase	-33.43	794.01	495.14	1736.17	1949.26	-0.27	-0.31	-22.15	-23.15
7	Niger @ Malanville	-9.05	506.67	451.77	360.38	373.96	0.58	0.61	-5.25	-4.85
8	Danube @ Ceatal Izmail	-16.76	10.73	-7.83	29.72	23.96	0.67	0.83	0.63	0.66
9	Ganges-Brahmaputra @ Harding Bridge	-25.59	82.23	35.6	7.07	18.49	0.77	0.75	0.15	0.55
10	Yellow River @ Huayuankou	-67.66	-3.93	-68.93	-40.77	-65.64	0.54	0.2	0.39	-0.18
11	Yangtze @ Datong	-2.08	-9.99	-11.87	-36.72	-37.98	0.88	0.88	0.64	0.63
12	Murray @ Lock 9 Upstream	-53.31	832.45	335.41	196.11	84.54	0.47	0.48	-8.13	-3.53
13	Indus @ Kotri	-90.79								
14	Amu-Darya @ Chatly	-65.8								

Table B.2: Dams capacity used for irrigation, irrigated fraction and paddy irrigated fraction, ET and irrigation bias at large river basin scale

Id	**Basin**	**Dams for irrig.** $10^6 m^3$	**Irrigated fraction**	**Irrigated paddy fraction**	**NoIrr-Gleam mm/d**	**Irr-Gleam mm/d**	**NoIrr-Fluxcom mm/d**	**Irr-Fluxcom mm/d**	**Irrigation bias mm/d**
1	Nile	173411	0.010	0.001	0.015	0.114	-0.508	-0.361	0.044
2	Mississippi	16915	0.037	0.002	0.110	0.142	-0.079	-0.047	-0.030
3	Niger	16400	0.001	0.001	0.009	0.055	-0.485	-0.427	0.023
4	Yangtze	19186	0.082	0.091	-0.216	-0.188	-0.370	-0.342	-0.102
5	Ganges	32589	0.178	0.080	-0.016	0.280	-0.364	-0.068	-0.124
6	Indus	44828	0.190	0.052	0.079	0.470	-0.724	-0.323	-0.043
7	Murray	17484	0.021	0.001	-0.006	0.087	-0.162	-0.069	0.067
8	Huang He	2337	0.078	0.021	0.080	0.163	-0.061	0.022	-0.042
9	Colorado Ari	6355	0.021	0.000	0.000	0.053	-0.327	-0.273	-0.031
10	Rio Grande US	19478	0.021	0.000	0.095	0.163	-0.208	-0.140	0.036
11	Danube	1762	0.037	0.000	-0.044	0.080	-0.433	-0.308	0.120
12	Mekong	4379	0.027	0.030	-0.265	-0.068	-0.431	-0.234	0.103
13	Columbia	22713	0.044	0.000	-0.343	-0.245	-0.246	-0.148	-0.038
14	Amu-Darya	25500	0.072	0.002	-0.010	0.161	-0.611	-0.440	-0.073

List of abbreviations

Symbols

I_k^{max} Maximum volume of water intercepted in the canopy.
LW Longwave Radiation.
R_n Net Radiation.
SW Shortwave Radiation.
W_i Absolute soil moisture in layer i.
α_{sw} Albedo.
β user-dependent parameter to define the soil moisture target.
β_{ET} Resistance coefficient to potential evaporation.
λ Heat of Vaporization.
θ Volumetric Soil Moisture.
r_a The aerodynamic resistance.
r_{leaf} The leaf resistance.
r_{struct} The structural resistance.

A

AAI Area Actually Irrigated.
ABL Atmospheric Boundary Layer.
AEI Area Equipped for Irrigated.
AR5 Fifth Assessment Report from the IPCC.
AR6 Sixth Assessment Report from the IPCC.

B

BLUEGEM Biosphere and Land Use Exchanges with Groundwater and soils in Earth system Models.
BNPE La Banque Nationale des Prélèvements quantitatifs en Eau.

C

CMIP5 Coupled Model Intercomparison Project Phase 5.
CMIP6 Coupled Model Intercomparison Project Phase 6.
CO_2 Carbon Dioxide.

CRD Cumulative Root Density.
CRUNCEP CRU TS3.2 and NCEP reanalysis combination dataset.

D

D Deep drainage.
DGVM Dynamic Global Vegetation Model.
DJF Austral Summer.

E

ESM Earth System Model.
ET Evapo-Transpiration.

F

FAO Food and Agriculture Organization of the United Nations.
Fluxcom An initiative to upscale biosphere-atmosphere fluxes from FLUXNET sites to continental and global scales.

G

GCM General Circulation Model.
GHM Global Hydrology Models.
Gleam Global Land Evaporation Amsterdam Model.
GPP Gross Primary Production.
GRACE Gravity Recovery and Climate Experiment.
GRanD Global Reservoir and Dams dataset.
GRDC Global Runoff Data Centre.
GSWP3 Global Soil Wetness Project Phase 3.
GW Groundwater.
GWL Global Warming Level.

H

HID Historical Irrigation Dataset.

I

IGEM Impact of Groundwater on Earth system Models.
IPCC Intergovernmental Panel on Climate Change.
IPSL Institut Pierre-Simon Laplace.

J

JJA Boreal Summer.

L

LAI Leaf Area Index.
LIAISE Land surface Interactions with the Atmosphere over the Iberian Semi-arid Environment.
LMDZ Laboratoire de Météorologie Dynamique - Zoom.
LSM Land Surface Model.
LUH Land-Use Harmonization.

M

MIRCA2000 Global data set of monthly irrigated and rainfed crop areas around the year 2000.

O

ORCHIDEE ORganizing Carbon and Hydrology In Dynamics EcosystEm.

P

P Precipitation.
PET Potential Evapo-Transpiration.
PFT Plant Functional Type.

R

R Total Runoff.
RCP Representative Concentration Pathway.

S

SECHIBA Schématisation des Echanges Hydriques à l'interface entre la Biosphère et l'Atmosphère.
SHF Sensible Heat Flux.
SIC Sea Ice Content.
SM Soil Moisture.
SSP Shared Socioeconomic Pathways.
SST Sea Surface Temperature.
STOMATE Saclay Toulouse Orsay Model for Analysis of Terrestrial Ecosytems.
SW Surface water.

T

Tas Mean Air Temperature.
Tasmax Average Daily Maximum Temperature.

Tasmin Average Daily Minimum Temperature.
TOPMODEL TOPography-based hydrological MODEL.
TWSA Total Water Storage Anomaly.

U

USDA U.S. Department of Agriculture.

V

VPD Vapor Pressure Deficit.

W

WFDEI WATCH Forcing Data methodology applied to ERA-Interim reanalysis data.
WT Water Table.

Bibliography

Adler, Robert, Mathew Sapiano, George Huffman, Jian-jian Wang, Guojun Gu, David Bolvin, Long Chiu, Udo Schneider, Andreas Becker, Eric Nelkin, Pingping Xie, Ralph Ferraro, and Dong-Bin Shin (2018). "The Global Precipitation Climatology Project (GPCP) Monthly Analysis (New Version 2.3) and a Review of 2017 Global Precipitation". In: *Atmosphere* 9.4, p. 138. ISSN: 2073-4433. DOI: 10.3390/atmos9040138. URL: http://www.mdpi.com/2073-4433/9/4/138 cited on page 60.

Agreste (2010). *Recensement Agricole 2010* cited on page 118.

Alexander, Lisa V., X. Zhang, T. C. Peterson, J. Caesar, B. Gleason, A. M. G. Klein Tank, M. Haylock, D. Collins, B. Trewin, F. Rahimzadeh, et al. (2006). "Global observed changes in daily climate extremes of temperature and precipitation". In: *Journal of Geophysical Research* 111.D5, p. D05109. ISSN: 0148-0227. DOI: 10.1029/2005JD006290. URL: http://doi.wiley.com/10.1029/2005JD006290 cited on page 77.

Alléon, Julien (2022). *Technical Note: Description of the energy budgets in ORCHIDEE*. Tech. rep. Paris, France: Laboratoire des Sciences du Climat et de l'Environnement, p. 106. URL: http://forge.ipsl.jussieu.fr/orchidee/attachment/wiki/Documentation/LMDZ_coupling/Technical_note__Current_energy_budget_in_ORCHIDEE.pdf cited on pages 32, 34, 36, 37, 39, 40.

Anyah, Richard O., Christopher P. Weaver, Gonzalo Miguez-Macho, Ying Fan, and Alan Robock (2008). "Incorporating water table dynamics in climate modeling: 3. Simulated groundwater influence on coupled land-atmosphere variability". In: *Journal of Geophysical Research* 113.D7, p. D07103. ISSN: 0148-0227. DOI: 10.1029/2007JD009087. URL: http://doi.wiley.com/10.1029/2007JD009087 cited on pages 25, 49, 74.

Arboleda Obando, Pedro Felipe, Agnès Ducharne, Frédérique Cheruy, Anne Jost, Josefine Ghattas, Jeanne Colin, and Camille Nous (2022). "Influence of Hillslope Flow on Hydroclimatic Evolution Under Climate Change". In: *Earth's Future* 10.9, pp. 1–24. ISSN: 23284277. DOI: 10.1029/2021EF002613 cited on pages 25, 28, 30, 47.

Band, Lawrence E., Pitman Patterson, Ramakrishna Nemani, and Steven W. Running (1993). "Forest ecosystem processes at the watershed scale: incorporating hillslope hydrology". In: *Agricultural and Forest Meteorology* 63.1-2, pp. 93–126. ISSN: 01681923. DOI: 10.1016/0168-1923(93)90024-C. URL: https://linkinghub.elsevier.com/retrieve/pii/016819239390024C cited on pages 49, 53.

Barella-Ortiz, A., J. Polcher, A. Tuzet, and K. Laval (2013). "Potential evaporation estimation through an unstressed surface-energy balance and its sensitivity to climate change". In: *Hydrology and Earth System Sciences* 17.11, pp. 4625–4639. ISSN: 1607-7938. DOI: 10.5194/hess-17-4625-2013. URL: https://hess.copernicus.org/articles/17/4625/2013/ cited on page 88.

Barlage, Michael, Fei Chen, Roy Rasmussen, Zhe Zhang, and Gonzalo Miguez-Macho (2021). "The Importance of Scale-Dependent Groundwater Processes in Land-Atmosphere Interactions Over the Central United States". In: *Geophysical Research Letters* 48.5, pp. 1–10. ISSN: 0094-8276. DOI: 10.1029/2020GL092171. URL: https://onlinelibrary.wiley.com/doi/10.1029/2020GL092171 cited on page 49.

Beck, Hylke E., Albert I.J.M. Van Dijk, Vincenzo Levizzani, Jaap Schellekens, Diego G. Miralles, Brecht Martens, and Ad De Roo (2017). "MSWEP: 3-hourly 0.25° global gridded precipitation (1979-2015) by merging gauge, satellite, and reanalysis data". In: *Hydrology and Earth System Sciences* 21.1, pp. 589–615. ISSN: 16077938. DOI: 10.5194/hess-21-589-2017 cited on page 60.

Beck, Hylke E., Niklaus E. Zimmermann, Tim R. McVicar, Noemi Vergopolan, Alexis Berg, and Eric F. Wood (2018). "Present and future köppen-geiger climate classification maps at 1-km resolution". In: *Scientific Data* 5, pp. 1–12. ISSN: 20524463. DOI: 10.1038/sdata.2018.214 cited on pages 50, 68, 69.

Berg, Alexis, Kirsten Findell, Benjamin Lintner, Alessandra Giannini, Sonia I. Seneviratne, Bart Van Den Hurk, Ruth Lorenz, Andy Pitman, Stefan Hagemann, Arndt Meier, Frédérique Cheruy, Agnès Ducharne, Sergey Malyshev, and P. C.D. Milly (2016). "Land-atmosphere feedbacks amplify aridity increase over land under global warming". In: *Nature Climate Change* 6.9, pp. 869–874. ISSN: 17586798. DOI: 10.1038/nclimate3029 cited on pages 12, 49, 75.

Berg, Alexis, Benjamin R. Lintner, Kirsten L. Findell, Sergey Malyshev, Paul C. Loikith, and Pierre Gentine (2014). "Impact of Soil Moisture–Atmosphere Interactions on Surface Temperature Distribution". In: *Journal of Climate* 27.21, pp. 7976–7993. ISSN: 0894-8755. DOI: 10.1175/JCLI-D-13-00591.1. URL: http://journals.ametsoc.org/doi/10.1175/JCLI-D-13-00591.1 cited on page 5.

Berg, Alexis and Justin Sheffield (2019). "Evapotranspiration Partitioning in CMIP5 Models: Uncertainties and Future Projections". In: *Journal of Climate* 32.10, pp. 2653–2671. ISSN: 0894-8755. DOI: 10.1175/JCLI-D-18-0583.1. URL: http://journals.ametsoc.org/doi/10.1175/JCLI-D-18-0583.1%20https://journals.ametsoc.org/jcli/article/32/10/2653/343869/Evapotranspiration-Partitioning-in-CMIP5-Models cited on page 12.

Berg, Alexis, Justin Sheffield, and P. C. D. Milly (2017). "Divergent surface and total soil moisture projections under global warming". In: *Geophysical Research Letters* 44.1, pp. 236–244. ISSN: 00948276. DOI: 10.1002/2016GL071921. URL: http://doi.wiley.com/10.1002/2016GL071921 cited on page 5.

Beven, K. J. (2012). *Rainfall-runoff modelling: the primer*, pp. 1–457. ISBN: 9781119951001. DOI: 10.1002/9781119951001. URL: http://www.scopus.com/inward/record.url?eid=2-s2.0-84888749158&partnerID=tZOtx3y1 cited on page 6.

Beven, K. J. and M. J. Kirby (1979). "A physically based, variable contributing area model of basin hydrology". In: *Hydrological Sciences Bulletin* 24.1, pp. 43–69. ISSN: 0303-6936. DOI: 10.1080/02626667909491834. URL: http://www.tandfonline.com/doi/abs/10.1080/02626667909491834 cited on pages 22, 49, 53, 74.

Beven, Keith J, Mike J Kirkby, Jim E Freer, and Rob Lamb (2021). "A history of TOPMODEL". In: *Hydrology and Earth System Sciences* 25.2, pp. 527–549. ISSN: 1607-7938. DOI: 10.5194/hess-25-527-2021. URL: https://hess.copernicus.org/articles/25/527/2021/ cited on page 50.

Bitencourt, Daniel P., Márcia V. Fuentes, Alberto E. Franke, Rafael B. Silveira, and Maikon P. A. Alves (2020). "The climatology of cold and heat waves in Brazil from 1961 to 2016". In: *International Journal of Climatology* 40.4, pp. 2464–2478. ISSN: 0899-8418. DOI: 10.1002/joc.6345. URL: https://onlinelibrary.wiley.com/doi/10.1002/joc.6345 cited on page 77.

Blyth, Eleanor M., Vivek K. Arora, Douglas B. Clark, Simon J. Dadson, Martin G. De Kauwe, David M. Lawrence, Joe R. Melton, Julia Pongratz, Rachael H. Turton, Kei Yoshimura, and Hua Yuan (2021). "Advances in Land Surface Modelling". In: *Current Climate Change Reports* 7.2, pp. 45–71. ISSN: 2198-6061. DOI: 10.1007/s40641-021-00171-5. URL: https://link.springer.com/10.1007/s40641-021-00171-5 cited on pages 22, 23, 28.

Boucher, O., G. Myhre, and A. Myhre (2004). "Direct human influence of irrigation on atmospheric water vapour and climate". In: *Climate Dynamics* 22.6-7, pp. 597–603. ISSN: 0930-7575. DOI: 10.1007/s00382-004-0402-4. URL: http://link.springer.com/10.1007/s00382-004-0402-4 cited on page 29.

Boucher, Olivier, Jérôme Servonnat, Anna Lea Albright, Olivier Aumont, Yves Balkanski, Vladislav Bastrikov, Slimane Bekki, Rémy Bonnet, Sandrine Bony, Laurent Bopp, et al. (2020). "Presentation and Evaluation of the IPSL-CM6A-LR Climate Model". In: *Journal of Advances in Modeling Earth Systems* 12.7, pp. 1–52. ISSN: 1942-2466. DOI: 10.1029/2019MS002010. URL: https://onlinelibrary.wiley.com/doi/abs/10.1029/2019MS002010 cited on pages 31, 50, 51, 55, 88–90.

Brouillet, Audrey and Sylvie Joussaume (2019). "Investigating the Role of the Relative Humidity in the Co-Occurrence of Temperature and Heat Stress Extremes in CMIP5 Projections". In: *Geophysical Research Letters* 46.20, pp. 11435–11443. ISSN: 0094-8276. DOI: 10.1029/2019GL084156. URL: https://onlinelibrary.wiley.com/doi/abs/10.1029/2019GL084156 cited on page 77.

Brunner, Philip, Peter G. Cook, and Craig T. Simmons (2011). "Disconnected Surface Water and Groundwater: From Theory to Practice". In: *Ground Water* 49.4, pp. 460–467. ISSN:

0017467X. DOI: 10.1111/j.1745-6584.2010.00752.x. URL: https://onlinelibrary.wiley.com/doi/10.1111/j.1745-6584.2010.00752.x cited on page 74.

Brutsaert, Wilfried (2005). *Hydrology*. Vol. 43. 07. Cambridge University Press, pp. 43–4036–43–4036. ISBN: 9780521824798. DOI: 10.1017/CBO9780511808470. URL: https://www.cambridge.org/core/product/identifier/9780511808470/type/book cited on pages 6, 8, 9, 54.

Budyko, M I (1974). *Climate and life*. Ed. by D H Miller. New York: Academic Press, INC., p. 526. ISBN: 0121394506 cited on page 4.

Burn, Donald H. and Mohamed A. Hag Elnur (2002). "Detection of hydrologic trends and variability". In: *Journal of Hydrology* 255.1-4, pp. 107–122. ISSN: 00221694. DOI: 10.1016/S0022-1694(01)00514-5 cited on page 61.

Cai, Danlu, Klaus Fraedrich, Frank Sielmann, Yanning Guan, and Shan Guo (2016). "Land-Cover Characterization and Aridity Changes of South America (1982–2006): An Attribution by Ecohydrological Diagnostics". In: *Journal of Climate* 29.22, pp. 8175–8189. ISSN: 0894-8755. DOI: 10.1175/JCLI-D-16-0024.1. URL: http://journals.ametsoc.org/doi/10.1175/JCLI-D-16-0024.1 cited on page 4.

Campoy, A., A. Ducharne, F. Cheruy, F. Hourdin, J. Polcher, and J. C. Dupont (2013). "Response of land surface fluxes and precipitation to different soil bottom hydrological conditions in a general circulation model". In: *Journal of Geophysical Research: Atmospheres* 118.19, pp. 10, 725–10, 739. ISSN: 2169897X. DOI: 10.1002/jgrd.50627. URL: http://doi.wiley.com/10.1002/jgrd.50627 cited on pages 32, 33, 41, 49, 51, 52, 54, 90, 131.

Campoy, Aurélien (2013). "Influence de l'hydrologie souterraine sur la modélisation du climat à l'échelle régionale et globale". NNT : . tel-00934826. Université Pierre et Marie Curie - Paris VI, p. 184 cited on pages 35, 37, 41.

Carsel, Robert F. and Rudolph S Parrish (1988). "Developing joint probability distributions of soil water retention characteristics". In: *Water Resources Research* 24.5, pp. 755–769. ISSN: 00431397. DOI: 10.1029/WR024i005p00755. URL: http://doi.wiley.com/10.1029/WR024i005p00755 cited on pages 33, 41, 52.

Cherlet, M, C Hutchinson, J Reynolds, J Hill, S Sommer, and G von Maltitz (2018). *World Atlas of Desertification*. Third edit. Luxembourg: Publication office of the European Union, p. 252. DOI: 10.2760/06292 cited on page 69.

Cheruy, F. (2018). "Etude par modélisation des interactions surface-atmosphère à l'échelle globale". HDR. Sorbonne Universite, p. 111 cited on pages 36, 37, 43, 44.

Cheruy, F., J. L. Dufresne, S. Aït Mesbah, J. Y. Grandpeix, and F. Wang (2017). "Role of Soil Thermal Inertia in Surface Temperature and Soil Moisture-Temperature Feedback". In: *Journal of Advances in Modeling Earth Systems* 9.8, pp. 2906–2919. ISSN: 19422466. DOI: 10.1002/2017MS001036. URL: http://doi.wiley.com/10.1002/2017MS001036 cited on page 57.

Cheruy, Frédérique, Agnés Ducharne, Frédéric Hourdin, Ionela Musat, Etienne Vignon, Guillaume Gastineau, Vladislav Bastrikov, Nicolas Vuichard, Binta Diallo, Jean-Louis Dufresne, et al. (2020). "Improved near surface continental climate in IPSL-CM6A-LR by combined evolutions of atmospheric and land surface physics". In: *Journal of Advances in Modeling Earth Systems*. ISSN: 1942-2466. DOI: 10.1029/2019MS002005. URL: https://onlinelibrary.wiley.com/doi/abs/10.1029/2019MS002005 cited on pages 23, 31, 32, 43, 50, 51, 55, 59, 60, 89, 114, 115.

Chiarelli, Davide Danilo, Corrado Passera, Lorenzo Rosa, Kyle Frankel Davis, Paolo D'Odorico, and Maria Cristina Rulli (2020). "The green and blue crop water requirement WATNEEDS model and its global gridded outputs". In: *Scientific Data* 7.1, pp. 1–9. ISSN: 20524463. DOI: 10.1038/s41597-020-00612-0 cited on page 87.

Chou, Chia, John C. H. Chiang, Chia-Wei Lan, Chia-Hui Chung, Yi-Chun Liao, and Chia-Jung Lee (2013). "Increase in the range between wet and dry season precipitation". In: *Nature Geoscience* 6.4, pp. 263–267. ISSN: 1752-0894. DOI: 10.1038/ngeo1744. URL: http://dx.doi.org/10.1038/ngeo1744%20http://www.nature.com/articles/ngeo1744 cited on pages 10, 12.

Clark, Martyn P, Ying Fan, David M Lawrence, Jennifer C Adam, Diogo Bolster, David J Gochis, Richard P Hooper, Mukesh Kumar, L Ruby Leung, D Scott Mackay, Reed M Maxwell, Chaopeng Shen, C Sean Swenson, and Xubin Zeng (2015). "Improving the representation of hydrological processes in Earth System Models". In: *Water Resources Research*, pp. 1–28. ISSN: 00221694. DOI: 10.1002/2015WR017096.Received. arXiv: 2014WR016527 [10.1002] cited on pages 20, 22, 49.

Condon, Laura E., Adam L. Atchley, and Reed M. Maxwell (2020). "Evapotranspiration depletes groundwater under warming over the contiguous United States". In: *Nature Communications* 11.1, p. 873. ISSN: 2041-1723. DOI: 10.1038/s41467-020-14688-0. URL: http://dx.doi.org/10.1038/s41467-020-14688-0%20http://www.nature.com/articles/s41467-020-14688-0 cited on pages 20, 50, 75.

Condon, Laura E. and Reed M. Maxwell (2017). "Systematic shifts in Budyko relationships caused by groundwater storage changes". In: *Hydrology and Earth System Sciences* 21.2, pp. 1117–1135. ISSN: 1607-7938. DOI: 10.5194/hess-21-1117-2017. URL: https://hess.copernicus.org/articles/21/1117/2017/ cited on page 4.

Cook, B. I., J. S. Mankin, K. Marvel, A. P. Williams, J. E. Smerdon, and K. J. Anchukaitis (2020). "Twenty-First Century Drought Projections in the CMIP6 Forcing Scenarios". In: *Earth's Future* 8.6, pp. 1–20. ISSN: 2328-4277. DOI: 10.1029/2019EF001461. URL: https://onlinelibrary.wiley.com/doi/10.1029/2019EF001461 cited on page 12.

Cook, Benjamin I., Justin S. Mankin, and Kevin J. Anchukaitis (2018). "Climate Change and Drought: From Past to Future". In: *Current Climate Change Reports* 4.2, pp. 164–179. ISSN: 2198-6061. DOI: 10.1007/s40641-018-0093-2. URL: http://link.springer.com/10.1007/s40641-018-0093-2 cited on pages 6, 75.

Cook, Benjamin I., Sonali P. Shukla, Michael J. Puma, and Larissa S. Nazarenko (2015). "Irrigation as an historical climate forcing". In: *Climate Dynamics* 44.5-6, pp. 1715–1730. ISSN: 14320894. DOI: 10.1007/s00382-014-2204-7 cited on pages 19, 26, 87, 88.

Cuthbert, M. O., T. Gleeson, N. Moosdorf, K. M. Befus, A. Schneider, J. Hartmann, and B. Lehner (2019). "Global patterns and dynamics of climate–groundwater interactions". In: *Nature Climate Change* 9.2, pp. 137–141. ISSN: 17586798. DOI: 10.1038/s41558-018-0386-4. URL: http://dx.doi.org/10.1038/s41558-018-0386-4 cited on pages 9, 49.

D'Odorico, Paolo, Davide Danilo Chiarelli, Lorenzo Rosa, Alfredo Bini, David Zilberman, and Maria Cristina Rulli (2020). "The global value of water in agriculture". In: *Proceedings of the National Academy of Sciences* 117.36, pp. 21985–21993. ISSN: 0027-8424. DOI: 10.1073/pnas.2005835117. URL: https://pnas.org/doi/full/10.1073/pnas.2005835117 cited on page 116.

D'Orgeval, T, J Polcher, and P De Rosnay (2008). "Sensitivity of the West African hydrological cycle in ORCHIDEE to infiltration processes". In: *Hydrol. Earth Syst. Sci.* 12, pp. 1387–1401 cited on pages 4, 51, 52, 90.

D'Orgeval, Tristan (2006). "Impact du changement climatique sur le cycle de l'eau en Afrique de l'Ouest : Modélisation et incertitudes". PhD thesis. Université Paris 6, p. 187. URL: http://dods.ipsl.jussieu.fr/orchidee/WEBORCHIDEE/ANOTER/These_dOrgeval.pdf,%20187%20p%20http://dods.ipsl.jussieu.fr/orchidee/WEBORCHIDEE/ANOTER/These_dOrgeval.pdf,%20187%20p cited on pages 33–36, 38–41.

Danabasoglu, G., J. F. Lamarque, J. Bacmeister, D. A. Bailey, A. K. DuVivier, J. Edwards, L. K. Emmons, J. Fasullo, R. Garcia, A. Gettelman, et al. (2020). "The Community Earth System Model Version 2 (CESM2)". In: *Journal of Advances in Modeling Earth Systems* 12.2, pp. 1–35. ISSN: 19422466. DOI: 10.1029/2019MS001916 cited on page 76.

Decharme, Bertrand, Christine Delire, Marie Minvielle, Jeanne Colin, Jean-Pierre Vergnes, Antoinette Alias, David Saint-Martin, Roland Séférian, Stéphane Sénési, and Aurore Voldoire (2019). "Recent Changes in the ISBA-CTRIP Land Surface System for Use in the CNRM-CM6 Climate Model and in Global Off-Line Hydrological Applications". In: *Journal of Advances in Modeling Earth Systems* 11.5, pp. 1207–1252. ISSN: 1942-2466. DOI: 10.1029/2018MS001545. URL: https://onlinelibrary.wiley.com/doi/abs/10.1029/2018MS001545 cited on pages 24, 50, 74, 77, 127.

Döll, P., H. Hoffmann-Dobrev, F. T. Portmann, S. Siebert, A. Eicker, M. Rodell, G. Strassberg, and B. R. Scanlon (2012). "Impact of water withdrawals from groundwater and surface water on continental water storage variations". In: *Journal of Geodynamics* 59-60, pp. 143–156. ISSN: 02643707. DOI: 10.1016/j.jog.2011.05.001. URL: http://dx.doi.org/10.1016/j.jog.2011.05.001 cited on pages 18, 87, 102, 103, 105, 117.

Douville, H., K. Raghavan, J. Renwick, R. P. Allan, P. A. Arias, M. Barlow, R. Cerezo-Mota, A. Cherchi, T. Y. Gan, J. Gergis, et al. (2021). "Water Cycle Changes". In: *Climate Change 2021: The Physical Science Basis. Contribution of Working Group I to the Sixth Assessment Report of the Intergovernmental Panel on Climate Change*. Ed. by V. Masson-

Delmotte, P. Zhai, A. Pirani, S. L. Connors, C. Péan, S. Berger, N. Caud, Y. Chen, L. Goldfarb, M. I. Gomis, et al. Cambridge University Press cited on pages 3, 75.

Druel, Arsène, Simon Munier, Anthony Mucia, Clément Albergel, and Jean-Christophe Calvet (2022). "Implementation of a new crop phenology and irrigation scheme in the ISBA land surface model using SURFEX_v8.1". In: *Geoscientific Model Development* 15.22, pp. 8453–8471. ISSN: 1991-9603. DOI: 10.5194/gmd-15-8453-2022. URL: https://gmd.copernicus.org/articles/15/8453/2022/ cited on page 27.

Ducharne, A, C Ottlé, F Maignan, N Vuichard, J Ghattas, F Wang, P Peylin, J Polcher, M Guimberteau, P Maugis, S Tafasca, A Tootchi, A Verhoef, and H Mizuochi (2018). *The hydrol module of ORCHIDEE: scientific documentation [rev 3977] and on*. Tech. rep. Paris, France: Institut Pierre Simon Laplace (IPSL), p. 47. URL: http://forge.ipsl.jussieu.fr/orchidee/attachment/wiki/Documentation/eqs_hydrol_25April2018_Ducharne.pdf cited on pages 34, 37, 39, 41.

Ducharne, Agnès, Catherine Golaz, Etienne Leblois, Katia Laval, Jan Polcher, Emmanuel Ledoux, and Ghislain De Marsily (2003). "Development of a high resolution runoff routing model, calibration and application to assess runoff from the LMD GCM". In: *Journal of Hydrology* 280.1-4, pp. 207–228. ISSN: 00221694. DOI: 10.1016/S0022-1694(03)00230-0 cited on pages 42, 43, 114.

Ducharne, Agnès, Randal D Koster, Max J Suarez, Marc Stieglitz, and Praveen Kumar (2000). "A catchment-based approach to modeling land surface processes in a general circulation model: 2. Parameter estimation and model demonstration". In: *Journal of Geophysical Research: Atmospheres* 105.D20, pp. 24823–24838. ISSN: 01480227. DOI: 10.1029/2000JD900328. URL: http://doi.wiley.com/10.1029/2000JD900328 cited on pages 24, 49.

Dunn, Robert J. H., Lisa V. Alexander, Markus G. Donat, Xuebin Zhang, Margot Bador, Nicholas Herold, Tanya Lippmann, Rob Allan, Enric Aguilar, Abdoul Aziz Barry, et al. (2020). "Development of an Updated Global Land In Situ-Based Data Set of Temperature and Precipitation Extremes: HadEX3". In: *Journal of Geophysical Research: Atmospheres* 125.16, pp. 1–28. ISSN: 2169-897X. DOI: 10.1029/2019JD032263. URL: https://onlinelibrary.wiley.com/doi/10.1029/2019JD032263 cited on page 80.

Famiglietti, J. S. (2014). "The global groundwater crisis". In: *Nature Climate Change* 4.11, pp. 945–948. ISSN: 1758-678X. DOI: 10.1038/nclimate2425. URL: http://dx.doi.org/10.1038/nclimate2425%20http://www.nature.com/articles/nclimate2425 cited on pages 2, 19.

Fan, Y., M. Clark, D. M. Lawrence, S. Swenson, L. E. Band, S. L. Brantley, P. D. Brooks, W. E. Dietrich, A. Flores, G. Grant, et al. (2019). "Hillslope Hydrology in Global Change Research and Earth System Modeling". In: *Water Resources Research*, pp. 1737–1772. ISSN: 19447973. DOI: 10.1029/2018WR023903 cited on pages 8, 10, 20, 22, 49, 53, 54.

Fan, Y., H. Li, and G. Miguez-Macho (2013). "Global Patterns of Groundwater Table Depth". In: *Science* 339.6122, pp. 940–943. ISSN: 0036-8075. DOI: 10.1126/science.1229881.

URL: https://www.sciencemag.org/lookup/doi/10.1126/science.1229881 cited on page 53.

Fan, Ying and Gonzalo Miguez-Macho (2011). "A simple hydrologic framework for simulating wetlands in climate and earth system models". In: *Climate Dynamics* 37.1-2, pp. 253–278. ISSN: 0930-7575. DOI: 10.1007/s00382-010-0829-8. URL: http://link.springer.com/10.1007/s00382-010-0829-8 cited on pages 25, 49, 53.

Fan, Ying, Gonzalo Miguez-Macho, Christopher P. Weaver, Robert Walko, and Alan Robock (2007). "Incorporating water table dynamics in climate modeling: 1. Water table observations and equilibrium water table simulations". In: *Journal of Geophysical Research: Atmospheres* 112.D10, pp. 1–17. ISSN: 01480227. DOI: 10.1029/2006JD008111. URL: http://doi.wiley.com/10.1029/2006JD008111 cited on page 49.

Feddema, Johannes J. (2005). "A Revised Thornthwaite-Type Global Climate Classification". In: *Physical Geography* 26.6, pp. 442–466. ISSN: 0272-3646. DOI: 10.2747/0272-3646.26.6.442. URL: https://www.tandfonline.com/doi/full/10.2747/0272-3646.26.6.442 cited on pages 1, 50, 68, 69.

Felfelani, Farshid, David M. Lawrence, and Yadu Pokhrel (2021). "Representing Intercell Lateral Groundwater Flow and Aquifer Pumping in the Community Land Model". In: *Water Resources Research* 57.1, pp. 1–24. ISSN: 0043-1397. DOI: 10.1029/2020WR027531. URL: https://onlinelibrary.wiley.com/doi/10.1029/2020WR027531 cited on pages 27, 53, 88.

Ferguson, Ian M. and Reed M. Maxwell (2012). "Human impacts on terrestrial hydrology: climate change versus pumping and irrigation". In: *Environmental Research Letters* 7.4, p. 044022. ISSN: 1748-9326. DOI: 10.1088/1748-9326/7/4/044022. URL: https://iopscience.iop.org/article/10.1088/1748-9326/7/4/044022 cited on page 20.

Fisher, Rosie A. and Charles D. Koven (2020). "Perspectives on the Future of Land Surface Models and the Challenges of Representing Complex Terrestrial Systems". In: *Journal of Advances in Modeling Earth Systems* 12.4. ISSN: 1942-2466. DOI: 10.1029/2018MS001453. URL: https://onlinelibrary.wiley.com/doi/10.1029/2018MS001453 cited on pages 20, 22.

Forster, Piers M., Amanda C. Maycock, Christine M. McKenna, and Christopher J. Smith (2020). "Latest climate models confirm need for urgent mitigation". In: *Nature Climate Change* 10.1, pp. 7–10. ISSN: 1758-678X. DOI: 10.1038/s41558-019-0660-0. URL: http://dx.doi.org/10.1038/s41558-019-0660-0%20http://www.nature.com/articles/s41558-019-0660-0 cited on page 10.

Forzieri, Giovanni, Diego G Miralles, Philippe Ciais, Ramdane Alkama, Youngryel Ryu, Gregory Duveiller, Ke Zhang, Eddy Robertson, Markus Kautz, Brecht Martens, et al. (2020). "Increased control of vegetation on global terrestrial energy fluxes". In: *Nature Climate Change* 10.4, pp. 356–362. ISSN: 1758-678X. DOI: 10.1038/s41558-020-0717-0. URL: http://dx.doi.org/10.1038/s41558-020-0717-0%20http://www.nature.com/articles/s41558-020-0717-0 cited on pages 10, 12.

Frenken, Karen and Virginie Gillet (2012). *Irrigation water requirement and water withdrawal by country*. Tech. rep. Rome: Food and Agriculture Organization, p. 265. URL: http://www.fao.org/aquastat/en/data-analysis/irrig-water-use/ cited on pages 87, 100–102.

Furusho-Percot, Carina, Klaus Goergen, Carl Hartick, Ketan Kulkarni, Jessica Keune, and Stefan Kollet (2019). "Pan-European groundwater to atmosphere terrestrial systems climatology from a physically consistent simulation". In: *Scientific Data* 6.1, p. 320. ISSN: 2052-4463. DOI: 10.1038/s41597-019-0328-7. URL: http://www.nature.com/articles/s41597-019-0328-7 cited on page 49.

Gaetani, Marco, Serge Janicot, Mathieu Vrac, Adjoua Moise Famien, and Benjamin Sultan (2020). "Robust assessment of the time of emergence of precipitation change in West Africa". In: *Scientific Reports* 10.1, p. 7670. ISSN: 2045-2322. DOI: 10.1038/s41598-020-63782-2. URL: http://www.nature.com/articles/s41598-020-63782-2 cited on page 69.

Gascoin, Simon (2009). "Etude des paramétrisations hydrologiques d ' un modèle de surface continentale : importance des aquifères et des premiers centimètres du sol". PhD thesis. Université Pierre et Marie Curie - Paris VI cited on pages 22, 28, 131.

Gascoin, Simon, Agnès Ducharne, Pierre Ribstein, Marion Carli, and Florence Habets (2009). "Adaptation of a catchment-based land surface model to the hydrogeological setting of the Somme River basin (France)". In: *Journal of Hydrology* 368.1-4, pp. 105–116. ISSN: 00221694. DOI: 10.1016/j.jhydrol.2009.01.039. URL: http://dx.doi.org/10.1016/j.jhydrol.2009.01.039 cited on page 50.

Gedney, N. and P. M. Cox (2003). "The Sensitivity of Global Climate Model Simulations to the Representation of Soil Moisture Heterogeneity". In: *Journal of Hydrometeorology* 4.6, pp. 1265–1275. ISSN: 1525-755X. DOI: 10.1175/1525-7541(2003)004<1265:TSOGCM>2.0.CO;2. URL: http://journals.ametsoc.org/doi/10.1175/1525-7541(2003)004%5C%3C1265:TSOGCM%5C%3E2.0.CO;2 cited on page 49.

Genuchten, M. Th. van (1980). "A Closed-form Equation for Predicting the Hydraulic Conductivity of Unsaturated Soils". In: *Soil Science Society of America Journal* 44.5, pp. 892–898. ISSN: 03615995. DOI: 10.2136/sssaj1980.03615995004400050002x. URL: http://doi.wiley.com/10.2136/sssaj1980.03615995004400050002x cited on pages 41, 52.

Gibson, Katherine E.B., Justin P. Gibson, and Patricio Grassini (2019). "Benchmarking irrigation water use in producer fields in the US central Great Plains". In: *Environmental Research Letters* 14.5. ISSN: 17489326. DOI: 10.1088/1748-9326/ab17eb cited on page 117.

Gilbert, James M., Reed M. Maxwell, and David J. Gochis (2017). "Effects of Water-Table Configuration on the Planetary Boundary Layer over the San Joaquin River Watershed, California". In: *Journal of Hydrometeorology* 18.5, pp. 1471–1488. ISSN: 1525-755X. DOI: 10.1175/JHM-D-16-0134.1. URL: https://journals.ametsoc.org/jhm/article/18/5/1471/69708/Effects-of-WaterTable-Configuration-on-the cited on page 14.

Giuntoli, I., J.-P. Vidal, C. Prudhomme, and D. M. Hannah (2015). "Future hydrological extremes: the uncertainty from multiple global climate and global hydrological models". In: *Earth System Dynamics* 6.1, pp. 267–285. ISSN: 2190-4987. DOI: 10.5194/esd-6-267-2015. URL: http://www.earth-syst-dynam.net/6/267/2015/%20https://www.earth-syst-dynam.net/6/267/2015/ cited on page 12.

Gleeson, Tom, Kevin M. Befus, Scott Jasechko, Elco Luijendijk, and M. Bayani Cardenas (2016). "The global volume and distribution of modern groundwater". In: *Nature Geoscience* 9.2, pp. 161–164. ISSN: 17520908. DOI: 10.1038/ngeo2590 cited on pages 1, 2, 49.

Gleeson, Tom, Lars Marklund, Leslie Smith, and Andrew H. Manning (2011). "Classifying the water table at regional to continental scales". In: *Geophysical Research Letters* 38.5, n/a–n/a. ISSN: 00948276. DOI: 10.1029/2010GL046427. URL: http://doi.wiley.com/10.1029/2010GL046427 cited on pages 9, 49.

Gleeson, Tom, Thorsten Wagener, Petra Döll, Samuel C. Zipper, Charles West, Yoshihide Wada, Richard Taylor, Bridget Scanlon, Rafael Rosolem, Shams Rahman, et al. (2021). "GMD perspective: The quest to improve the evaluation of groundwater representation in continental- to global-scale models". In: *Geoscientific Model Development* 14.12, pp. 7545–7571. ISSN: 1991-9603. DOI: 10.5194/gmd-14-7545-2021. URL: https://gmd.copernicus.org/articles/14/7545/2021/ cited on pages 22, 49.

Golaz, Jean-christophe, Peter M Caldwell, Luke P. Van Roekel, Mark R Petersen, Qi Tang, Jonathan D Wolfe, Guta Abeshu, Valentine Anantharaj, Xylar S. Asay-Davis, David C Bader, et al. (2019). "The DOE E3SM Coupled Model Version 1: Overview and Evaluation at Standard Resolution". In: *Journal of Advances in Modeling Earth Systems* 11.7, pp. 2089–2129. ISSN: 1942-2466. DOI: 10.1029/2018MS001603. URL: https://onlinelibrary.wiley.com/doi/abs/10.1029/2018MS001603 cited on page 76.

Graaf, I.E.M. de, L.P.H. van Beek, Y. Wada, and M.F.P. Bierkens (2014). "Dynamic attribution of global water demand to surface water and groundwater resources: Effects of abstractions and return flows on river discharges". In: *Advances in Water Resources* 64, pp. 21–33. ISSN: 03091708. DOI: 10.1016/j.advwatres.2013.12.002. URL: http://dx.doi.org/10.1016/j.advwatres.2013.12.002%20https://linkinghub.elsevier.com/retrieve/pii/S0309170813002467 cited on pages 106, 114, 116.

Graaf, Inge E. M. de, Tom Gleeson, L. P. H. (Rens) van Beek, Edwin H Sutanudjaja, and Marc F. P. Bierkens (2019). "Environmental flow limits to global groundwater pumping". In: *Nature* 574.7776, pp. 90–94. ISSN: 0028-0836. DOI: 10.1038/s41586-019-1594-4. URL: http://dx.doi.org/10.1038/s41586-019-1594-4%20http://www.nature.com/articles/s41586-019-1594-4 cited on pages 75, 127.

Grafton, R. Q., J. Williams, C. J. Perry, F. Molle, C. Ringler, P. Steduto, B. Udall, S. A. Wheeler, Y. Wang, D. Garrick, and R. G. Allen (2018). "The paradox of irrigation efficiency". In: *Science* 361.6404, pp. 748–750. ISSN: 0036-8075. DOI: 10.1126/science.

aat9314. URL: https://www.science.org/doi/10.1126/science.aat9314 cited on pages 18, 19.

Grafton, R. Quentin, John Williams, and Qiang Jiang (2017). "Possible pathways and tensions in the food and water nexus". In: *Earth's Future* 5.5, pp. 449–462. ISSN: 23284277. DOI: 10.1002/2016EF000506. URL: http://doi.wiley.com/10.1002/2016EF000506 cited on page 86.

Greve, P., M. L. Roderick, A. M. Ukkola, and Y. Wada (2019). "The aridity Index under global warming". In: *Environmental Research Letters* 14.12, p. 124006. ISSN: 1748-9326. DOI: 10.1088/1748-9326/ab5046. URL: https://iopscience.iop.org/article/10.1088/1748-9326/ab5046 cited on page 69.

Greve, Peter, Boris Orlowsky, Brigitte Mueller, Justin Sheffield, Markus Reichstein, and Sonia I. Seneviratne (2014). "Global assessment of trends in wetting and drying over land". In: *Nature Geoscience* 7.10, pp. 716–721. ISSN: 1752-0894. DOI: 10.1038/ngeo2247. URL: http://www.nature.com/articles/ngeo2247 cited on page 10.

Guimberteau, M., G. Drapeau, J. Ronchail, B. Sultan, J. Polcher, J.-M. Martinez, C. Prigent, J.-L. Guyot, G. Cochonneau, J. C. Espinoza, et al. (2012a). "Discharge simulation in the sub-basins of the Amazon using ORCHIDEE forced by new datasets". In: *Hydrology and Earth System Sciences* 16.3, pp. 911–935. ISSN: 1607-7938. DOI: 10.5194/hess-16-911-2012. URL: https://hess.copernicus.org/articles/16/911/2012/ cited on pages 19, 42, 52, 90, 114.

Guimberteau, Matthieu (2010). "Modélisation de l'hydrologie continentale et influences de l'irrigation sur le cycle de l'eau". Sciences de la terre. Université Pierre et Marie Curie Paris VI, p. 194 cited on page 39.

Guimberteau, Matthieu, Katia Laval, Alain Perrier, and Jan Polcher (2012b). "Global effect of irrigation and its impact on the onset of the Indian summer monsoon". In: *Climate Dynamics* 39.6, pp. 1329–1348. ISSN: 0930-7575. DOI: 10.1007/s00382-011-1252-5. URL: http://link.springer.com/10.1007/s00382-011-1252-5 cited on pages 26, 29, 87, 88, 94, 101.

Gupta, Hoshin V, Harald Kling, Koray K Yilmaz, and Guillermo F Martinez (2009). "Decomposition of the mean squared error and NSE performance criteria : Implications for improving hydrological modelling". In: *Journal of Hydrology* 377.1-2, pp. 80–91. ISSN: 0022-1694. DOI: 10.1016/j.jhydrol.2009.08.003. URL: http://dx.doi.org/10.1016/j.jhydrol.2009.08.003 cited on page 143.

Haddeland, Ingjerd, Dennis P. Lettenmaier, and Thomas Skaugen (2006). "Effects of irrigation on the water and energy balances of the Colorado and Mekong river basins". In: *Journal of Hydrology* 324.1-4, pp. 210–223. ISSN: 00221694. DOI: 10.1016/j.jhydrol.2005.09.028. URL: https://linkinghub.elsevier.com/retrieve/pii/S0022169405004877 cited on pages 27, 88.

Hanasaki, N., S. Kanae, T. Oki, K. Masuda, K. Motoya, N. Shirakawa, Y. Shen, and K. Tanaka (2008a). "An integrated model for the assessment of global water resources – Part

1: Model description and input meteorological forcing". In: *Hydrology and Earth System Sciences* 12.4, pp. 1007–1025. ISSN: 1607-7938. DOI: 10.5194/hess-12-1007-2008. URL: https://hess.copernicus.org/articles/12/1007/2008/ cited on pages 27, 87, 88, 94, 116.

Hanasaki, N., S. Kanae, T. Oki, K. Masuda, K. Motoya, N. Shirakawa, Y. Shen, and K. Tanaka (2008b). "An integrated model for the assessment of global water resources – Part 2: Applications and assessments". In: *Hydrology and Earth System Sciences* 12.4, pp. 1027–1037. ISSN: 1607-7938. DOI: 10.5194/hess-12-1027-2008. URL: https://hess.copernicus.org/articles/12/1027/2008/ cited on page 116.

Hanasaki, Naota, Sayaka Yoshikawa, Yadu Pokhrel, and Shinjiro Kanae (2018). "A global hydrological simulation to specify the sources of water used by humans". In: *Hydrology and Earth System Sciences* 22.1, pp. 789–817. ISSN: 1607-7938. DOI: 10.5194/hess-22-789-2018. URL: https://hess.copernicus.org/articles/22/789/2018/ cited on pages 17, 18, 87.

Heavens, N. G., D. S. Ward, and M. M. Natalie (2013). "Studying and Projecting Climate Change with Earth System Models". In: *Nature Education Knowledge*, 4(5):4. URL: https://www.nature.com/scitable/knowledge/library/studying-and-projecting-climate-change-with-earth-103087065/ cited on page 21.

Helsel, D. R. and R. M. Hirsch (1992). "Statistical methods in water resources". In: *Statistical methods in water resources* May. ISSN: 00401706. DOI: 10.2307/1269385 cited on page 143.

Hoogeveen, J., J.-M. Faurès, L. Peiser, J. Burke, and N. van de Giesen (2015). "GlobWat – a global water balance model to assess water use in irrigated agriculture". In: *Hydrology and Earth System Sciences* 19.9, pp. 3829–3844. ISSN: 1607-7938. DOI: 10.5194/hess-19-3829-2015. URL: https://hess.copernicus.org/articles/19/3829/2015/ cited on pages 18, 87, 100.

Horton, Radley M., Justin S. Mankin, Corey Lesk, Ethan Coffel, and Colin Raymond (2016). "A Review of Recent Advances in Research on Extreme Heat Events". In: *Current Climate Change Reports* 2.4, pp. 242–259. ISSN: 2198-6061. DOI: 10.1007/s40641-016-0042-x. URL: http://dx.doi.org/10.1007/s40641-016-0042-x%20http://link.springer.com/10.1007/s40641-016-0042-x cited on pages 49, 78.

Horton, Robert E (1945). "Erosional development of streams and their drainage basins; Hydrophysical approach to quantitative morphology". In: *Bulletin of the Geological Society of America* 56, pp. 275–370 cited on page 6.

Hourdin, Frédéric, Jean Yves Grandpeix, Catherine Rio, Sandrine Bony, Arnaud Jam, Frédérique Cheruy, Nicolas Rochetin, Laurent Fairhead, Abderrahmane Idelkadi, Ionela Musat, Jean Louis Dufresne, Alain Lahellec, Marie Pierre Lefebvre, and Romain Roehrig (2013). "LMDZ5B: The atmospheric component of the IPSL climate model with revisited parameterizations for clouds and convection". In: *Climate Dynamics* 40.9-10, pp. 2193–2222. ISSN: 09307575. DOI: 10.1007/s00382-012-1343-y cited on page 43.

Hourdin, Frédéric, Catherine Rio, Jean Yves Grandpeix, Jean Baptiste Madeleine, Frédérique Cheruy, Nicolas Rochetin, Arnaud Jam, Ionela Musat, Abderrahmane Idelkadi, Laurent Fairhead, et al. (2020). "LMDZ6A: The Atmospheric Component of the IPSL Climate Model With Improved and Better Tuned Physics". In: *Journal of Advances in Modeling Earth Systems* 12.7, pp. 1–37. ISSN: 19422466. DOI: 10.1029/2019MS001892 cited on pages 43, 55.

Hurk, Bart van den, Hyungjun Kim, Gerhard Krinner, Sonia I. Seneviratne, Chris Derksen, Taikan Oki, Hervé Douville, Jeanne Colin, Agnès Ducharne, Frederique Cheruy, et al. (2016). "LS3MIP (v1.0) contribution to CMIP6: the Land Surface, Snow and Soil moisture Model Intercomparison Project – aims, setup and expected outcome". In: *Geoscientific Model Development* 9.8, pp. 2809–2832. ISSN: 1991-9603. DOI: 10.5194/gmd-9-2809-2016. URL: https://gmd.copernicus.org/articles/9/2809/2016/ cited on page 97.

Hurtt, George C., Louise Chini, Ritvik Sahajpal, Steve Frolking, Benjamin L. Bodirsky, Katherine Calvin, Jonathan C. Doelman, Justin Fisk, Shinichiro Fujimori, Kees Klein Goldewijk, et al. (2020). "Harmonization of global land use change and management for the period 850–2100 (LUH2) for CMIP6". In: *Geoscientific Model Development* 13.11, pp. 5425–5464. ISSN: 1991-9603. DOI: 10.5194/gmd-13-5425-2020. URL: https://gmd.copernicus.org/articles/13/5425/2020/ cited on pages 14, 94, 97.

IPCC (2013). *Climate Change 2013: The Physical Science Basis. Contribution of Working Group I to the Fifth Assessment Report of the Intergovernmental Panel on Climate Change*. Ed. by T.F. Stocker, D. Qin, G.-K. Plattner, M. Tignor, S.K. Allen, J. Boschung, A. Nauels, Y. Xia, V. Bex, and P.M. Midgley. First Edit. Cambridge, UK and New York, USA: Cambridge University Press, p. 1535 cited on pages 10, 12.

— (2021). *Climate Change 2021: The Physical Science Basis. Contribution of working group I to the Sixth Assessment Report of the Intergovernmental Panel on Climate Change*. Ed. by V. Masson-Delmotte, P. Zhai, A. Pirani, S.L. Connors, C. Péan, S. Berger, N. Caud, Y. Chen, L. Goldfarb, M.I. Gomis, et al. Cambridge, UK and New York, USA, p. 2391. ISBN: 9781009157896. DOI: 10.1017/9781009157896 cited on pages 2, 3, 10–13, 21, 80.

Jägermeyr, J., D. Gerten, J. Heinke, S. Schaphoff, M. Kummu, and W. Lucht (2015). "Water savings potentials of irrigation systems: global simulation of processes and linkages". In: *Hydrology and Earth System Sciences* 19.7, pp. 3073–3091. ISSN: 1607-7938. DOI: 10.5194/hess-19-3073-2015. URL: https://hess.copernicus.org/articles/19/3073/2015/ cited on pages 18, 87, 88, 91.

Jaramillo, Fernando and Georgia Destouni (2015). "Local flow regulation and irrigation raise global human water consumption and footprint". In: *Science* 350.6265, pp. 1248–1251. ISSN: 10959203. DOI: 10.1126/science.aad1010 cited on pages 5, 13, 14.

Jasechko, Scott, Hansjörg Seybold, Debra Perrone, Ying Fan, and James W. Kirchner (2021). "Widespread potential loss of streamflow into underlying aquifers across the USA". In: *Nature* 591.7850, pp. 391–395. ISSN: 0028-0836. DOI: 10.1038/s41586-021-03311-x.

URL: http://dx.doi.org/10.1038/s41586-021-03311-x%20http://www.nature.com/articles/s41586-021-03311-x cited on page 74.

Jasechko, Scott, Zachary D Sharp, John J Gibson, S Jean Birks, Yi Yi, and Peter J Fawcett (2013). "Terrestrial water fluxes dominated by transpiration". In: *Nature* 496.7445, pp. 347–350. ISSN: 0028-0836. DOI: 10.1038/nature11983. URL: http://www.nature.com/articles/nature11983 cited on pages 9, 10.

Jung, Martin, Sujan Koirala, Ulrich Weber, Kazuhito Ichii, Fabian Gans, Gustau Camps-Valls, Dario Papale, Christopher Schwalm, Gianluca Tramontana, and Markus Reichstein (2019). "The FLUXCOM ensemble of global land-atmosphere energy fluxes". In: *Scientific Data* 6.1, p. 74. ISSN: 2052-4463. DOI: 10.1038/s41597-019-0076-8. URL: http://www.nature.com/articles/s41597-019-0076-8 cited on pages 60, 87, 99.

Keune, Jessica, Fabian Gasper, Klaus Goergen, Andreas Hense, Prabhakar Shrestha, Mauro Sulis, and Stefan Kollet (2016). "Studying the influence of groundwater representations on land surface-atmosphere feedbacks during the European heat wave in 2003". In: *Journal of Geophysical Research: Atmospheres* 121.22, pp. 13, 301–13, 325. ISSN: 2169897X. DOI: 10.1002/2016JD025426. URL: http://doi.wiley.com/10.1002/2016JD025426 cited on page 14.

Klein Goldewijk, Kees, Arthur Beusen, Jonathan Doelman, and Elke Stehfest (2017). "Anthropogenic land use estimates for the Holocene – HYDE 3.2". In: *Earth System Science Data* 9.2, pp. 927–953. ISSN: 1866-3516. DOI: 10.5194/essd-9-927-2017. URL: https://essd.copernicus.org/articles/9/927/2017/ cited on page 86.

Kling, Harald, Martin Fuchs, and Maria Paulin (2012). "Runoff conditions in the upper Danube basin under an ensemble of climate change scenarios". In: *Journal of Hydrology* 424-425, pp. 264–277. ISSN: 00221694. DOI: 10.1016/j.jhydrol.2012.01.011. URL: http://dx.doi.org/10.1016/j.jhydrol.2012.01.011%20https://linkinghub.elsevier.com/retrieve/pii/S0022169412000431 cited on page 143.

Koech, Richard and Philip Langat (2018). "Improving Irrigation Water Use Efficiency: A Review of Advances, Challenges and Opportunities in the Australian Context". In: *Water* 10.12, p. 1771. ISSN: 2073-4441. DOI: 10.3390/w10121771. URL: http://www.mdpi.com/2073-4441/10/12/1771 cited on pages 18, 117.

Koirala, Sujan, Pat J.F. Yeh, Yukiko Hirabayashi, Shinjiro Kanae, and Taikan Oki (2014). "Global-scale land surface hydrologic modeling with the representation of water table dynamics". In: *Journal of Geophysical Research: Atmospheres* 119.1, pp. 75–89. ISSN: 2169-897X. DOI: 10.1002/2013JD020398. URL: https://onlinelibrary.wiley.com/doi/10.1002/2013JD020398 cited on pages 25, 74, 114.

Kollet, Stefan J. and Reed M. Maxwell (2008). "Capturing the influence of groundwater dynamics on land surface processes using an integrated, distributed watershed model". In: *Water Resources Research* 44.2, pp. 1–18. ISSN: 00431397. DOI: 10.1029/2007WR006004. URL: http://doi.wiley.com/10.1029/2007WR006004 cited on pages 14, 15.

Koster, Randal D. (2004). "Regions of Strong Coupling Between Soil Moisture and Precipitation". In: *Science* 305.5687, pp. 1138–1140. ISSN: 0036-8075. DOI: 10.1126/science.1100217. URL: https://www.sciencemag.org/lookup/doi/10.1126/science.1100217 cited on pages 2, 6, 48.

Koster, Randal D., Max J. Suarez, Agnès Ducharne, Marc Stieglitz, and Praveen Kumar (2000). "A catchment-based approach to modeling land surface processes in a general circulation model: 1. Model structure". In: *Journal of Geophysical Research: Atmospheres* 105.D20, pp. 24809–24822. ISSN: 01480227. DOI: 10.1029/2000JD900327. URL: http://doi.wiley.com/10.1029/2000JD900328%20http://doi.wiley.com/10.1029/2000JD900327 cited on pages 22, 24, 49.

Koster, Randal D., Y. C. Sud, Zhichang Guo, Paul A. Dirmeyer, Gordon Bonan, Keith W. Oleson, Edmond Chan, Diana Verseghy, Peter Cox, Harvey Davies, et al. (2006). "GLACE: The Global Land–Atmosphere Coupling Experiment. Part I: Overview". In: *Journal of Hydrometeorology* 7.4, pp. 590–610. ISSN: 1525-7541. DOI: 10.1175/JHM510.1. URL: http://journals.ametsoc.org/doi/10.1175/JHM510.1 cited on pages 6, 48.

Krakauer, Nir Y., Michael J. Puma, Benjamin I. Cook, Pierre Gentine, and Larissa Nazarenko (2016). "Ocean–atmosphere interactions modulate irrigation's climate impacts". In: *Earth System Dynamics* 7.4, pp. 863–876. ISSN: 2190-4987. DOI: 10.5194/esd-7-863-2016. URL: https://esd.copernicus.org/articles/7/863/2016/ cited on page 23.

Krinner, G., Nicolas Viovy, Nathalie de Noblet-Ducoudré, Jérôme Ogée, Jan Polcher, Pierre Friedlingstein, Philippe Ciais, Stephen Sitch, and I. Colin Prentice (2005). "A dynamic global vegetation model for studies of the coupled atmosphere-biosphere system". In: *Global Biogeochemical Cycles* 19.1, pp. 1–33. ISSN: 08866236. DOI: 10.1029/2003GB002199 cited on pages 22, 32–34, 51, 88–90.

Krinner, Gerhard, Viatcheslav Kharin, Romain Roehrig, John Scinocca, and Francis Codron (2020). "Historically-based run-time bias corrections substantially improve model projections of 100 years of future climate change". In: *Communications Earth and Environment* 1.1, pp. 1–7. ISSN: 26624435. DOI: 10.1038/s43247-020-00035-0. URL: http://dx.doi.org/10.1038/s43247-020-00035-0 cited on page 131.

Kumar, Sanjiv, Matthew Newman, Yan Wang, and Ben Livneh (2019). "Potential Reemergence of Seasonal Soil Moisture Anomalies in North America". In: *Journal of Climate* 32.10, pp. 2707–2734. ISSN: 0894-8755. DOI: 10.1175/JCLI-D-18-0540.1. URL: https://journals.ametsoc.org/view/journals/clim/32/10/jcli-d-18-0540.1.xml cited on page 6.

Laghari, A. N., D. Vanham, and W. Rauch (2012). "The Indus basin in the framework of current and future water resources management". In: *Hydrology and Earth System Sciences* 16.4, pp. 1063–1083. ISSN: 1607-7938. DOI: 10.5194/hess-16-1063-2012. URL: https://hess.copernicus.org/articles/16/1063/2012/ cited on pages 18, 104, 108.

Lawrence, David M., Rosie A. Fisher, Charles D. Koven, Keith W. Oleson, Sean C. Swenson, Gordon Bonan, Nathan Collier, Bardan Ghimire, Leo Kampenhout, Daniel Kennedy,

et al. (2019). "The Community Land Model Version 5: Description of New Features, Benchmarking, and Impact of Forcing Uncertainty". In: *Journal of Advances in Modeling Earth Systems* 11.12, pp. 4245–4287. ISSN: 1942-2466. DOI: 10.1029/2018MS001583. URL: https://onlinelibrary.wiley.com/doi/abs/10.1029/2018MS001583 cited on page 76.

Lawrence, David M., George C. Hurtt, Almut Arneth, Victor Brovkin, Kate V. Calvin, Andrew D. Jones, Chris D. Jones, Peter J. Lawrence, Nathalie De Noblet-Ducoudré, Julia Pongratz, Sonia I. Seneviratne, and Elena Shevliakova (2016). "The Land Use Model Intercomparison Project (LUMIP) contribution to CMIP6: Rationale and experimental design". In: *Geoscientific Model Development* 9.9, pp. 2973–2998. ISSN: 19919603. DOI: 10.5194/gmd-9-2973-2016 cited on page 24.

Lehner, Bernhard, Catherine Reidy Liermann, Carmen Revenga, Charles Vörösmarty, Balazs Fekete, Philippe Crouzet, Petra Döll, Marcel Endejan, Karen Frenken, Jun Magome, Christer Nilsson, James C. Robertson, Raimund Rödel, Nikolai Sindorf, and Dominik Wisser (2011). "High-resolution mapping of the world's reservoirs and dams for sustainable river-flow management". In: *Frontiers in Ecology and the Environment* 9.9, pp. 494–502. ISSN: 1540-9295. DOI: 10.1890/100125. URL: https://onlinelibrary.wiley.com/doi/abs/10.1890/100125 cited on page 100.

Leng, Guoyong, Maoyi Huang, Qiuhong Tang, Huilin Gao, and L. Ruby Leung (2014). "Modeling the Effects of Groundwater-Fed Irrigation on Terrestrial Hydrology over the Conterminous United States". In: *Journal of Hydrometeorology* 15.3, pp. 957–972. ISSN: 1525-755X. DOI: 10.1175/JHM-D-13-049.1. URL: https://journals.ametsoc.org/jhm/article/15/3/957/5972/Modeling-the-Effects-of-GroundwaterFed-Irrigation cited on pages 26, 88.

Leng, Guoyong, Maoyi Huang, Qiuhong Tang, and L. Ruby Leung (2015). "A modeling study of irrigation effects on global surface water and groundwater resources under a changing climate". In: *Journal of Advances in Modeling Earth Systems* 7.3, pp. 1285–1304. ISSN: 1942-2466. DOI: 10.1002/2015MS000437. URL: https://onlinelibrary.wiley.com/doi/10.1002/2015MS000470%20https://onlinelibrary.wiley.com/doi/10.1002/2015MS000437 cited on pages 18, 26, 88.

Leng, Guoyong, Maoyi Huang, Qiuhong Tang, William J. Sacks, Huimin Lei, and L. Ruby Leung (2013). "Modeling the effects of irrigation on land surface fluxes and states over the conterminous United States: Sensitivity to input data and model parameters". In: *Journal of Geophysical Research: Atmospheres* 118.17, pp. 9789–9803. ISSN: 2169897X. DOI: 10.1002/jgrd.50792. URL: http://doi.wiley.com/10.1002/jgrd.50792 cited on page 26.

Leng, Guoyong, L. Ruby Leung, and Maoyi Huang (2017). "Significant impacts of irrigation water sources and methods on modeling irrigation effects in the ACME Land Model". In: *Journal of Advances in Modeling Earth Systems* 9.3, pp. 1665–1683. ISSN: 1942-2466. DOI: 10.1002/2016MS000885. URL: https://onlinelibrary.wiley.com/doi/abs/10.1002/

2016MS000885%20https://onlinelibrary.wiley.com/doi/10.1002/2016MS000885 cited on pages 26, 88.

Leung, L. Ruby, Maoyi Huang, Yun Qian, and Xu Liang (2011). "Climate–soil–vegetation control on groundwater table dynamics and its feedbacks in a climate model". In: *Climate Dynamics* 36.1-2, pp. 57–81. ISSN: 0930-7575. DOI: 10.1007/s00382-010-0746-x. URL: http://link.springer.com/10.1007/s00382-010-0746-x cited on pages 25, 74.

Lian, Xu, Shilong Piao, Chris Huntingford, Yue Li, Zhenzhong Zeng, Xuhui Wang, Philippe Ciais, Tim R. McVicar, Shushi Peng, Catherine Ottlé, Hui Yang, Yuting Yang, Yongqiang Zhang, and Tao Wang (2018). "Partitioning global land evapotranspiration using CMIP5 models constrained by observations". In: *Nature Climate Change* 8.7, pp. 640–646. ISSN: 1758-678X. DOI: 10.1038/s41558-018-0207-9. URL: http://dx.doi.org/10.1038/s41558-018-0207-9%20http://www.nature.com/articles/s41558-018-0207-9 cited on page 10.

Liang, Xu (2003). "A new parameterization for surface and groundwater interactions and its impact on water budgets with the variable infiltration capacity (VIC) land surface model". In: *Journal of Geophysical Research* 108.D16, p. 8613. ISSN: 0148-0227. DOI: 10.1029/2002JD003090. URL: http://doi.wiley.com/10.1029/2002JD003090 cited on page 25.

Liu, Zhiyong, Linyin Cheng, Guoyi Zhou, Xiaohong Chen, Kairong Lin, Wenfeng Zhang, Xiuzhi Chen, and Ping Zhou (2020). "Global Response of Evapotranspiration Ratio to Climate Conditions and Watershed Characteristics in a Changing Environment". In: *Journal of Geophysical Research: Atmospheres* 125.7, e2020JD032371. ISSN: 2169-897X. DOI: 10.1029/2020JD032371. URL: https://onlinelibrary.wiley.com/doi/abs/10.1029/2020JD032371 cited on page 4.

Lo, Min Hui, Hao Wei Wey, Eun Soon Im, Lois Iping Tang, Ray G. Anderson, Ren Jie Wu, Rong You Chien, Jiangfeng Wei, Amir Agha Kouchak, and Yoshihide Wada (2021). "Intense agricultural irrigation induced contrasting precipitation changes in Saudi Arabia". In: *Environmental Research Letters* 16.6. ISSN: 17489326. DOI: 10.1088/1748-9326/ac002e cited on pages 19, 20, 88.

Lo, Min-Hui and James S. Famiglietti (2011). "Precipitation response to land subsurface hydrologic processes in atmospheric general circulation model simulations". In: *Journal of Geophysical Research* 116.D5, p. D05107. ISSN: 0148-0227. DOI: 10.1029/2010JD015134. URL: http://doi.wiley.com/10.1029/2010JD015134 cited on pages 22, 24, 49, 57, 74.

— (2013). "Irrigation in California's Central Valley strengthens the southwestern U.S. water cycle". In: *Geophysical Research Letters* 40.2, pp. 301–306. ISSN: 00948276. DOI: 10.1002/grl.50108. URL: http://doi.wiley.com/10.1002/grl.50108 cited on pages 19, 87, 88.

Loomis, B. D., S. B. Luthcke, and T. J. Sabaka (2019). "Regularization and error characterization of GRACE mascons". In: *Journal of Geodesy* 93.9, pp. 1381–1398. ISSN: 0949-7714. DOI: 10.1007/s00190-019-01252-y. URL: https://doi.org/10.1007/s00190-019-

01252-y%20http://link.springer.com/10.1007/s00190-019-01252-y cited on page 100.

Lorenz, Ruth, Daniel Argüeso, Markus G. Donat, Andrew J. Pitman, Bart Van Den Hurk, Alexis Berg, David M. Lawrence, Frédérique Chéruy, Agnès Ducharne, Stefan Hagemann, Arndt Meier, P. C.D. Milly, and Sonia I. Seneviratne (2016). "Influence of land-atmosphere feedbacks on temperature and precipitation extremes in the GLACE-CMIP5 ensemble". In: *Journal of Geophysical Research* 121.2, pp. 607–623. ISSN: 21562202. DOI: 10.1002/2015JD024053 cited on pages 49, 77.

Louis, Jean-François (1979). "A parametric model of vertical eddy fluxes in the atmosphere". In: *Boundary-Layer Meteorology* 17.2, pp. 187–202. ISSN: 0006-8314. DOI: 10.1007/BF00117978. URL: http://link.springer.com/10.1007/BF00117978 cited on page 43.

Lurton, Thibaut, Yves Balkanski, Vladislav Bastrikov, Slimane Bekki, Laurent Bopp, Pascale Braconnot, Patrick Brockmann, Patricia Cadule, Camille Contoux, Anne Cozic, et al. (2020). "Implementation of the CMIP6 Forcing Data in the IPSL-CM6A-LR Model". In: *Journal of Advances in Modeling Earth Systems* 12.4, pp. 1–22. ISSN: 1942-2466. DOI: 10.1029/2019MS001940. URL: https://onlinelibrary.wiley.com/doi/10.1029/2019MS001940 cited on pages 51, 89.

Luyssaert, Sebastiaan, Mathilde Jammet, Paul C. Stoy, Stephan Estel, Julia Pongratz, Eric Ceschia, Galina Churkina, Axel Don, Karlheinz Erb, Morgan Ferlicoq, et al. (2014). "Land management and land-cover change have impacts of similar magnitude on surface temperature". In: *Nature Climate Change* 4.5, pp. 389–393. ISSN: 1758-678X. DOI: 10.1038/nclimate2196. URL: http://www.nature.com/articles/nclimate2196 cited on page 14.

Manabe, Syukuro (1969). "CLIMATE AND THE OCEAN CIRCULATION I. THE ATMOSPHERIC CIRCULATION AND THE HYDROLOGY OF THE EARTH'S SURFACE". In: *Monthly Weather Review* 97.11, pp. 739–774. ISSN: 0027-0644. DOI: 10.1175/1520-0493(1969)097<0739:CATOC>2.3.CO;2. URL: http://journals.ametsoc.org/doi/10.1175/1520-0493(1969)097%5C%3C0739:CATOC%5C%3E2.3.CO;2 cited on page 22.

Maquin, Mathilde (2016). "Développement d'un modèle hydrologique de colonne représentant l'interaction nappe - végétation - atmosphère et applications à l'échelle du bassin versant." PhD thesis. Université Paris Saclay (COmUE) cited on page 127.

Markovich, Katherine H., Reed M. Maxwell, and Graham E. Fogg (2016). "Hydrogeological response to climate change in alpine hillslopes". In: *Hydrological Processes* 30.18, pp. 3126–3138. ISSN: 08856087. DOI: 10.1002/hyp.10851. URL: http://doi.wiley.com/10.1002/hyp.10851 cited on pages 9, 50, 53.

Martens, Brecht, Diego G. Miralles, Hans Lievens, Robin van der Schalie, Richard A. M. de Jeu, Diego Fernández-Prieto, Hylke E. Beck, Wouter A. Dorigo, and Niko E. C. Verhoest (2017). "GLEAM v3: satellite-based land evaporation and root-zone soil moisture". In: *Geoscientific Model Development* 10.5, pp. 1903–1925. ISSN: 1991-9603. DOI: 10.5194/

gmd-10-1903-2017. URL: https://www.geosci-model-dev.net/10/1903/2017/ cited on pages 10, 60, 99.

Martinez, J. Alejandro, Francina Dominguez, and Gonzalo Miguez-Macho (2016a). "Effects of a Groundwater Scheme on the Simulation of Soil Moisture and Evapotranspiration over Southern South America". In: *Journal of Hydrometeorology* 17.11, pp. 2941–2957. ISSN: 1525-755X. DOI: 10.1175/JHM-D-16-0051.1. URL: http://journals.ametsoc.org/doi/10.1175/JHM-D-16-0051.1 cited on page 49.

— (2016b). "Impacts of a Groundwater Scheme on Hydroclimatological Conditions over Southern South America". In: *Journal of Hydrometeorology* 17.11, pp. 2959–2978. ISSN: 1525-755X. DOI: 10.1175/JHM-D-16-0052.1. URL: http://journals.ametsoc.org/doi/10.1175/JHM-D-16-0052.1 cited on page 49.

Martínez-De La Torre, Alberto and Gonzalo Miguez-Macho (2019). "Groundwater influence on soil moisture memory and land-atmosphere fluxes in the Iberian Peninsula". In: *Hydrology and Earth System Sciences* 23.12, pp. 4909–4932. ISSN: 16077938. DOI: 10.5194/hess-23-4909-2019 cited on pages 9, 49.

Maxwell, Reed M and Laura E Condon (2016). "Connections between groundwater flow and transpiration partitioning". In: *Science* 353.6297, pp. 377–380. ISSN: 0036-8075. DOI: 10.1126/science.aaf7891. URL: https://www.sciencemag.org/lookup/doi/10.1126/science.aaf7891 cited on pages 14, 16, 49.

McColl, Kaighin A., Seyed Hamed Alemohammad, Ruzbeh Akbar, Alexandra G. Konings, Simon Yueh, and Dara Entekhabi (2017). "The global distribution and dynamics of surface soil moisture". In: *Nature Geoscience* 10.2, pp. 100–104. ISSN: 17520908. DOI: 10.1038/ngeo2868 cited on page 10.

Mekonnen, M. M. and A. Y. Hoekstra (2011). "The green, blue and grey water footprint of crops and derived crop products". In: *Hydrology and Earth System Sciences* 15.5, pp. 1577–1600. ISSN: 1607-7938. DOI: 10.5194/hess-15-1577-2011. URL: https://hess.copernicus.org/articles/15/1577/2011/ cited on page 87.

Miguez-Macho, Gonzalo and Ying Fan (2021). "Spatiotemporal origin of soil water taken up by vegetation". In: *Nature* 598.7882, pp. 624–628. ISSN: 0028-0836. DOI: 10.1038/s41586-021-03958-6. URL: https://www.nature.com/articles/s41586-021-03958-6 cited on pages 9, 10, 14, 15.

Miguez-Macho, Gonzalo, Ying Fan, Christopher P. Weaver, Robert Walko, and Alan Robock (2007). "Incorporating water table dynamics in climate modeling: 2. Formulation, validation, and soil moisture simulation". In: *Journal of Geophysical Research: Atmospheres* 112.D13, 2006JD008112. ISSN: 0148-0227. DOI: 10.1029/2006JD008112. URL: https://onlinelibrary.wiley.com/doi/10.1029/2006JD008112 cited on pages 25, 74.

Miller, Matthew P., Susan G. Buto, David D. Susong, and Christine A. Rumsey (2016). "The importance of base flow in sustaining surface water flow in the Upper Colorado River Basin". In: *Water Resources Research* 52.5, pp. 3547–3562. ISSN: 00431397. DOI:

10.1002/2015WR017963. URL: http://doi.wiley.com/10.1002/2015WR017963 cited on page 9.

Milly, P. C. D. (1992). "Potential Evaporation and Soil Moisture in General Circulation Models". In: *Journal of Climate* 5.3, pp. 209–226. ISSN: 0894-8755. DOI: 10.1175/1520-0442(1992)005<0209:PEASMI>2.0.CO;2. URL: https://journals.ametsoc.org/downloadpdf/journals/clim/5/3/1520-0442_1992_005_0209_peasmi_2_0_co_2.pdf cited on page 39.

Milly, P. C. D., Sergey L. Malyshev, Elena Shevliakova, Krista A. Dunne, Kirsten L. Findell, Tom Gleeson, Zhi Liang, Peter Phillipps, Ronald J. Stouffer, and Sean Swenson (2014). "An Enhanced Model of Land Water and Energy for Global Hydrologic and Earth-System Studies". In: *Journal of Hydrometeorology* 15.5, pp. 1739–1761. ISSN: 1525-755X. DOI: 10.1175/JHM-D-13-0162.1. URL: https://journals.ametsoc.org/jhm/article/15/5/1739/6045/An-Enhanced-Model-of-Land-Water-and-Energy-for cited on page 25.

Milly, P. C.D. and K. A. Dunne (2016). "Potential evapotranspiration and continental drying". In: *Nature Climate Change* 6.10, pp. 946–949. ISSN: 17586798. DOI: 10.1038/nclimate3046 cited on pages 12, 69.

Miralles, Diego G., Pierre Gentine, Sonia I. Seneviratne, and Adriaan J. Teuling (2019). "Land-atmospheric feedbacks during droughts and heatwaves: state of the science and current challenges". In: *Annals of the New York Academy of Sciences* 1436.1, pp. 19–35. ISSN: 00778923. DOI: 10.1111/nyas.13912. URL: https://onlinelibrary.wiley.com/doi/10.1111/nyas.13912 cited on pages 4, 6, 7.

Mishra, Srikanta (2009). "Uncertainty and sensitivity analysis techniques for hydrologic modeling". In: *Journal of Hydroinformatics* 11.3-4, pp. 282–296. ISSN: 14647141. DOI: 10.2166/hydro.2009.048 cited on page 94.

Mizuochi, Hiroki, Agnès Ducharne, Frédérique Cheruy, Josefine Ghattas, Amen Al-Yaari, Jean-Pierre Wigneron, Vladislav Bastrikov, Philippe Peylin, Fabienne Maignan, and Nicolas Vuichard (2021). "Multivariable evaluation of land surface processes in forced and coupled modes reveals new error sources to the simulated water cycle in the IPSL (Institute Pierre Simon Laplace) climate model". In: *Hydrology and Earth System Sciences* 25.4, pp. 2199–2221. ISSN: 1607-7938. DOI: 10.5194/hess-25-2199-2021. URL: https://hess.copernicus.org/articles/25/2199/2021/ cited on pages 35, 51, 59, 87, 89, 101.

Moene, Arnold F. and Jos C. van Dam (2014). *Transport in the Atmosphere-Vegetation-Soil Continuum*. First Edit. New York: Cambridge University Press, p. 450. ISBN: 9780521195683 cited on pages 9, 10, 36, 39, 43.

Molod, A., L. Takacs, M. Suarez, and J. Bacmeister (2015). "Development of the GEOS-5 atmospheric general circulation model: evolution from MERRA to MERRA2". In: *Geoscientific Model Development* 8.5, pp. 1339–1356. ISSN: 1991-9603. DOI: 10.5194/gmd-8-1339-2015. URL: https://gmd.copernicus.org/articles/8/1339/2015/ cited on page 24.

Mu, Mengyuan, Martin G. De Kauwe, Anna M. Ukkola, Andy J. Pitman, Weidong Guo, Sanaa Hobeichi, and Peter R. Briggs (2021). "Exploring how groundwater buffers the influence of heatwaves on vegetation function during multi-year droughts". In: *Earth System Dynamics* 12.3, pp. 919–938. ISSN: 2190-4987. DOI: 10.5194/esd-12-919-2021. URL: https://esd.copernicus.org/articles/12/919/2021/ cited on pages 10, 76.

Mualem, Yechezkel (1976). "A new model for predicting the hydraulic conductivity of unsaturated porous media". In: *Water Resources Research* 12.3, pp. 513–522. ISSN: 00431397. DOI: 10.1029/WR012i003p00513. URL: http://doi.wiley.com/10.1029/WR012i003p00513 cited on pages 41, 52.

Ngo-Duc, T., K. Laval, G. Ramillien, J. Polcher, and A. Cazenave (2007). "Validation of the land water storage simulated by Organising Carbon and Hydrology in Dynamic Ecosystems (ORCHIDEE) with Gravity Recovery and Climate Experiment (GRACE) data". In: *Water Resources Research* 43.4. ISSN: 00431397. DOI: 10.1029/2006WR004941 cited on pages 28, 34, 42, 43, 52, 53, 90, 91.

Ngo-Duc, Thanh, Jan Polcher, and Katia Laval (2005). "A 53-year forcing data set for land surface models". In: *Journal of Geophysical Research: Atmospheres* 110.D6, n/a–n/a. ISSN: 01480227. DOI: 10.1029/2004JD005434. URL: http://doi.wiley.com/10.1029/2004JD005434 cited on page 43.

Niu, Guo Yue, Zong Liang Yang, Robert E. Dickinson, Lindsey E. Gulden, and Hua Su (2007). "Development of a simple groundwater model for use in climate models and evaluation with Gravity Recovery and Climate Experiment data". In: *Journal of Geophysical Research Atmospheres* 112.7, pp. 1–14. ISSN: 01480227. DOI: 10.1029/2006JD007522 cited on page 24.

O'Neill, Brian C., Claudia Tebaldi, Detlef P. van Vuuren, Veronika Eyring, Pierre Friedlingstein, George Hurtt, Reto Knutti, Elmar Kriegler, Jean-Francois Lamarque, Jason Lowe, Gerald A. Meehl, Richard Moss, Keywan Riahi, and Benjamin M. Sanderson (2016). "The Scenario Model Intercomparison Project (ScenarioMIP) for CMIP6". In: *Geoscientific Model Development* 9.9, pp. 3461–3482. ISSN: 1991-9603. DOI: 10.5194/gmd-9-3461-2016. URL: https://gmd.copernicus.org/articles/9/3461/2016/ cited on page 55.

Oki, Taikan, Teruyuki Nishimura, and Paul Dirmeyer (1999). "Assessment of Annual Runoff from Land Surface Models Using Total Runoff Integrating Pathways (TRIP)". In: *Journal of the Meteorological Society of Japan. Ser. II* 77.1B, pp. 235–255. ISSN: 0026-1165. DOI: 10.2151/jmsj1965.77.1B_235. URL: https://www.jstage.jst.go.jp/article/jmsj1965/77/1B/77_1B_235/_article cited on pages 53, 114.

Oliveira, Luiza Vargas de (2022). "Irrigation in the ORCHIDEE model : Evaluating inputs and results in metropolitan France". Internship report. Ecole Normale Superieure, p. 37 cited on pages 118–120.

Ozdogan, Mutlu, Matthew Rodell, Hiroko Kato Beaudoing, and David L. Toll (2010). "Simulating the effects of irrigation over the united states in a land surface model based on

satellite-derived agricultural data". In: *Journal of Hydrometeorology* 11.1, pp. 171–184. ISSN: 1525755X. DOI: 10.1175/2009JHM1116.1 cited on pages 88, 94.

Padrón, Ryan S., Lukas Gudmundsson, Bertrand Decharme, Agnès Ducharne, David M. Lawrence, Jiafu Mao, Daniele Peano, Gerhard Krinner, Hyungjun Kim, and Sonia I. Seneviratne (2020). "Observed changes in dry-season water availability attributed to human-induced climate change". In: *Nature Geoscience* 13.7, pp. 477–481. ISSN: 1752-0894. DOI: 10.1038/s41561-020-0594-1. URL: http://dx.doi.org/10.1038/s41561-020-0594-1%20http://www.nature.com/articles/s41561-020-0594-1 cited on page 75.

Perkins, S. E. and L. V. Alexander (2013). "On the Measurement of Heat Waves". In: *Journal of Climate* 26.13, pp. 4500–4517. ISSN: 0894-8755. DOI: 10.1175/JCLI-D-12-00383.1. URL: http://journals.ametsoc.org/doi/10.1175/JCLI-D-12-00383.1 cited on pages 61, 80.

Perkins, Sarah E. (2015). "A review on the scientific understanding of heatwaves-Their measurement, driving mechanisms, and changes at the global scale". In: *Atmospheric Research* 164-165, pp. 242–267. ISSN: 01698095. DOI: 10.1016/j.atmosres.2015.05.014. URL: http://dx.doi.org/10.1016/j.atmosres.2015.05.014 cited on pages 12, 49, 78.

Piao, Shilong, Pierre Friedlingstein, Philippe Ciais, N. de Noblet-Ducoudre, David Labat, and Sönke Zaehle (2007). "Changes in climate and land use have a larger direct impact than rising CO2 on global river runoff trends". In: *Proceedings of the National Academy of Sciences* 104.39, pp. 15242–15247. ISSN: 0027-8424. DOI: 10.1073/pnas.0707213104. URL: http://www.pnas.org/cgi/doi/10.1073/pnas.0707213104 cited on pages 12, 14.

Pokhrel, Yadu, Farshid Felfelani, Yusuke Satoh, Julien Boulange, Peter Burek, Anne Gädeke, Dieter Gerten, Simon N. Gosling, Manolis Grillakis, Lukas Gudmundsson, et al. (2021). "Global terrestrial water storage and drought severity under climate change". In: *Nature Climate Change* 11.3, pp. 226–233. ISSN: 1758-678X. DOI: 10.1038/s41558-020-00972-w. URL: http://dx.doi.org/10.1038/s41558-020-00972-w%20http://www.nature.com/articles/s41558-020-00972-w cited on page 12.

Pokhrel, Yadu, Naota Hanasaki, Sujan Koirala, Jaeil Cho, Pat J.F. Yeh, Hyungjun Kim, Shinjiro Kanae, and Taikan Oki (2012). "Incorporating Anthropogenic Water Regulation Modules into a Land Surface Model". In: *Journal of Hydrometeorology* 13.1, pp. 255–269. ISSN: 1525-755X. DOI: 10.1175/JHM-D-11-013.1. URL: https://journals.ametsoc.org/jhm/article/13/1/255/70367/Incorporating-Anthropogenic-Water-Regulation cited on pages 27, 88, 116.

Pokhrel, Yadu N., Naota Hanasaki, Yoshihide Wada, and Hyungjun Kim (2016). "Recent progresses in incorporating human land-water management into global land surface models toward their integration into Earth system models". In: *Wiley Interdisciplinary Reviews: Water* 3.4, pp. 548–574. ISSN: 20491948. DOI: 10.1002/wat2.1150. URL: http://doi.wiley.com/10.1002/wat2.1150 cited on pages 23, 87, 94, 101, 105, 115, 124, 128.

Pokhrel, Yadu N., Sujan Koirala, Pat J.-F. Yeh, Naota Hanasaki, Laurent Longuevergne, Shinjiro Kanae, and Taikan Oki (2015). "Incorporation of groundwater pumping in a global Land Surface Model with the representation of human impacts". In: *Water Resources Research* 51.1, pp. 78–96. ISSN: 00431397. DOI: 10.1002/2014WR015602. arXiv: 2014WR016527 [10.1002]. URL: http://doi.wiley.com/10.1002/2014WR015602 cited on pages 27, 88, 116.

Polcher, J., B. McAvaney, P. Viterbo, M.-A. Gaertner, A. Hahmann, J.-F. Mahfouf, J. Noilhan, T. Phillips, A. Pitman, C.A. Schlosser, J.-P. Schulz, B. Timbal, D. Verseghy, and Y. Xue (1998). "A proposal for a general interface between land surface schemes and general circulation models". In: *Global and Planetary Change* 19.1-4, pp. 261–276. ISSN: 09218181. DOI: 10.1016/S0921-8181(98)00052-6. URL: https://linkinghub.elsevier.com/retrieve/pii/S0921818198000526 cited on pages 37, 44.

Polcher, Jan (2003). *Les processus de surfacè a l'echelle globale et leurs interactions avec l'atmosphère. - Habilitation à diriger des recherches*. Tech. rep. cited on page 42.

Portmann, Felix T., Stefan Siebert, and Petra Döll (2010). "MIRCA2000-Global monthly irrigated and rainfed crop areas around the year 2000: A new high-resolution data set for agricultural and hydrological modeling". In: *Global Biogeochemical Cycles* 24.1, n/a–n/a. ISSN: 08866236. DOI: 10.1029/2008GB003435. URL: http://doi.wiley.com/10.1029/2008GB003435 cited on pages 100, 149.

Puma, M. J. and B. I. Cook (2010). "Effects of irrigation on global climate during the 20th century". In: *Journal of Geophysical Research* 115.D16, p. D16120. ISSN: 0148-0227. DOI: 10.1029/2010JD014122. URL: http://doi.wiley.com/10.1029/2010JD014122 cited on pages 26, 87, 88, 92.

Puy, Arnald, Emanuele Borgonovo, Samuele Lo Piano, Simon A. Levin, and Andrea Saltelli (2021). "Irrigated areas drive irrigation water withdrawals". In: *Nature Communications* 12.1, pp. 1–12. ISSN: 20411723. DOI: 10.1038/s41467-021-24508-8. URL: http://dx.doi.org/10.1038/s41467-021-24508-8 cited on pages 103, 119.

Quesada, Benjamin, Robert Vautard, Pascal Yiou, Martin Hirschi, and Sonia I. Seneviratne (2012). "Asymmetric European summer heat predictability from wet and dry southern winters and springs". In: *Nature Climate Change* 2.10, pp. 736–741. ISSN: 1758-678X. DOI: 10.1038/nclimate1536. URL: http://dx.doi.org/10.1038/nclimate1536%20http://www.nature.com/articles/nclimate1536 cited on pages 6, 48, 77.

Rashid, Mehnaz, Rong-You Chien, Agnès Ducharne, Hyungjun Kim, Pat J.F. Yeh, Christophe Peugeot, Aaron Boone, Xiaogang He, Luc Séguis, Yutaro Yabu, Moussa Boukari, and Min-Hui Lo (2019). "Evaluation of Groundwater Simulations in Benin from the ALMIP2 Project". In: *Journal of Hydrometeorology* 20.2, pp. 339–354. ISSN: 1525-755X. DOI: 10.1175/JHM-D-18-0025.1. URL: http://journals.ametsoc.org/doi/10.1175/JHM-D-18-0025.1 cited on page 74.

Ringeval, B., B. Decharme, S. L. Piao, P. Ciais, F. Papa, N. de Noblet-Ducoudré, C. Prigent, P. Friedlingstein, I. Gouttevin, C. Koven, and A. Ducharne (2012). "Modelling sub-grid

wetland in the ORCHIDEE global land surface model: evaluation against river discharges and remotely sensed data". In: *Geoscientific Model Development* 5.4, pp. 941–962. ISSN: 1991-9603. DOI: 10.5194/gmd-5-941-2012. URL: https://gmd.copernicus.org/articles/5/941/2012/ cited on page 28.

Rodell, M., H. K. Beaudoing, T. S. L'Ecuyer, W. S. Olson, J. S. Famiglietti, P. R. Houser, R. Adler, M. G. Bosilovich, C. A. Clayson, D. Chambers, et al. (2015). "The observed state of the water cycle in the early twenty-first century". In: *Journal of Climate* 28.21, pp. 8289–8318. ISSN: 08948755. DOI: 10.1175/JCLI-D-14-00555.1 cited on page 4.

Rodell, M., J. S. Famiglietti, D. N. Wiese, J. T. Reager, H. K. Beaudoing, F. W. Landerer, and M.-H. Lo (2018). "Emerging trends in global freshwater availability". In: *Nature* 557.7707, pp. 651–659. ISSN: 0028-0836. DOI: 10.1038/s41586-018-0123-1. URL: http://www.nature.com/articles/s41586-018-0123-1 cited on pages 2, 19, 113.

Roderick, Michael L., Peter Greve, and Graham D. Farquhar (2015). "On the assessment of aridity with changes in atmospheric CO2". In: *Water Resources Research* 51.7, pp. 5450–5463. ISSN: 0043-1397. DOI: 10.1002/2015WR017031. URL: https://onlinelibrary.wiley.com/doi/abs/10.1002/2015WR017031 cited on page 12.

Rosnay, P. de, J. Polcher, M. Bruen, and K. Laval (2002). "Impact of a physically based soil water flow and soil-plant interaction representation for modeling large-scale land surface processes". In: *Journal of Geophysical Research: Atmospheres* 107.D11, ACL 3–1–ACL 3–19. ISSN: 01480227. DOI: 10.1029/2001JD000634. URL: http://doi.wiley.com/10.1029/2001JD000634 cited on pages 32, 41, 51, 52, 90.

Rosnay, P. de, Jan Polcher, Katia Laval, and M. Sabre (2003). "Integrated parameterization of irrigation in the land surface model ORCHIDEE. Validation over Indian Peninsula". In: *Geophysical Research Letters* 30.19, p. 1986. ISSN: 0094-8276. DOI: 10.1029/2003GL018024. URL: http://doi.wiley.com/10.1029/2003GL018024 cited on pages 26, 29, 88.

Rost, Stefanie, Dieter Gerten, Alberte Bondeau, Wolfgang Lucht, Janine Rohwer, and Sibyll Schaphoff (2008). "Agricultural green and blue water consumption and its influence on the global water system". In: *Water Resources Research* 44.9, pp. 1–17. ISSN: 00431397. DOI: 10.1029/2007WR006331. URL: http://doi.wiley.com/10.1029/2007WR006331 cited on page 87.

Russo, Simone, Jana Sillmann, and Erich M. Fischer (2015). "Top ten European heatwaves since 1950 and their occurrence in the coming decades". In: *Environmental Research Letters* 10.12. ISSN: 17489326. DOI: 10.1088/1748-9326/10/12/124003 cited on page 80.

Sacks, William J., Benjamin I. Cook, Nikolaus Buenning, Samuel Levis, and Joseph H. Helkowski (2009). "Effects of global irrigation on the near-surface climate". In: *Climate Dynamics* 33.2-3, pp. 159–175. ISSN: 0930-7575. DOI: 10.1007/s00382-008-0445-z. URL: http://link.springer.com/10.1007/s00382-008-0445-z cited on pages 91, 95, 98, 100, 102, 103, 110, 120, 143, 145.

Save, Himanshu, Srinivas Bettadpur, and Byron D. Tapley (2016). "High-resolution CSR GRACE RL05 mascons". In: *Journal of Geophysical Research: Solid Earth* 121.10, pp. 7547–7569. ISSN: 21699313. DOI: 10.1002/2016JB013007. URL: http://doi.wiley.com/10.1002/2016JB013007 cited on page 100.

Scanlon, Bridget R., Zizhan Zhang, Himanshu Save, David N. Wiese, Felix W. Landerer, Di Long, Laurent Longuevergne, and Jianli Chen (2016). "Global evaluation of new GRACE mascon products for hydrologic applications". In: *Water Resources Research* 52.12, pp. 9412–9429. ISSN: 00431397. DOI: 10.1002/2016WR019494. URL: https://onlinelibrary.wiley.com/doi/10.1111/j.1752-1688.1969.tb04897.x%20http://doi.wiley.com/10.1002/2016WR019494 cited on page 100.

Schneider, A., A. Jost, C. Coulon, M. Silvestre, S. Théry, and A. Ducharne (2017a). "Global-scale river network extraction based on high-resolution topography and constrained by lithology, climate, slope, and observed drainage density". In: *Geophysical Research Letters* 44.6, pp. 2773–2781. ISSN: 00948276. DOI: 10.1002/2016GL071844. URL: http://doi.wiley.com/10.1002/2016GL071844 cited on page 55.

Schneider, Ana (2017). "Estimation of the base flow time constant for global scale applications". PhD thesis. Sorbonne University, p. 186 cited on pages 9, 107.

Schneider, Udo, Peter Finger, Anja Meyer-Christoffer, Elke Rustemeier, Markus Ziese, and Andreas Becker (2017b). "Evaluating the Hydrological Cycle over Land Using the Newly-Corrected Precipitation Climatology from the Global Precipitation Climatology Centre (GPCC)". In: *Atmosphere* 8.12, p. 52. ISSN: 2073-4433. DOI: 10.3390/atmos8030052. URL: http://www.mdpi.com/2073-4433/8/3/52 cited on pages 60, 127.

Seland, Øyvind, Mats Bentsen, Dirk Olivié, Thomas Toniazzo, Ada Gjermundsen, Lise Seland Graff, Jens Boldingh Debernard, Alok Kumar Gupta, Yan-chun He, Alf Kirkevåg, et al. (2020). "Overview of the Norwegian Earth System Model (NorESM2) and key climate response of CMIP6 DECK, historical, and scenario simulations". In: *Geoscientific Model Development* 13.12, pp. 6165–6200. ISSN: 1991-9603. DOI: 10.5194/gmd-13-6165-2020. URL: https://gmd.copernicus.org/articles/13/6165/2020/ cited on page 76.

Sellers, P. J., Y. Mintz, Y. C. Sud, and A. Dalcher (1986). "A Simple Biosphere Model (SIB) for Use within General Circulation Models". In: *Journal of the Atmospheric Sciences* 43.6, pp. 505–531. ISSN: 0022-4928. DOI: 10.1175/1520-0469(1986)043<0505:ASBMFU>2.0.CO;2. URL: https://journals.ametsoc.org/view/journals/atsc/43/6/1520-0469_1986_043_0505_asbmfu_2_0_co_2.xml?tab_body=pdf cited on pages 22, 23.

Sen, Pranab Kumar (1968). "Estimates of the Regression Coefficient Based on Kendall's Tau". In: *Journal of the American Statistical Association* 63.324, p. 1379. ISSN: 01621459. DOI: 10.2307/2285891. URL: https://www.jstor.org/stable/2285891%20https://www.jstor.org/stable/2285891?origin=crossref cited on page 61.

Seneviratne, Sonia I., Thierry Corti, Edouard L. Davin, Martin Hirschi, Eric B. Jaeger, Irene Lehner, Boris Orlowsky, and Adriaan J. Teuling (2010). "Investigating soil moisture-climate interactions in a changing climate: A review". In: *Earth-Science Reviews* 99.3-4,

pp. 125–161. ISSN: 00128252. DOI: 10.1016/j.earscirev.2010.02.004. URL: http://dx.doi.org/10.1016/j.earscirev.2010.02.004 cited on pages 2–5, 7, 9, 10, 48, 55, 56.

Seneviratne, Sonia I., Micah Wilhelm, Tanja Stanelle, Bart Van Den Hurk, Stefan Hagemann, Alexis Berg, Frederique Cheruy, Matthew E. Higgins, Arndt Meier, Victor Brovkin, et al. (2013). "Impact of soil moisture-climate feedbacks on CMIP5 projections: First results from the GLACE-CMIP5 experiment". In: *Geophysical Research Letters* 40.19, pp. 5212–5217. ISSN: 00948276. DOI: 10.1002/grl.50956 cited on pages 2, 28, 49.

Sergeant, Flore, René Therrien, Ludovic Oudin, Anne Jost, and François Anctil (2021). "Evolution of Arctic rivers recession flow: Global assessment and data-based attribution analysis". In: *Journal of Hydrology* 601.June, p. 126577. ISSN: 00221694. DOI: 10.1016/j.jhydrol.2021.126577. URL: https://linkinghub.elsevier.com/retrieve/pii/S0022169421006247 cited on pages 74, 75.

Short Gianotti, Daniel J., Ruzbeh Akbar, Andrew F. Feldman, Guido D. Salvucci, and Dara Entekhabi (2020). "Terrestrial Evaporation and Moisture Drainage in a Warmer Climate". In: *Geophysical Research Letters* 47.5, pp. 1–12. ISSN: 0094-8276. DOI: 10.1029/2019GL086498. URL: https://onlinelibrary.wiley.com/doi/10.1029/2019GL086498 cited on page 4.

Siebert, S., J. Burke, J. M. Faures, K. Frenken, J. Hoogeveen, P. Döll, and F. T. Portmann (2010). "Groundwater use for irrigation - A global inventory". In: *Hydrology and Earth System Sciences* 14.10, pp. 1863–1880. ISSN: 10275606. DOI: 10.5194/hess-14-1863-2010 cited on pages 14, 17, 26, 87, 88, 93, 103.

Siebert, S., P. Döll, J. Hoogeveen, J. M. Faures, K. Frenken, and S. Feick (2005). "Development and validation of the global map of irrigation areas". In: *Hydrology and Earth System Sciences* 9.5, pp. 535–547. ISSN: 16077938. DOI: 10.5194/hess-9-535-2005 cited on page 118.

Siebert, Stefan and Petra Döll (2010). "Quantifying blue and green virtual water contents in global crop production as well as potential production losses without irrigation". In: *Journal of Hydrology* 384.3-4, pp. 198–217. ISSN: 00221694. DOI: 10.1016/j.jhydrol.2009.07.031. URL: http://dx.doi.org/10.1016/j.jhydrol.2009.07.031 cited on pages 17, 86, 87.

Siebert, Stefan, Matti Kummu, Miina Porkka, Petra Döll, Navin Ramankutty, and Bridget R. Scanlon (2015). "A global data set of the extent of irrigated land from 1900 to 2005". In: *Hydrology and Earth System Sciences* 19.3, pp. 1521–1545. ISSN: 1607-7938. DOI: 10.5194/hess-19-1521-2015. URL: http://dx.doi.org/10.13019/M20599%5C%5Cnhttps://mygeohub.org/publications/8/2%20https://www.hydrol-earth-syst-sci.net/19/1521/2015/ cited on pages 14, 17, 86, 97.

Singh, Deepti, Sonali P. McDermid, Benjamin I. Cook, Michael J. Puma, Larissa Nazarenko, and Maxwell Kelley (2018). "Distinct Influences of Land Cover and Land Management on Seasonal Climate". In: *Journal of Geophysical Research: Atmospheres* 123.21, pp. 12, 017–

12, 039. ISSN: 2169-897X. DOI: 10.1029/2018JD028874. URL: https://onlinelibrary.wiley.com/doi/10.1029/2018JD028874 cited on page 26.

Smerdon, Brian D. (2017). "A synopsis of climate change effects on groundwater recharge". In: *Journal of Hydrology* 555, pp. 125–128. ISSN: 00221694. DOI: 10.1016/j.jhydrol.2017.09.047. URL: https://doi.org/10.1016/j.jhydrol.2017.09.047%20https://linkinghub.elsevier.com/retrieve/pii/S0022169417306510 cited on pages 9, 12, 50.

Song, Xiaomeng, Jianyun Zhang, Chesheng Zhan, Yunqing Xuan, Ming Ye, and Chonggang Xu (2015). "Global sensitivity analysis in hydrological modeling: Review of concepts, methods, theoretical framework, and applications". In: *Journal of Hydrology* 523.225, pp. 739–757. ISSN: 00221694. DOI: 10.1016/j.jhydrol.2015.02.013. URL: http://dx.doi.org/10.1016/j.jhydrol.2015.02.013%20https://linkinghub.elsevier.com/retrieve/pii/S0022169415001249 cited on pages 94, 97.

Subin, Z. M., P. C. D. Milly, B. N. Sulman, S. Malyshev, and E. Shevliakova (2014). "Resolving terrestrial ecosystem processes along a subgrid topographic gradient for an earth-system model". In: *Hydrology and Earth System Sciences Discussions* 11.7, pp. 8443–8492. ISSN: 1812-2116. DOI: 10.5194/hessd-11-8443-2014. URL: https://hess.copernicus.org/preprints/11/8443/2014/ cited on page 25.

Swenson, Sean C., Martyn Clark, Ying Fan, David M. Lawrence, and Justin Perket (2019). "Representing Intrahillslope Lateral Subsurface Flow in the Community Land Model". In: *Journal of Advances in Modeling Earth Systems* 11.12, pp. 4044–4065. ISSN: 1942-2466. DOI: 10.1029/2019MS001833. URL: https://onlinelibrary.wiley.com/doi/abs/10.1029/2019MS001833 cited on pages 24, 53, 127.

Tafasca, Salma (2020). "Évaluation de l'impact des propriétés du sol sur l'hydrologie simulée dans le modèle ORCHIDEE". PhD thesis. Sorbonne Université cited on pages 32, 34, 37–39.

Tafasca, Salma, Agnès Ducharne, and Christian Valentin (2020). "Weak sensitivity of the terrestrial water budget to global soil texture maps in the ORCHIDEE land surface model". In: *Hydrology and Earth System Sciences* 24.7, pp. 3753–3774. ISSN: 1607-7938. DOI: 10.5194/hess-24-3753-2020. URL: https://hess.copernicus.org/articles/24/3753/2020/ cited on pages 32, 34, 35, 51, 89, 90.

Taylor, Richard G., Bridget Scanlon, Petra Döll, Matt Rodell, Rens van Beek, Yoshihide Wada, Laurent Longuevergne, Marc Leblanc, James S. Famiglietti, Mike Edmunds, et al. (2013). "Ground water and climate change". In: *Nature Climate Change* 3.4, pp. 322–329. ISSN: 1758-678X. DOI: 10.1038/nclimate1744. URL: http://www.nature.com/articles/nclimate1744 cited on page 87.

Tebaldi, Claudia, Kevin Debeire, Veronika Eyring, Erich Fischer, John Fyfe, Pierre Friedlingstein, Reto Knutti, Jason Lowe, Brian O'Neill, Benjamin Sanderson, et al. (2021). "Climate model projections from the Scenario Model Intercomparison Project (ScenarioMIP)

of CMIP6". In: *Earth System Dynamics* 12.1, pp. 253–293. ISSN: 21904987. DOI: 10.5194/esd-12-253-2021 cited on pages 10, 55.

Thiery, Wim, Edouard L. Davin, David M. Lawrence, Annette L. Hirsch, Mathias Hauser, and Sonia I. Seneviratne (2017). "Present-day irrigation mitigates heat extremes". In: *Journal of Geophysical Research* 122.3, pp. 1403–1422. ISSN: 21562202. DOI: 10.1002/2016JD025740 cited on pages 19, 74, 75, 77, 126.

Thiery, Wim, Auke J Visser, Erich M Fischer, Mathias Hauser, Annette L Hirsch, David M Lawrence, Quentin Lejeune, L Edouard, and Sonia I Seneviratne (2018). *Supplementary Information - Warming of hot extremes alleviated by expanding irrigation* cited on page 26.

Thiery, Wim, Auke J. Visser, Erich M. Fischer, Mathias Hauser, Annette L. Hirsch, David M. Lawrence, Quentin Lejeune, Edouard L. Davin, and Sonia I. Seneviratne (2020). "Warming of hot extremes alleviated by expanding irrigation". In: *Nature Communications* 11.1, pp. 1–7. ISSN: 20411723. DOI: 10.1038/s41467-019-14075-4. URL: http://dx.doi.org/10.1038/s41467-019-14075-4 cited on pages 19, 26, 77, 87.

Tootchi, Ardalan (2019). "Development of a global wetland map and application to describe hillslope hydrology in the ORCHIDEE land surface model". PhD thesis. Sorbonne Université, p. 218 cited on pages 25, 28, 31, 54, 59.

Tootchi, Ardalan, Anne Jost, and Agnès Ducharne (2019). "Multi-source global wetland maps combining surface water imagery and groundwater constraints". In: *Earth System Science Data* 11.1, pp. 189–220. ISSN: 18663516. DOI: 10.5194/essd-11-189-2019 cited on pages 28, 52, 53, 74.

Tóth, J. (1963). "A theoretical analysis of groundwater flow in small drainage basins". In: *Journal of Geophysical Research* 68.16, pp. 4795–4812. ISSN: 01480227. DOI: 10.1029/JZ068i016p04795. URL: http://doi.wiley.com/10.1029/JZ068i016p04795 cited on page 9.

Vergnes, J.-P., B. Decharme, and F. Habets (2014). "Introduction of groundwater capillary rises using subgrid spatial variability of topography into the ISBA land surface model". In: *Journal of Geophysical Research: Atmospheres* 119.19, pp. 11, 065–11, 086. ISSN: 2169897X. DOI: 10.1002/2014JD021573. URL: http://doi.wiley.com/10.1002/2014JD021573 cited on pages 24, 127.

Vicente-Serrano, S. M., M. Peña-Gallardo, J. Hannaford, C. Murphy, J. Lorenzo-Lacruz, F. Dominguez-Castro, J. I. López-Moreno, S. Beguería, I. Noguera, S. Harrigan, and J.-P. Vidal (2019). "Climate, Irrigation, and Land Cover Change Explain Streamflow Trends in Countries Bordering the Northeast Atlantic". In: *Geophysical Research Letters* 46.19, pp. 10821–10833. ISSN: 0094-8276. DOI: 10.1029/2019GL084084. URL: https://onlinelibrary.wiley.com/doi/abs/10.1029/2019GL084084 cited on pages 14, 19, 87.

Vicente-Serrano, Sergio M., Tim R. McVicar, Diego G. Miralles, Yuting Yang, and Miquel Tomas-Burguera (2020). "Unraveling the influence of atmospheric evaporative demand on drought and its response to climate change". In: *WIREs Climate Change* 11.2, pp. 1–31.

ISSN: 1757-7780. DOI: 10.1002/wcc.632. URL: https://onlinelibrary.wiley.com/doi/10.1002/wcc.632 cited on pages 6, 12.

Vidal, Jean-Philippe, Benoît Hingray, Claire Magand, Eric Sauquet, and Agnès Ducharne (2016). "Hierarchy of climate and hydrological uncertainties in transient low-flow projections". In: *Hydrology and Earth System Sciences* 20.9, pp. 3651–3672. ISSN: 1607-7938. DOI: 10.5194/hess-20-3651-2016. URL: https://www.hydrol-earth-syst-sci.net/20/3651/2016/ cited on page 12.

Voldoire, A., D. Saint-Martin, S. Sénési, B. Decharme, A. Alias, M. Chevallier, J. Colin, J.-F. Guérémy, M. Michou, M.-P. Moine, et al. (2019). "Evaluation of CMIP6 DECK Experiments With CNRM-CM6-1". In: *Journal of Advances in Modeling Earth Systems* 11.7, pp. 2177–2213. ISSN: 1942-2466. DOI: 10.1029/2019MS001683. URL: https://onlinelibrary.wiley.com/doi/abs/10.1029/2019MS001683 cited on pages 55, 77.

Vörösmarty, C. J., B. M. Fekete, M. Meybeck, and R. B. Lammers (2000). "Global system of rivers: Its role in organizing continental land mass and defining land-to-ocean linkages". In: *Global Biogeochemical Cycles* 14.2, pp. 599–621. ISSN: 08866236. DOI: 10.1029/1999GB900092. URL: http://doi.wiley.com/10.1029/1999GB900092 cited on page 53.

Vrese, Philipp de and Stefan Hagemann (2018). "Uncertainties in modelling the climate impact of irrigation". In: *Climate Dynamics* 51.5-6, pp. 2023–2038. ISSN: 14320894. DOI: 10.1007/s00382-017-3996-z. URL: http://dx.doi.org/10.1007/s00382-017-3996-z cited on pages 44, 116.

Vrese, Philipp de, Stefan Hagemann, and Martin Claussen (2016a). "Asian irrigation, African rain: Remote impacts of irrigation". In: *Geophysical Research Letters* 43.8, pp. 3737–3745. ISSN: 00948276. DOI: 10.1002/2016GL068146. URL: http://doi.wiley.com/10.1002/2016GL068146 cited on page 20.

Vrese, Philipp de, Jan-Peter Schulz, and Stefan Hagemann (2016b). "On the Representation of Heterogeneity in Land-Surface–Atmosphere Coupling". In: *Boundary-Layer Meteorology* 160.1, pp. 157–183. ISSN: 0006-8314. DOI: 10.1007/s10546-016-0133-1. URL: http://link.springer.com/10.1007/s10546-016-0133-1 cited on page 44.

Vuichard, N. and D. Papale (2015). "Filling the gaps in meteorological continuous data measured at FLUXNET sites with ERA-Interim reanalysis". In: *Earth System Science Data* 7.2, pp. 157–171. ISSN: 1866-3516. DOI: 10.5194/essd-7-157-2015. URL: https://www.earth-syst-sci-data.net/7/157/2015/ cited on pages 23, 28.

Wada, Y., D. Wisser, and M. F. P. Bierkens (2014). "Global modeling of withdrawal, allocation and consumptive use of surface water and groundwater resources". In: *Earth System Dynamics* 5.1, pp. 15–40. ISSN: 2190-4987. DOI: 10.5194/esd-5-15-2014. URL: https://esd.copernicus.org/articles/5/15/2014/ cited on pages 18, 87.

Wada, Yoshihide and Marc F P Bierkens (2014). "Sustainability of global water use: past reconstruction and future projections". In: *Environmental Research Letters* 9.10, p. 104003. ISSN: 1748-9326. DOI: 10.1088/1748-9326/9/10/104003. URL: https://iopscience.iop.org/article/10.1088/1748-9326/9/10/104003 cited on page 1.

Wada, Yoshihide, L. P.H. Van Beek, and Marc F.P. Bierkens (2012). "Nonsustainable groundwater sustaining irrigation: A global assessment". In: *Water Resources Research* 48.1. ISSN: 00431397. DOI: 10.1029/2011WR010562. URL: http://doi.wiley.com/10.1029/2011WR010562 cited on pages 18, 87, 101.

Wada, Yoshihide, Dominik Wisser, Stephanie Eisner, Martina Flörke, Dieter Gerten, Ingjerd Haddeland, Naota Hanasaki, Yoshimitsu Masaki, Felix T. Portmann, Tobias Stacke, Zachary Tessler, and Jacob Schewe (2013). "Multimodel projections and uncertainties of irrigation water demand under climate change". In: *Geophysical Research Letters* 40.17, pp. 4626–4632. ISSN: 00948276. DOI: 10.1002/grl.50686 cited on pages 20, 87.

Walko, Robert L., Larry E. Band, Jill Baron, Timothy G. F. Kittel, Richard Lammers, Tsengdar J. Lee, Dennis Ojima, Roger A. Pielke, Chris Taylor, Christina Tague, Craig J. Tremback, and Pier Luigi Vidale (2000). "Coupled Atmosphere–Biophysics–Hydrology Models for Environmental Modeling". In: *Journal of Applied Meteorology* 39.6, pp. 931–944. ISSN: 0894-8763. DOI: 10.1175/1520-0450(2000)039<0931:CABHMF>2.0.CO;2. URL: http://journals.ametsoc.org/doi/10.1175/1520-0450(2000)039%5C%3C0931:CABHMF%5C%3E2.0.CO;2 cited on page 49.

Wang, F., F. Cheruy, and J. L. Dufresne (2016). "The improvement of soil thermodynamics and its effects on land surface meteorology in the IPSL climate model". In: *Geoscientific Model Development* 9.1, pp. 363–381. ISSN: 19919603. DOI: 10.5194/gmd-9-363-2016 cited on page 35.

Wang, Fuxing, Agnès Ducharne, Frédérique Cheruy, Min Hui Lo, and Jean Yves Grandpeix (2018). "Impact of a shallow groundwater table on the global water cycle in the IPSL land–atmosphere coupled model". In: *Climate Dynamics* 50.9-10, pp. 3505–3522. ISSN: 14320894. DOI: 10.1007/s00382-017-3820-9 cited on pages 28, 32, 49, 51, 57, 74, 90.

Wang, Lixin, Stephen P Good, and Kelly K Caylor (2014). "Global synthesis of vegetation control on evapotranspiration partitioning". In: *Geophysical Research Letters* 41.19, pp. 6753–6757. ISSN: 00948276. DOI: 10.1002/2014GL061439. URL: http://doi.wiley.com/10.1002/2014GL061439 cited on page 10.

Watkins, Michael M., David N. Wiese, Dah-Ning Yuan, Carmen Boening, and Felix W. Landerer (2015). "Improved methods for observing Earth's time variable mass distribution with GRACE using spherical cap mascons". In: *Journal of Geophysical Research: Solid Earth* 120.4, pp. 2648–2671. ISSN: 21699313. DOI: 10.1002/2014JB011547. URL: http://doi.wiley.com/10.1002/2014JB011547 cited on page 100.

Wei, Jiangfeng, Paul A. Dirmeyer, Dominik Wisser, Michael G. Bosilovich, and David M. Mocko (2013). "Where does the irrigation water go? An estimate of the contribution of irrigation to precipitation using MERRA". In: *Journal of Hydrometeorology* 14.1, pp. 275–289. ISSN: 1525755X. DOI: 10.1175/JHM-D-12-079.1 cited on pages 6, 19.

Wei, Zhongwang, Kei Yoshimura, Lixin Wang, Diego G. Miralles, Scott Jasechko, and Xuhui Lee (2017). "Revisiting the contribution of transpiration to global terrestrial evapotranspiration". In: *Geophysical Research Letters* 44.6, pp. 2792–2801. ISSN: 00948276. DOI:

10.1002/2016GL072235. URL: http://doi.wiley.com/10.1002/2016GL072235 cited on page 10.

Wu, Wen-Ying, Min-Hui Lo, Yoshihide Wada, James S. Famiglietti, John T. Reager, Pat J.F. Yeh, Agnès Ducharne, and Zong-Liang Yang (2020). "Divergent effects of climate change on future groundwater availability in key mid-latitude aquifers". In: *Nature Communications* 11.1, p. 3710. ISSN: 2041-1723. DOI: 10.1038/s41467-020-17581-y. URL: http://dx.doi.org/10.1038/s41467-020-17581-y%20http://www.nature.com/articles/s41467-020-17581-y cited on pages 12, 50, 74.

Wu, X., N. Vuichard, P. Ciais, N. Viovy, N. de Noblet-Ducoudré, X. Wang, V. Magliulo, M. Wattenbach, L. Vitale, P. Di Tommasi, et al. (2016). "ORCHIDEE-CROP (v0), a new process-based agro-land surface model: model description and evaluation over Europe". In: *Geoscientific Model Development* 9.2, pp. 857–873. ISSN: 1991-9603. DOI: 10.5194/gmd-9-857-2016. URL: https://gmd.copernicus.org/articles/9/857/2016/ cited on pages 32, 90.

Al-Yaari, A., A Ducharne, W Thiery, F Cheruy, and D. Lawrence (2022). "The Role of Irrigation Expansion on Historical Climate Change: Insights From CMIP6". In: *Earth's Future* 10.11, pp. 1–29. ISSN: 2328-4277. DOI: 10.1029/2022EF002859. URL: https://onlinelibrary.wiley.com/doi/10.1029/2022EF002859 cited on pages 20, 87, 126.

Al-Yaari, A., A. Ducharne, F. Cheruy, W. T. Crow, and J. P. Wigneron (2019). "Satellite-based soil moisture provides missing link between summertime precipitation and surface temperature biases in CMIP5 simulations over conterminous United States". In: *Scientific Reports* 9.1, pp. 1–12. ISSN: 20452322. DOI: 10.1038/s41598-018-38309-5. URL: http://dx.doi.org/10.1038/s41598-018-38309-5 cited on pages 19, 49, 87.

Yin, Z., X. H. Wang, C. Ottlé, F. Zhou, M. Guimberteau, J. Polcher, S. S. Peng, S. L. Piao, L. Li, Y. Bo, X. L. Chen, X. D. Zhou, H. Kim, and P. Ciais (2020). "Improvement of the Irrigation Scheme in the ORCHIDEE Land Surface Model and Impacts of Irrigation on Regional Water Budgets Over China". In: *Journal of Advances in Modeling Earth Systems* 12.4, pp. 1–20. ISSN: 1942-2466. DOI: 10.1029/2019MS001770. URL: https://onlinelibrary.wiley.com/doi/abs/10.1029/2019MS001770 cited on pages 27, 29, 31, 32, 34, 89, 91, 113, 116.

Yin, Zun, Catherine Ottlé, Philippe Ciais, Feng Zhou, Xuhui Wang, Polcher Jan, Patrice Dumas, Shushi Peng, Laurent Li, Xudong Zhou, Yan Bo, Yi Xi, and Shilong Piao (2021). "Irrigation, damming, and streamflow fluctuations of the Yellow River". In: *Hydrology and Earth System Sciences* 25.3, pp. 1133–1150. ISSN: 1607-7938. DOI: 10.5194/hess-25-1133-2021. URL: https://hess.copernicus.org/articles/25/1133/2021/ cited on pages 18, 128.

Yokohata, Tokuta, Tsuguki Kinoshita, Gen Sakurai, Yadu Pokhrel, Akihiko Ito, Masashi Okada, Yusuke Satoh, Etsushi Kato, Tomoko Nitta, Shinichiro Fujimori, et al. (2020). "MIROC-INTEG-LAND version 1: a global biogeochemical land surface model with human water management, crop growth, and land-use change". In: *Geoscientific Model De-*

velopment 13.10, pp. 4713–4747. ISSN: 1991-9603. DOI: 10.5194/gmd-13-4713-2020. URL: https://gmd.copernicus.org/articles/13/4713/2020/ cited on page 25.

Zampieri, Matteo, Fabio D'Andrea, Robert Vautard, Philippe Ciais, Nathalie de Noblet-Ducoudré, and Pascal Yiou (2009). "Hot European Summers and the Role of Soil Moisture in the Propagation of Mediterranean Drought". In: *Journal of Climate* 22.18, pp. 4747–4758. ISSN: 1520-0442. DOI: 10.1175/2009JCLI2568.1. URL: http://journals.ametsoc.org/doi/10.1175/2009JCLI2568.1 cited on page 48.

Zelinka, Mark D., Timothy A. Myers, Daniel T. McCoy, Stephen Po-Chedley, Peter M. Caldwell, Paulo Ceppi, Stephen A. Klein, and Karl E. Taylor (2020). "Causes of Higher Climate Sensitivity in CMIP6 Models". In: *Geophysical Research Letters* 47.1, pp. 1–12. ISSN: 0094-8276. DOI: 10.1029/2019GL085782. URL: https://onlinelibrary.wiley.com/doi/abs/10.1029/2019GL085782 cited on page 10.

Zeng, Yujin, Zhenghui Xie, Shuang Liu, Jinbo Xie, Binghao Jia, Peihua Qin, and Junqiang Gao (2018). "Global Land Surface Modeling Including Lateral Groundwater Flow". In: *Journal of Advances in Modeling Earth Systems* 10.8, pp. 1882–1900. ISSN: 19422466. DOI: 10.1029/2018MS001304. URL: http://doi.wiley.com/10.1029/2018MS001304 cited on page 24.

Zhang, Xuebin, Lisa Alexander, Gabriele C. Hegerl, Philip Jones, Albert Klein Tank, Thomas C. Peterson, Blair Trewin, and Francis W. Zwiers (2011). "Indices for monitoring changes in extremes based on daily temperature and precipitation data". In: *WIREs Climate Change* 2.6, pp. 851–870. ISSN: 1757-7780. DOI: 10.1002/wcc.147. URL: https://onlinelibrary.wiley.com/doi/10.1002/wcc.147 cited on page 77.

Zhang, Xuebin, Gabriele Hegerl, Francis W. Zwiers, and Jesse Kenyon (2005). "Avoiding Inhomogeneity in Percentile-Based Indices of Temperature Extremes". In: *Journal of Climate* 18.11, pp. 1641–1651. ISSN: 1520-0442. DOI: 10.1175/JCLI3366.1. URL: http://journals.ametsoc.org/doi/10.1175/JCLI3366.1 cited on page 77.

Zhao, Y, A Ducharne, B Sultan, P Braconnot, and R Vautard (2015). "Estimating heat stress from climate-based indicators: present-day biases and future spreads in the CMIP5 global climate model ensemble". In: *Environmental Research Letters* 10.8, p. 084013. ISSN: 1748-9326. DOI: 10.1088/1748-9326/10/8/084013. URL: https://iopscience.iop.org/article/10.1088/1748-9326/10/8/084013 cited on pages 77, 131.

Zhou, Sha, A. Park Williams, Benjamin R. Lintner, Alexis M. Berg, Yao Zhang, Trevor F. Keenan, Benjamin I. Cook, Stefan Hagemann, Sonia I. Seneviratne, and Pierre Gentine (2021a). "Soil moisture–atmosphere feedbacks mitigate declining water availability in drylands". In: *Nature Climate Change* 11.1, pp. 38–44. ISSN: 1758-678X. DOI: 10.1038/s41558-020-00945-z. URL: http://dx.doi.org/10.1038/s41558-020-00945-z%20http://www.nature.com/articles/s41558-020-00945-z cited on page 6.

Zhou, Xudong, Jan Polcher, and Patrice Dumas (2021b). "Representing Human Water Management in a Land Surface Model Using a Supply/Demand Approach". In: *Water Resources Research* 57.4, pp. 1–33. ISSN: 0043-1397. DOI: 10.1029/2020WR028133. URL:

https://onlinelibrary.wiley.com/doi/10.1029/2020WR028133 cited on pages 18, 128.

Zhu, Zaichun, Jian Bi, Yaozhong Pan, Sangram Ganguly, Alessandro Anav, Liang Xu, Arindam Samanta, Shilong Piao, Ramakrishna Nemani, and Ranga Myneni (2013). "Global Data Sets of Vegetation Leaf Area Index (LAI)3g and Fraction of Photosynthetically Active Radiation (FPAR)3g Derived from Global Inventory Modeling and Mapping Studies (GIMMS) Normalized Difference Vegetation Index (NDVI3g) for the Period 1981 to 2". In: *Remote Sensing* 5.2, pp. 927–948. ISSN: 2072-4292. DOI: 10.3390/rs5020927. URL: http://www.mdpi.com/2072-4292/5/2/927 cited on page 99.

Zipper, Samuel C., Jessica Keune, and Stefan J. Kollet (2019). "Land use change impacts on European heat and drought: Remote land-atmosphere feedbacks mitigated locally by shallow groundwater". In: *Environmental Research Letters* 14.4, p. 44012. ISSN: 17489326. DOI: 10.1088/1748-9326/ab0db3. URL: http://dx.doi.org/10.1088/1748-9326/ab0db3 cited on pages 14, 75.

Zobler, L. (1986). *A world soil hydrology file for global climate modeling, Technical Memorandum 87802, National Aeronautics and Space Administration*. Washington cited on pages 33, 52, 90.